A single wake oscillator model for coupled cross-flow and in-line vortex-induced vibrations of marine structures

Qu, Yang

Important note
To cite this publication, please use the final published version (if applicable).
Please check the document version above.

A SINGLE WAKE-OSCILLATOR MODEL FOR COUPLED CROSS-FLOW AND IN-LINE VORTEX-INDUCED VIBRATIONS OF MARINE STRUCTURES

A SINGLE WAKE-OSCILLATOR MODEL FOR COUPLED CROSS-FLOW AND IN-LINE VORTEX-INDUCED VIBRATIONS OF MARINE STRUCTURES

Dissertation

for the purpose of obtaining the degree of doctor
at Delft University of Technology
by the authority of the Rector Magnificus prof. dr. ir. T.H.J.J. van der Hagen
chair of the Board for Doctorates
to be defended publicly on
Monday 15 April 2019 at 12:30 o'clock

by

Yang QU

Master of Science in Mechanical Engineering, China University of Petroleum, China
born in Shandong, China.

This dissertation has been approved by the promotor.

Composition of the doctoral committee:
  Rector Magnificus, Chairperson
  Prof. dr. A.V. Metrikine, Delft University of Technology, promotor

  Independent members:
  Prof. dr. ir. W.S.J. Uijttewaal, Delft University of Technology
  Prof. dr. P.G. Steeneken, Delft University of Technology
  Prof. dr. E. Pavlovskaia, University of Aberdeen, Scotland, UK
  Prof. dr. S. Sævik, Norwegian University of Science and Technology, Norway
  Prof. dr. L. Huang, The University of Hong Kong, China
  Prof. dr. O. Doaré, ENSTA ParisTech, France

To my family

献给我的家人

CONTENTS

SUMMARY

Vortex-induced vibration (VIV) is a well-known phenomenon for civil and offshore structures. Currently, the prediction of this type of vibration in practice currently mainly relies on the force-decomposition method. However, the limitations of this method have restricted the applicability of the method, and alternative models are therefore needed to meet increasing demands for the more accurate prediction of VIV under more complicated conditions. The wake oscillator model overcomes the main limitations of the force-decomposition method to some extent, and it is one of the promising models that has gained popularity in recent years. Although the concept of the wake oscillator was first proposed over half a century ago and has been developed much since then, the existing wake oscillator models still have some limitations, which have restricted their applications.

The main objective of this study is to improve the wake oscillator model for better modelling of the VIV of cylindrical structures, and efforts are made in this thesis to (a) reproduce the free and forced vibration experiments by introducing nonlinear coupling, and (b) develop a single wake oscillator equation that is coupled to both cross-flow and in-line motions for the prediction of coupled cross-flow and in-line VIV.

An existing wake oscillator model, which serves as the foundation for further improvements, is reviewed. Before proceeding to improve the lift force model, different drag force models, as well as their influence on the dynamic characteristics of the lift force that conforms to the forced vibration experiment, are investigated. Three different drag force models are analysed, and it is demonstrated that all three models result in a similar lift force. The identified lift force exhibits an obvious resonance pattern at small amplitudes of cylinder oscillation; however, this is no clear resonance pattern at large amplitudes.

The evolution of the lift force with the amplitude of vibration may be the result of nonlinearity. Therefore, the possibility of improving the predictive capabilities of the wake oscillator models by means of tuning their nonlinearity is investigated. Nonlinearity is introduced through the coupling between the wake oscillator equation and the cylinder motion in the form of multiplications of displacement, velocity and acceleration of the cylinder. Both constant and frequency dependent coupling coefficients are considered. The model with constant coupling coefficients is shown to be able to quantitatively reproduce the added damping measured in the forced vibration experiments over most of the range of frequencies and amplitudes that are of interest. However, it fails to capture the negative added mass observed in experiments. The model with frequency dependent coupling is formulated in the time domain with the help of convolution integrals. A single set of frequency dependent, complex-valued functions—which are the Laplace transforms of corresponding convolution kernels—that reproduce the forced vibration experiments fairly well is determined over a limited range of frequencies. However, it proved to be not possible to extend these functions to the infinite fre-

quency domain such that the causality principle and the energy conservation would be satisfied.

With respect to the development of the wake oscillator model for the prediction of coupled cross-flow and in-line VIV, the original wake oscillator model without nonlinear coupling is adopted, and a new in-line coupling term is introduced to include the effect of in-line motion. The in-line coupling term is inspired by the experimental observation as well as the heuristic inference from the dynamics of a pendulum. The new wake oscillator model has been validated against experiments with a rigid cylinder and is shown to be able to predict the appearance of the super-upper branch in coupled cross-flow and in-line VIV when the mass ratio of the system decreases.

The new wake oscillator model is then applied in the modelling of the coupled cross-flow and in-line VIV of flexible cylinders, and it is validated against a series of experiments where a top-tensioned riser is subjected to step flows. The model is shown to be able to capture most features of the VIV of flexible cylinders, and a good agreement is observed between the simulation results and experimental measurements. It is interesting to note that while it is conventionally expected that the VIV of flexible cylinders subjected to uniform flow is dominated by a single frequency, a multi-frequency response is observed in the simulation results over the range of flow velocities through which the transition of the dominant mode of vibration occurs.

The importance of in-line coupling and its influence on the prediction of the coupled cross-flow and in-line VIV of the flexible cylinder is studied through comparisons of simulation results of the VIV of a flexible riser obtained with different models. Both the cases of uniform and linearly sheared flow are analysed. It is shown that for the sheared flow cases, the response of the riser predicted by the models with and without in-line coupling is similar, while that for the uniform flow cases is significantly different. This difference is found to be related to the energy transfer between the fluid and the structure. For the sheared flow cases, the energy transfer predicted by all models is found to mainly depend on the reduced velocity. For the uniform flow cases, the energy transfer according to the model without in-line coupling is primarily dependent on the amplitude of vibration, while for that with in-line coupling, the motion trajectory also plays an important role.

The fatigue damage predicted by the model with and without in-line coupling is also studied. In general, the model with in-line coupling predicts a higher fatigue damage rate, compared to the model without in-line coupling, as a result of significant contributions from higher harmonics.

SAMENVATTING

Wervel-geïnduceerde trillingen (Engels: Vortex-Induced Vibration, afgekort tot: VIV) zijn een bekend verschijnsel in de civiele en offshore techniek. De voorspelling van deze trillingen is momenteel voornamelijk gebaseerd op de zogenaamde 'force-decomposition' methode. Deze methode is echter slechts toepasbaar in een beperkt aantal gevallen. Er zijn daarom alternatieve modellen nodig voor een betere voorspelling van VIV in gecompliceerdere gevallen. Het zogenaamde 'wake oscillator model' verbetert in zekere mate de grootste tekortkomingen van de 'force-decomposition' methode. Dit veelbelovende model heeft de afgelopen jaren aan populariteit gewonnen. Alhoewel de basis van het wake oscillator model meer dan 50 jaar geleden is ontwikkeld, hebben de huidige wake oscillator modellen nog beperkingen die hun toepasbaarheid begrenzen.

Het doel van deze studie is het verbeteren van de wake oscillator zodat dit model VIV rond cilindrische constructies beter beschrijft. In deze thesis is gepoogd om: a) de forceerde trilling-experimenten te reproduceren door gebruik te maken van niet-lineaire koppelingstermen, en b) een wake oscillator te ontwikkelen die slechts met één vergelijking bewegingen van de constructie zowel parallel aan, als dwars op de stromingsrichting kan beschrijven.

Een bestaand wake oscillator model wordt besproken, dat dient als de basis voor verdere verbetering. Voordat met verbetering van het model voor de lift kracht wordt begonnen, worden eerst verschillende modellen voor beschrijving van de weerstandskracht onderzocht. Hierbij wordt gekeken naar de invloed van de weerstandskracht op de dynamische eigenschappen van de lift kracht tijdens modelering van geforceerde trilling-experimenten. Drie verschillende modellen voor beschrijven van de weerstandskracht zijn onderzocht. Er wordt aangetoond dat in alle drie de modellen een vergelijkbare lift kracht wordt gevonden. De geïdentificeerde lift krachten vertonen een duidelijk resonantie patroon wanneer de cilindrische constructie met een kleine amplitude beweegt. Dit is in duidelijke tegenstelling met de resonantie patronen wanneer de bewegingsamplitudes groot zijn.

De verandering van de resonantie patronen bij het verloop van kleine naar grote bewegingsamplituden zou het gevolg van niet-lineariteiten kunnen zijn. Daarom is onderzocht of de geforceerde trilling-experimenten beter beschreven kunnen worden door introductie van niet-lineariteiten in de koppelingstermen tussen de wake oscillator vergelijking en de bewegingsvergelijking van de cilindrische constructie. Deze niet-lineariteiten bestaan uit vermenigvuldigingen met de cilinder verplaatsing, snelheid en versnelling. Zowel constante als frequentie-afhankelijke koppelingscoëfficiënten zijn onderzocht. Het model met constante koppelingscoëfficiënten is in staat om kwantitatief de toegevoegde demping te beschrijven, zoals gemeten in de geforceerde trilling-experimenten over een groot bereik van de frequenties en amplitudes van belang. Het model kan echter niet de gemeten negatieve toegevoegde massa beschrijven. In het frequentie afhankelijke model, wordt de frequentie afhankelijkheid gemodelleerd door gebruik te maken van

convolutie-integralen in het tijdsdomein. Frequentie afhankelijke, complexe functies zijn bepaald, waarvan de Laplacetransformatie de convolutie kern is. Het frequentie afhankelijke model kan de geforceerde trilling-experimenten redelijk goed beschrijven over een beperkt bereik van frequenties. Het is echter niet gelukt de complexe functies uit te breiden over het oneindige frequentie bereik, zodat de convolutie op een correcte manier een causaal signaal beschrijft dat voldoet aan de wet van behoud van energie.

Voor de beschrijving van de gekoppelde cilinder bewegingen door VIV in zowel de dwarsstroomse richting als de richting parallel aan de stroming is het originele wake oscillator model toegepast met een nieuw toegevoegde parallelle koppeling. Deze extra term is toegevoegd om het effect van de parallelle beweging goed te beschrijven. Deze term is gebaseerd op zowel experimentele waarnemingen als op heuristische beschouwingen gebaseerd op de dynamica van een starre slinger. Deze nieuwe wake oscillator is gevalideerd tegen experimenten met een starre cilinder en er wordt aangetoond dat dit model de 'super-upper branch' van VIV, in het geval van gekoppelde bewegingen in de dwarsstroomse richting en de richting parallel aan de stroming, kan beschrijven wanneer de massa ratio van het systeem afneemt.

Het nieuwe wake oscillator model is vervolgens toegepast op een flexibele cilinder op de gekoppelde bewegingen in dwarsstroomse richting en de richting parallel aan de stroming. Het model is gevalideerd tegen een serie experimenten waarin een 'top-tensioned riser' is onderworpen aan een stapsgewijze stroming. Er wordt getoond dat het model in staat is de belangrijkste kenmerken van VIV van flexibele cilinders te beschrijven. Een goede overeenkomst tussen simulatie en experimentele resultaten is waargenomen. Het is interessant om op te merken dat er doorgaans wordt aangenomen dat VIV van flexibele cilinders onderworpen aan een uniforme stroming gedomineerd wordt door een enkele frequentie, terwijl de waargenomen responsie in de simulatie gekenmerkt wordt door meerdere frequenties in het bereik van stromingssnelheden waarin de transitie naar de dominante trilling vorm plaatsvindt.

De invloed van de koppelingsterm in de richting parallel aan de stroming op het gekoppelde bewegingsgedrag van de flexibele cilinder zowel in de stromingsrichting als in de dwarsstroomse richting is onderzocht door middel van het vergelijken van de simulaties met verschillende modellen. Zowel gevallen met uniforme stroming als met over de diepte verlopende stromingssnelheden zijn onderzocht.

Er wordt aangetoond dat in de gevallen met verlopende stroming, de responsie van de riser zoals beschreven door de modellen met een koppelingsterm in de richting parallel aan de stroming sterk overeenkomt met responsie beschreven door modellen zonder deze koppelingsterm. Voor gevallen met uniforme stroming is dit duidelijk niet het geval. Dit verschil is gerelateerd aan de energie overdracht tussen vloeistof en constructie. Er is gevonden dat voor de gevallen met verlopende stroming, de gemodelleerde energie overdracht voornamelijk afhankelijk is van de gereduceerde snelheid. Voor de gevallen met uniforme stroming is de energie overdracht in het geval van geen koppelingsterm in de parallelle richting voornamelijk afhankelijk van de bewegingsamplitude, terwijl voor de gevallen met koppelingstermen in deze richting, het bewegingspatroon ook een sterke rol speelt.

De vermoeiingsschades die voorspeld wordt door het model met en zonder koppelingsterm in de parallelle richting zijn onderzocht. In het algemeen kan gezegd worden

dat het model met koppelingsterm in deze meer vermoeiingsschade voorspelt. Dit wordt veroorzaakt door de aanwezigheid van hogere harmonische componenten in de responsie.

1

INTRODUCTION

1.1. VORTEX-INDUCED VIBRATIONS IN ENGINEERING

Vortex-induced vibration (VIV) is a well-known phenomenon to civil engineers as it often occurs in flexible cylindrical structures, such as chimneys, cables of suspended bridges, suspended power lines, offshore risers and mooring cables, that are subjected to air or water flows. This vibration can lead to the rapid accumulation of fatigue damage, or it can even result in the sudden collapse of a structure. For example, in January 2002, a tall circular steel support structure that was part of the Vertigo thrill ride at Cedar Point suddenly collapsed as a result of VIV (Klamo, 2007).

The phenomenon of VIV has been extensively studied in the past decades, and the main driver behind this is the fast development of the offshore oil and gas industry. As the exploration of fossil sources extends to deep oceans, many structural components that are used for drilling and production can be several thousand meters long, which makes them particularly susceptible to VIV. Being dominated by tension, the offshore risers normally possess natural frequencies that are densely spaced. Therefore, resonant response due to vortex shedding can take place over a wide range of flow velocities. Also, with low fundamental frequencies, the VIV of these structures often occurs in higher modes. The vibration at these high modes leads to significant fatigue damage, and the prediction of VIV has thus been one of the key issues in the analysis and design of offshore structures.

The VIV of offshore structures often manifests itself in a complicated manner. With flow conditions that change temporally and spatially in the ocean environment, the global behaviour of a structure is a result of a complicated interaction between the structure and flow at local positions as well as its influence on the nearby regions. With vortices being shed at different frequencies along the slender body, the response of the structure contains multiple frequencies. Under such circumstances, each point on the structure has a motion that is not simply harmonic, but rather is amplitude-modulated in both space and time (Gopalkrishnan, 1993). The complexity of the problem and limited understanding of the underlying mechanism make the prediction of the VIV of flex-

1
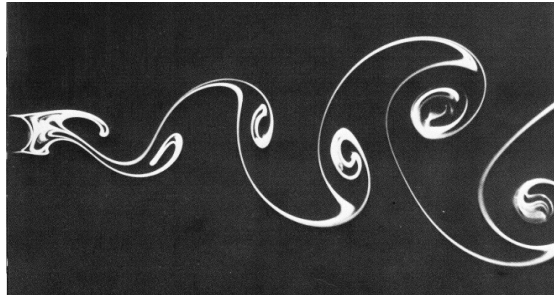
Figure 1.1: Van Karman vortex street behind a stationary cylinder (van Dyke, 1982)

ible cylinders difficult. In practice, the fatigue damage of offshore structures due to VIV is mostly estimated based on empirical methods, and large safety factors are applied.

1.2. THE PHENOMENON OF VORTEX-INDUCED VIBRATION

As a flow passes a circular cylinder, due to the fluid viscosity, a boundary layer will be formed, and the flow will separate from the cylinder, resulting in vortex shedding downstream of the cylinder (Fig. 1.1). The formation of the vortex shedding depends on the dimension of the cylinder as well as the fluid conditions, which can be characterised by the Reynolds number

$$\text{Re} = \frac{VD}{\mu} \tag{1.1}$$

where V is the undisturbed flow velocity, D is the cylinder diameter and μ is the kinematic viscosity (about 1.1×10^{-6} m^2/s for sea water). The vortex shedding takes place for Reynolds numbers larger than 40. For a Reynolds number higher than 300, the vortex street evolves from laminar to fully turbulent. It should also be pointed out that after a certain Reynolds number (approximately 200,000–500,000) the two-dimensional (2D) character of the flow breaks down, and strong three-dimensional (3D) effects are observed. In such a situation, the vortex shedding is no longer coherent in the spanwise direction, and vortices are shed in cells (Sumer and Fredsøe, 2006).

One main property of vortex shedding is its periodicity. For a fixed cylinder, vortices are shed alternatively from both sides of the cylinder, and its frequency is given by

$$\omega_s = 2\pi \frac{\text{St}V}{D} \tag{1.2}$$

where St is an experimentally measured number known as the Strouhal number. Although influenced by many factors, the value of the Strouhal number remains surprisingly constant around 0.2 over a large range of Reynolds numbers (Norbegr, 2001).

As fluid flows around the circular cylinder, the alternate shedding of vortices in the near wake gives rise to a fluctuating cross-flow force on the cylinder. In the cases where

1

the cylinder is free to move, the fluctuating hydrodynamic force can result in self-excited oscillation of the body. With certain phase differences between the hydrodynamic force and body motion, energy may transfer from the fluid to the body, which in turn amplifies the magnitude of the oscillation. As the amplitude of the body vibration increases, it affects the vortex shedding process and consequently alternates the direction of the energy transfer. This change of energy transfer results in a self-exciting and self-limiting vibration of the structure, which is known as VIV. Experiments have demonstrated that for an elastically-mounted rigid cylinder, the VIV reaches maximum when the vortex shedding frequency approaches the natural frequency of the system. Within a certain range of flow velocities that brackets the natural frequency of the system, the vortex shedding frequency will deviate from the Strouhal relation, and it collapses onto the oscillation frequency of the cylinder, resulting in the sustained vibration of the cylinder over a wide range of flow velocities. This phenomenon is known as lock-in.

1.3. STATE OF THE ART IN THE PREDICTION OF VORTEX-INDUCED VIBRATION

Driven by the urgent demand from the oil and gas industry, VIV has been extensively studied in the past century to develop a prediction tool that can be applied in the design of offshore structures. Due to the complexity of the fluid-structure interaction problem, most knowledge about VIV to date has been obtained from physical experiments. It is the VIV of rigid cylinders that has been the focus of early research. Two types of experiments have been adopted by the majority of researchers to investigate the problem: free and forced vibration tests. In the free vibration tests an elastically supported rigid cylinder vibrates due to the fluid-structure interaction, and the characteristics of the motion are analysed. The forced vibration test, on the other hand, investigates the hydrodynamic forces acting on and the wake structure behind a cylinder that is forced to vibrate with constant amplitude and frequency. Recent reviews of these studies can be found in the papers by Williamson and Govardhan (2004) and Sarpkaya (2004). The accumulated results from the investigation of the VIV of rigid cylinders have provided some insights into the fundamental mechanism of VIV. However, the understanding of the VIV of a rigid cylinder is still inadequate for the development of proper prediction models. The strong nonlinearity of the problem cannot be fully understood by studying only the nearly harmonic oscillation of a rigid cylinder, and the obtained results can only be applied to the prediction of the VIV of flexible cylinders under specific conditions.

The ultimate solution for the prediction of VIV may lie in the application of advanced numerical techniques, such as the computational fluid dynamics (CFD). The CFD approach is based on solving the Navier-Stokes equations numerically for the fluid-structure coupled system. This approach allows for the modelling of a realistic flow field but requires a large amount of data storage and computational time. A possible approach to reduce the computational cost is to apply the so-called strip theory according to which the interaction between the structure and flow is only simulated at certain locations along the span. With this approach, simulations have been conducted on long flexible cylinders with large aspect ratios at high Reynolds numbers (Schulz and Meling, 2004; Willden and Graham, 2004; Yamamoto et al., 2004). Although the simulation re-

sults agree quite well with the experiments, the strip theory neglects the 3D effect of the flow and can only be considered as a reasonable approximation of certain cases (Holmes et al., 2006). With the advances in computer technology in recent years, it is feasible to conduct a full 3D CFD simulation of the VIV of long flexible cylinders in a more detailed manner with an acceptable amount of computation time (Huang et al., 2010). However, the computational time for single simulation is still significant, which means it is not yet a practical solution for industry.

The industry currently relies mainly on the force-decomposition method for the prediction of the VIV of flexible structures. This method, originally based on the work by Sarpkaya (1978), is semi-empirical. The basis of the method is the use of a hydrodynamic forces database, which is obtained from forced vibration tests. In such tests, a rigid cylinder is forced to vibrate harmonically in a steady flow with a prescribed motion, and the hydrodynamic forces acting on the cylinder are measured. The fluid forces are recorded with a cylinder oscillating over a certain range of frequencies and amplitudes, which are further decomposed into a part in phase with the cylinder acceleration (acts as added mass) and another part in phase with the cylinder velocity (acts as added damping). The obtained hydrodynamic forces are directly applied as the forcing term in the equation of motion of the flexible structure, and the amplitude and frequency of the response are normally obtained through an iterative procedure in the frequency domain. Based on this concept, several prediction tools, such as SHEAR7 and VIVANA, have been developed. Despite its wide application in the industry, the force-decomposition approach has several key limitations. First, there are still concerns regarding the use of the force obtained from forced vibration experiments to predict free vibration (Carberry et al., 2004; Hover et al., 1998). Second, as mentioned in the previous subsection, the VIV of flexible cylinders normally exhibits multiple frequency responses. In such circumstances, the results obtained from the pure harmonic test at a single frequency cannot be directly applied (Gopalkrishnan, 1993). Third, the forced vibration experiments are usually conducted with the motion of the cylinder restricted to one – either cross-flow (Gopalkrishnan, 1993; Morse and Williamson, 2009) or in-line (Aronsen, 2007) – direction. However, in reality, the structure almost always vibrates in both directions simultaneously. The coupled cross-flow and in-line motion has a significant effect on the dynamics of the wake and consequently influences the fluid forces (Dahl et al., 2007; Jauvtis and Williamson, 2004). An attempt has been made to conduct two degree of freedom forced vibrations to build a more advanced force database. However, the large number of control parameters makes it difficult to build a complete database with sufficient resolution, and interpolation of the relatively sparse database is not an ideal option due to the strong nonlinearity of the problem (Dahl, 2008).

The wake oscillator model is another type of model that is more often used in the research field than in the industry for the description of VIV. The fundamental idea of this method is to describe the dynamics of the wake using an effective nonlinear oscillator, whose motion is coupled to the dynamics of the cylinder. Instead of modelling the real flow field, this model attempts to reproduce the main features of VIV observed in experiments, and it is thus phenomenological. The concept of the wake oscillator can be dated back to the 1950s when Birkhoff (1953) tried to find expressions for the Strouhal frequency and vortex spacing in the wake through a linear oscillator that de-

scribes the motion of the angle between the wake axis and incoming flow. Bishop and Hassan (1964) was the first to suggest the idea of using a van der Pol nonlinear oscillator for the description of the hydrodynamic force. A large number of wake oscillators have been proposed since then in the 1970s and 1980s (Hartlen and Currie, 1970; Iwan and Blevins, 1974; Landl, 1975; Skop and Griffin, 1973). For a detailed description of these models, please refer to the review written by Gabbai and Benaroya (2005). In more recent studies, one main contribution is from Facchinetti et al. (2004) in which a classical van der Pol oscillator is used to model the near wake dynamics, and the effects of several types of linear coupling terms (displacement, velocity and acceleration) modelling the fluid-structure interaction are investigated. Facchinetti et al. (2004) found that the acceleration coupling is most appropriate for the modelling of most of the features of VIV. This van der Pol oscillator model was further improved by properly including the effect of the stall term, dropping the assumption of a small angle of attack (Ogink and Metrikine, 2010). As the importance of the effect of the in-line motion on the wake dynamics is emphasised by an increasing number of studies, the development of the wake oscillator model that can describe the coupled cross-flow and in-line VIV becomes the focus of recent research (Bai and Qin, 2014; Kim and Perkins, 2002; Postnikov et al., 2017; Srinil and Zanganeh, 2012).

The wake oscillator model has a certain advantage over the force-decomposition method with regard to the fact that it is a time domain model. Therefore, instead of using an iterative scheme, as the force-decomposition model does, the model will find the response's amplitude and frequency of its own accord. Also, being a time domain approach, the wake oscillator model can take into account the nonlinearity of the structure. The promising results in the simulation of the VIV of flexible cylinders with the wake oscillator model have made it an increasingly attractive alternative to the force-decomposition model (Bai and Qin, 2014; Ge et al., 2009; Violette et al., 2007; Xu et al., 2008; Zanganeh and Srinil, 2016).

Apart from the three types of models described above, other models have also been developed – for detailed information, please refer to the review by Gabbai and Benaroya (2005). A new method for the time domain modelling of VIV has recently been developed by Thorsen et al. (2014). This method is based on a synchronization model which simulates how the instantaneous frequency of the lift force reacts to the structure motion. The phase difference between the synchronized lift force and the velocity of the structure is defined such that the added damping obtained from the model matches that measured from the forced vibration tests. This method has been applied in the prediction of the VIV of flexible cylinders subject to stationary and oscillating flows and the results are promising (Thorsen et al., 2015, 2016).

1.4. WAKE OSCILLATOR MODELS AND THEIR LIMITATIONS

The wake oscillator model has gained popularity in recent years due to its low computational cost and acceptable performance in reproducing the experiment results. Especially with the efforts devoted to derive the reduced-order model from the first-principle model, the underlying connection between the wake oscillator model and fluid dynamics becomes clearer (Gabbai and Benaroya, 2008; Mottaghi and Benaroya, 2016). However, the model still has several limitations, which prevent it from being widely applied

1

in the prediction of VIV.

Although the wake oscillator model qualitatively captures the main characteristics of VIV, applying it in the prediction of VIV requires it to reproduce the experiments more quantitatively. In fact, this has been the focus of recent studies, and much effort has been placed on the modification of existing oscillator equations such that a better reproduction of the results from free vibration experiments of elastically supported rigid cylinders can be achieved. Attention has only recently been placed on the development of a wake oscillator model that can also reproduce the forced vibration experiments (Ogink and Metrikine, 2010), which, in the authors' opinion, is of high importance. In contrast to the free vibration experiments, the forced vibration experiments, in which a certain amplitude and frequency of the harmonic motion of a cylinder is maintained, provide additional insights into the interaction mode between hydrodynamic forces and cylinder motion. Only with the reproduction of the main features of the forced vibration experiments can the wake oscillator model be classified as a useful one, as it will contain correct nonlinearities that describe the interaction between the flow and structure. Based on the wake oscillator proposed by Facchinetti et al. (2004), Ogink and Metrikine (2010) tried to reproduce the forced vibration experiments using frequency-dependent coupling terms. After failing to identify a single set of coefficients that satisfy the experiments at different amplitudes, Ogink and Metrikine (2010) concluded that the nonlinearity contained in the oscillator equation is not correct.

Another main limitation of the model comes from its capability in the modelling of coupled cross-flow and in-line VIV. Although a large number of wake oscillator models have been developed for the prediction of the cross-flow response of a structure, only a few attempts have been made to model the coupled cross-flow and in-line VIV (Bai and Qin, 2014; Ge et al., 2009; Kim and Perkins, 2002; Postnikov et al., 2017; Srinil and Zanganeh, 2012). For the latter, the approach of introducing a second nonlinear wake oscillator for the description of the oscillating drag force, in addition to the one that describes the lift force, has been widely employed; see, for example, Kim and Perkins (2002); Postnikov et al. (2017); Srinil and Zanganeh (2012). Efforts have been made to tune the model to the experimental measurements, and the influence of the empirical parameters on the simulation results have been investigated (Postnikov et al., 2017; Srinil and Zanganeh, 2012). Although good agreements between the simulation and experiments have been achieved, the phenomenon of the 'super-upper' branch – characterised by the appearance of a large amplitude of cross-flow vibration at a small mass ratio (Williamson and Govardhan, 2004) – which is the most important characteristic of coupled cross-flow and in-line VIV, has not yet been captured. The match between the simulation and experiments are obtained by applying different tuning parameters as the experimental condition, such as mass ratio, changes. The use of the second wake oscillator that is coupled with the in-line motion for the description of the oscillating drag force seems logical, as experiments have demonstrated that VIVs also occur when the motion of the cylinder is limited to the in-line direction (Konstantinidis, 2014; Nakamura et al., 2001; Nishihara et al., 2005). However, it should be kept in mind that both the cross-flow and in-line hydrodynamic forces have the same origin, which is the dynamics of the wake. It is physically more reasonable to use only one oscillator to describe the dynamics of the wake, and this oscillator should be coupled to both cross-flow and in-line

1

motions of the cylinder.

1.5. THESIS AIMS

It can be concluded from above-presented discussion that despite a relatively good understanding of VIV by the research community, the quantitative prediction thereof still relies on empirical methods. The conventional force-decomposition approach has reached a bottleneck due to its incapability to accurately predict the VIV at multiple frequencies as well as the coupled cross-flow and in-line vibrations. On the other hand, the wake oscillator model begins to reveal its potential to overcome the drawbacks of the force-decomposition method, and it is a promising method for further development. However, there are still several major limitations that restrict the practical application of the existing wake oscillator models. The first main limitation is that the correspondence between the results of the cross-flow free and forced vibration tests and the model predictions is unsatisfactory. The second limitation is that the currently existing wake oscillator models that describe the coupled cross-flow and in-line VIV by introducing a second wake oscillator equation violate the physics of the process.

In correspondance with the above-mentioned main limitations of the currently existing wake oscillator models, the aim of this research is twofold. The first one is to improve the wake oscillator model proposed by Ogink and Metrikine (2010) such that a better agreement with the cross-flow free and forced vibration tests is achieved. The second one is to develop a model that describes the coupled cross-flow and in-line VIV with a single wake oscillator equation.

1.6. THESIS OUTLINES

This thesis is structured as follows:

In Chapter 2, the wake oscillator model proposed by Ogink and Metrikine (2010) is first reviewed, and the review provides the basis for further improvements. The correct reproduction of the hydrodynamic force measured in experiments requires the proper modelling of both lift and drag forces. A preliminary investigation into the influence of different drag force models on the characteristic of the fluctuating lift force that satisfies the test results is conducted.

In Chapter 3, a new wake oscillator model with nonlinear coupling is proposed in order to have a better reproduction of the forced vibration experiments. First, a set of nonlinear coupling terms in the form of multiplications of displacement, velocity and acceleration of the cylinder with constant coupling coefficients is adopted. Although promising, an obvious discrepancy is still observed between the simulation and experiments. To remove this discrepancy, the model is further enhanced by making the nonlinear coupling terms frequency-dependent by means of introduction of convolution integrals in the time domain. Attempts are made to determine the kernels of the convolution integrals that satisfy the forced vibration experiments.

In Chapter 4, an advanced wake oscillator equation that is coupled to both the cross-flow and in-line motions is developed. A new in-line coupling term is introduced based on the experimental observation as well as heuristic inference. The new model is validated against free vibration experiments regarding the coupled cross-flow and in-line

1

VIV of elastically supported rigid cylinders, and it proved to be able to capture the super-upper branch.

Chapter 5 concerns the modelling of the coupled cross-flow and in-line VIV of flexible cylinders. The structure is modelled as a geometrically nonlinear Euler-Bernoulli beam, whereas the interaction between the fluid and structure is described by the wake oscillator model proposed in Chapter 4. The coupled system is solved using the finite element method and applied to the simulation of a set of experiments where a vertical flexible riser is subjected to a step flow. A comparison is made between the simulation results and experimental measurements with regard to the amplitude, frequency and dominant modes of the riser vibrations in both cross-flow and in-line directions as well as the mean in-line deflection. A discussion is also presented with regard to the multiple frequency responses predicted by the model at some flow velocities that are not reported by the experiments.

Chapter 6 is devoted to the comparison between the proposed model and another two models without in-line coupling. Comparisons are made based on the simulation results of the VIV of a flexible cylinder subjected to both uniform and linearly sheared flows. The differences between the predictions from the three models are highlighted from the following points of view: response pattern, motion trajectory and fluid-structure energy transfer. The fatigue damage estimation from the three models is also discussed in the last section of this chapter, with a focus on the investigation into contributions from higher harmonics.

Finally, in Chapter 7 the main findings of this thesis are summarised.

2

WAKE OSCILLATOR MODEL BY OGINK AND METRIKINE

2.1. INTRODUCTION

In the development of the wake oscillator model, most studies have focused on the improvement of oscillator equations that are able to reproduce the results of free vibration experiments. Their goal is to find a model that can simultaneously predict the range of flow velocities, over which lock-in takes place, and the maximum amplitude of cylinder oscillation. It is only recently that attention has been placed on the development of the hydrodynamic force model that can also reproduce forced vibration experiments (Ogink and Metrikine, 2010; Thorsen et al., 2014).

Ogink and Metrikine (2010) are the first authors who attempted to develop such a wake oscillator model that is able to reproduce both the free and forced vibration experiments. In their work, they tried to formulate the total hydrodynamic force as a summation of the ideal inviscid inertia force and a 'vortex force'. This is a common approach taken in most wake oscillator models. The novelty of their work lies in the formulation of the vortex force. Different from other models where only the component of the vortex force in the cross-flow direction is considered, the vortex force in their model is formulated as a vector normal to the cylinder axis and is decomposed into instantaneous lift and drag forces. The quasi-steady assumption is adopted regarding the drag force, while the influence of the wake dynamics is taken into account by relating the lift force to a wake oscillator that is coupled with the motion of the structure. According to the quasi-steady assumption, the data measured in the static (fixed cylinder) situation can be directly applied in the description of the dynamics of the interaction between a structure and fluid (van der Burgh, 1999). The quasi-steady assumption for the drag force is not fully correct physically as it disregards the time that the wake needs to adopt to any new position of the cylinder. However, this assumption is reasonable as a starting point in the development of the model. In this thesis an attempt is made to improve the model in this regard. The advantage of this force decomposition is threefold: (a) it provides the
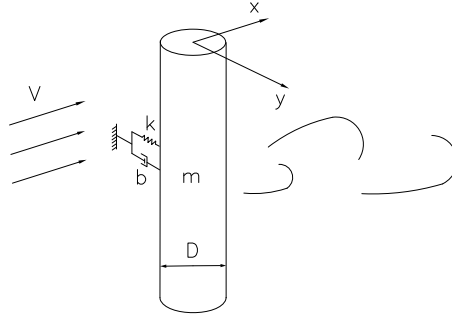
Figure 2.1: Cross-flow VIV of an elastically supported rigid cylinder subjects to uniform flow.

possibility of not only modelling the cross-flow hydrodynamic force but also the in-line force, and the influence of the wake dynamics on both forces have been accounted for through the lift force; (b) the assumption of a linearized stall term that has been taken in previous wake oscillator models is relaxed, and the authors found that the free vibration experiments can be better reproduced if the nonlinear stall effect is considered; and (c) when the cylinder oscillates in the still fluid, this force decomposition leads to that given by the Morison equation.

Despite all of the advantages described above, there are also several problems related to this force decomposition that need to be investigated. One of them is the quasi-steady assumption of the drag force. This assumption is physically incorrect, and whether it provides a reasonable approximation or if another drag force model is required should be studied. The remainder of this chapter is structured as follows. In Section 2.2, the basic mathematical description of the wake oscillator model by Ogink and Metrikine (2010) is briefly presented. Three drag force models, including the one used by Ogink and Metrikine (2010), are investigated in Section 2.3, and the main conclusions are stated in Section 2.4.

2.2. MODEL DESCRIPTION

This section contains a recollection of the wake oscillator model proposed by Ogink and Metrikine (2010). The purpose is to provide a general review of the model.

Fig. 2.1 illustrates the VIV of a rigid cylinder elastically supported in the cross-flow direction. The cylinder has mass m, and its motion is constrained to the cross-flow direction only where it is supported by a spring with stiffness k and dash pot with damping b. The cross-flow displacement of the cylinder $Y(t)$ can be described as

$$m\frac{d^2 Y}{dt^2} + b\frac{dY}{dt} + kY = F_Y. \tag{2.1}$$

On the right-hand side of Eq. (2.1), F_Y is the cross-flow hydrodynamic force acting on the cylinder. This force is assumed to be expressible as a superposition of a vortex force F_{VY} and an ideal inviscid inertia force F_{AY} associated with the potential added mass of
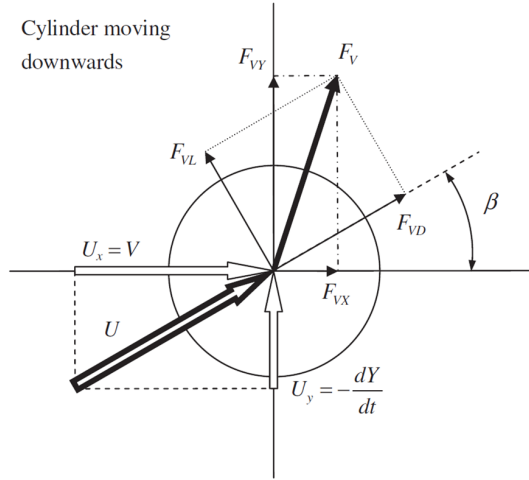
Figure 2.2: Decomposition of the vortex force in drag, lift, cross-flow and in-line directions (Ogink and Metrikine, 2010).

the fluid

$$F_Y = F_{VY} + F_{AY} = \frac{1}{2}\rho DLV^2 C_{VY} - m_a \frac{d^2 Y}{dt^2}. \tag{2.2}$$

In Eq.(2.2), ρ is the mass density of the fluid, D is the diameter, L is the length of the cylinder, C_{VY} is the cross-flow vortex force coefficient, $m_a = C_a \pi \rho D^2 L/4$ is the added mass and the value for C_a is 1, as follows from the potential theory. Moving the potential inertia term to the left-hand side of Eq.(2.1) and defining the structural natural frequency in still water $\omega_n = \sqrt{k/(m+m_a)}$ and damping ratio $\zeta = b/\left(2\sqrt{(m+m_a)k}\right)$, Eq.(2.1) becomes

$$\frac{d^2 Y}{dt^2} + 2\zeta\omega_n \frac{dY}{dt} + \omega_n^2 Y = \frac{F_{VY}}{m+m_a}. \tag{2.3}$$

Note here that F_{VY} corresponds to the cross-flow component of the total instantaneous vortex force F_V caused by vorticity, which includes the effect of stall. In other studies, such as Facchinetti et al. (2004) and Skop and Balasubramanian (1997), the stall effect has been normally taken into account by adding a constant linear damping term at the left-hand side of the structural equation Eq.(2.1), and the damping coefficient related to the stall is determined by assuming that the cylinder velocity is much smaller than the flow velocity V. This assumption has been relaxed in the model proposed by Ogink and Metrikine (2010), where the total instantaneous vortex force F_V is decomposed into a drag part F_{VD} and a lift part F_{VL}, both of which are illustrated in Fig.2.2. As can be seen from this figure, the drag force F_{VD}, defined as being in-line with the relative flow velocity $U = \sqrt{V^2 + \left(\frac{dY}{dt}\right)^2}$, models the stall effect, and the lift force F_{VL} that acts in the direction perpendicular to the U formulates the excitation by vortex shedding. The magnitudes of drag and lift forces are related to the relative flow velocity U and are defined

as

$$F_{VL} = \frac{1}{2}\rho DLU^2 C_{VL}, F_{VD} = \frac{1}{2}\rho DLU^2 C_{VD} \tag{2.4}$$

where C_{VL} and C_{VD} are lift and drag coefficients. The effects of the wake dynamics are taken into account by the lift coefficient C_{VL} (with the wake variable that is governed by the wake oscillator, to be discussed later).

Then, the cross-flow vortex force F_{VY} is the summation of projections of F_{VL} and F_{VD} in the cross-flow direction, and it can be written as

$$F_{VY} = F_{VD}\sin\beta + F_{VL}\cos\beta \tag{2.5}$$

where β is the angle between the direction of relative flow velocity U and the undisturbed flow V. The angle β is given by

$$\sin\beta = -\frac{dY}{dt}\sqrt{V^2 + \left(\frac{dY}{dt}\right)^2} \quad\text{and}\quad \cos\beta = V\sqrt{V^2 + \left(\frac{dY}{dt}\right)^2}. \tag{2.6}$$

Substitution of Eqs.(2.4) and (2.6) into Eq. (2.5) results in

$$F_{VY} = \frac{1}{2}\rho DL\left(-C_{VD}\frac{dY}{dt} + C_{VL}V\right)\sqrt{V^2 + \left(\frac{dY}{dt}\right)^2}. \tag{2.7}$$

Furthermore, the corresponding force coefficient C_{VY} can be obtained as

$$C_{VY} = \frac{F_{VY}}{\frac{1}{2}\rho DLV^2} = \left(-C_{VD}\frac{dY}{dt}/V + C_{VL}\right)\sqrt{1 + \left(\frac{dY}{dt}/V\right)^2}. \tag{2.8}$$

Similarly, the in-line vortex force F_{VX} and coefficient C_{VX} can be obtained as

$$F_{VX} = F_{VD}\cos\beta - F_{VL}\sin\beta = \frac{1}{2}\rho DL\left(C_{VD}V + C_{VL}\frac{dY}{dt}\right)\sqrt{V^2 + \left(\frac{dY}{dt}\right)^2} \tag{2.9}$$

$$C_{VX} = \frac{F_{VX}}{\frac{1}{2}\rho DLV^2} = \left(C_{VD} + C_{VL}\frac{dY}{dt}/V\right)\sqrt{1 + \left(\frac{dY}{dt}/V\right)^2}. \tag{2.10}$$

The final expression of the total cross-flow hydrodynamic force is obtained by substituting Eq.(2.7) into Eq.(2.2)

$$F_Y = \frac{1}{2}\rho DL\left(-C_{VD}\frac{dY}{dt} + C_{VL}V\right)\sqrt{V^2 + \left(\frac{dY}{dt}\right)^2} - m_a\frac{d^2Y}{dt^2}. \tag{2.11}$$

As presented in Ogink and Metrikine (2010), by setting $V = 0$ Eq.(2.11) transforms into

$$F_Y = -\frac{1}{2}\rho DLC_{VD}\frac{dY}{dt}\left|\frac{dY}{dt}\right| - m_a\frac{d^2Y}{dt^2} \tag{2.12}$$

which is the Morison equation.

The wake oscillator that describes the fluctuating nature of the vortex is based on the van der Pol equation that reads

$$\frac{d^2q}{dt^2} + \epsilon\omega_s(q^2 - 1)\frac{dq}{dt} + \omega_s^2 q = S \tag{2.13}$$

where ϵ is the tuning paramter, and ω_s is the Strouhal frequency, $\omega_s = 2\pi \text{St}V/D$. The forcing term S on the right-hand side models the effects of the cylinder motion on the wake. The dimensionless wake variable q is associated with the lift force coefficient C_{VL} as

$$C_{VL} = \frac{q}{2}C_{L0}. \tag{2.14}$$

With $S = 0$, Eq.(2.13) describes the lift force that the wake imposes on a fixed cylinder. In such case, the steady solution of Eq.(2.13) reaches a limit cycle with the amplitude $q_{max} = 2$. Therefore, the coefficient $1/2$ in Eq.(2.14) is used to ensure the amplitude of oscillation of C_{VL} equals to C_{L0} for a fixed cylinder.

The usage of the van der Pol type oscillator in Eq.(2.13) is based on the similar characteristics between the vortex-shedding process and self-limitation and self-excitation of nonlinear oscillators. Any nonlinear oscillator that generates a limit cycle can potentially be used to represent the vortex-shedding process. However, the most commonly used nonlinear oscillators are the van der Pol and the Rayleigh equations or a combination of both. The Rayleigh equation is similar to the van der Pol equation except for the nonlinear damping term, which is in the form of velocity. The damping term of the Rayleigh equation reads $((\frac{dq}{dt})^2 - 1)\frac{dq}{dt}$.

With regard to the forcing term on the right-hand side of Eq.(2.13), Facchinetti et al. (2004) have proven that a linear coupling – with respect to the acceleration of the cylinder – models most of the important features of the VIV qualitatively. In the model proposed by Ogink and Metrikine (2010), both acceleration and velocity couplings are used:

$$S = \frac{A}{D}\frac{dY^2}{dt^2} + \omega_s\frac{B}{D}\frac{dY}{dt} \tag{2.15}$$

where A and B are coupling coefficients, which can be tuned to meet the experimental results.

The problem can be made dimensionless using the following dimensionless parameters:

$$\tau = \omega_s t, \Omega_n = \omega_n/\omega_s, y = Y/D. \tag{2.16}$$

Substitution of Eq.(2.16) into Eqs.(2.3), (2.13) and (2.15) results in

$$\ddot{y} + 2\zeta\Omega_n\dot{y} + \Omega_n^2 y = \frac{1}{\pi(m^* + C_a)}\frac{1}{2\pi^3\text{St}^2}C_{VY} \tag{2.17}$$

$$\ddot{q} + \epsilon(q^2 - 1)\dot{q} + q = s \tag{2.18}$$

$$s = A\ddot{y} + B\dot{y}. \tag{2.19}$$

The dimensionless form of C_{VX} and C_{VY} can be obtained by substituting Eq.(2.16) into Eqs.(2.8) and (2.10), and they read

$$C_{VX} = (C_{VD} + 2\pi\text{St}\dot{y}C_{VL})\sqrt{1 + 4\pi^2\text{St}^2\dot{y}^2} \tag{2.20}$$

$$C_{VY} = (-2\pi \mathrm{St}\dot{y}C_{VD} + C_{VL})\sqrt{1 + 4\pi^2\mathrm{St}^2\dot{y}^2}. \tag{2.21}$$

Here, the overdot stands for the derivative with respect to the dimensionless time τ, and $m^* = \frac{m}{\frac{1}{4}\rho\pi LD^2}$ is the mass ratio. The lift force coefficient C_{VL} is related to q as defined by Eq.(2.14), while the definition of the drag force coefficient C_{VD} will be given in the next section.

The coupled system described by Eqs.(2.17-2.19) and (2.21) governs the VIV of rigid cylinders in the cross-flow direction. This system can be used in the simulation of free vibrations of rigid cylinders at different nominal reduced velocities V_n. The definition of V_n is given as $V_n = \frac{2\pi V}{\omega_n D}$ which can also be expressed with dimensionless parameters as $V_n = \frac{1}{\mathrm{St}\Omega_n}$.

For the forced vibration, the motion of the cylinder is prescribed with a dimensionless frequency $\Omega = \omega/\omega_s$ (ω is the dimensional frequency of the cross-flow motion of the cylinder) and a dimensionless amplitude y_0. This motion is given as $y = y_0\sin(\Omega\tau)$. The results of forced vibration are normally presented against the true reduced velocity $V_r = \frac{2\pi V}{\omega D}$, which can be alternatively written using the dimensionless parameters as $V_r = \frac{1}{\mathrm{St}\Omega}$. The forced vibration can be modelled by substituting $y = y_0\sin(\Omega\tau)$ into Eqs.(2.18) and (2.19), which then gives

$$\ddot{q} + \epsilon(q^2 - 1)\dot{q} + q = s \tag{2.22}$$

$$s = -Ay_0\Omega^2\sin(\Omega\tau) + By_0\Omega\cos(\Omega\tau). \tag{2.23}$$

The cross-flow force coefficient $C_y = \frac{F_Y}{\frac{1}{2}\rho DLV^2}$ can be calculated from Eq. (2.11), and its dimensionless form is given as

$$C_y = (-2\pi\mathrm{St}\dot{y}C_{VD} + C_{VL})\sqrt{1 + 4\pi^2\mathrm{St}^2\dot{y}^2} - 2C_a\pi^3\mathrm{St}^2\ddot{y}. \tag{2.24}$$

Since the cylinder does not move in the in-line direction, the in-line force coefficient C_x is equal to C_{VX} and is given as

$$C_x = C_{VX} = (C_{VD} + 2\pi\mathrm{St}\dot{y}C_{VL})\sqrt{1 + 4\pi^2\mathrm{St}^2\dot{y}^2}. \tag{2.25}$$

Then, the component of the cross-flow force coefficient that is in phase with cylinder acceleration C_{ya} and in phase with cylinder velocity C_{yv}, the mean in-line force coefficient C_{x0} and the magnitude of fluctuating in-line force coefficient C_{x2} can be obtained through the Fourier series:

$$C_{ya} = \frac{2}{T}\int_{\tau_0}^{\tau_0+T} C_y\sin(\Omega\tau)\,d\tau \tag{2.26}$$

$$C_{yv} = -\frac{2}{T}\int_{\tau_0}^{\tau_0+T} C_y\cos(\Omega\tau)\,d\tau \tag{2.27}$$

$$C_{x0} = \frac{1}{T}\int_{\tau_0}^{\tau_0+T} C_x\,d\tau \tag{2.28}$$

$$C_{x2} = \left(\left(\frac{2}{T} \int_{\tau_0}^{\tau_0+T} C_x \sin(2\Omega\tau)\, d\tau \right)^2 + \left(\frac{2}{T} \int_{\tau_0}^{\tau_0+T} C_x \cos(2\Omega\tau)\, d\tau \right)^2 \right)^{\frac{1}{2}} \qquad (2.29)$$

where $T = 2\pi/\Omega$ is the non-dimensional period. It needs to be noticed here that the definition of C_{yv} given by Eq.(2.27) is such that a negative value of C_{yv} corresponds to the case of energy flows into the structure.

2.3. THE DRAG FORCE MODEL

In the previous section, the basis of the hydrodynamic force model proposed by Ogink and Metrikine (2010) has been described. To summarise, the total hydrodynamic force has been assumed to be normal to the cylinder axis and divided into an ideal inviscid inertia force and a vortex force due to the vorticity. The vortex force is further decomposed into a drag force that is parallel to the instantaneous relative flow velocity and a lift force that is perpendicular to it. Therefore, the proper representation of the total hydrodynamic force requires the correct modelling of both lift and drag forces. Efforts have been made by Ogink and Metrikine (2010) to improve the lift force model in order to reproduce the experimental measurements. However, little is known yet about whether the drag force adopted by Ogink and Metrikine (2010) is appropriate. Trying to reproduce the experimental measurements, with a drag force model that is likely to be deficient, by improving the modelling of the lift force may be difficult, if not impossible, as the lift force model needs to compensate for the errors introduced by the drag force model. Therefore, in this section, the assumptions made with regard to the drag force model adopted by Ogink and Metrikine (2010) as well as their limitations are discussed, and their influence on the modelling of the lift force is investigated.

2.3.1. LIMITATIONS OF THE DRAG FORCE MODEL

The drag force model proposed by Ogink and Metrikine (2010) adopts the quasi-steady assumption, which assumes that the instantaneous drag force acting on an oscillating cylinder keeps its stationary value, while the change in the dynamics of the wake is taken into account through the instantaneous lift force that is coupled with the cylinder motion. The quasi-steady assumption regarding the drag force is physically not fully appropriate, as it ignores the time that the wake needs to develop. Due to the viscosity, when the position of the cylinder changes, the wake behind it cannot immediately reach its steady-state configuration, and the drag force thus no longer keeps its steady value. Moreover, for the sake of simplification, only the mean value of the steady drag force has been adopted in the model by Ogink and Metrikine (2010). This is mainly because its oscillatory part, which should be coupled with the lift, at double the frequency of vortex shedding, is small and normally ignored. However, due to the increase in the correlation length of vortex shedding and the strength of vortices when the cylinder moves, the oscillatory component of the drag force may become non-negligible. More importantly, this fluctuating force may contain crucial information regarding the wake dynamics and can play an important role in the formulation of hydrodynamic forces. Another drawback related to the current drag force model is that it neglects the added mass introduced by the dynamics of the wake in the direction parallel to the instantaneous flow velocity. The limitations of the model as a result of ignoring such an inertial component can be em-

phasised by the case of a rigid cylinder oscillating in still water. In such a case, according to Eq.(2.12), the current model is reduced to the well-known Morison equation with a fixed value of inviscid added mass coefficient. This is contradictory to the experimental measurements, which show that the added mass coefficient deviates from its inviscid value and strongly depends on the amplitude and frequency of cylinder oscillation (Sarpkaya, 1977).

To summarise, the main shortcomings of the drag force model is threefold: (a) making a quasi-steady assumption, (b) ignoring the oscillatory component, and (c) neglecting the inertia force introduced by the dynamics of the wake in the direction of the drag force. In this section, the influence of the first two drawbacks on the modelling of the lift force is investigated, while the third one is not studied.

In this section, the investigation is based on three drag force models, which are given as

$$C_{VD} = C_{D0} \tag{2.30}$$

$$C_{VD} = C_{D0}\left(\Omega, y_0\right) \tag{2.31}$$

$$C_{VD} = C_{D0}\left(\Omega, y_0\right) + \alpha\left(\Omega, y_0\right) C_{VL}^2. \tag{2.32}$$

The first drag force model, Eq.(2.30), is the same one as proposed by Ogink and Metrikine (2010), where the drag force coefficient is assumed to be constant and to maintain the steady mean value that is measured on a fixed cylinder. In the second drag force model, given by Eq.(2.31), the quasi-steady assumption is relaxed to some extent by making the drag force coefficient frequency- and amplitude-dependent. The third model, Eq.(2.32), in addition to the mean drag force coefficient, contains an oscillatory component, which is coupled to the lift force in the same form as derived from the fixed cylinder (Qin, 2004). It needs to be pointed out that introducing only the frequency-dependent drag coefficient is not correct, as such frequency-dependent damping should always be accompanied by a frequency-varying inertial component. However, only the frequency-dependent damping is considered here in order to understand what the frequency dependence of the drag coefficient could be if the frequency dependence of the added mass coefficient in the frequency band were weak.

2.3.2. DETERMINATION OF THE LIFT FORCE THAT CONFORMS TO THE EXPERIMENTS

In this subsection, the lift force that reproduces the experimental measurements is determined based on the drag force models proposed in the previous subsection. So far, the most complete, publicly available forced vibration measurements are reported by Gopalkrishnan (1993). In this work, the component of cross-flow force coefficient in phase with the cylinder acceleration C_{ya} and that in phase with the cylinder velocity C_{yv}, the mean in-line force coefficient C_{x0} and the amplitude of the oscillatory in-line force coefficient C_{x2} are reported. Among these four types of measurements, C_{ya} and C_{yv} are of the highest interest, as they govern the cross-flow response of the structure in free vibration. The other two measurements regarding the force in the in-line direction would play important roles when the cylinder is also allowed to move in that direction. The ideal scenario would be that all four measurements can be reproduced by one and the same model for the hydrodynamic force. However, this may be impossible for the

drag force models proposed here. Therefore, the priority of this work is to reproduce the measurements of C_{ya} and C_{yv}.

As for the oscillatory lift force coefficient C_{VL}, although it may physically contain multiple frequency components, the assumption here is that mainly the part at the frequency of cylinder oscillation contributes to C_{ya} and C_{yv}. This assumption, strictly speaking, is open to discussion, as the other harmonics at an integer multiple frequency of cylinder motion must have an influence on the results. Since no experimental measurement is available at those frequencies, it is difficult to evaluate whether their influences are significant or negligible. This leaves no better option than to neglect the influence of higher harmonics and to assume that the oscillatory lift force coefficient has the form $C_{VL} = C_{VL0} \sin(\Omega \tau + \phi_{VL})$. C_{VL0} represents the amplitude of the lift force coefficient, while ϕ_{VL} designates the phase difference between the lift force and cylinder motion $y = y_0 \sin(\Omega \tau)$.

For the first drag force model, by substituting $C_{VL} = C_{VL0} \sin(\Omega \tau + \phi_{VL})$ and $y = y_0 \sin(\Omega \tau)$ into Eqs.(2.21) and (2.26–2.29) and applying the numerical integration, the fluid force coefficient C_{ya} and C_{yv} can be obtained with a given C_{VL0} and ϕ_{VL}. The values of C_{VL0} and ϕ_{VL} that satisfy the experimental measurements are identified by minimising the error between the calculations and measurements:

$$\text{error} = \left(C_{ya;model} - C_{ya;meaured}\right)^2 + \left(C_{yv;model} - C_{yv;meaured}\right)^2. \qquad (2.33)$$

The value of C_{D0} needs to be specified in advance; here, the value $C_{D0} = 1.1856$ is taken as measured on the fixed cylinder. A Matlab built-in function 'lsqnonlin', based on the interior-reflective Newton method (Coleman and Li, 1996, 1994), has been used for the minimisation procedure, and the values of C_{VL0} and ϕ_{VL} are obtained at each frequency and amplitude of cylinder oscillation with an error smaller than 10^{-6}. The results are plotted in Fig.2.3.

From Fig.2.3 it can be seen that the dynamic characteristics of the lift force coefficient, regarding its amplitude and phase, change as the amplitude of cylinder oscillation increases. Three different patterns are generally observed, and they can be categorised as a small amplitude pattern ($y_0 = 0.2, 0.4$), a medium amplitude pattern ($y_0 = 0.6, 0.8, 1.0$) and a large amplitude pattern ($y_0 = 1.2$). When the cylinder oscillates at small amplitudes – $y_0 = 0.2$ and 0.4 – then the frequency dependence of the amplitude and phase of the lift force, although not exact, is in good agreement with the phenomenon of resonance; i.e. the amplitude peak is accompanied by a sharp change of the phase. For $y_0 = 0.2$, as depicted in plot (a) in Fig.2.3, the phase of the lift force remains constant at small frequencies and changes around $\Omega = 0.9$ from 0.8π to just below 0. When the cylinder oscillates at $y_0 = 0.4$, the resonance is less obvious than in the case of $y_0 = 0.2$; however, a peak in the amplitude is still observed and is accompanied by a phase change around $\Omega = 0.9$. It must be pointed out that the amplitude of the lift force in the case of $y_0 = 0.4$ is not double of that at $y_0 = 0.2$. When the cylinder oscillates at medium amplitudes, i.e. $y_0 = 0.6, 0.8$ and 1.0, the phase change is observed around $\Omega = 0.9$. However, instead of a peak in the amplitude, which is seen when the cylinder oscillates at small amplitudes, the phase change is accompanied by a local minimum in amplitude, and the trough becomes deeper as the amplitude of cylinder oscillation increases. Finally, when the cylinder oscillates at a large amplitude ($y_0 = 1.2$), the phase
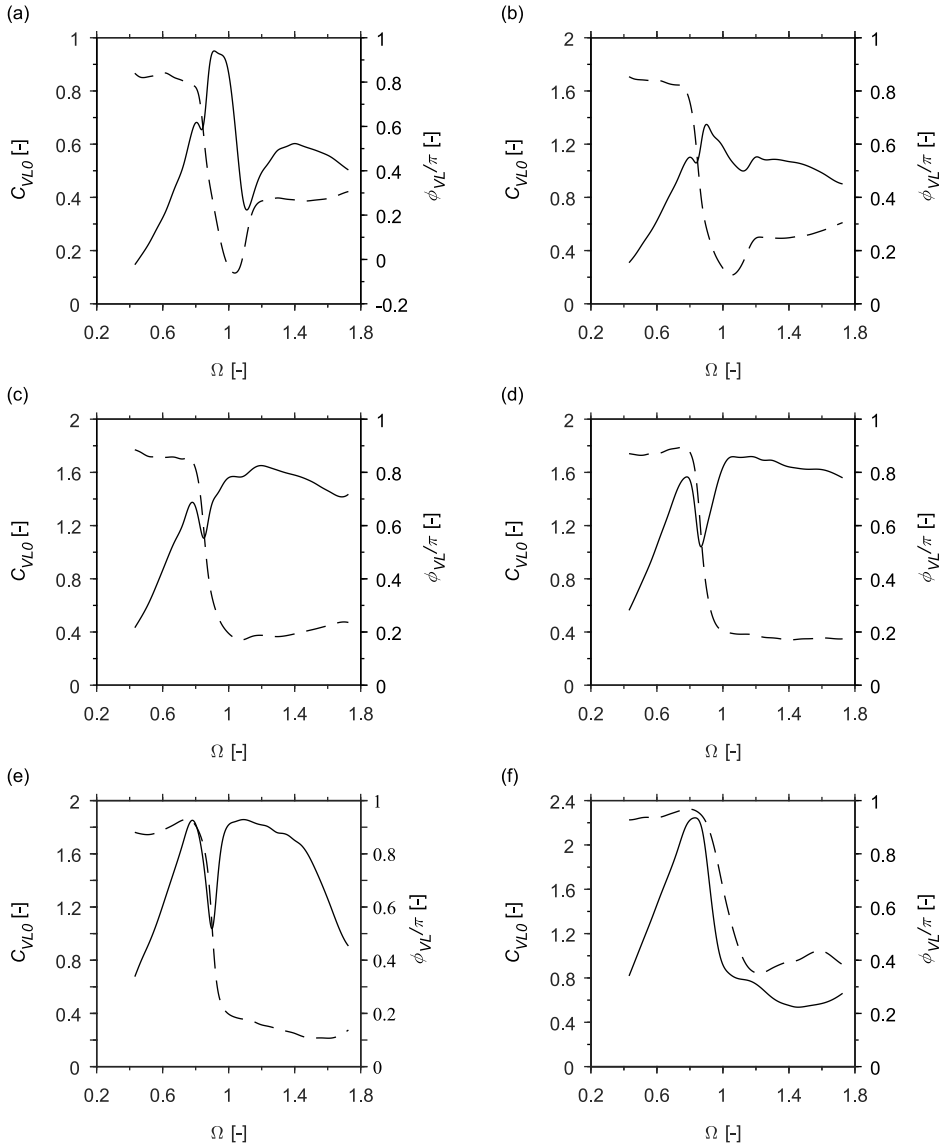
2

Figure 2.3: Amplitudes (solid lines) and phases (dashed lines) of the oscillatory lift force coefficient that conforms to the forced vibration measurements with first drag force model at different amplitudes of cylinder oscillation (a) $y_0 = 0.2$, (b) $y_0 = 0.4$, (c) $y_0 = 0.6$, (d) $y_0 = 0.8$, (e) $y_0 = 1.0$ and (f) $y_0 = 1.2$.
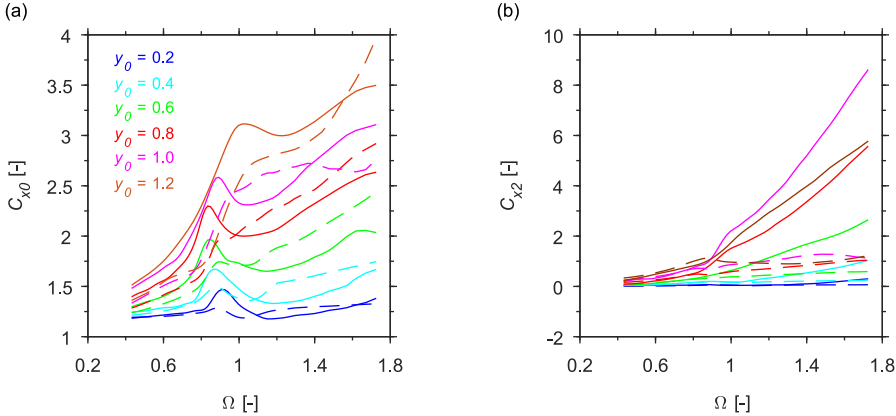
(a)

(b)

Figure 2.4: Force coefficients obtained from the first drag force model (dashed lines) in comparison with the measurements (solid lines) for (a) mean in-line force coefficient C_{x0} and (b) oscillatory in-line force coefficient C_{x2}.

of the lift force is again characterised by a sharp change around $\Omega = 1$. However, different from the small and medium amplitude patterns, the phase change is associated with neither a peak nor a trough of the amplitude-frequency dependence. It seems that after the amplitude of the lift force reaches a minimum, instead of increasing, as observed in the case of a medium amplitude pattern, it maintains relatively small values at high frequencies. In general, the lift force determined from the first drag force model follows the resonance pattern at small amplitudes of cylinder motion, whereas at medium and large amplitudes of cylinder motion, its pattern is not consistent with the dependence typical for the resonance phenomenon.

With the obtained lift force, the values of C_{x0} and C_{x2} are calculated based on the first drag force model, and the results are depicted in Fig.2.4 in comparison with the experimental results. Fig.2.4(a) illustrates that the calculated mean in-line force coefficients C_{x0} are in qualitative agreement with the measurements. The increasing trend of the mean in-line force coefficients with respect to the increasing frequency is well captured. However, over the range of $\Omega = 0.7-1.2$, where VIV usually occurs, the first model generally underestimates the mean in-line force. As for the oscillatory in-line force, Fig.2.4(b) demonstrates good agreement between the results of the model and the measurements over the range of low frequencies, but at high frequencies, the model significantly underestimates C_{x2} for amplitudes of cylinder oscillation larger than 0.2. It is interesting to notice that the discrepancy starts to emerge around $\Omega = 1.0$, which is the point at which the frequency of cylinder oscillation equals the Strouhal frequency and corresponds to a wake change between the 2P mode and the 2S mode (Williamson and Roshko, 1988).

For the second drag force model, since one extra coefficient $C_{D0}\left(\Omega, y_0\right)$ needs to be identified, the reproduction of the measurement of C_{x0} is also considered in the minimi-
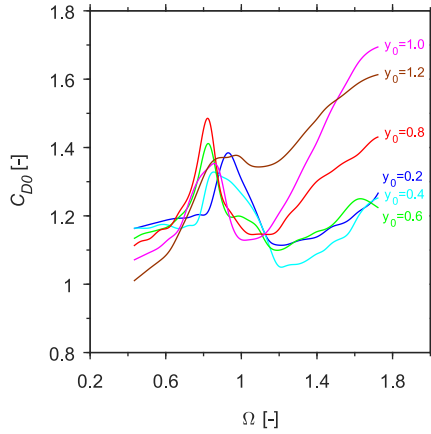
2

Figure 2.5: Frequency- and amplitude- dependent drag force coefficient obtained from the second drag force model.

sation procedure, and the definition of error becomes

$$
\begin{aligned}
\text{error} = {} & \left(C_{ya;model} - C_{ya;meaured}\right)^2 + \left(C_{yv;model} - C_{yv;meaured}\right)^2 \\
& + \left(C_{x0;model} - C_{x0;meaured}\right)^2 .
\end{aligned}
\tag{2.34}
$$

Applying the same minimisation routine, the values of C_{VL0}, ϕ_{VL} and $C_{D0}\left(\Omega, y_0\right)$ that meet the experimental results based on the second drag force model have been determined. It was found that the values of C_{VL0} and ϕ_{VL} are almost the same as those calculated with the first drag force model. Therefore, the results of C_{VL0} and ϕ_{VL} are not presented here, and only the frequency- and amplitude-dependent $C_{D0}\left(\Omega, y_0\right)$ are depicted in Fig.2.5. At all amplitudes, the variation of the $C_{D0}\left(\Omega, y_0\right)$ against frequency follows a similar pattern, which exhibits a local peak around $\Omega = 0.9$. No general trend is observed regarding the variation of $C_{D0}\left(\Omega, y_0\right)$ with respect to the amplitude. The values of C_{x2} are also calculated for the second drag force model with the obtained oscillatory lift force coefficient. However, no obvious difference is found compared to those calculated from the first model, and the results are thus not presented here.

The third drag force model, in addition to the frequency- and amplitude-dependent drag force coefficient, takes into account the oscillatory component with unknown coefficient $\alpha\left(\Omega, y_0\right)$. With a total of four unknown coefficients to be determined, the measurements of C_{x2} are included in the minimisation procedure, and the definition of the error becomes

$$
\begin{aligned}
error = {} & \left(C_{ya;model} - C_{ya;meaured}\right)^2 + \left(C_{yv;model} - C_{yv;meaured}\right)^2 \\
& + \left(C_{x0;model} - C_{x0;meaured}\right)^2 + \left(C_{x2;model} - C_{x2;meaured}\right)^2 .
\end{aligned}
\tag{2.35}
$$

Attempts have been made to minimise the errors between the model results and the measured C_{ya}, C_{yv}, C_{x0} and C_{x2} with Eq.(2.35). However, at many data points, especially

for a high amplitude $y_0 = 1.2$, it proved to be difficult to minimise the error such that it is smaller than 10^{-6}. More importantly, the large oscillating in-line forces C_{x2} at high frequencies and large amplitudes of cylinder oscillation can only be reproduced with the value of α in Eq.(2.32) being extremely large. This could be a result of the quadratic coupling relation between the lift and drag forces as derived from the stationary cylinder may to be no longer valid when the cylinder moves. However, it should be pointed out again that the influence of higher harmonics of the lift force is neglected here, and it is possible that to correctly model the hydrodynamic force, the higher harmonic components of the lift force need to be taken into account.

Since it is not possible to satisfy all four measurements with the third drag force model, an attempt was made to identify the lift force based on only three measurements, namely C_{ya}, C_{yv} and C_{x0}. With only three types of measurements to satisfy, one of the two parameters – $C_{D0}(\Omega, y_0)$ and $\alpha(\Omega, y_0)$ – in the third drag force model needs to be specified in advance. From the first and second drag force models, the resulted C_{VL0} and ϕ_{VL} seem to be insensitive to the value of $C_{D0}(\Omega, y_0)$. Therefore, this study assumes that the value of $C_{D0}(\Omega, y_0)$ is fixed and taken as 1.1856. Then, the values of C_{VL0}, ϕ_{VL} and $\alpha(\Omega, y_0)$ are obtained by minimising the error defined by Eq.(2.34) with tolerance 10^{-6}. The results reveal that, although not exact, the values of C_{VL0} and ϕ_{VL} have similar patterns to those obtained from the first and second drag models. The main differences are observed at high frequencies. Three examples of C_{VL0} and ϕ_{VL} obtained at $y_0 = 0.4$, $y_0 = 0.8$ and $y_0 = 1.2$ are presented in Fig.2.6 in comparison with results from the first drag model. The corresponding values of $\alpha(\Omega, y_0)$ are plotted in Fig.2.7. When a cylinder oscillates at a low frequency, it is expected that the value of α should be the same as that obtained from the fixed cylinder. However, it can be seen from Fig.2.7 that the values of α generally increase from negative values at low frequencies to positive at high frequencies. This is in contrast to the fact that for a fixed cylinder, the value of α is positive Qin (2004). With the obtained values of C_{VL0}, ϕ_{VL} and α, C_{x2} was calculated, the values of which are again found to be similar to those calculated with the first and second drag force models and hence not presented here.

2.3.3. DISCUSSION ON THE DYNAMIC CHARACTERISTICS OF THE LIFT FORCE

In the previous subsection, the lift forces that satisfy the experimental results have been identified based on three drag force models. The dynamic characteristics of the lift force obtained from the three models are almost the same. At a small amplitude of cylinder oscillation, the lift force reproduces the resonance phenomenon, which somehow reveals the similarity between the wake dynamics and an oscillator. However, at medium and large amplitudes, the dynamic characteristics of the lift force are such that the phase change still follows the resonance pattern, while the amplitude of the lift force does not. The contradiction to the resonance pattern at medium and large amplitudes of cylinder oscillation can explain why, in the work by Ogink and Metrikine (2010), the wake oscillator model with frequency-dependent coupling only works well for small amplitudes of vibration.

One possible explanation for the contradiction could be the neglected added mass in the instantaneous flow direction (only the ideal added mass is accounted for in this direction). To fulfil the experimental results, the lift force is designed to compensate
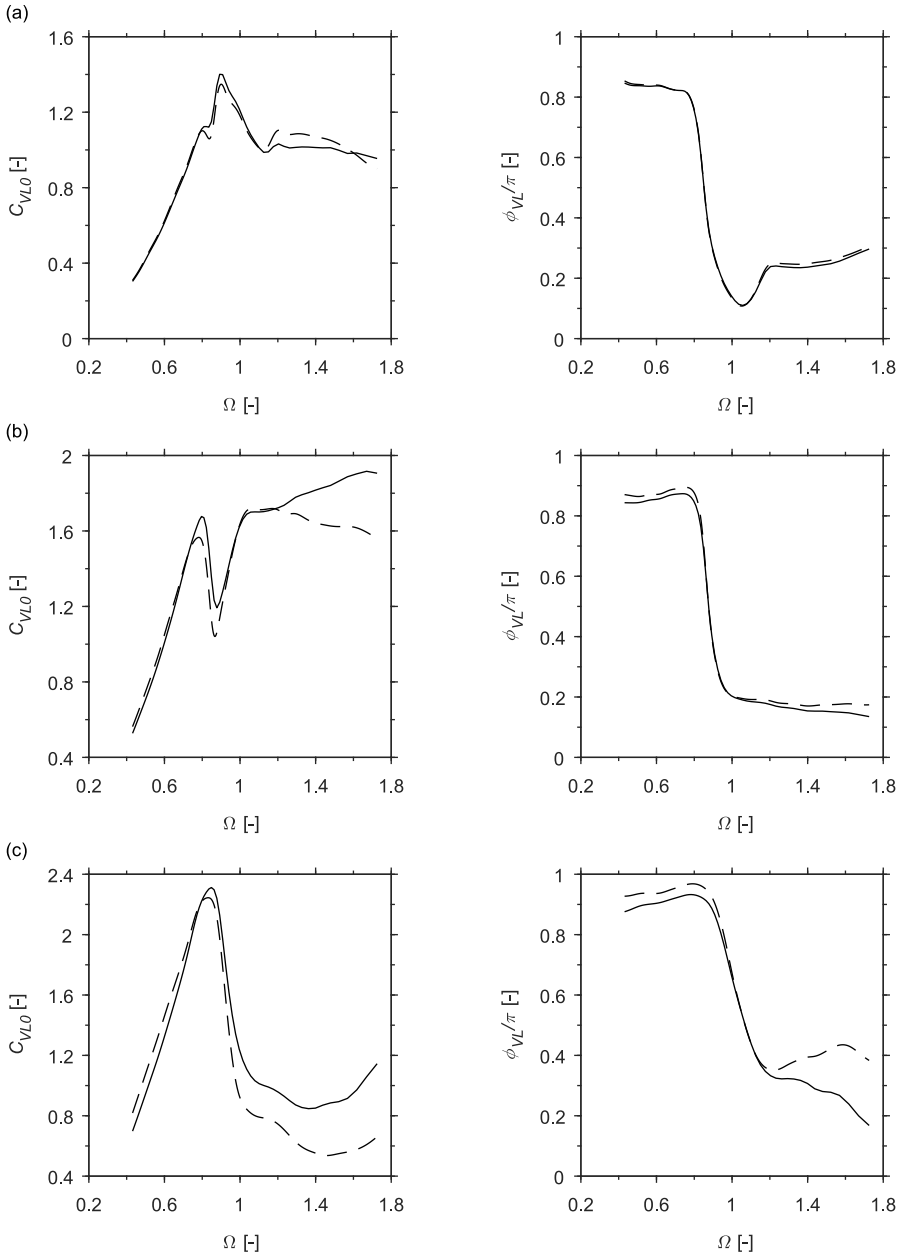
2

(a)

(b)

(c)

Figure 2.6: A comparison of the oscillatory lift force coefficients obtained from the first (dashed line) and third (solid line) drag force models at different amplitudes of cylinder oscillation (a) $y_0 = 0.4$, (b) $y_0 = 0.8$ and (c) $y_0 = 1.2$.
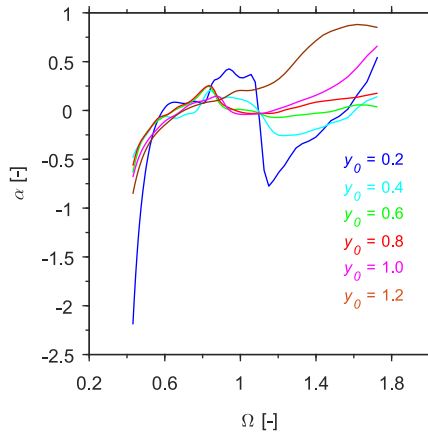
Figure 2.7: Frequency- and amplitude-dependent α obtained from the third drag force model.

for the added mass component missed in the instantaneous flow direction, which could result in the misdistribution between the inertia and damping components of the lift force. Another possible explanation is the higher harmonic components. In the analysis conducted in this section, only the component at the frequency of cylinder oscillation is considered. It is possible that at medium and high amplitudes, the dynamics of the lift force are such that there are substantial energy transfers to other frequencies at the point of resonance due to some unaccounted for nonlinear mechanism. This can result in the reduction in the amplitude of lift force at the fundamental frequency, as observed.

Although taking into account the added mass effect due to the dynamics of the wake in the instantaneous flow direction may be crucial in the formulation of the hydrodynamic force model, the form in which the added mass should be incorporated into the model is still unclear and will not be investigated further. Therefore, in the next chapter the focus will still be placed on the improvement of the nonlinearity of the wake oscillator equation.

2.4. CONCLUSIONS

In this chapter, the wake oscillator model proposed by Ogink and Metrikine (2010) has been reviewed. This model, different from others, involves force decomposition. The total hydrodynamic force, in addition to the potential added mass, is expressed as the summation of lift (perpendicular to the relative flow velocity) and drag (parallel to the relative flow velocity) forces. Therefore, the reproduction of the forced vibration experiments requires the appropriate modelling of both lift and drag forces. The focus of this chapter has been on the examination of the possible influence of drag force models on the dynamic characteristic of lift force that satisfies the experimental results.

Three different drag force models have been investigated. The first model is the one proposed by Ogink and Metrikine (2010). It assumes that the instantaneous drag force coefficient is constant and keeps the mean steady value measured on a fixed cylinder.

In the second model, the instantaneous drag force coefficient is still assumed to be constant, but its value varies as the frequency or amplitude of cylinder oscillation changes. In the third model, in addition to the constant drag force, an oscillatory part coupled with the lift force is introduced, and the coupling relation maintains the same form as that identified on a fixed cylinder. Compared to the first model, the second model relaxes the quasi-steady assumption of the drag force by making the damping component, which was introduced in the relative flow direction, frequency- and amplitude-dependent, while the third model tries to incorporate the oscillating component of the drag force.

The oscillatory lift forces, at the frequency of cylinder oscillation, that satisfy the available experimental measurements have been identified based on the three drag force models. It has been demonstrated that the lift forces obtained from the three drag force models are almost the same, and the dynamic characteristics of the lift force can be categorised into three different patterns that correspond to small, medium and large amplitudes of cylinder oscillation. When the cylinder oscillates at small amplitudes, the evolution of the phase and amplitude of the lift force with respect to the frequency of cylinder oscillation follows the typical characteristic of resonance, namely the amplitude peak is accompanied by a sharp change in the phase. For medium amplitudes of cylinder oscillation, a phase change is also observed. However, instead of a peak, a local trough in the amplitude of the lift force is observed when a phase change occurs. At large amplitudes of cylinder oscillation, the evolution of the phase of the lift force with respect to the frequency is again characterised by a jump; however, in contrast to the small and medium amplitude patterns, the phase jump is associated with neither a peak nor a local minimum in the lift force amplitude.

The reproduction of the oscillatory in-line force coefficient C_{x2} is also presented. It has been demonstrated that all three models satisfy the measured C_{x2} well at low frequencies, while they significantly underestimate it at high frequencies. The discrepancy happens to occur at the frequency, which, according to other studies, corresponds to the change of wake pattern from a 2P (for a large amplitude of cylinder oscillation is P+S) to a 2S mode.

The results obtained in this chapter indicate that making the drag force coefficient frequency- and amplitude-dependent or introducing an oscillatory drag force component does not have a significant impact on the lift force that satisfies the experimental measurements. Therefore, in the next chapter, the first drag force model will be applied, and attention will be placed on the improvement of the lift force model by introducing extra nonlinearity to the wake oscillator equation. However, it should be reminded that the dynamic characteristic of the lift force at a large amplitude of cylinder oscillation could be the result of neglecting the inertia force in the direction of relative flow.

3

MODELLING OF CROSS-FLOW VORTEX-INDUCED VIBRATION OF AN ELASTICALLY SUPPORTED RIGID CYLINDER BY MEANS OF A WAKE OSCILLATOR MODEL WITH NONLINEAR COUPLING

3.1. INTRODUCTION

In the work by Ogink and Metrikine (2010), the main goal was to develop a wake oscillator model that is able to reproduce both free and forced vibration experiments. Attempts have been made to achieve this goal by making the linear coupling used in the classical wake oscillator models frequency-dependent. However, one of the main problems they encountered is that they were not able to find one set of frequency-dependent coefficients that would satisfy the forced vibration experiments at different amplitudes of cylinder oscillation. This is an indication of the improper nonlinearity used in the model. One of the possible improvements to the model is to use another nonlinear oscillator instead of the van der Pol equation. Utilising the van der Pol oscillator in the first place is barely an assumption, and any nonlinear oscillator that generates a limit cycle can potentially be used in the description of vortex formation. However, several studies have demonstrated that the van der Pol equation describes well the vortex shedding process (Marzouk et al., 2007; Nayfeh et al., 2003), which makes it unreasonable to replace that equation. Another possible approach is to introduce nonlinear coupling, which has not been studied before and therefore forms the focus of this chapter.

Without knowing the exact type of nonlinear coupling that should be used, a reasonable start would be to represent the nonlinearities in the form of polynomials as multiplications of the displacement, velocity and acceleration of cylinder oscillation. If the nonlinearities of the coupling are polynomial in nature, then this representation should theoretically be able to model the system well for all frequencies and amplitudes of cylinder oscillation. If that is not the case, then according to the Weierstrass approximation theorem, the system can still be approximated to an arbitrary accuracy by polynomials within a given range of frequencies and amplitudes of cylinder oscillation. However, this is accompanied by the drawback of using high-order polynomials, which make the model too complicated and potentially unstable. Therefore, a combination of low-order polynomials is adopted in this chapter.

The remainder of this chapter is structured as follows. In Section 3.2, as a preliminary test, a set of nonlinear coupling terms in the form of polynomials up to the order of cubic is introduced, and attempts are made to tune the wake oscillator model to both the forced and free vibration experiments. The nonlinear coupling is further enhanced in Section 3.3, where the convolution integrals are introduced in the time domain to reproduce the forced vibration experiments. The focus is on finding the frequency-dependent complex-valued functions that meet the experimental measurements and determining the corresponding kernels of the convolution integrals. The final conclusions are presented in Section 3.4.

3.2. IMPROVED WAKE OSCILLATOR MODEL WITH NONLINEAR COUPLING

In this section, a study of the wake oscillator model with one set of nonlinear couplings in the form of low-order polynomials is presented. The purpose of choosing low-order polynomials is to avoid instabilities that may be introduced by high-order polynomials. Notice that the first drag force model, with constant drag force coefficient, as presented in the previous chapter is adopted in this chapter.

3.2.1. DESCRIPTION OF THE NONLINEAR COUPLING

The nonlinear couplings used in this section are given as

$$S = \sum_{n=0}^{3} \left[\frac{A_n}{D^{n+1}} |Y|^n \frac{d^2 Y}{dt^2} + \omega_s \frac{B_n}{D^{n+1}} |Y|^n \frac{dY}{dt} \right], \quad \text{n is interger.} \tag{3.1}$$

The above equation describes a combination of nonlinearities that are dependent on the displacement of cylinder motion up to a cubic term. Using the dimensionless parameters given in Eq.(2.16), the dimensionless form of Eq.(3.1) is obtained as

$$s = \sum_{n=0}^{3} \left[A_n |y|^n \ddot{y} + B_n |y|^n \dot{y} \right]. \tag{3.2}$$

The nonlinear coupling terms inevitably result in a force on the wake oscillator that contains multiple frequency components. Here, it is assumed that the influence of the frequency components other than that of cylinder oscillation on the response of the oscillator is negligible. By substituting the cylinder motion $y = y_0 \sin(\Omega \tau)$ into Eq.(3.2) and

applying a Fourier series expansion, the force component acting on the wake oscillator at the frequency of cylinder oscillation can be obtained as

$$s_\Omega = -(A_0 + \frac{8}{3\pi} A_1 y_0 + \frac{3}{4} A_2 y_0^2 + \frac{32}{15\pi} A_3 y_0^3) y_0 \Omega^2 \sin(\Omega\tau)$$
$$+ (B_0 + \frac{4}{3\pi} B_1 y_0 + \frac{1}{4} B_2 y_0^2 + \frac{8}{15\pi} B_3 y_0^3) y_0 \Omega \cos(\Omega\tau). \tag{3.3}$$

Comparing Eq.(3.3) with Eq.(2.23), the following expressions for A and B are obtained

$$A = A_0 + \frac{8}{3\pi} A_1 y_0 + \frac{3}{4} A_2 y_0^2 + \frac{32}{15\pi} A_3 y_0^3, B = B_0 + \frac{4}{3\pi} B_1 y_0 + \frac{1}{4} B_2 y_0^2 + \frac{8}{15\pi} B_3 y_0^3. \tag{3.4}$$

Eq.(3.4) demonstrates that by considering only the excitation on the wake oscillator at the frequency of cylinder oscillation, the new nonlinear coupling terms can be expressed as acceleration and velocity couplings with amplitude-dependent coefficients A and B. The amplitude dependency is described by cubic polynomials given be Eq.(3.4). It has been pointed out by Ogink and Metrikine (2010) that to comply with the measurements from the forced vibration experiment, the coupling coefficients A and B should also be frequency-dependent, which is not considered here. Still the model is tuned in the next subsection to investigate the extent to which it can reproduce the forced and free vibration experiments.

3.2.2. TUNING OF THE MODEL TO THE FORCED VIBRATION EXPERIMENTS
In this and the following subsections, the improved wake oscillator model with nonlinear coupling proposed in Section 3.2.1 is tuned to both forced and free vibration experiments. When doing this, one can start by tuning the model to the forced vibration experiments and then, with the same tuning parameters, conduct free vibration simulations and compare the results with experimental data, or vice versa. In this section, the first approach is taken.

Since the objective of this part is to tune the model to the forced vibration experiments by Gopalkrishnan (1993), it is reasonable to use $C_{D0} = 1.1856$, $C_{L0} = 0.3842$ and St = 0.1932, as measured in the experiments. This leaves tuning parameters A_0, A_1, A_2, A_3, B_0, B_1, B_2, B_3 and ϵ to be determined. The large number of tuning parameters makes the model difficult to be tuned. Therefore, an alternative approach is taken here to determine the values of the tuning parameters.

As described in Section 3.2.1, if only the force component acting on the wake oscillator at the frequency of cylinder oscillation is considered, then the nonlinear coupling described by Eq.(3.2) formulates amplitude-dependent coefficients A and B. The amplitude dependency is given by Eq.(3.4). The amplitude-dependent A and B can be obtained by tuning the wake oscillator model Eqs.(2.22) and (2.23) to the forced vibration measurements at each amplitude. Then, the values of the nonlinear coupling coefficients A_0, A_1, A_2, A_3, B_0, B_1, B_2 and B_3 can be determined by finding the best fit of A and B against the amplitude of cylinder oscillation using Eq.(3.4).

To model the forced vibration, Eqs.(2.22) and (2.23) are solved numerically in the time domain, using a fifth-order Runge-Kutta method. The simulation runs for 150 periods of cylinder oscillation at a certain reduced velocity, and only the steady response

of the last 50 periods is used for the analysis. With Eqs.(2.26) and (2.27), the coefficients C_{ya} and C_{yv} are calculated by averaging over the last 50 periods. The coefficients have been determined over the range of reduced velocities from $V_r = 3$ to $V_r = 12$ with a step size of $\mathrm{d}V_r = 0.1$.

When tuning Eqs.(2.22) and (2.23) to the forced vibration experiments, it is found that a smaller value of ϵ results in better agreement. However, a smaller ϵ also means a weak self-excitation in free vibration, as it decides the magnitude of negative added damping in the van der Pol kernel. Therefore, $\epsilon = 0.05$ is taken to achieve a suitable balance between self-excitation and the proper reproduction of the forced vibration experiments. Another problem encountered by the author is that Eqs.(2.22) and (2.23) cannot be exactly tuned to the forced vibration measurements at specified amplitudes of forced motion. This is actually expected, as Ogink and Metrikine (2010) have already demonstrated that to reproduce the experimental results, the coupling coefficients, namely A and B, should be frequency-dependent. Despite of this drawback, a tuning result is considered to be a good one if it covers the main trend of the measurements and quantitatively reproduce the negative C_{yv} over the range of reduced velocities $V_r = 5-8$, as this is the main range where the VIV happens. With this criterion, a good set of tuning results is obtained and shown in Fig.3.1, in which dashed lines represent results of the model and solid lines are experimental measurements. The corresponding amplitude-dependent coefficients A and B are plotted in Fig.3.2 by squares.

To achieve the same tuning results by a wake oscillator with nonlinear coupling, which is described by Eqs.(2.22) and (3.2), tuning parameters A_0, A_1, A_2, A_3, B_0, B_1, B_2 and B_3 need to be carefully determined by finding an optimal fit of A and B with polynomials given by Eq.(3.4). Here, curve fittings are conducted using the least squares method, indicated by solid lines in Fig.3.2, and the corresponding nonlinear coupling coefficients are obtained as

$$A_0 = 1.5, A_1 = 8.5, A_2 = -11.1, A_3 = 2.6;$$
$$B_0 = 4.2, B_1 = 11.3, B_2 = -68.7, B3 = 50.5.$$

(3.5)

With the values of the tuning parameters given by Eq.(3.5), Eqs.(2.22) and (3.2) are solved numerically with $y = y_0 \sin(\Omega \tau)$, and the coefficients C_{ya} and C_{yv} are determined by Eqs.(2.26) and (2.27) over the range of reduced velocities from 3 to 12 for amplitudes $y_0 = 0.2, 0.4\ldots$, until 1.2. The results are plotted in Fig.3.3 where the simulation results and experimental measurements are compared. From Fig.3.3, it can be seen that the simulation results of the wake oscillator model with nonlinear coupling are in fairly good agreement with the experimental measurements. Especially the excitation region, represented by negative C_{yv}, is well captured. According to the simulation results, the values of C_{yv} are negative at reduced velocities between approximately 5 and 8 at small amplitudes, which means a positive power input to the vibration of the cylinder under this regime. As the amplitude increases, the net power input into the vibration of the cylinder drops, and the values of C_{yv} become positive. For amplitudes larger than 0.8, the values of C_{yv} are positive over the whole range of reduced velocities. However, some disagreements from the comparison should also be noted. First, although the general decreasing trend of C_{ya} is captured for all amplitudes of cylinder oscillation, the negative values that are observed in experiments for a high reduced velocity, especially over the range of
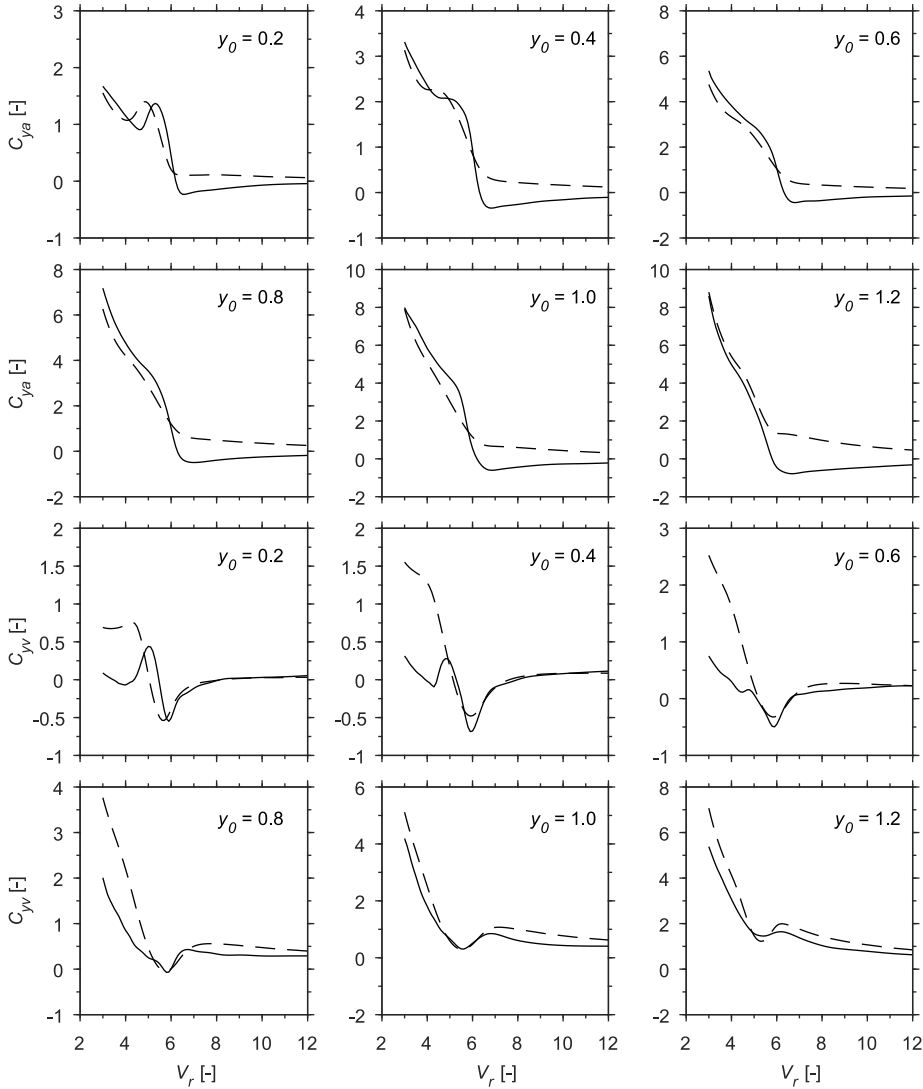
Figure 3.1: Tuning of the model to the forced vibration measurements at different amplitudes of cylinder oscillation. Solid lines represent measurements by Gopalkrishnan (1993) and dashed lines represent tuning results.

$V_r = 5-8$ where VIV normally occurs, have not been reproduced. This disagreement will lead to a major discrepancy in the reproduction of the free vibration experiments, which will be discussed later. Another main difference between the simulation results and experimental measurements shown in Fig.3.3 is that the model over-predicts the values of C_{yv} at low reduced velocities for all amplitudes. Especially for small amplitudes at $y_0 = 0.2$ and 0.4, the model fails to reproduce the negative C_{yv} around $V_r = 4$. Despite this discrepancy, the results of C_{yv} illustrated in Fig.3.3 are considered to be acceptable
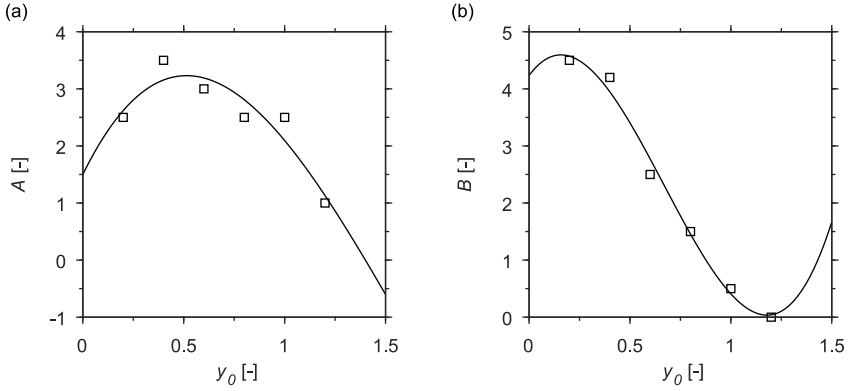
Figure 3.2: Determined values of (a) A and (b) B as a function of amplitude of cylinder oscillation (marked by squares), and curve fit (solid lines) found by least square method.

because it is mainly the other excitation region at $V_r = 5-8$ that plays an important role in VIV.
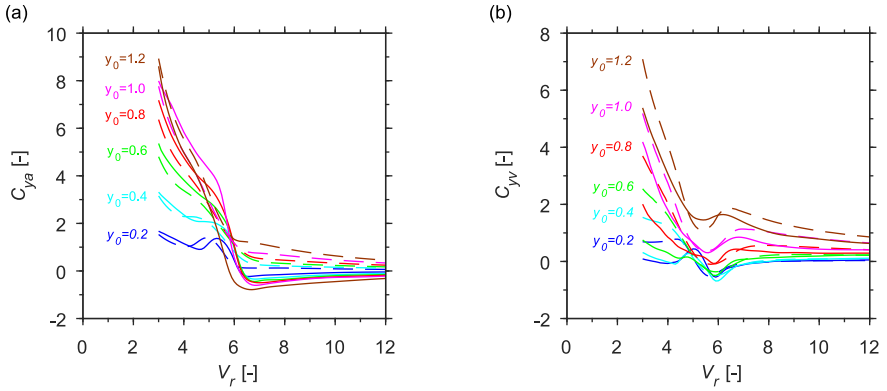
Figure 3.3: A comparison of the nonlinear coupling wake oscillator model and the forced vibration measurements for the force coefficient (a) in phase with acceleration C_{ya} and (b) in phase with velocity C_{yv}. Solid lines represent measurements by Gopalkrishnan (1993) and dashed lines represent model results.

3.2.3. Comparison with free vibration experiments

With the same tuning parameters given in Section 3.2.2, the wake oscillator model with nonlinear coupling is used to simulate the vibration of an elastically supported rigid cylinder that is free to move only in the cross-flow direction. The coupled system is governed by the following equations:

$$\ddot{y} + 2\zeta\Omega_n\dot{y} + \Omega_n^2 y = \frac{1}{\pi(m^* + C_a)} \frac{1}{2\pi^3 \mathrm{St}^2} (-2\pi\mathrm{St}\dot{y}C_{VD} + C_{VL})\sqrt{1 + 4\pi^2\mathrm{St}^2\dot{y}^2} \qquad (3.6)$$

$$\ddot{q} + \epsilon(q^2 - 1)\dot{q} + q = \sum_{n=0}^{3} \left[A_n |y|^n \ddot{y} + B_n |y|^n \dot{y} \right]. \tag{3.7}$$

The above equations are solved numerically using a fifth-order Runge-Kutta method. The simulation runs for a time duration that corresponds to 150 cycles of vortex shedding (follows the Strouhal relation) at a certain reduced velocity V_n, and only the steady response of the last 50 cycles is used for analysis. The simulation results are presented with regard to the maximum amplitude A_y^* of dimensionless displacement and frequency ratio Ω/Ω_n. The A_y^* is determined by finding the maximum displacement recorded in the last 50 periods, and Ω is determined as the frequency corresponding to the highest peak in the Fourier spectrum of the analysed time series. This has been done for reduced velocities V_n ranging from 2 to 12 with a step $\mathrm{d}V_n = 0.1$. A series of experiments conducted by Khalak and Williamson (1999) are used for the comparison. The reason for choosing these experiments is that they are in the range of Reynolds numbers similar to that in the experiments by Gopalkrishnan (1993). The simulation and experimental results are depicted in Fig.3.4. Different experiments are characterised by a different mass ratio m^* and mass-damping ratio $m^*\zeta$.

As seen in Fig.3.4, the main characteristics of the experiments are well captured. With similar mass-damping ratios $m^*\zeta$, the model predicts almost the same peak amplitudes for all three cases, and a wider lock-in range at a smaller mass ratio is also captured. This is consistent with the experimental finding that the peak amplitude is controlled principally by the product of $m^*\zeta$, whereas the range of lock-in is controlled primarily by m^* (Khalak and Williamson, 1999). The maximum simulated amplitudes for all three cases are found at $V_n \approx 6$, with values around 0.8, while the results from the experiments reveal a slightly higher value at $V_n \approx 5$. This can be explained by the fact that the present parameters, namely C_{D0}, C_{L0}, St and the tuning parameters, are taken based on the forced vibration experiments that are conducted under a different condition.

From the comparison, a discrepancy can also be observed regarding the lock-in range and cylinder oscillation frequency for the small mass ratio case. The lock-in range is significantly underestimated by the model for the case $m^* = 2.4$. While the model predicts the vibration of the cylinder to reduce to negligible amplitudes for $V_n > 9$, the experiments indicate that the cylinder maintains a moderate oscillation until $V_n \approx 12$. As for the frequency of cylinder oscillation, the model predicts that the cylinder will vibrate at approximately the natural frequency of the system; this is consistent with the experimental results for $m^* = 10.3$ and $m^* = 20.6$. For the small mass ratio case, $m^* = 2.4$, the experiments demonstrate the deviation of the frequency of cylinder oscillation from the natural frequency. Within the lock-in range, the frequency of cylinder oscillation gradually increases with increasing reduced velocity and reaches a maximum value 1.5 times the natural frequency of the system. Although the rising trend of the frequency of cylinder oscillation is also observed in the simulation results, the model predicts much smaller values, with a maximum slightly higher than the natural frequency. The source of these discrepancies can be traced in the simulation results of the forced vibration experiments, as illustrated in Fig.3.3, where the model fails to capture the negative C_{ya}, analogous to added mass, over the range of oscillation frequencies where VIV takes place. The added mass introduced by the vortices has a significant influence on the response of the cylinder, especially for a small mass ratio system, since the natural frequency of the
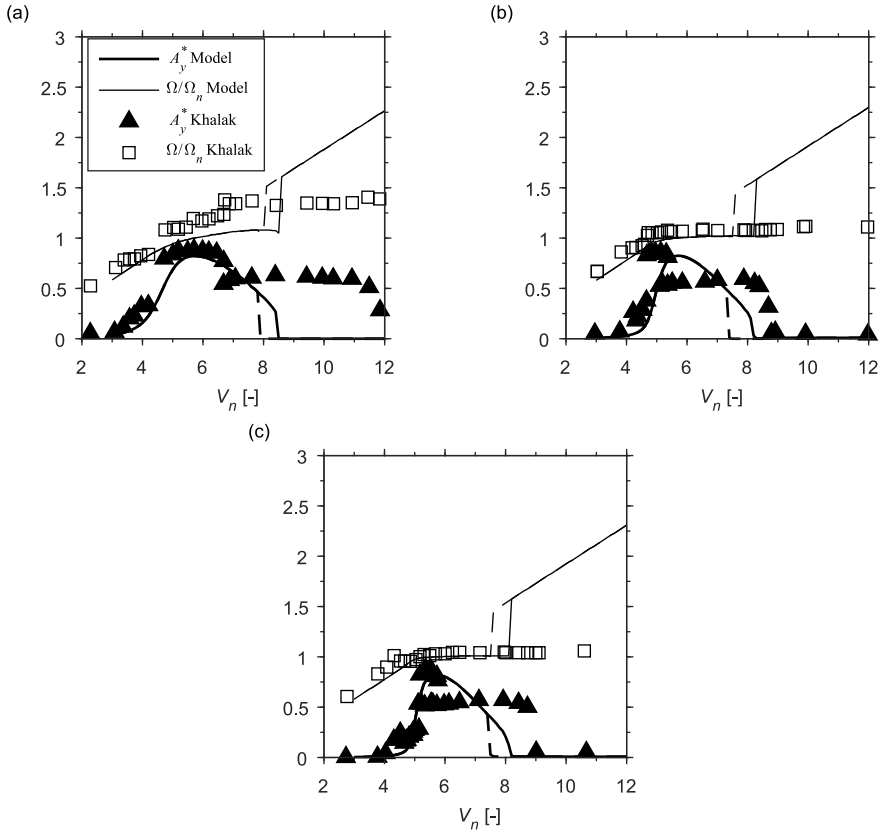
Figure 3.4: A comparison of the nonlinear coupling wake oscillator model and the free vibration measurements by Khalak and Williamson (1999) for (a) $m^* = 2.4, m^*\zeta = 0.014$; (b) $m^* = 10.3, m^*\zeta = 0.017$; and (c) $m^* = 20.6$, $m^*\zeta = 0.019$.

light cylinder when VIV occurs can be significantly different from that measured in still water. Without reproducing the negative added mass, it is expected that the model will predict a narrower lock-in range as well as a lower response frequency in free vibration simulations for small mass ratio systems.

Attempts have been made to capture the negative added mass without changing the added damping too much. This is difficult, as a frequency-dependent added mass is always accompanied by frequency-dependent added damping. Nevertheless, one possible way to achieve this goal is to introduce an additional restoring force. For detailed information and results, please refer to Appendix A.

3.3. ENHANCED MODEL WITH FREQUENCY-DEPENDENT NON-LINEAR COUPLING

As described in the previous section, a first attempt to improve the existing wake oscillator model by introducing nonlinear coupling terms is promising. However, one main drawback of the model is that it is not able to capture the negative added mass at high reduced velocities. In this section, the model is further enhanced by making the nonlinear coupling frequency-dependent.

3.3.1. DERIVATION OF FREQUENCY-DEPENDENT NONLINEAR COUPLING

In the time domain, the frequency dependency can be achieved by means of convolution integrals, and the nonlinear terms follow the same form as those in Eq.(3.2). To make the model as simple as possible, this study starts with the coupling

$$s = \int_0^\tau h_0(\tilde{\tau}) \dot{y}(\tau - \tilde{\tau}) d\tilde{\tau} + \int_0^\tau h_1(\tilde{\tau}) |y(\tau - \tilde{\tau})| \dot{y}(\tau - \tilde{\tau}) d\tilde{\tau} + \int_0^\tau h_2(\tilde{\tau}) y(\tau - \tilde{\tau})^2 \dot{y}(\tau - \tilde{\tau}) d\tilde{\tau} \quad (3.8)$$

which contains less nonlinear terms than Eq.(3.2). The reason for using less nonlinear terms is that the coupling given by Eq.(3.8) is already sufficient to generate a fairly suitable reproduction of the forced vibration measurements, as will be shown later.

Excitation on the wake oscillator, described by Eq.(3.8), contains multiple harmonic components due to nonlinearity. To have the formulas written in a clear format, the equations are formulated as a complex-valued form in the following part. Substituting the cylinder motion $y = -i\frac{y_0}{2}(e^{i\Omega\tau} - e^{-i\Omega\tau})$ into Eq.(3.8), and assuming that the components at a frequency higher than 3Ω have a minor influence on the results, Eq.(3.8) can be approximated, using Fourier expansion, as

$$s \approx K_1 e^{i\Omega\tau} + \bar{K}_1 e^{-i\Omega\tau} - (K_3 e^{i3\Omega\tau} + \bar{K}_3 e^{-i3\Omega\tau}) \quad (3.9)$$

where

$$\begin{aligned} K_1 &= \frac{1}{2} y_0 \Omega H_0(\Omega) + \frac{2}{3\pi} y_0^2 \Omega H_1(\Omega) + \frac{1}{8} y_0^3 \Omega H_2(\Omega) \\ K_3 &= \frac{1}{3\pi} y_0^2 \Omega H_1(3\Omega) + \frac{1}{8} y_0^3 \Omega H_2(3\Omega) \end{aligned} \quad (3.10)$$

and when steady state is reached, i.e. $\tau \to \infty$,

$$H_0(\Omega) = \int_0^\infty h_0(\tilde{\tau}) e^{-i\Omega\tilde{\tau}} d\tilde{\tau} \quad (3.11)$$

$$H_1(\Omega) = \int_0^\infty h_1(\tilde{\tau}) e^{-i\Omega\tilde{\tau}} d\tilde{\tau} \quad (3.12)$$

$$H_2(\Omega) = \int_0^\infty h_2(\tilde{\tau}) e^{-i\Omega\tilde{\tau}} d\tilde{\tau}. \quad (3.13)$$

The overbar in the equation above and in the remainder of this chapter designates the complex conjugation.

Eqs.(3.11-3.13) indicate that the time domain kernels $h_0(t)$, $h_1(t)$ and $h_2(t)$ are the inverse Laplace transforms of $H_0(\Omega)$, $H_1(\Omega)$ and $H_2(\Omega)$ respectively provided that the Laplace variable s is given by s = iΩ. To find the kernels of the convolution integrals, $H_0(\Omega)$, $H_1(\Omega)$ and $H_2(\Omega)$ must first be determined. This can be done by tuning the wake oscillator model described by Eqs.(2.22) and (3.9) to the forced vibration experiments at each frequency.

The steady state solution of Eqs.(2.22) and (3.9) can be sought for in the form of $q = q_1 e^{i\Omega\tau} + \bar{q}_1 e^{-i\Omega\tau} + q_3 e^{i3\Omega\tau} + \bar{q}_3 e^{-i3\Omega\tau}$. Substituting the latter expression into Eqs.(2.22) and (3.9), a collection of multipliers of $e^{i\Omega\tau}$ and $e^{i3\Omega\tau}$ yields two equations:

$$-i\epsilon q_1^2 \bar{q}_3 \Omega + \bar{q}_1 + i\epsilon \bar{q}_1 \Omega - 2i\epsilon q_3 \bar{q}_3 \bar{q}_1 \Omega - i\epsilon q_1 \bar{q}_1^{\,2} - \bar{q}_1 \Omega^2 - K_1 = 0$$
$$-i\epsilon \bar{q}_1^{\,3} \Omega + 3i\epsilon \bar{q}_3 \Omega - 9\bar{q}_3 \Omega^2 - 3i\epsilon q_3 \bar{q}_3^{\,2} \Omega + \bar{q}_3 - 6i\epsilon q_1 \bar{q}_1 \bar{q}_3 \Omega + K_3 = 0. \tag{3.14}$$

The hydrodynamic coefficients C_{ya} and C_{yv} are measured at the frequency of cylinder oscillation, and Eqs.(2.26) and (2.27) can be rewritten in the complex form as

$$-C_{yv} + iC_{ya} = \frac{2}{T} \int_{\tau_0}^{\tau_0+T} C_y \exp(i\Omega\tau)\, d\tau$$
$$= \frac{2}{T} \int_{\tau_0}^{\tau_0+T} C_{VY} \exp(i\Omega\tau)\, d\tau + iC_a \pi^3 \mathrm{St}^2 \Omega^2 y_0. \tag{3.15}$$

Substituting $q = q_1 e^{i\Omega\tau} + \bar{q}_1 e^{-i\Omega\tau} + q_3 e^{i3\Omega\tau} + \bar{q}_3 e^{-i3\Omega\tau}$ and $y = -i\frac{y_0}{2}(e^{i\Omega\tau} - e^{-i\Omega\tau})$ into Eq.(3.15) results in

$$-C_{yv} + iC_{ya} \approx \sqrt{1 + 4\pi^2 \mathrm{St}^2 \Omega^2 y_0^2}\left(-\frac{1}{2} q_1 C_{L0} - \frac{1}{4} \bar{q}_1 C_{L0} + \frac{3}{2}\pi \mathrm{St}\, y_0 C_{D0}\Omega\right) - \frac{1}{2} q_1 C_{L0}$$
$$+ \frac{1}{4}\bar{q}_1 C_{L0} + \frac{1}{2}\pi \mathrm{St}\, y_0 C_{D0}\Omega + 2iC_a\pi^3 \mathrm{St}^2 y_0 \Omega^2 \tag{3.16}$$
$$+ \frac{1}{4} q_3 C_{L0}\left(\sqrt{1 + 4\pi^2 \mathrm{St}^2 \Omega^2 y_0^2} - 1\right).$$

The approximation in Eq. (3.16) is obtained using

$$\sqrt{1 + 4\pi^2 \mathrm{St}^2 y_0^2 \Omega^2 \cos(\Omega\tau)^2} \approx \frac{1}{2}\sqrt{1 + 4\pi^2 \mathrm{St}^2 y_0^2 \Omega^2}\,(1 + \cos(2\Omega\tau)) + \frac{1}{2}(1 - \cos(2\Omega\tau)). \tag{3.17}$$

At a specific frequency Ω, if the values of $H_0(\Omega)$, $H_1(\Omega)$, $H_2(\Omega)$, $H_1(3\Omega)$ and $H_2(3\Omega)$ are already known, C_{ya} and C_{yv} at a certain amplitude y_0 can be calculated by solving algebraic equations Eqs.(3.14) and (3.16). Likewise, with measurements of C_{ya} and C_{yv} known, the values of $H_0(\Omega)$, $H_1(\Omega)$, $H_2(\Omega)$, $H_1(3\Omega)$ and $H_2(3\Omega)$ can be determined by solving the equation system formulated by Eqs.(3.14) and (3.16) at five amplitudes y_0.

Using the method described above, attempts were made to tune the model to the forced vibration experiments at different combinations of five amplitudes y_0. However, no solution was found through Eqs.(3.14) and (3.16). Thus, instead of being tuned to five amplitudes at each frequency, the model is tuned to three amplitudes by solving Eqs.(3.14) and (3.16), neglecting the third harmonic components by setting $K_3 = 0$. Some of the tuning results using different combinations of amplitudes are presented in Fig.3.5.
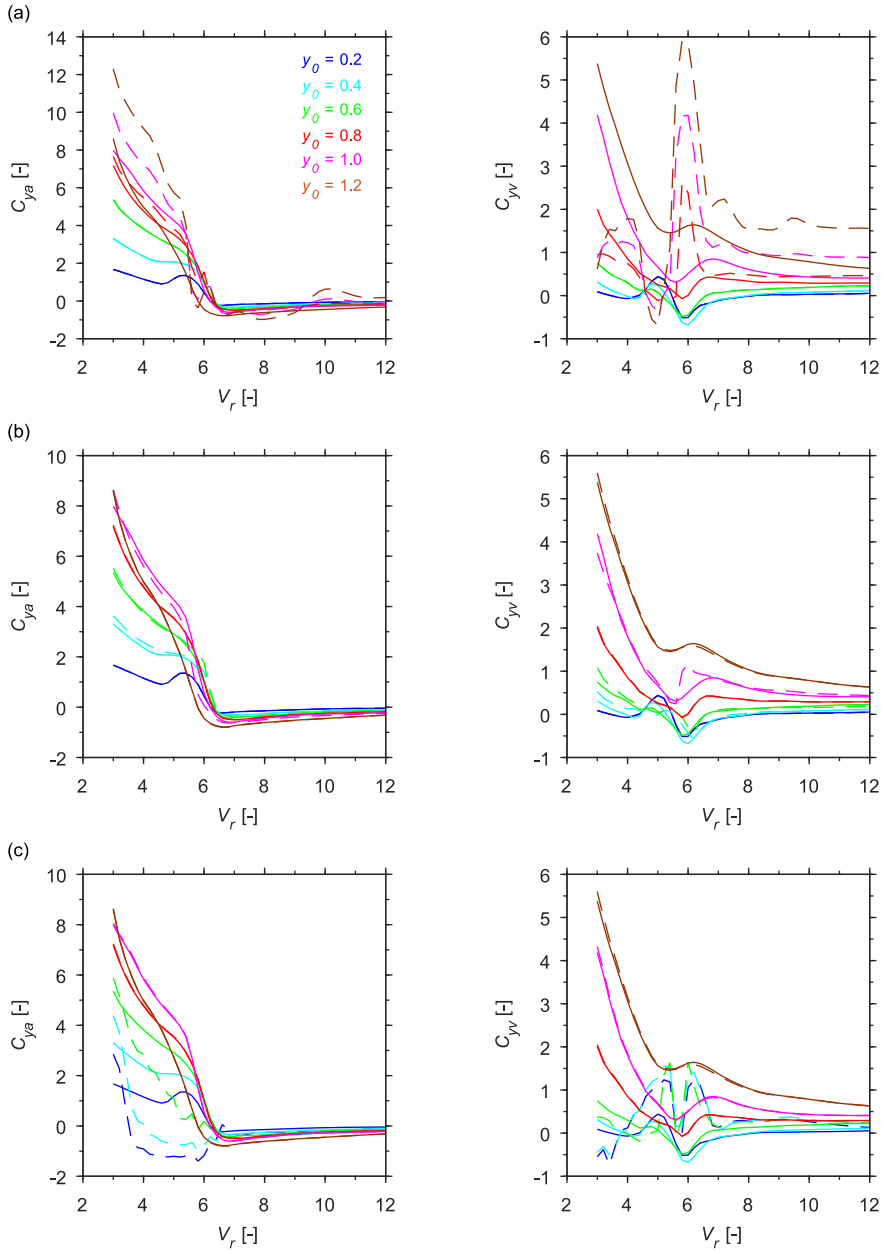
Figure 3.5: Tuning of the model with nonlinear coupling to the forced vibration measurements at amplitudes (a) $y_0 = 0.2, 0.4, 0.6$; (b) $y_0 = 0.2, 0.8, 1.2$; and (c) $y_0 = 0.8, 1.0, 1.2$. Solid lines represent measurements by Gopalkrishnan (1993) and dashed lines represent tuning results.

If the nonlinear couplings used in Eq.(3.8) are correct, then the choice of the three amplitudes to which the model is tuned should theoretically not affect the results in a significant way. However, from Fig.3.5, it can be seen that this is not the case here. The tuning results are highly sensitive to the choice of amplitudes, which is a strong indication that the coupling terms used here do not contain the correct nonlinearities. Despite this conclusion, it was found that with current model, it is possible to obtain an acceptable reproduction of experiments by tuning the model to $y0 = 0.2, 0.8, 1.2$; see plot (b) in Fig.3.5. The corresponding $H_0(\Omega)$, $H_1(\Omega)$ and $H_2(\Omega)$ are presented in Fig.3.6.

3.3.2. DETERMINATION OF THE CONVOLUTION KERNELS

In the previous subsection, the values of $H_0(\Omega)$, $H_1(\Omega)$ and $H_2(\Omega)$ have been determined within a finite frequency range according to the forced vibration experiments. Also, it has been demonstrated that the kernels $h_0(t)$, $h_1(t)$ and $h_2(t)$ are given by the inverse Laplace transforms of $H_0(\Omega)$, $H_1(\Omega)$ and $H_2(\Omega)$. However, before performing an inverse Laplace transform, the values of $H_0(\Omega)$, $H_1(\Omega)$ and $H_2(\Omega)$ within a finite range of frequencies need to be extended over the entire frequency domain. This process of extension is not arbitrary. To obtain a kernel in the time domain that follows the principle of causality, the frequency domain values need to be extended following the Kramers-Kronig relations (Elmore and Heald, 1989). For a complex function $\chi(\Omega) = \chi_1(\Omega) + i\chi_2(\Omega)$, the Kramers-Kronig relations are given by

$$\chi_1(\Omega) = \frac{2}{\pi} \mathscr{P} \int_0^\infty \frac{\Omega' \chi_2(\Omega')}{\Omega'^2 - \Omega^2} d\Omega'$$
$$\chi_2(\Omega) = -\frac{2\Omega}{\pi} \mathscr{P} \int_0^\infty \frac{\chi_1(\Omega')}{\Omega'^2 - \Omega^2} d\Omega' \tag{3.18}$$

where $\mathscr{P}$ denotes the Cauchy principle value. In this study, both real and imaginary parts are available only in a limited range of frequencies, which makes it impossible to extend them to the whole frequency domain by directly applying Eq.(3.18). Therefore, in this study, the spectrum of $H_0(\Omega)$, $H_1(\Omega)$ and $H_2(\Omega)$ is extended with complex curve fitting. The basic idea of this method is to approximate the frequency domain responses with basic functions that already meet Kromers-Kronig relations. The most widely used general fitting methodology was proposed by Gustavsen and Semlyen (1999), and it is used to fit the measured or calculated frequency domain responses with rational function approximations. The same method will be used in this paper.

According to Gustavsen and Semlyen (1999), a complex function $H(\Omega)$ can be approximated as

$$H(\Omega) = \sum_{n=1}^N \left(\frac{c_n}{i\Omega - a_n} + \frac{\bar{c}_n}{i\Omega - \bar{a}_n} \right) + d + i\Omega h. \tag{3.19}$$

The residual c_n and poles a_n are either real or complex quantities, while d and h are real. The inverse Laplace transform of Eq.(3.19) results in the kernel $h(\tau)$ as

$$h(\tau) = \sum_{n=1}^N [2\exp(a_n^{\text{re}})(c_n^{\text{re}}\cos(a_n^{\text{im}}\tau) - c_n^{\text{im}}\sin(a_n^{\text{im}}\tau))] + d\delta(\tau) + h\frac{d}{d\tau}\delta(\tau). \tag{3.20}$$

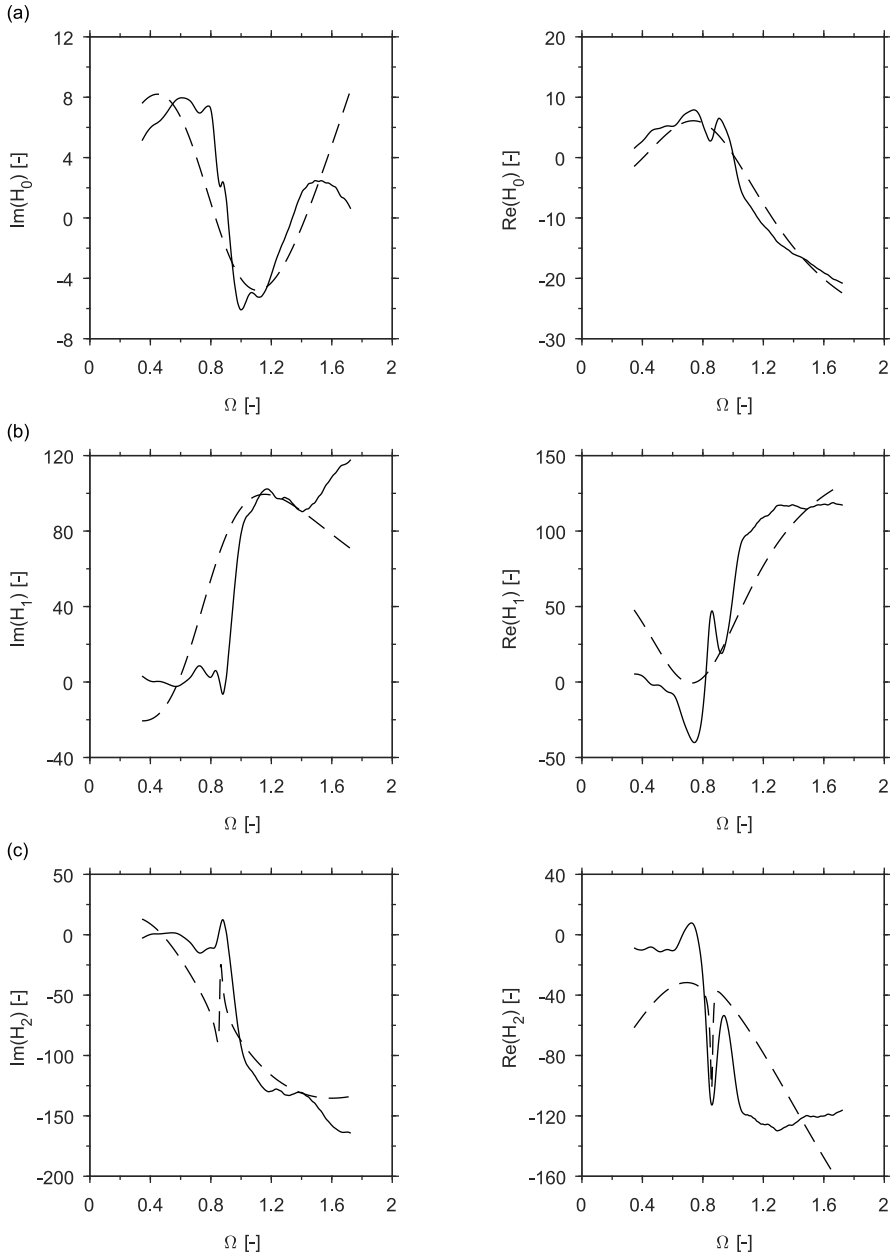Figure 3.6: Frequency-dependent $H_0\,(\Omega)$, $H_1\,(\Omega)$ and $H_2\,(\Omega)$ determined from the forced vibration measurements, represented by solid lines, as well as curve fitting results, represented by dashed lines.

in which δ denotes the Dirac delta function, and the superscripts 're' and 'im' denote the real and imaginary parts of c and a. From Eq.(3.20) it can be noted that the poles a

should have negative real parts to ensure that $\lim_{\tau \to \infty} h(\tau) = 0$.

Using this method, attempts were made to fit the complex curves of $H_0(\Omega)$, $H_1(\Omega)$ and $H_2(\Omega)$, as illustrated in Fig.3.6, with a well-developed publicly available Matlab package (vectfit3). The Matlab package is based on the work by Gustavsen and Semlyen (1999), Gustavsen (2006) and Deschrijver et al. (2008). However, obtaining good fits for all three curves was found to be impossible. For $H_0(\Omega)$, positive a_n^{re} are encountered for fitting results with $N > 2$. For $H_1(\Omega)$ and $H_2(\Omega)$, this study did not find any fit, as regardless of the number of poles used, poles with positive real parts always exist. By imposing constraints of $a_n^{re} < 0$ on the process of approximation, it is possible to obtain some fitting results for $H_1(\Omega)$ and $H_2(\Omega)$. However, these fitting results are poor. Fig.3.6 presents the fitting results of three curves with $N = 2$. Approximations have also been conducted with $N > 2$, but it was found that increasing the number of poles does not improve the fitting results.

3.4. Conclusions

In this chapter, attempts were made to improve the reproduction of forced vibration experiments by introducing nonlinear coupling to the wake oscillator equation. A set of nonlinear terms in the form of multiplications of acceleration, velocity and displacement of the cylinder up to the order of cubic was taken as a preliminary test. First, the coefficients of the nonlinear coupling terms were assumed to be constant, and the model was tuned to the forced vibration experiments. The simulation results reveal that the model is able to quantitatively reproduce the added damping measured in the forced vibration experiments over most of the range of frequencies and amplitudes that are of interest; however, it fails to capture the negative added mass. The model with the same tuning parameters was then applied to the simulation of free vibration experiments. It has been demonstrated that the model predictions are in good agreement with the free vibration experiments with high mass ratios regarding the maximum amplitude of cylinder oscillation, the frequency of cylinder oscillation and the range of lock-in. However, for small mass ratio experiments, the model significantly under-predicts the frequency of cylinder oscillation and the range of lock-in.

The model was further enhanced by introducing frequency-dependent nonlinear coupling. The frequency dependency was formulated in the time domain by means of convolution integrals. A set of frequency-dependent complex-valued functions that satisfy the forced vibration experimental measurements at all amplitudes fairly well was determined. These complex-valued functions were calculated by tuning the model to experimental measurements at three different amplitudes. Choosing the amplitudes to which the model is tuned has a significant influence on the results, which indicates that the nonlinearity in the model is still deficient.

The complex-valued functions were determined over a limited range of frequencies and need to be extended to the infinite frequency domain following the Kramers-Kronig relations. A widely used online complex curve fitting software was adopted to extend the spectrum. The theoretical basis of this method is to fit the frequency-dependent complex-valued functions with rational functions that already conform to the Kromers-Kronig relations. Using this method, attempts were made to find good fittings. However, the author has failed to obtain good fittings with rational functions that correspond to

decaying oscillatory signals in the time domain.

As a preliminary test, the results presented in this chapter highlight the potential possibility of improving the wake oscillator model by introducing nonlinear coupling. However, since the nonlinear coupling adopted in this chapter is insufficient in principle, it will not be used in the rest of this thesis.

3

4

MODELLING OF COUPLED CROSS-FLOW AND IN-LINE VORTEX-INDUCED VIBRATION OF AN ELASTICALLY SUPPORTED RIGID CYLINDER

4.1. INTRODUCTION

In the modelling of VIV, the in-line response is normally not of interest, as its amplitude is small compared to the cross-flow response. However, due to its doubled oscillating frequency, relative to the cross-flow, the in-line vibration may introduce significant fatigue damage to the structure. Also, studies have demonstrated that the presence of the in-line vibration may alter the wake pattern and consequently influence the cross-flow response. More importantly, in practical situations, the flexible structures possess multiple natural frequencies and are usually allowed to vibrate in different directions. In such cases, it is possible that resonance occurs in both cross-flow and in-line directions. Therefore, an advanced model that is capable of predicting the coupled cross-flow and in-line VIV is necessary and in urgent need for practical purpose.

Introducing a second wake oscillator equation that is coupled with the in-line motion to describe the oscillating drag force is a common approach taken by the researchers. However, in most cases, the two wake oscillators are uncoupled, and the one that describes the lift force is solely dependent on the cross-flow motion of the cylinder, while the oscillating drag force is predicted by the other oscillator, which is only coupled with the in-line motion. Bear in mind that the lift and drag forces have the same origin and are interdependent on each other. Therefore, the model with two wake oscillators may be said to contradict the fundamental mechanism of coupled cross-flow and in-line VIV.

This contradiction may be the reason that the existing double wake oscillator models cannot capture the super-upper branch, which is a distinct characteristic related to the coupled cross-flow and in-line VIV. It is physically more reasonable to use only one oscillator to describe the dynamics of the wake, and this oscillator should be coupled to both cross-flow and in-line motions of the cylinder. The development of such a wake oscillator model is the main objective of this chapter.

In Section 4.2, the model that describes the two degrees of freedom VIV of an elastically supported rigid cylinder is presented, with the focus on the introduction of an in-line coupling term to the wake oscillator equation. The proposed model is then validated against the existing experiments in Section 4.3. Final conclusions are provided in Section 4.4.

4.2. MODEL DESCRIPTION
In this section, the governing equations for the motion of an elastically supported rigid cylinder that is allowed to move in both cross-flow and in-line directions, the definition of hydrodynamic forces as well as the wake oscillator that is coupled to both in-line and cross-flow motion are presented.

4.2.1. GOVERNING EQUATIONS FOR THE STRUCTURE
Consider a rigid cylinder that is elastically supported in both cross-flow (represented by the y axis) and in-line (represented by the x axis) directions; see Fig.4.1. The displacements of the cylinder X and Y along the in-line and cross-flow directions can be described as

$$m\frac{d^2 X}{dt^2} + b\frac{dX}{dt} + kX = F_X \tag{4.1}$$

$$m\frac{d^2 Y}{dt^2} + b\frac{dY}{dt} + kY = F_Y \tag{4.2}$$

where m is the mass of the cylinder, and b and k are the viscous damping coefficient and the stiffness of the supports of the cylinder respectively. It should be noted here that there are experiments that have been conducted with unequal mass, stiffness and damping in different directions due to the set-up of the apparatus (Dahl et al., 2006; Moe and Wu, 1990); this is not considered here as they are generally equal in real applications. Furthermore, F_X and F_Y on the right-hand side of the equations are the in-line and cross-flow hydrodynamic forces acting on the cylinder, both of which are assumed to be expressible as a superposition of vortex force and an ideal inviscid inertia force associated with the potential added mass of the fluid:

$$F_X = F_{VX} + F_{AX} = F_{VX} - m_a \frac{d^2 X}{dt^2} \tag{4.3}$$

$$F_Y = F_{VY} + F_{AY} = F_{VY} - m_a \frac{d^2 Y}{dt^2}. \tag{4.4}$$

Moving the potential inertia force to the left-hand side of the equation, Eqs. (4.1) and (4.2) become

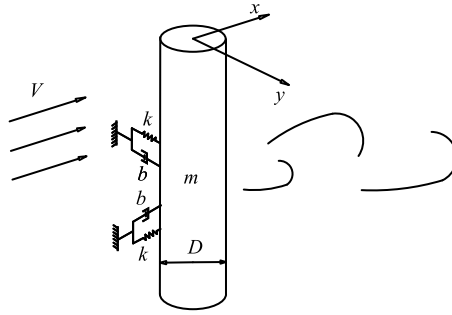$$\frac{d^2 X}{dt^2} + 2\zeta\omega_n\frac{dX}{dt} + \omega_n^2 Y = \frac{F_{VX}}{m + m_a}. \tag{4.5}$$

Figure 4.1: Coupled cross-flow and in-line VIV of an elastically supported rigid cylinder subjects to uniform flow.

$$\frac{d^2Y}{dt^2} + 2\zeta\omega_n\frac{dY}{dt} + \omega_n^2 Y = \frac{F_{VY}}{m + m_a} \tag{4.6}$$

where $\omega_n = \sqrt{k/(m + m_a)}$ is the structural natural frequency in still water, and $\zeta = b/(2\omega_n(m + m_a))$ is the damping ratio.

4.2.2. DEFINITION OF HYDRODYNAMIC FORCES

Following the same force decomposition as described in Section 2.2, the total vortex force is decomposed into an instantaneous drag force F_{VD} that acts along the relative flow velocity U and an instantaneous lift force F_{VL} in the perpendicular direction. The magnitudes of both forces are proportional to the square of the relative flow velocity and are given as

$$F_{VD} = \frac{1}{2}C_{VD}\rho DLU^2 \tag{4.7}$$

and

$$F_{VL} = \frac{1}{2}C_{VL}\rho DLU^2 \tag{4.8}$$

in which C_{VD} is the drag force coefficient, and C_{VL} is the instantaneous lift force coefficient, which is associated with the wake variable as $C_{VL} = \frac{q}{2}C_{L0}$. Since the cylinder also moves in the in-line direction, the relative flow velocity is now given as $U = \sqrt{\left(V - \frac{dX}{dt}\right)^2 + \left(\frac{dY}{dt}\right)^2}$. With the instantaneous lift and drag force defined above, the vortex forces F_{VX} and F_{VY} can then be written as

$$F_{VX} = \frac{1}{2}C_{VL}\rho DLU^2 \sin(\beta) + \frac{1}{2}C_{VD}\rho DLU^2 \cos(\beta) \tag{4.9}$$

$$F_{VY} = \frac{1}{2}C_{VL}\rho DLU^2 \cos(\beta) + \frac{1}{2}C_{VD}\rho DLU^2 \sin(\beta) \tag{4.10}$$

in which the angle β is the angle between the direction of the relative flow velocity U and that of undisturbed flow velocity V. This angle is given as

$$\sin\beta = -\frac{dY}{dt}/U, \quad \text{and} \quad \cos\beta = \left(V - \frac{dX}{dt}\right)/U. \tag{4.11}$$

The force definition described above is simply an extension of the one proposed by Ogink and Metrikine (2010), see Fig.2.2, by releasing the constraint in the in-line direction. In their model, the drag force coefficient is assumed to be constant and equals the steady component of the drag force measured from a stationary cylinder. One main problem with the utilisation of the constant drag force coefficient is that the model is not able to predict the pure in-line free vibration, since the cylinder, according to the force definition, is only subjected to a constant drag force when its motion in the cross-flow direction is constrained. One straightforward approach to deal with this shortcoming is to introduce an oscillating instantaneous drag force that is coupled with the instantaneous lift force in the following form:

$$C_{VD} = C_{DM} + \alpha C_{VL}^2 \tag{4.12}$$

where C_{DM} is constant, and the second quadratic term describes the relationship between the fluctuating lift and drag forces that are derived from a fixed cylinder (Qin, 2004). According to the definition of Eq.(4.12), the total drag force is composed of a steady part and an oscillating component. The magnitude of the steady drag force is the summation of C_{DM} and the mean value of αC_{VL}^2, and the latter component is proportional to the quadratic of the lift force coefficient's magnitude. Since the steady part of the drag force only damps the energy out from the structure, the author found that the cross-flow motion would be significantly underestimated due to the extra damping introduced by a large lift force. Recall that the same drag force model has already been investigated in Section 2.3. It has been shown that to satisfy the forced vibration experiments, the value of α varies much from negative to positive as the frequency of cylinder oscillation increases. It is thus not a surprise here that applying a positive constant α does not generate good predictions. Therefore, the instantaneous drag force coefficient is still assumed to be constant $C_{VD} = C_{DM}$. Meanwhile, a fluctuating force is directly introduced in the in-line direction and coupled with the lift force in the same manner as Eq.(4.12). In this way, the in-line vortex force F_{VX} is reformulated as

$$F_{VX} = \frac{1}{2}C_{VL}\rho DLU^2 \sin(\beta) + \frac{1}{2}C_{DM}\rho DLU^2 \cos(\beta) + \frac{1}{2}\alpha C_{VL}^2 \rho DLU_x|U_x| \tag{4.13}$$

where $U_x = V - \frac{dX}{dt}$ is the in-line component of the relative flow velocity U. When the cylinder dose not move, i.e. $\frac{dY}{dt} = 0$ and $\frac{dX}{dt} = 0$, Eq. (4.13) reduces to

$$F_{VX} = \frac{1}{2}\left(C_{DM} + \alpha C_{VL}^2\right)\rho DLV^2 \tag{4.14}$$

which is in the same form as proposed by Qin (2004) for the coupled lift and drag force on a fixed cylinder.

After performing the necessary substitutions into Eqs.(4.5) and (4.6), the structure's final equation of motion can be written as

$$\frac{d^2 X}{dt^2} + 2\zeta\omega_n \frac{dX}{dt} + \omega_n^2 Y = \frac{1}{2}\rho D V^2 \frac{C_{VX}}{m + m_a} \tag{4.15}$$

$$\frac{d^2 Y}{dt^2} + 2\zeta\omega_n \frac{dY}{dt} + \omega_n^2 Y = \frac{1}{2}\rho D V^2 \frac{C_{VY}}{m + m_a} \tag{4.16}$$

where

$$C_{VX} = -C_{VL}\frac{U}{V^2}\frac{dY}{dt} + C_{DM}\frac{U}{V^2}\left(V - \frac{dX}{dt}\right) + \alpha C_{VL}^2\left(1 - \frac{1}{V}\frac{dX}{dt}\right)|1 - \frac{1}{V}\frac{dX}{dt}| \tag{4.17}$$

and

$$C_{VY} = C_{VL}\frac{U}{V^2}\left(V - \frac{dX}{dt}\right) - C_{DM}\frac{U}{V^2}\frac{dY}{dt}. \tag{4.18}$$

Using the dimensionless parameters in Eq.(2.16) and parameter $x = X/D$, the dimensionless forms of Eqs.(4.15-4.18) can be obtained as

$$\ddot{x} + 2\zeta\Omega_n\dot{x} + \Omega_n^2 x = \frac{1}{(m^* + C_a)}\frac{1}{2\pi^3 \text{St}^2}C_{VX} \tag{4.19}$$

$$\ddot{y} + 2\zeta\Omega_n\dot{y} + \Omega_n^2 y = \frac{1}{(m^* + C_a)}\frac{1}{2\pi^3 \text{St}^2}C_{VY} \tag{4.20}$$

$$\begin{aligned}C_{VX} = &\left(C_{DM}(1 - 2\pi \text{St}\dot{x}) + 2\pi \text{St}\dot{y}C_{VL}\right)\sqrt{(1 - 2\pi \text{St}\dot{x})^2 + \left(2\pi \text{St}\dot{y}\right)^2}\\ &+ \alpha C_{VL}^2(1 - 2\pi \text{St}\dot{x})|1 - 2\pi \text{St}\dot{x}|\end{aligned} \tag{4.21}$$

$$C_{VY} = \left(-2\pi \text{St}\dot{y}C_{DM} + C_{VL}(1 - 2\pi \text{St}\dot{x})\right)\sqrt{(1 - 2\pi \text{St}\dot{x})^2 + \left(2\pi \text{St}\dot{y}\right)^2}. \tag{4.22}$$

4.2.3. WAKE OSCILLATOR COUPLED TO BOTH CROSS-FLOW AND IN-LINE DEGREES OF FREEDOM OF THE STRUCTURE

In the cross-flow VIV, the use of the oscillator to describe the wake dynamics comes from the experimental observation that 'the wake swings from side to side, somewhat like the tail of a swimming fish' (Birkhoff, 1953) as well as experimental measurements of lift and drag forces that 'responded to forcing rather as a simple oscillator would under similar circumstances' (Bishop and Hassan, 1964). The dynamics of the wake in the cross-flow VIV is dominated by alternate vortex shedding; therefore, the resultant lift force can be reasonably represented by an oscillator driven by the acceleration of cross-flow motion. Different from cross-flow VIV, for which the dynamics of the wake are dominated by the alternate vortex shedding, the in-line VIV is characterised by two response branches that correspond to different wake patterns. For the first branch (denoted as the SS branch) that occurs at a lower reduced velocity – defined as $V_n = \frac{2\pi V}{\omega_n D}$, within the range roughly between 1 and 2.5 – symmetric vortex shedding is observed, while for the second branch (denoted as the AS branch), the vortices are shed alternatively above $V_n \approx 2.5$, (Aguirre Romano, 1978). The priority of this work is to model the second excitation region of in-line VIV, as it corresponds to wake dynamics that are similar to those

in the cross-flow vibration. To simulate the first response branch due to the symmetric vortex shedding, another model may be needed and is not in the scope of this thesis.

In the second excitation region, Konstantinidis (2014) pointed out that the response of the cylinder is steady, and the fluctuation of the wake, represented by the transverse velocity fluctuation, is synchronised to half of the frequency of cylinder oscillation. From forced in-line vibration experiments, Aronsen (2007) also demonstrated that the lift force in this region contains significant components at both 0.5 and 1.5 times the frequency of cylinder oscillation. These facts suggest that the coupling between the in-line motion and the wake variable may be in the form that ensures parametric excitation of the lift force by the in-line vibration. To pursue this idea, the wake oscillator equation is now extended to include a parametric excitation term, and it is given as

$$\frac{d^2 q}{dt^2} + \epsilon\omega_s(q^2 - 1)\frac{dq}{dt} + \omega_s^2 q - \kappa\frac{d^2 X}{dt^2} q = \frac{A}{D}\frac{d^2 Y}{dt^2}. \tag{4.23}$$

The reason for using $\frac{d^2 X}{dt^2} q$ instead of other combinations, such as $\frac{dX}{dt} q$, is a reasonable guess based on the work by Nishi et al. (2008) in which the classic van der Pol wake oscillator equation was derived by replacing the wake behind the cylinder by a rigid bar. The coupling between the dynamics of the rigid bar, represented by the rotation angle, and the cross-flow motion of the cylinder was assumed to follow the same form as the dynamics of a rigid pendulum with a moving foundation. If the same assumption holds in the in-line direction, then the coupling between the wake oscillator and the in-line motion should be in the form of $\frac{d^2 X}{dt^2} q$, as can be derived from the Lagrange equation. For a more detailed derivation, please refer to Appendix B. The dimensionless form of Eq.(4.23) is given as

$$\ddot{q} + \epsilon(q^2 - 1)\dot{q} + q - \kappa\ddot{x}q = A\ddot{y}. \tag{4.24}$$

If only the in-line vibration is considered, and ignoring the damping term, then substituting $x = x_0 \sin(\Omega\tau)$ into Eq.(4.24) yields

$$\ddot{q} + q + \kappa\Omega^2 x_0 \sin(\Omega\tau)q = 0. \tag{4.25}$$

Eq.(4.25) is of the type generally known as the Mathieu's equation, the stability of which has been widely studied, and the transition curves that separate stable and unstable regions have been derived (Kovacic et al., 2018). It has been shown that Eq.(4.25) has several instability zones. The one of most interest to the current study – with Ω corresponding to reduced velocity smaller than 3, which is associated with the in-line VIV – is plotted in Fig.4.2(a), with $\kappa = 5$.

It can be seen from Fig.4.2(a) that Eq.(4.25) is unstable around $\Omega = 2$, and as the amplitude x_0 increases, the system is unstable over a wider range of Ω. The instability around $\Omega = 2$ is desirable because it introduces energy to the system and leads to synchronisation between the wake variable q and external forcing (in-line oscillation x) as well as the amplification of the magnitude of q. However, the unstable region does not have an upper bound with respect to the frequency of oscillation. At $x_0 > 0.1$, the unstable region will extend to infinity as the frequency of oscillation increases. This unbounded region of instability is against experimental observation, where the synchronisation as well as the amplification of the lift force is bounded within a certain range of
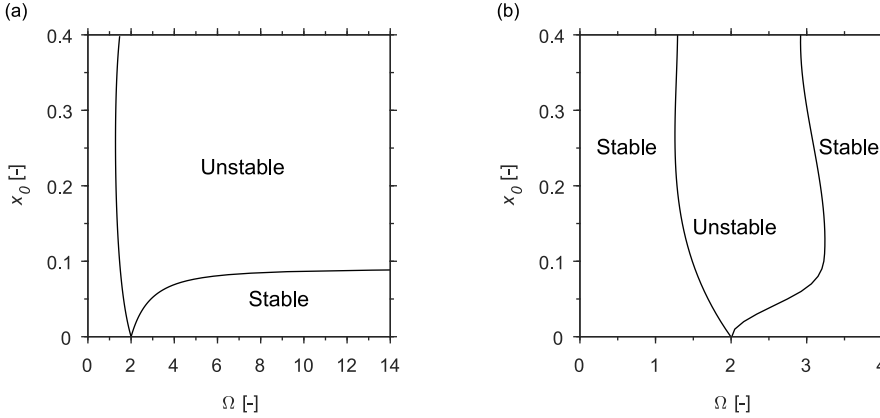
Figure 4.2: Stability maps of the model with (a) original in-line coupling term and (b) modified in-line coupling term. The coefficient of coupling $\kappa = 5$ is taken.

reduced velocities (Aronsen, 2007; Nishihara et al., 2005). To achieve a bounded unstable region, the term $\ddot{x}q$ is modified into $\frac{\ddot{x}}{1+\ddot{x}^2}q$ so that Eq.(4.25) becomes

$$\ddot{q} + \epsilon(q^2 - 1)\dot{q} + q - \kappa \frac{\ddot{x}}{1 + \ddot{x}^2}q = A\ddot{y} \qquad (4.26)$$

and the corresponding dimensional form is given as

$$\frac{d^2q}{dt^2} + \epsilon\omega_s(q^2 - 1)\frac{dq}{dt} + \omega_s^2 q - \kappa \frac{\omega_s^4 D \frac{d^2X}{dt^2}}{\omega_s^4 D^2 + \left(\frac{d^2X}{dt^2}\right)^2}q = \frac{A}{D}\frac{d^2Y}{dt^2}. \qquad (4.27)$$

The stability map of Eq.(4.26), after removing the damping term, with external in-line forcing is plotted in Fig.4.2(b), with $\kappa = 5$. The stability map is obtained numerically by applying the Floquet theory (Bittanti and Colaneri, 2009). As can be seen in Fig.4.2(b), the unstable region around $\Omega = 2$ is now bounded. To further illustrate the differences between the two terms, the response of q according to Eqs.(4.24) and (4.26) subjected to external forcing at $x_0 = 0.1$ is calculated with $\kappa = 5$ and $\epsilon = 0.08$, and the results are illustrated in Fig.4.3, where the maximum amplitude of the wake variable q_{max} and the frequency ratio Ω_q/Ω (Ω_q is obtained at the peak frequency) are presented. The results are shown against reduced velocity $V_r = 1/\text{St}/\Omega$. It is clear that the original in-line coupling term, as depicted in Fig.4.3(a), results in a lock-in range extended to small reduced velocities without any sign of lockout. The amplitude of q continuously increases as the reduced velocity decreases, and it reaches a value as high as 11 at $V_r = 0.5$. For the modified coupling term, Fig.4.3(b) demonstrates that the lock-in range is bounded approximately over the range of reduced velocities between $V_r = 1.5$ and 3.5. The amplification of q only occurs within the lock-in range; outside of this range, q oscillates at an amplitude close to 2. The comparison in Fig.4.3 indicates that the modified in-line coupling term is consistent with the experimental observation and will therefore be used in the rest of this thesis.
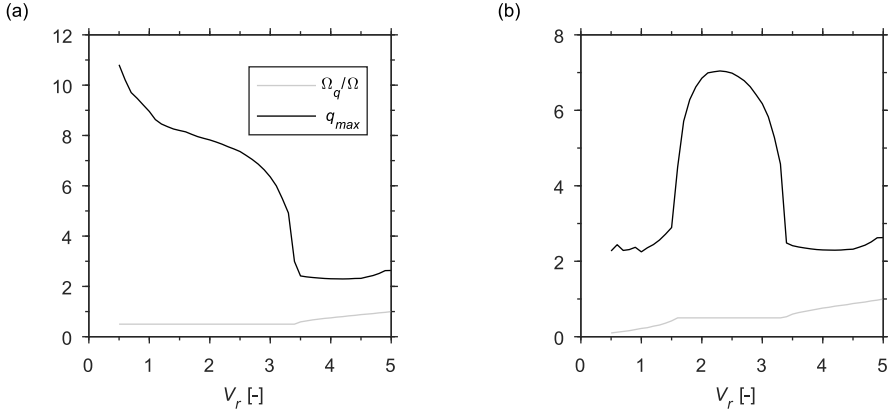
Figure 4.3: Dynamics of the wake variable q subjected to external in-line forcing at $x_0 = 0.1$ with coefficient $\kappa = 5$ and $\epsilon = 0.08$ for (a) original in-line coupling term and (b) modified in-line coupling term.

It must be clarified that the modification of the in-line coupling term to formulate a bounded unstable region is purely a mathematical manipulation, and whether the underlying mechanism of VIV in reality is in the same form is not known. Furthermore, although the results from the model with the original in-line coupling term do not meet the forced vibration experiments, it was found that this term actually works well in the simulations of free vibration of rigid cylinders and that of flexible cylinders subjected to uniform flow. In such cases, no obvious oscillation of the structure is observed at small reduced velocities where, according to the simulation results of forced vibration, a significant amplification of wake variable q occurs. This means that, different from the case of forced vibration, the coupled system is stable. However, the modified coupling term is still preferred. This is because in the cases where the flexible cylinder is subjected to the sheared flow, the vibration excited at high flow velocities will propagate to the low-velocity region and lead to instability, as demonstrated in this section.

4.3. MODEL VALIDATION AGAINST EXPERIMENTAL MEASUREMENTS

With the coupled system defined by Eqs.(4.19-4.22) as well as the wake oscillator in Eq.(4.26), the series of 2DOF VIV experiments reported by Jauvtis and Williamson (2004) have been simulated. In these experiments, the cylinder has the same natural frequency and mass ratio in the cross-flow and in-line directions.

4.3.1. COUPLED CROSS-FLOW AND IN-LINE FREE VIBRATIONS

Although several experiments have been conducted with mass ratio m^* varying from 1.5 to 25.0 and $(m^* + C_a)\zeta = 0.001$ to 0.1, detailed experimental data of cylinder responses are only reported for the cases of $m^* = 7.0$ with $\zeta = 0.0015$ and $m^* = 2.6$ with $\zeta = 0.0036$. These two cases demonstrate one of the main characteristics of the coupled

cross-flow and in-line VIV, namely the phenomenon of the super-upper branch. Jauvtis and Williamson (2004) discovered that the influence of the in-line freedom on the cross-flow response is surprisingly small provided that the mass ratio higher is than $m^* = 6$. However, as the mass ratio decreases to be smaller than $m^* = 6$, a new response branch, termed a 'super-upper' branch, appears in the cross-flow direction, with a peak cross-flow amplitude as large as $1.5D$. It will be shown later that with the model presented in the current study, this phenomenon is well captured.

The model is first tuned to the measurements of the experiment, with $m^* = 7$. The hydrodynamic coefficients on a stationary cylinder are assumed to be $St = 0.2$, $C_{L0} = 0.3$ and $\alpha = 2.2$ (to generate an oscillating drag force coefficient around 0.1). The mean drag force coefficient is assumed to be 1.2, then $C_{DM} = 1.2 - \alpha C_{L0}^2 / 2$. Since the model is not able to predict both the upper and lower branches of the cylinder response simultaneously (Ogink and Metrikine, 2010), two different sets of tuning parameters have been used to capture those branches separately. The case in which the model is tuned to the upper branch is referred to as 'Case U', and the other case is 'Case L'. The simulation results of the model in comparison with the experimental measurements are illustrated in Fig.4.4 against reduced velocity $V_n = 1/St/\Omega_n$. The tuning parameters used for Case U are $A = 8$, $\epsilon = 0.08$ and $\kappa = 5$; for Case L, they are $A = 20$, $\epsilon = 0.8$ and $\kappa = 5$.

The simulation results, as shown in Fig.4.4, are generally in good agreement with the experimental measurements, and the main characteristics of the coupled cross-flow and in-line VIV are well reproduced. According to the experiments, apart from the conventional lock-in region that is observed from the cross-flow-only vibration, an additional lock-in regime, which occurs at lower reduced velocities around $V_n \approx 2.5$, is identified. The latter regime corresponds to the same wake patterns observed in the pure in-line vibration with two response branches, SS and AS; therefore, it is denoted as an in-line vibration mode. Since the cross-flow response of the SS branch is almost zero, and the associated wake dynamics with symmetric vortex shedding are not considered by the current model, the results presented next are only for the AS response branch. As can be seen from Fig.4.4(c), the current model captures the lock-in regime associated with in-line vibration mode well. Within this lock-in range, the simulated frequency of the cross-flow response locks on to half of the natural frequency, $\Omega_y/\Omega_n = 0.5$ (Ω_y is the dimensionless cross-flow frequency), which is consistent with the experimental measurements, while the width of the lock-in is smaller than that of the experimental results. This is because, as discussed previously, in this study's model, only the AS response branch is considered. For the response amplitude, as illustrated in Figs.4.4(a) and (b), the upper and lower response branches are quantitatively captured by Case U and Case L respectively. Coupled cross-flow and in-line motions that are associated with the AS response branch around $V_n \approx 2.5$ are well captured in the Case U, although the predicted AS response branch occurs at slightly smaller reduced velocities, and its cross-flow amplitude is somehow underestimated. As for the in-line response, the amplitude of the AS response is in good agreement with the experiment. The model results of the in-line response corresponding to the upper branch of cross-flow vibration is larger than the experimental measurements, and that corresponding to lower branch is slightly over-predicted by Case L.

With the same tuning parameters, the model is then used to predict the coupled
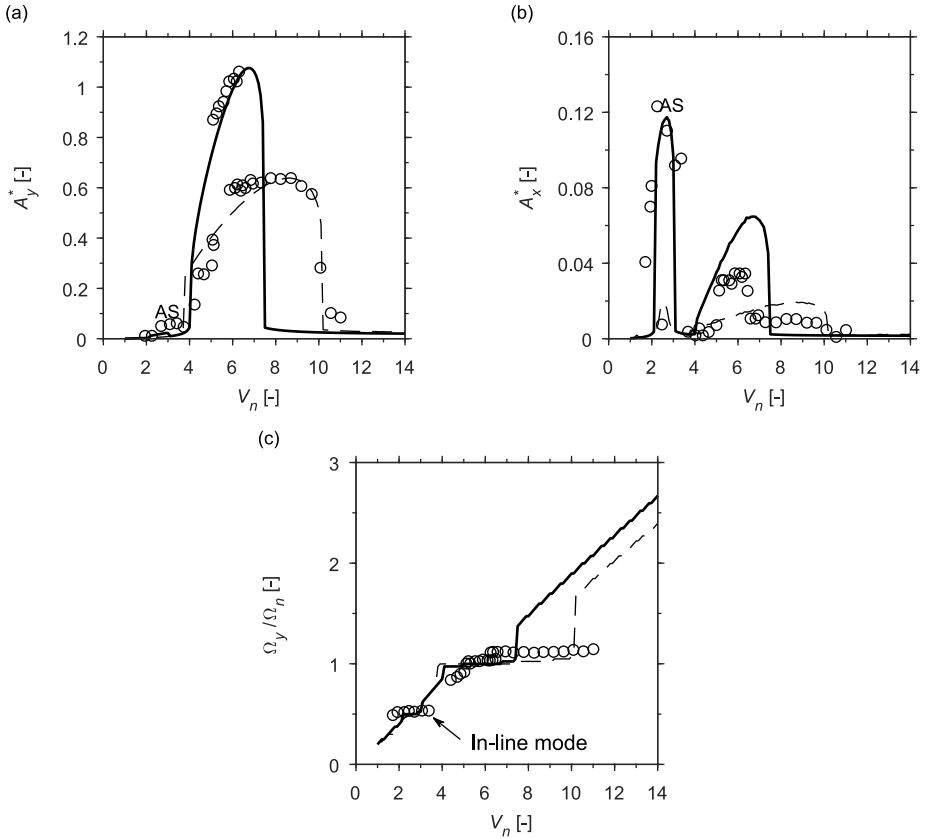
4

Figure 4.4: A comparison of numerical (lines) and experimental response (circles) with $m^* = 7$ and $(m^* + C_a)\zeta = 0.0117$ for (a) Cross-flow response amplitude, (b) In-line response amplitude and (c) Cross-flow response frequency. Solid lines represent "Case U", dashed lines represent "Case L", circles represent experimental data by Jauvtis and Williamson (2004).

cross-flow and in-line VIV of the experiment with $m^* = 2.6$ and $(m^* + C_a)\zeta = 0.013$. Fig.4.5 illustrates the prediction of the model in comparison with the experimental measurements. From Fig.4.5, it can be seen that the agreement between the prediction and experimental measurements is good. The super-upper branch, with the peak amplitude reaching $1.5D$, which is not observed in the previous case ($m^* = 7$) is quantitatively captured. To the author's knowledge, this characteristic of the coupled cross-flow and in-line VIV of rigid cylinders has never been truly captured by any wake oscillator models in the past. For the moment, the only model in which attempts were made to account for the effect of the mass ratio on the prediction of coupled cross-flow and in-line VIV is that by Srinil and Zanganeh (2012) – an empirical formula of tuning parameters with respect to m^* or ζ that meet the experimental measurements are derived therein. This is apparently an alternative approach for practical purposes when the model itself is not able to provide the correct prediction.
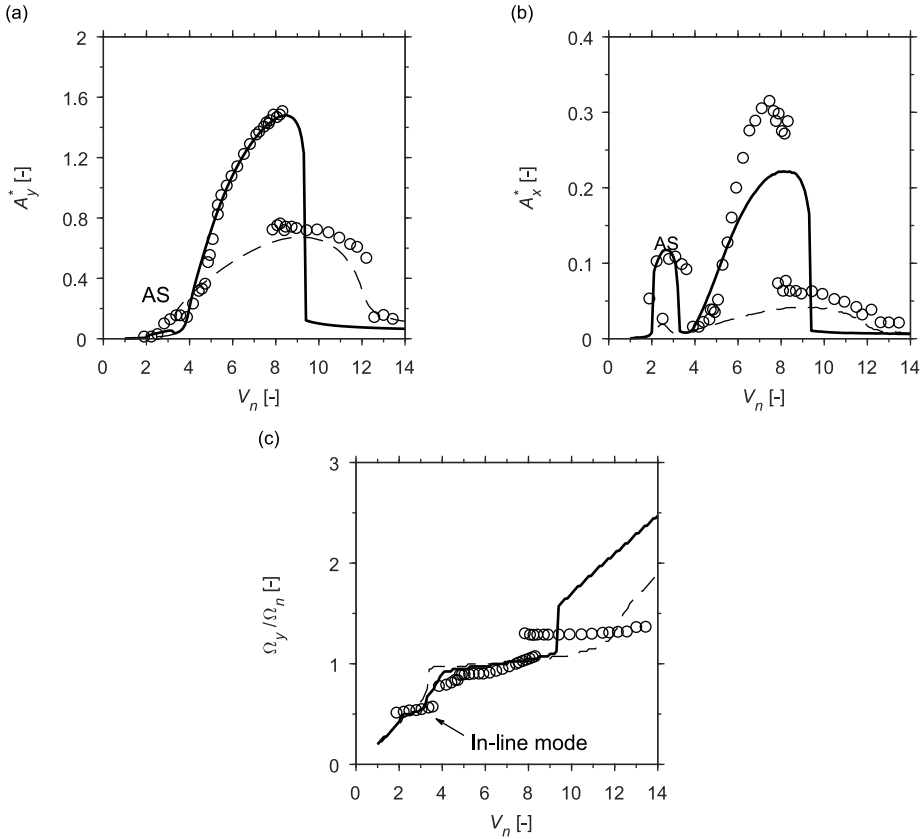
Figure 4.5: A comparison of numerical (lines) and experimental response (circles) with $m^* = 2.6$ and $(m^* + C_a)\zeta = 0.013$ for (a) Cross-flow response amplitude, (b) In-line response amplitude and (c) Cross-flow response frequency. Solid lines represent "Case U", dashed lines represent "Case L", circles represent experimental data by Jauvtis and Williamson (2004).

The phase difference between cross-flow and in-line vibrations and the corresponding trajectory shapes of cylinder motion are plotted in Fig.4.6 in which the phase angle ϕ_{xy} is defined in the same way as given by (Jauvtis and Williamson, 2004). It can be seen from Fig.4.6(a) that the model with the tuning parameters of Case U correctly predicts the general trend of measurements for reduced velocities smaller than 8. However, for the lower branch, while the experimental data are maintained at a constant close to 320° with an increased reduced velocity, the predicted phase by Case L continually increases and finally exceeds 360°. The predicted motion trajectory shapes corresponding to specific reduced velocities are depicted in Fig.4.6(b) based on the last 40 cycles of steady response. In general, the trajectory shapes are consistent with the experimental findings (Jauvtis and Williamson, 2004). For the coupled motion around $V_n \approx 3$, the typical figure-of-eight-type motion is predicted. As the reduced velocity increases, the figure eight starts to become elongated in the cross-flow direction and gradually transforms

into a crescent pattern. Different from experiments in which the super-upper branch ends with a crescent pattern at the maximum amplitude, the predicted response continues to evolve and ends at the maximum amplitude with a shape of eight again.
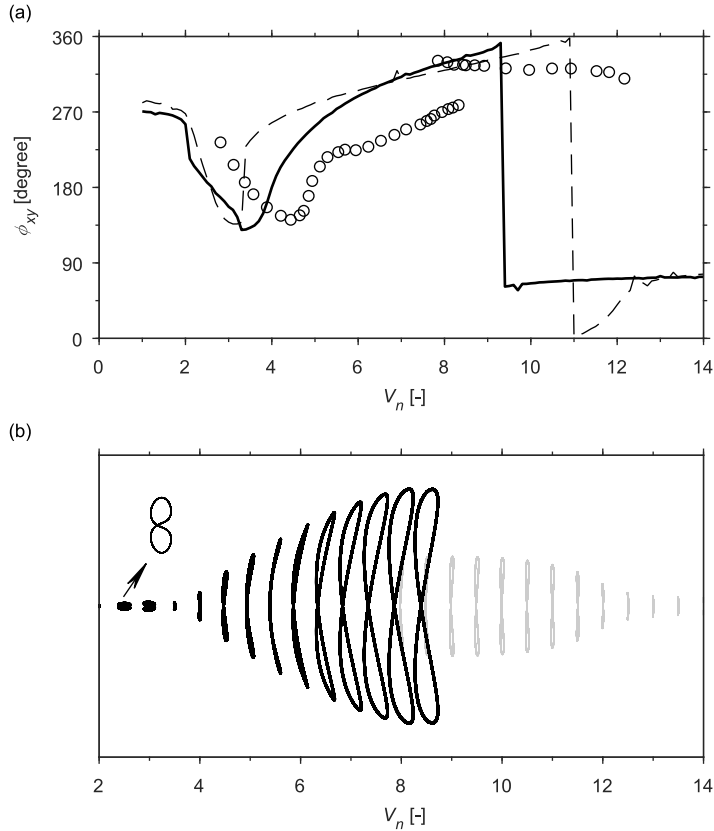

Figure 4.6: Phase and trajectory of cross-flow and in-line motions with $m^* = 2.6$ and $(m^* + C_a)\zeta = 0.013$ for (a) phase angle (solid line represents Case U, dashed line represents Case L, circles represent experimental data by Jauvtis and Williamson (2004)) and (b) trajectory (Case U is represented by color black, Case L is represented by color grey).

4.3.2. Influence of the mass ratio and Griffin plots

In recent decades, discussions have been had on the main influential factors that affect the peak amplitude (typically cross-flow) of VIV. Although Govardhan and Williamson (2006) have proven that for the cross-flow-only VIV, it is possible to collapse the peak amplitude data of different cylinders against unique parameter $(m^* + C_a)\zeta$ if the influence of the Reynolds number is taken into account, this is most likely not the case for the coupled cross-flow and in-line VIV, as Jauvtis and Williamson (2004) have explicitly demonstrated that the magnitude of the mass ratio plays an important role in the appearance of the super-upper branch that yields large amplitudes in both cross-flow and

in-line directions. In this subsection, the model proposed in this paper is used to produce the 'Griffin' plots for the coupled cross-flow and in-line VIV and to investigate the influence of mass ratios on the peak cross-flow and in-line amplitudes. Since the maximum response is of most interest here, only Case U will be considered, and the same tuning parameters as those in Section 4.3.1 will be used for the rest of this section.

In the series of experiments conducted by Jauvtis and Williamson (2004), although the maximum peak amplitudes against $(m^* + C_a)\zeta$ are reported, in most cases the exact values of m^* and ζ at which the specific experiment is conducted are not given. Therefore, the simulation results are obtained at several mass ratios picked from the range that is used by the experiments, while the varied $(m^* + C_a)\zeta$ is obtained by altering ζ. Fig.4.7 presents the predicted peak amplitudes of both cross-flow ($A^*_{y,max}$) and in-line ($A^*_{x,max}$) peak amplitude against $(m^* + C_a)\zeta$, with each curve representing a constant m^*. It can be seen from Figs.4.7(a) and (b) that for a specific $(m^* + C_a)\zeta$, the predicted
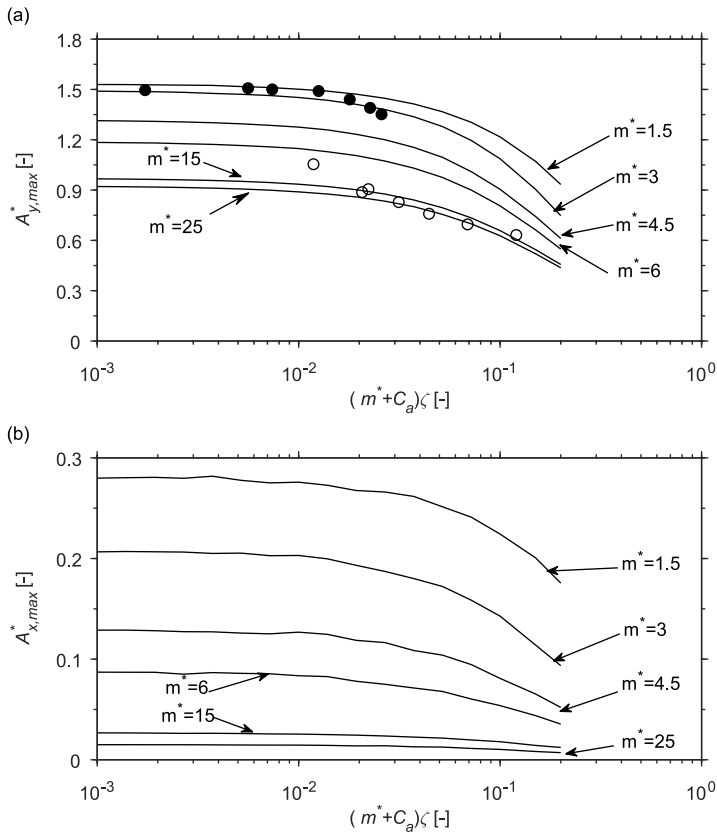

Figure 4.7: Griffin plots of peak amplitudes for coupled cross-flow and in-line VIV based on experimental (symbols) and prediction (lines) results for (a) Cross-flow peak amplitude and (b) In-line peak amplitude. Dots represent experimental data for $2.5 < m^* < 4$, and circles represent experimental data for $6 < m^* < 25$ (Jauvtis and Williamson, 2004).

peak amplitudes based on different m^* and corresponding ζ are different, which clearly indicates the independent effect of m^* on the peak amplitude. At a fixed mass ratio, the variation of peak amplitudes against $(m^* + C_a)\zeta$ follows the same trend as that observed from cross-flow-only experiments (Govardhan and Williamson, 2006). In general, the peak amplitude first increases rapidly as $(m^* + C_a)\zeta$ decreases, and it then gradually reaches a saturation limit when $(m^* + C_a)\zeta$ becomes small. The measured cross-flow peak amplitudes are also plotted in Fig.4.7(a), and it can be seen that these amplitudes for $2.5 < m^* < 4$ (represented by solid dots) almost collapse between the curves of prediction with $m^* = 1.5$ and $m^* = 3$. Moreover, those measurements for $6 < m^* < 25$ (represented by circles) are also well predicted. With regard to the maximum attainable peak amplitude, the predictions of the model demonstrate the increase in the peak amplitude from around $0.9D$ for a cross-flow response and $0.02D$ for an in-line response at $m^* = 25$ to over $1.6D$ and $0.26D$ respectively at $m^* = 1.5$. It seems that the lower limit of the peak amplitude is reached at $m^* = 25$ for both cross-flow and in-line vibrations, and the upper limit is also reached for the cross-flow vibration, while the upper limit of the in-line peak amplitude can still be extended as m^* further decreases from 1.5.

To further investigate the influence of m^*, the model is used to predict the peak amplitude at a specific $(m^* + C_a)\zeta \approx 0.013$ with a varying m^*, and the results are presented in Fig.4.8 in comparison with experimental measurements. Overall, there is a good agreement between the predictions and experimental results. The general trend of an increasing peak amplitude with a decreasing m^* is well predicted by the model. For m^* higher than 6, the predicted peak amplitudes in both directions are less dependent on the variation of m^*, and they display a trend of convergence as m^* further increases. This is consistent with the experimental observation that at $m^* > 6$, the coupled cross-flow and in-line VIV shows no obvious difference compared to the cross-flow-only VIV, and the peak amplitude mainly depends on the value of $(m^* + C_a)\zeta$ ((Govardhan and Williamson, 2006; Jauvtis and Williamson, 2004).
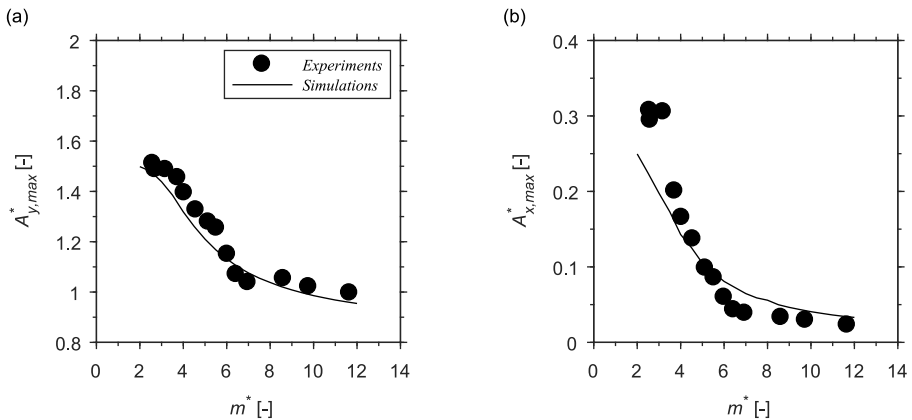

Figure 4.8: A Comparison of predicted (lines) and experimentally measured (dots and circles) peak amplitudes with varying mass ratio for (a) Cross-flow peak amplitude and (b) In-line peak amplitude. Experimental data is taken from the work by Jauvtis and Williamson (2004)

4.4. CONCLUSIONS

In this chapter, a wake oscillator model for the prediction of the coupled cross-flow and in-line VIV of an elastically supported rigid cylinder has been presented. The model includes improvements with respect to the conventional van der Pol wake oscillator by introducing a new in-line coupling term as well as by enhancing the expression for the in-line force such that it can fluctuate when the cylinder moves in the in-line direction only.

Based on the experimental observation and heuristic inference from the dynamics of a rigid suspended pendulum, the in-line coupling term, in its dimensionless form, $q\ddot{x}$ has been introduced. The stability of the model with $q\ddot{x}$, when subjected to a pure in-line forced vibration, has been studied and shown to not be in agreement with experimental observation. Therefore, a more sophisticated term $q\frac{\ddot{x}}{1+\ddot{x}^2}$, which has the same qualitative dynamic effect as $q\ddot{x}$, has been adopted.

First, the new model has been tuned to the free vibration experiment of an elastically supported rigid cylinder with mass ratio $m^* = 7$. Two different sets of tuning parameters have been applied to reproduce the upper and lower branches separately. It has been shown that the simulation results are in good agreement with the experimental measurements, and the main characteristics of the coupled cross-flow and in-line VIV are well captured. With the same tuning parameters, the model has then been applied to predict another free vibration experiment with smaller mass ratio $m^* = 2.6$. It has been demonstrated that the prediction is in good agreement with the experimental measurements. Most importantly, the appearance of the super-upper branch, as a result of a decreasing mass ratio, has been well captured.

The new model has also been used to predict the experiments regarding the influence of mass and damping ratios on the peak amplitude. The comparison between the Griffin plot generated by the new model and the available experimental data suggests good agreement. The model also captures the experimental observation of an increasing trend of the peak amplitude as the mass ratio decreases, while keeping $(m^* + C_a)\zeta$ constant.

5

MODELLING OF COUPLED CROSS-FLOW AND IN-LINE VORTEX-INDUCED VIBRATIONS OF FLEXIBLE CYLINDRICAL STRUCTURES

5.1. INTRODUCTION

The VIV of flexible structures is an important source of fatigue damage of the offshore structures, and the reliable prediction thereof has been a long-standing problem. Although studies of a simpler case of a finite-span rigid cylinder placed in a uniform flow have shed light on the main mechanisms of VIV and have led to several prediction models for rigid cylinders, the modelling of the VIV of long, flexible cylinders is more difficult. The main challenges stem partly from the instinctively more complicated dynamics of those slender structures and partly from the complexity of the fluid-structure interaction that varies both spatially and temporally.

In most early studies of the VIV of flexible cylinders, the focus has been on the analysis and prediction of the vibrations of a top-tensioned riser, which can be adequately modelled as a tensioned beam or cable with appropriate boundary conditions. With a small amplitude of vibration, the structural dynamics model is normally assumed to be linear, and the cross-flow and in-line motions are considered separately. However, in practical applications, many long, slender structures, such as catenary risers, pipelines during laying processes and mooring cables, have a curved shape. Due to the high slenderness of the structure and complicated environmental loads, the dynamics of these structures often exhibit strong 3D nonlinear coupling motions. Therefore, a general, realistic, nonlinear model of the structure that is valid for both straight and curved struc-

tures is needed.

In previous chapters, efforts have been dedicated to the modelling of the VIV of rigid cylinders; the ultimate goal is to apply the same hydrodynamic force model for the VIV of flexible structures. Strictly speaking, it is not correct to apply the hydrodynamic force model developed for rigid cylinders to flexible ones, as the fluid-structure interaction process in the two cases are not the same. However, since the principal mechanisms of vortex shedding are similar for both cases, it is expected that the model may be able to capture the main characteristics of the VIV of flexible structures. In fact, several studies have applied the wake oscillator model to the simulation of the VIV of flexible cylinders, and the results are promising.

The remainder of the chapter is structured as follows. In Section 5.2, the models of both the structure and hydrodynamic force are described. The models are then applied to simulate the experiments by Chaplin et al. (2005), and the comparison between the results of the simulations and experiments are discussed in Section 5.3. Finally, the main conclusions are presented in Section 5.4.

5.2. Model description
In this section, the structural and hydrodynamic force models for the simulation of the VIV of flexible cylinders are described. The structure is modelled as an extensible Euler-Bernoulli beam, which can deal with both the straight and curved configurations, and a 3D nonlinear coupled motion is considered. A local reference frame is introduced at each location along the cylinder within which the wake oscillator model presented in Chapter 4 is applied to model the hydrodynamic force.

5.2.1. Weak form of nonlinear equations of motion of the structure
The flexible cylinder is simplified into a beam. In line with the Euler-Bernoulli beam theory, only the axial and bending deformations are considered. This is a reasonable simplification in most cases when the shear deformation and torsion are negligible, and it is computationally more efficient. The configuration of the structure is described by the position vector $\mathbf{r}(p,t)$ of the cylinder axis as

$$\mathbf{r}(p,t) = \begin{bmatrix} x(p,t) \\ y(p,t) \\ z(p,t) \end{bmatrix} \tag{5.1}$$

where p is the Lagrange coordinate or arc-length measured along the undeformed cylinder, and t is the time. For the convenience of writing, the following notation will be used to represent the partial derivative with respect to p: $\mathbf{r}_{,p} = \partial \mathbf{r}/\partial p$ and overdots represent the derivative with respect to time.

The weak form of the equations of motion is given as

$$\delta W_I + \delta W_S - \delta W_E = 0 \tag{5.2}$$

where δW_I denotes the virtual work of inertia forces, δW_S is the virtual work of internal (elastic) forces, and δW_E is the virtual work of external forces.

The expressions of virtual work of inertia force is given as

$$\delta W_I = \int_0^L m_0 \ddot{\mathbf{r}}^T \delta \mathbf{r} \, dp \tag{5.3}$$

where L is the length of undeformed beam.

The virtual work of internal forces, as proposed by Gerstmayr and Irschik (2008), is divided into two parts: one due to the bending moment and another due to the axial force. That virtual work reads as follows:

$$\delta W_S = \int_0^L (EA\epsilon_0 \delta\epsilon_0 + EIK\delta K) \, dp \tag{5.4}$$

in which E is the modulus of elasticity, A is the cross-sectional area and I is the second moment of the area. Furthermore, ϵ_0 is the axial strain, which is defined as

$$\epsilon_0 = |\mathbf{r},_p| - 1 \tag{5.5}$$

and K, interpreted by Géradin and Cardona (2001) as the *material measure of curvature*, is defined as

$$K = \frac{|\mathbf{r},_p \times \mathbf{r},_{pp}|}{|\mathbf{r},_p|^2} \tag{5.6}$$

The variation of axial strain ϵ_0 is given by

$$\delta\epsilon_0 = \frac{1}{|\mathbf{r},_p|} \mathbf{r}^\top,_p \delta\mathbf{r},_p. \tag{5.7}$$

The variation of K reads

$$\begin{aligned}
\delta K = &- 2 \frac{|\mathbf{r},_p \times \mathbf{r},_{pp}|}{|\mathbf{r},_p|^4} \mathbf{r}^T,_p \delta\mathbf{r},_p \\
&+ \frac{1}{|\mathbf{r},_p|^2 |\mathbf{r},_p \times \mathbf{r},_{pp}|} \left(\mathbf{r},_p \times \mathbf{r},_{pp}\right)^\top \left(\delta\mathbf{r},_p \times \mathbf{r},_{pp} + \mathbf{r},_p \times \delta\mathbf{r},_{pp}\right).
\end{aligned} \tag{5.8}$$

5.2.2. HYDRODYNAMIC FORCE MODEL

In Chapter 4, the wake oscillator model has been developed for the VIV of rigid cylinders subjected to a uniform flow that is perpendicular to their axis. However, in many engineering applications of long, flexible cylinders, the flow may not be uniform (shear flow) and, in many cases, not perpendicular to the axis of the cylinder, such as in the case of a catenary riser. In such cases, the independence principle is normally applied; it assumes that the flow dynamics are essentially dependent on the normal component of free stream with respect to the cylinder axis, while the component that is aligned with the cylinder axis has a negligible impact (Bourguet and Triantafyllou, 2015). Several studies have demonstrated that the independence principle is only valid within a certain range of inclination angles (Lucor and Karniadakis, 2003; Ramberg, 1983). Here, the inclination angle is defined as the angle between the incoming flow and the plane that is perpendicular to the cylinder axis. For a fixed cylinder, it is generally shown that the above-mentioned principle provides an accurate prediction for inclination angles smaller than
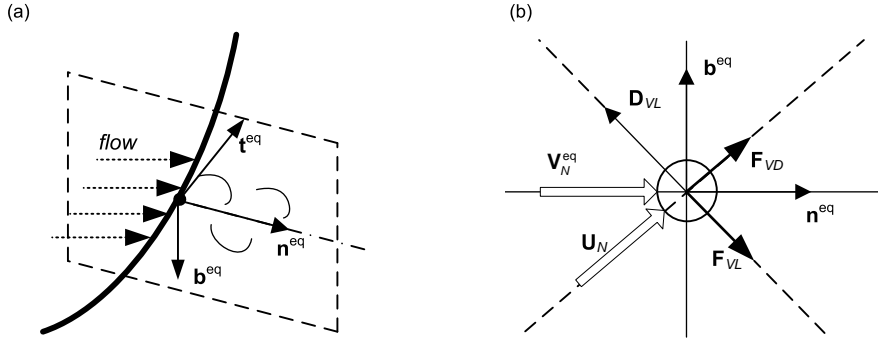
Figure 5.1: Local vortex shedding for a curved beam and definition of the local coordinate system: (a) local coordinate system and (b) force decomposition in plane $\mathbf{b}^{\mathrm{eq}} - \mathbf{n}^{\mathrm{eq}}$.

40° (Zhao et al., 2009). As for cases in which the cylinder is free to move in the cross-flow direction, the principle is qualitatively valid up to 65° but with a decreasing range of lock-ins and a maximum amplitude of vibration as the inclination angle increases (Jain and Modarres-Sadeghi, 2013).

To apply the wake oscillator for the modelling of the VIV of flexible cylinders, a local coordinate must first be established for each cross-section. Since the VIV of a flexible structure is normally characterised as finite amplitude motions around the equilibrium position, it is reasonable to build up the local coordinate system based on the equilibrium position of the structure. Consider a segment of a cylinder at its equilibrium position subjected to the flow, as illustrated in Fig.5.1(a). Using the local frame described by the tangential unit vector $\mathbf{t}^{\mathrm{eq}}$, in-line unit vector $\mathbf{n}^{\mathrm{eq}}$ and cross-flow unit vector $\mathbf{b}^{\mathrm{eq}}$, according to the independence principle, the vortex shedding process is assumed to take place in the plane that is perpendicular to the orientation of the beam, i.e. the $\mathbf{b}^{\mathrm{eq}} - \mathbf{n}^{\mathrm{eq}}$ plane. Here, the superscript 'eq' signifies that the vectors are obtained in the equilibrium position. According to O'Neill (2006), the tangential unit vector $\mathbf{t}^{\mathrm{eq}}$ is given as

$$\mathbf{t}^{\mathrm{eq}} = \frac{\mathbf{r}^{\mathrm{eq}}_{,p}}{|\mathbf{r}^{\mathrm{eq}}_{,p}|}. \tag{5.9}$$

Under the equilibrium configuration, the free stream velocity at a specific location of the structure is $\mathbf{V}^{\mathrm{eq}}$, and its component within the plane of vortex shedding, i.e. $\mathbf{b}^{\mathrm{eq}} - \mathbf{n}^{\mathrm{eq}}$, is obtained as

$$\mathbf{V}^{\mathrm{eq}}_N = \mathbf{V}^{\mathrm{eq}} - \left((\mathbf{V}^{\mathrm{eq}})^{\mathsf{T}} \, \mathbf{t}^{\mathrm{eq}} \right) \mathbf{t}^{\mathrm{eq}}. \tag{5.10}$$

The in-line unit vector $\mathbf{n}^{\mathrm{eq}}$ is defined to be in the same direction as $\mathbf{V}^{\mathrm{eq}}_N$, and it reads

$$\mathbf{n}^{\mathrm{eq}} = \frac{\mathbf{V}^{\mathrm{eq}}_N}{|\mathbf{V}^{\mathrm{eq}}_N|}. \tag{5.11}$$

The cross-flow unit vector $\mathbf{b}^{\mathrm{eq}}$ is defined as the following cross product:

$$\mathbf{b}^{\mathrm{eq}} = \mathbf{t}^{\mathrm{eq}} \times \mathbf{n}^{\mathrm{eq}}. \tag{5.12}$$

The unit vectors $\mathbf{t}^{\mathrm{eq}}$, $\mathbf{n}^{\mathrm{eq}}$ and $\mathbf{b}^{\mathrm{eq}}$ formulate the local coordinate system within which the wake oscillator proposed in Chapter 4 is applied. The unit vector $\mathbf{b}^{\mathrm{eq}}$ corresponds to the cross-flow direction of the rigid cylinder, and the unit vector $\mathbf{n}^{\mathrm{eq}}$ corresponds to the in-line direction. Within the plane $\mathbf{b}^{\mathrm{eq}} - \mathbf{n}^{\mathrm{eq}}$, the force decomposition is the same as that for a rigid cylinder and is depicted in Fig.5.1(b). It has to be pointed out that this local coordinate system is based on the equilibrium configuration of the structure and does not change as the structure vibrates. The same rule applies to the corresponding parameters (with the superscript 'eq') that are derived from the equilibrium position. Within the local coordinate, the wake oscillator equation (see Eq.(4.27)) can be written as

$$\ddot{q} + \omega_s \left(q^2 - 1 \right) \dot{q} + \omega_s^2 q - \kappa \frac{\omega_s^4 D \ddot{\mathbf{r}}^{\mathsf{T}} \mathbf{n}^{\mathrm{eq}}}{\omega_s^4 D^2 + (\ddot{\mathbf{r}}^{\mathsf{T}} \mathbf{n}^{\mathrm{eq}})^2} q = \frac{A}{D} \ddot{\mathbf{r}}^{\mathsf{T}} \mathbf{b}^{\mathrm{eq}} \tag{5.13}$$

where $\omega_s = 2\pi \mathrm{St} |\mathbf{V}_N^{\mathrm{eq}}| / D$. The instantaneous lift and drag forces per unit length are defined as

$$\mathbf{F}_{VL} = \frac{1}{2} \rho D \frac{C_{L0}}{2} q |\mathbf{U}_N|^2 \mathbf{D}_{VL} \tag{5.14}$$

$$\mathbf{F}_{VD} = \frac{1}{2} \rho D C_{DM} |\mathbf{U}_N| \mathbf{U}_N \tag{5.15}$$

where $\mathbf{U}_N$ is the relative flow velocity within plane $\mathbf{b}^{\mathrm{eq}} - \mathbf{n}^{\mathrm{eq}}$, which is given as

$$\mathbf{U}_N = \mathbf{V}_N^{\mathrm{eq}} - \left(\dot{\mathbf{r}} - \left(\dot{\mathbf{r}}^{\mathsf{T}} \mathbf{t}^{\mathrm{eq}} \right) \mathbf{t}^{\mathrm{eq}} \right) \tag{5.16}$$

and $\mathbf{D}_{VL}$ is the unit vector in the $\mathbf{b}$-$\mathbf{n}$ plane that is perpendicular to $\mathbf{U}_N$ and is given as

$$\mathbf{D}_{VL} = \frac{\mathbf{t}^{\mathrm{eq}} \times \mathbf{U}_N}{|\mathbf{t}^{\mathrm{eq}} \times \mathbf{U}_N|}. \tag{5.17}$$

The extra in-line oscillating force, denoted by $\mathbf{F}_{OI}$ is given as

$$\mathbf{F}_{OI} = \frac{1}{2} \rho D \alpha \frac{C_{L0}^2}{4} q^2 |\mathbf{U}_{NX}| \mathbf{U}_{NX} \tag{5.18}$$

where

$$\mathbf{U}_{NX} = \mathbf{V}_N^{\mathrm{eq}} - \left((\mathbf{n}^{\mathrm{eq}})^{\mathsf{T}} \dot{\mathbf{r}} \right) \mathbf{n}^{\mathrm{eq}}. \tag{5.19}$$

Apart from the hydrodynamic force, the structure is also subjected to a hydrostatic force when submerged in the fluid. The concept of effective tension is normally used in off-shore engineering to take into account the effect of hydrostatic fluid pressure. The effective tension approach states that the total effect of the structure's fluid pressure – internal or external – on a section of the structure can be replaced by the buoyancy force that follows the Archimedes' principle and an axial tension equal to $P_e A_e - P_i A_i$, where P_e is the external fluid pressure, A_e is the corresponding external area of the cross-section, P_i is the internal fluid pressure, and A_i is the corresponding internal area of the cross-section. The buoyancy force is treated as the external distributed force, while the tension $P_e A_e - P_i A_i$ will be taken as the internal force and incorporated into the equation of motion of the structure. For simplicity, the $P_e A_e - P_i A_i$ is calculated based on the equilibrium configuration of the structure and does not change during the vibration.

In the current model, the 3D vortex patterns in the fluid are not taken into account. The dynamics of the wake variable q, as described by Eq.(5.13), are only controlled by the motion of the structure at the location where the wake oscillator acts on, without any direct influence from adjacent ones. As a result, the distribution of q along the structure may be discontinuous. However, this is physically not rigorous, as the hydrodynamic force should evolve along the span in a continuous manner because of the viscosity of the fluid. The continuity of the wake variable q along the span is enforced in the next subsection by applying a Hermite shape function to interpolate q with the finite element method.

5.2.3. FINITE ELEMENT FORMULATION

Fig.5.2 depicts a two-noded beam element, which is the same as the lower-order element proposed by Gerstmayr and Shabana (2006), with two nodes A and B at each end. Each node is defined by six degrees of freedom that consist of the nodal global position vector and slope vector:

$$\mathbf{u}_j = \begin{bmatrix} \mathbf{r}_j^\mathsf{T} & \mathbf{r}_{j,p}^\mathsf{T} \end{bmatrix}^\mathsf{T} \quad j = A, B. \tag{5.20}$$

Then, the beam element coordinates are given by the vector

$$\mathbf{u} = \begin{bmatrix} \mathbf{u}_A^\mathsf{T} & \mathbf{u}_B^\mathsf{T} \end{bmatrix}^\mathsf{T}. \tag{5.21}$$

The global position vector of an arbitrary point within the beam element, originally placed at p of the undeformed beam axis, in the deformed configuration can be interpolated in terms of the nodal coordinates and the element shape function as

$$\mathbf{r}(p, t) = \begin{bmatrix} x(p, t) \\ y(p, t) \\ z(p, t) \end{bmatrix} = \mathbf{S}\mathbf{u}. \tag{5.22}$$

Hermit shape functions are employed, and the shape function matrix S is written as

$$\mathbf{S} = [S_1\mathbf{I} \quad S_2\mathbf{I} \quad S_3\mathbf{I} \quad S_4\mathbf{I}] \tag{5.23}$$

where $\mathbf{I}$ is the 3×3 unit matrix, and functions $S_i = S_i(p)$ are given by

$$\left. \begin{aligned} S_1 &= 2\left(\frac{p}{L}\right)^3 - 3\left(\frac{p}{L}\right)^2 + 1, & S_2 &= L\left(\frac{p}{L}\right)^3 - 2L\left(\frac{p}{L}\right)^2 + p \\ S_3 &= 3\left(\frac{p}{L}\right)^2 - 2\left(\frac{p}{L}\right)^3, & S_4 &= L\left(\frac{p}{L}\right)^3 - L\left(\frac{p}{L}\right)^2 \end{aligned} \right\}. \tag{5.24}$$

By substituting Eq. (5.22) into Eq. (5.3), one obtains the virtual work of inertia force as

$$\delta W_I = \ddot{\mathbf{u}}^\mathsf{T} \int_0^L m_0 \mathbf{S}^\mathsf{T} \mathbf{S} dp \delta \mathbf{u} \tag{5.25}$$

from which the mass matrix of the structure element is determined as

$$\mathbf{M}_s^e = \int_0^L m_0 \mathbf{S}^\mathsf{T} \mathbf{S} dp \tag{5.26}$$
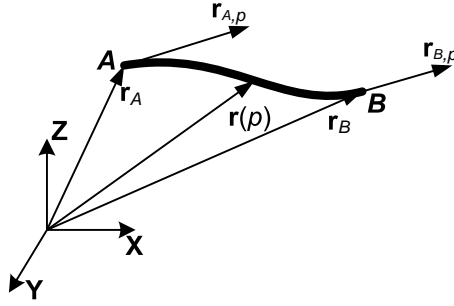
Figure 5.2: Two-noded beam element.

where m_0 is mass of the cylinder per unit length.

Similarly, by substituting Eq.(5.22) into Eq.(5.4), the stiffness matrix of the structure element $\mathbf{K}_s^e$ is obtained. The detailed derivation, as well as the final expression of $\mathbf{K}_s^e$, is provided in Appendix C.1.

For the structural damping, the Rayleigh damping model is applied for simplification, and it reads as follows:

$$\mathbf{C}_s^e = \alpha \mathbf{M}_s^e + \beta \mathbf{J}_s^{e,\text{eq}} \tag{5.27}$$

where $\mathbf{J}_s^{e,\text{eq}} = \frac{\partial \mathbf{K}^{e,\text{eq}} \mathbf{e}}{\partial \mathbf{e}}$ is the tangent stiffness matrix calculated under the equilibrium configuration.

The wake oscillators are uniformly distributed along the structure and therefore also need to be discretised in accordance with the beam element. With the same Hermite shape function as that used for the beam element, the wake variable q is interpolated as

$$q(p, t) = \mathbf{S}_q \mathbf{q} \tag{5.28}$$

where $\mathbf{q}$ is the wake element coordinates and consists of the wake variable as well as its derivative with respect to p at two nodes of beam element $\mathbf{q} = [q_A \quad q_{A,p} \quad q_B \quad q_{B,p}]^\top$. $\mathbf{S}_q$ is the shape function matrix and is written as

$$\mathbf{S}_q = [S_1 \quad S_2 \quad S_3 \quad S_4]. \tag{5.29}$$

Then, the mass matrix, damping matrix and stiffness matrix of the wake variable element can be obtained from Eq.(5.13) as

$$\mathbf{M}_q^e = \int_0^L \mathbf{S}_q^\top \mathbf{S}_q \, dp \tag{5.30}$$

$$\mathbf{C}_q^e = \int_0^L \omega_s \left(\mathbf{q}^\top \mathbf{S}_q^\top \mathbf{S}_q \mathbf{q} - 1 \right) \mathbf{S}_q^\top \mathbf{S}_q \, dp \tag{5.31}$$

$$\mathbf{K}_q^e = \int_0^L \omega_s^2 \mathbf{S}_q^\top \mathbf{S}_q \, dp + \kappa \int_0^L \frac{\omega_s^4 D \left(\ddot{\mathbf{u}}^\top \mathbf{S}^\top \mathbf{n}^{\text{eq}} \right)}{\omega_s^4 D^2 + (\ddot{\mathbf{u}}^\top \mathbf{S}^\top \mathbf{n}^{\text{eq}})^2} \mathbf{S}_q^\top \mathbf{S}_q \, dp. \tag{5.32}$$

By applying the principal of virtual work to Eq.(5.14), (5.15) and (5.18), the nodal hydro-dynamic forces are obtained as

$$
\begin{aligned}
\mathbf{F}^e &= \int_0^L \mathbf{S}^\top \left(\mathbf{F}_{VL} + \mathbf{F}_{VD} + \mathbf{F}_{OI} \right) dp \\
&= \frac{1}{2}\rho D \frac{C_{L0}}{2} \int_0^L |\overline{\mathbf{U}}_N|^2 \mathbf{S}^\top \overline{\mathbf{D}}_{VL} \mathbf{S}_q \mathbf{q} \, dp \\
&\quad + \frac{1}{2}\rho D C_{DM} \int_0^L |\overline{\mathbf{U}}_N| \mathbf{S}^\top \overline{\mathbf{U}}_N \, dp \\
&\quad + \frac{1}{2}\rho D \alpha \frac{C_{L0}^2}{4} \int_0^L \left(\mathbf{S}_q \mathbf{q} \right)^2 |\overline{\mathbf{U}}_{NX}| \mathbf{S}^\top \overline{\mathbf{U}}_{NX} \, dp
\end{aligned}
\tag{5.33}
$$

where $\overline{\mathbf{U}}_N$, $\overline{\mathbf{U}}_{NX}$ and $\overline{\mathbf{D}}_{VL}$ are obtained by substituting Eq.(5.22) into Eqs.(5.16), (5.17) and (5.19) and are given as

$$
\overline{\mathbf{U}}_N = V_N^{eq} - \left(\mathbf{S}\dot{\mathbf{u}} - \left(\dot{\mathbf{u}}^\top \mathbf{S}^\top \mathbf{t}^{eq} \right) \mathbf{t}^{eq} \right)
\tag{5.34}
$$

$$
\overline{\mathbf{U}}_{NX} = \mathbf{V}_N^{eq} - \left(\left(\mathbf{n}^{eq} \right)^\top \mathbf{S}\dot{\mathbf{u}} \right) \mathbf{n}^{eq}
\tag{5.35}
$$

$$
\overline{\mathbf{D}}_{VL} = \frac{\mathbf{t}^{eq} \times \overline{\mathbf{U}}_N}{|\mathbf{t}^{eq} \times \overline{\mathbf{U}}_N|}.
\tag{5.36}
$$

Similarly, the external nodal force of the wake oscillator can be obtained as

$$
\mathbf{R}^e = \frac{A}{D} \int_0^L \mathbf{S}_q^\top \ddot{\mathbf{u}}^\top \mathbf{S}^\top \mathbf{b}^{eq} dp.
\tag{5.37}
$$

After discretisation, the dynamics of the coupled system are described by ordinary differential equations that, in the matrix form, are given as

$$
\mathbf{M}_s^e \ddot{\mathbf{u}} + \mathbf{C}_s^e \dot{\mathbf{u}} + \mathbf{K}_s^e \mathbf{u} = \mathbf{F}^e
\tag{5.38}
$$

$$
\mathbf{M}_q^e \ddot{\mathbf{q}} + \mathbf{C}_q^e \dot{\mathbf{q}} + \mathbf{K}_q^e \mathbf{q} = \mathbf{R}^e.
\tag{5.39}
$$

Implicit Newmark time integration method is used to solve the above equation, and validation of the structural model is also performed, see Appendix C.2 and C.3.

5.3. MODEL VALIDATION AGAINST EXPERIMENTS

In this section, the model of the VIV of flexible cylinders that was developed in the previous section is used to simulate the experiments conducted by Chaplin et al. (2005), and the simulation results are compared to the experimental measurements.

5.3.1. EXPERIMENT DESCRIPTION AND COORDINATE SYSTEM

In the series of experiments conducted by (Chaplin et al., 2005), the cross-flow and in-line vibrations of a vertical tensioned riser were measured when being towed through the still water by a carriage at different speeds. The riser is 13.12 m long, with a diameter of $D = 0.028$ m, and only the lower 45% of its length is submerged in the flume and

Table 5.1: Properties of the riser model

Parameters	Values	Dimension
External diameter	0.028	m
Length	13.12	m
Aspect ratio	470	-
Submerged Length	5.94	m
Flexural Stiffness	29.88	Nm^2
Mass	1.845	kg/m
Mass ratio	3	-

subjected to a uniform current; the remaining part is in still water – see Fig.5.3. The two ends of the riser are connected to a stiff frame mounted on the carriage through universal joints, and the tension is provided by a set of springs at the top that allows the top end of the riser to move in the vertical direction. The detailed main parameters of the experiment are summarised in Table 5.1.

To model the experiments, a global Cartesian coordinate system with its origin at the bottom of the riser has been used; see Fig.5.4. The x-axis is aligned with the flow direction representing the in-line direction; the z-axis coincides with the vertical axis of the riser in its initial configuration, and the y axis is perpendicular to both, representing the cross-flow direction. The riser is pinned to the supporting structure at the bottom, which only allows rotation, while the top of the riser is pinned to an array of springs hanging from the supporting structure and is therefore can move in the z direction. When the riser vibrates, its configuration at any moment is described by the position vector $\mathbf{r}(p, t)$, where p is the coordinate along the riser.

When applying the model described in the previous section, an important part is to determine the equilibrium configuration of the structure, upon which the local coordinate system can be established. However, the mean in-line deflection of the structure, as a result of amplified in-line force, is not known in advance, and an iterative procedure thus is required. Here, for simplicity, the iteration is not included and the initial vertical configuration of the riser is considered to be its equilibrium configuration.

5.3.2. PREDICTED SINGLE AND MULTIPLE FREQUENCY RESPONSES

With the model described in Section 5.2, simulations are performed for the VIV of a riser under initial top tension $T = 810$ N at different flow velocities ranging from 0.1 m/s to 1.0 m/s, with a step of 0.02 m/s, resulting in a total of 45 cases. The same hydrodynamic force coefficients and tuning parameters of the upper case as those used in Section 4.3 have been applied, except that a different Strouhal number St = 0.17 is taken, as measured in the Delft-Flume experiments. The riser is discretised into 50 elements, and a convergence test has been conducted to assure the accuracy of the discretisation. For each case, the flow velocity is applied in a ramped manner, and the simulation time is chosen such that a minimum time window of steady-state response corresponding to at least 50 vortex shedding cycles (following the Strouhal relation) is achieved.

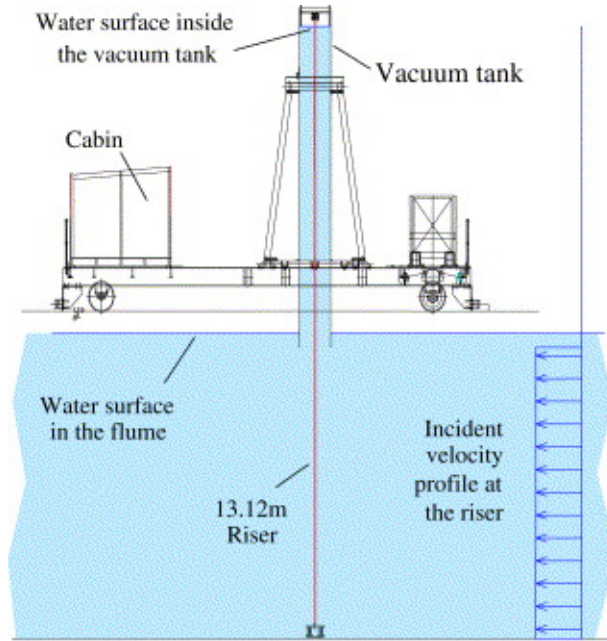For a flexible riser that is subjected to the uniform flow, despite the fact that several

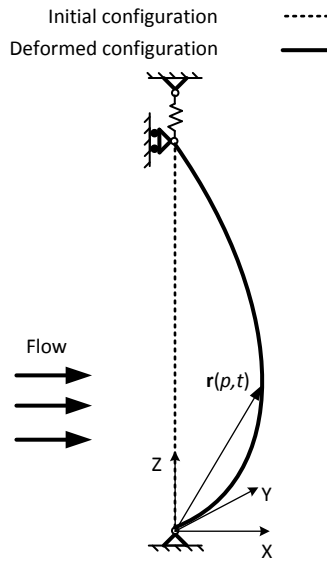Figure 5.3: Layout of the experiments (Chaplin et al., 2005).

Figure 5.4: Schematic of the global coordinate system and riser in its initial and deformed configurations.

modes may potentially be excited, it is normally expected that one will eventually dominate, and the motion of the riser would be characterised as a single frequency response. Although in the case of experiments to be simulated in this section, only half of the riser is subjected to flow, the behaviour of the riser should follow the same pattern, since it is expected that only one vortex shedding frequency is involved. However, the simulation results of the experiments reveal the presence of both single and multiple frequency responses. In what follows, two examples of riser responses at two different flow velocities $V = 0.5$ m/s and $V = 0.56$ m/s are presented to illustrate the typical riser response observed in the simulation results.

Case 1: $V = 0.5$ m/s, single frequency response.

An example of a simulated single frequency response is demonstrated here at flow velocity $V = 0.5$ m/s. The spatial and temporal characteristics of the structural response are analysed based on a 2D Fourier transform. Denoting the cross-flow displacement of the riser as $y(p/L, t)$, where p is the coordinate along the riser and L is the length of the riser, the 2D Fourier Transform of the displacement is defined as

$$\tilde{\mathbf{y}}(f, k) = \frac{1}{L} \int_0^L \int_0^{T_0} y(p/L, t) \, e^{-i2\pi f t} e^{-i2\pi k p/L} dt dp \tag{5.40}$$

where f is the frequency, k is the dimensionless wavenumber and T_0 is the duration of the data set. The above equation is the Continuous Fourier Transform and for the discrete displacements, as those obtained from the simulation, the Fast Fourier Transform (FFT) has been applied. The 2D FFT of the in-line displacement, with the mean in-line deflection subtracted, is calculated in the same way. In the following part, the 2D spectrum of the displacement of the riser is presented in the form of power spectral density (PSD), which is obtained as $|\tilde{\mathbf{y}}|^2 / T_0$. In Figs.5.5(a) and (b), the 2D PSD of cross-flow and in-line non-dimensional displacements are presented against the frequency and spatial wavenumber. The PSD is normalised by its maximum value. The frequency of oscillations – f_y for the cross-flow and f_x for the in-line – is normalised by the vortex shedding frequency f_s. where p is the coordinate along the riser. Only the positive frequency is presented in Figs.5.5(a) and (b), and positive wavenumbers are thus associated with travelling waves propagating towards $p/L = 0$ (downwards), while negative wavenumbers are associated with travelling waves moving in the opposite direction. Figs.5.5(a) and (b) also illustrate the wavenumbers of free vibration structural modes, indicated by vertical dashed lines, and the corresponding natural frequencies, indicated by red crosses, which are calculated using the finite element model described in the previous section. The modal shape and natural frequencies of the structure are obtained under the initial straight configuration under top tension that is equal to the mean value of the simulated varying top tension. Due to the variation of the tension along the riser as a result of gravity, the structural mode shapes are slightly different from sinusoidal shapes. For the sake of simplicity, the wavenumbers of the structural modes are still approximated using sinusoidal mode shapes.

As can be seen from Figs.5.5(a) and (b), the structural response is dominated by a single frequency in both the cross-flow and in-line directions. In the cross-flow direction, the riser oscillates at a peak frequency $f_y = 0.877 f_s$, and the in-line motion is dominated by the frequency $f_x = 1.754 f_s$, which is twice that of the cross-flow motion. The
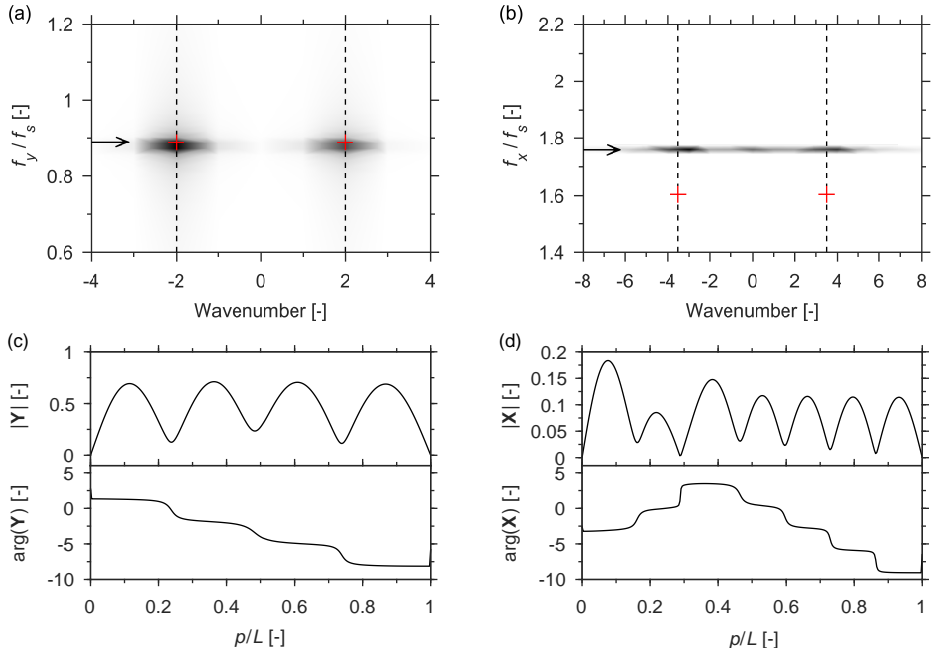
Figure 5.5: Spatio-temporal spectra of (a) cross-flow and (b) in-line displacements at flow velocity $V = 0.5$ m/s with (c) cross-flow and (d) in-line complex modes extracted at dominant frequencies which are indicated by arrows. The wavenumbers and natural frequencies of selected free vibration modes are indicated by black vertical dashed lines and red crosses respectively.

excited wavenumbers, different from the frequency that concentrates around a single value, seem to spread over a relatively wide range. This is partially caused by the numerical errors of FFT conducted in the space domain, as only a small number of spatial cycles are excited along the riser, and partially because of the variation of the top tension in time. Therefore, it is difficult to determine from Figs.5.5(a) and (b) the exact wavenumber at which the structure vibrates. In such cases, the complex modes extracted at the dominant frequency, as will be demonstrated later, are taken as references to decide on the main dominant wavenumber. It is clear from Fig.5.5(a) that in the cross-flow direction, the riser vibrates at a wavenumber and a frequency that are both close to the 4th free vibration mode, while in the in-line direction, as illustrated in Fig.5.5(b), the wavenumber close to the 7th free vibration mode is excited, but at a lower frequency than the corresponding natural frequency. It is conventionally expected that a single structural wavenumber will be excited at a given frequency, which is the case for the cross-flow motion. However, in the in-line direction, apart from the wavenumber close to 3.5, another wavenumber close to zero is also excited at the same frequency. This is because the top of the riser is not constrained in the vertical direction, and its vibration, at the same frequency of the in-line motion, leads to the periodic variation of the in-line offset, which resembles the shape corresponding to small wavenumbers.

The slightly different weights of positive and negative wavenumber peaks suggest

that the response of the structure is characterised by mixed standing-travelling waves. To further investigate the pattern of the riser response, the response modes of the structure are calculated using Fourier expansion following the same approach as given by Mukundan (2008). Denoting the cross-flow displacement of the riser as $y(p_r, t_j)$, the Fourier expansion of the times series of $y(p_r, t_j)$ at location p_r is given as:

$$y(p_r, t_j) = \text{Re}\left(\sum_{l=1}^{\Lambda} \hat{y}(p_r, \omega_l) e^{i\omega_l t_j}\right) \tag{5.41}$$

where $\hat{y}(p_r, \omega_l)$ is complex-valued and represents the lth Fourier coefficient corresponding to the frequency ω_l. Extracting $\hat{y}(p_r, \omega_l)$ at each location along the riser, one obtains the cross-flow response mode of the riser at a specific frequency ω_l, denoted as $\mathbf{Y}(p_r)$. The same process can be applied to the in-line motion to obtain the in-line response mode of the riser denoted as $\mathbf{X}(p_r)$.

The spanwise evolution of amplitudes and phase angles of the response modes $\mathbf{Y}(p_r)$ and $\mathbf{X}(p_r)$, is presented in Figs.5.5(c) and (d), for the dominant frequencies shown in Figs.5.5(a) and (b). The shapes of $|\mathbf{Y}(p_r)|$ and $|\mathbf{X}(p_r)|$ suggest that both cross-flow and in-line motions are dominated by the standing wave. However, the absence of the definite nodes reveals the underlying travelling character of the riser response in both directions. The cross-flow vibration, as depicted in Fig.5.5(c), is close to the 4th free vibration mode, while the in-line vibration exhibits a different pattern compared to the 7th mode, as can be seen in Fig.5.5(d). The underlying travelling character of the structural response can be better illustrated by the evolution of the phase of the complex modes. For the cross-flow motion, the general decreasing trend of the phase angle corresponds to travelling waves moving from $p/L = 0$ towards $p/L = 1$ (upwards). This is consistent with the fact that only the bottom half of the riser is subjected to the flow, and the energy should therefore be input over the same segment, carried away in the form of a travelling wave and dissipated over the upper half of the riser. The spanwise evolution of the phase angle of the in-line response mode indicates that the wave is excited close to $p/L = 0.4$ – still within the bottom half of the riser–and propagates in two directions towards both boundaries.

Case 2: $V = 0.56$ m/s, multiple frequency response.

Although a single frequency response is observed for most simulation cases, for a few, especially those within the range of flow velocities where the riser response is in transition from one mode to another, a multi-frequency response is detected. An example of a simulated multi-frequency response is given here at flow velocity $V = 0.56$ m/s, which lies in the transition of the cross-flow dominant mode from the 4th to the 5th mode. The 2D PSD of the steady-state riser response and the response modes of the dominant frequency are presented in Fig.5.6. As can be seen from Figs.5.6(a) and (b), the riser exhibits a response at several frequencies in both the cross-flow and in-line directions. The cross-flow response, as illustrated in Fig.5.6(a), has main peaks at frequencies $f_y = 0.810 f_s$, $0.975 f_s$ and $1.145 f_s$. Most energy concentrates at the frequency $f_y = 0.975 f_s$, which is the closest of the three frequencies to the Strouhal frequency. The secondary dominant frequency is $f_y = 0.810 f_s$. At frequency $1.145 f_s$, only small peaks are observed. The frequencies $f_y = 0.810 f_s$ and $0.975 f_s$ are close to the 4th and 5th natural frequencies of the structure respectively, and the wavenumbers excited at these two

frequencies are consistent with the corresponding free vibration modes. At frequency $f_y = 1.145 f_s$, the response of the riser deviates from the 6th natural frequency, although the excited wavenumber is close to the 6th free vibration mode. Concerning the in-line response, as portrayed in Fig.5.6(b), apart from the frequency components around $2 f_s$ as expected, significant energy concentrates at low frequencies of $f_x = 0.25 f_s$ and $0.3 f_s$. The source of these low frequency components will be discussed later. Three main frequency peaks are observed around $2 f_s$: $f_x = 1.780 f_s$, $1.949 f_s$ and $2.117 f_s$. Comparing these in-line frequencies with their cross-flow counterparts leads to ratios of $f_x / f_y = 2.20$, 2.00 and 1.85 respectively. Only the cross-flow frequency close to the Strouhal frequency apparently has a ratio of $f_x / f_y = 2$. All three in-line frequency-wavenumber pairs would not result from the free vibration analysis.
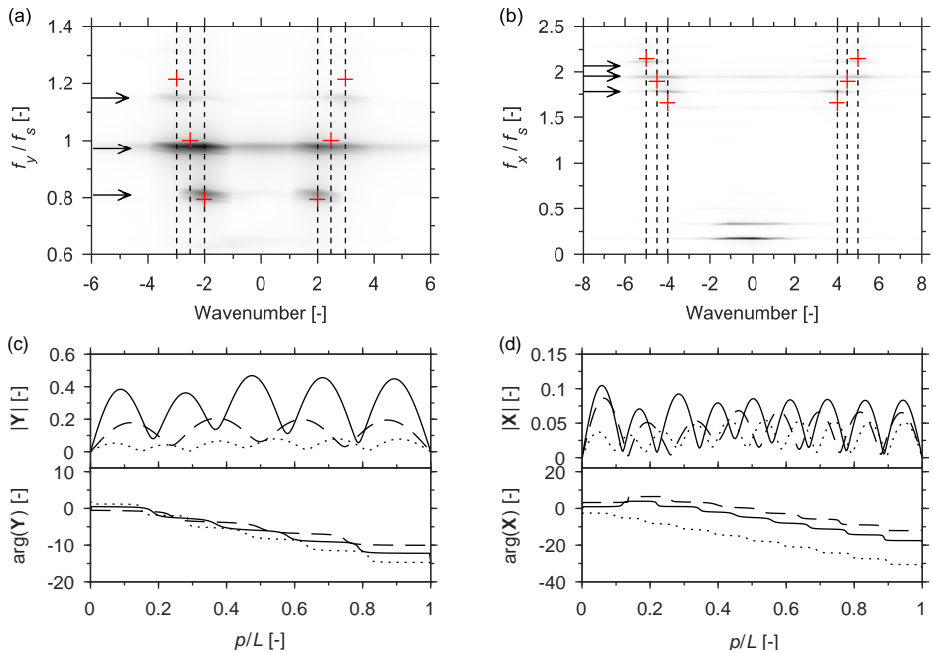

Figure 5.6: Spatio-temporal spectra of (a) cross-flow and (b) in-line displacements at flow velocity $V = 0.56$ m/s with (c) cross-flow and (d) in-line complex modes extracted at dominant frequencies which are indicated by arrows. The wavenumbers and natural frequencies of selected free vibration modes are indicated by black vertical dashed lines and red crosses respectively. In (c) dash line – $f_y = 0.810 f_s$; solid line – $f_y = 0.975 f_s$; dot line – $f_y = 1.145 f_s$. In (d) dashed line – $f_y = 1.780 f_s$; solid line – $f_y = 1.949 f_s$; dotted line – $f_y = 2.117 f_s$.

In Figs.5.6(c) and (d), the response modes of cross-flow and in-line response at frequencies – which are indicated by arrows in Figs.5.6(a) and (b) – are presented. Again, the well-defined cells in the amplitudes of the response modes – both cross-flow and in-line – suggest that the response of the riser at each frequency is dominated by standing waves. The response modes with the highest magnitude are at frequencies that are close to the Strouhal frequency (double the Strouhal frequency for the in-line response). The underlying travelling character of the response can be observed in the variations of the

phase angle along the riser, which suggests that the waves are excited within the bottom half of the riser and move towards the upper end, and the travelling waves seem to be more pronounced in the in-line response.

One interesting question that arises is whether the multi-frequency response is a result of coexisting multiple frequency components or a result of only one frequency that varies in time. To answer this question, the wavelet transform is performed for selected time series of cross-flow and in-line displacements at locations $p/L = 0.9$ and 0.95 respectively, where all dominant frequencies make significant contributions; the results are plotted in Fig.5.7. In these plots, the predominant response frequencies identified in the previous analysis are indicated by dashed lines, and for in-line vibration, only the frequency components around $f_x/f_s = 2$ are displayed. It is clear from Fig.5.7 that in the cross-flow response, the multiple frequency components instantaneously coexist and remain independent over the entire observation period, while those of the in-line vibration are characterised by a main dominant frequency that sweeps up and down across the dashed lines over time.

The multiple frequency response predicted by the proposed model for the VIV of flexible cylinders fully or partially subjected to a uniform flow has been only scarcely reported in the literature. The main reason, according to the author, is the difficulty in capturing and quantifying it in the experiments. First, the multiple frequency response is normally observed in the transition region, which requires a small increment of flow velocity to be captured. Second, the multiple frequency response seems to be fragile, and the balance between the different coexisting frequency components can be easily jeopardised by, for example, external disturbance. Finally, even though the multiple frequency response is observed in experiments, it is difficult to decide whether it corresponds to a steady response or a transition phase. Therefore, in most experiments, for example the one by Chaplin et al. (2005), only the time segment corresponding to a steady periodic motion with a constant amplitude is chosen for post processing; however, strong modulation of the response of the structure is observed in other time segments. To the author's knowledge, this phenomenon is only reported in the work by Seyed-Aghazadeh and Modarres-Sadeghi (2016). In their experiments, a uniform flexible cylinder is placed vertically in a re-circulating water tunnel subjected to a uniform flow. Only low modes of the structure are excited, and the flow velocity is increased in small increments. Seyed-Aghazadeh and Modarres-Sadeghi (2016) report that at a small reduced velocity, only first-mode excitation is observed in the cross-flow response of the cylinder. As the reduced velocity increases to a certain value, a second harmonic contribution, in addition to the first one, with the second structure mode shape is observed. The contribution from the second harmonic monotonically increases with increasing flow velocity and finally becomes dominant over the first mode.

It is a pity that in the work by Seyed-Aghazadeh and Modarres-Sadeghi (2016), although the frequency content of the in-line motion demonstrates a significant contribution from low frequencies when the transition occurs – see Fig.4(f) in Seyed-Aghazadeh and Modarres-Sadeghi (2016) – it is not clear whether this is due to the multiple frequency response or if it is simply the result of a mean in-line deflection due to the drag force. Gopalkrishnan (1993) has already demonstrated that for a rigid cylinder that is forced to vibrate with a prescribed beating motion, the 'instantaneous mean drag force
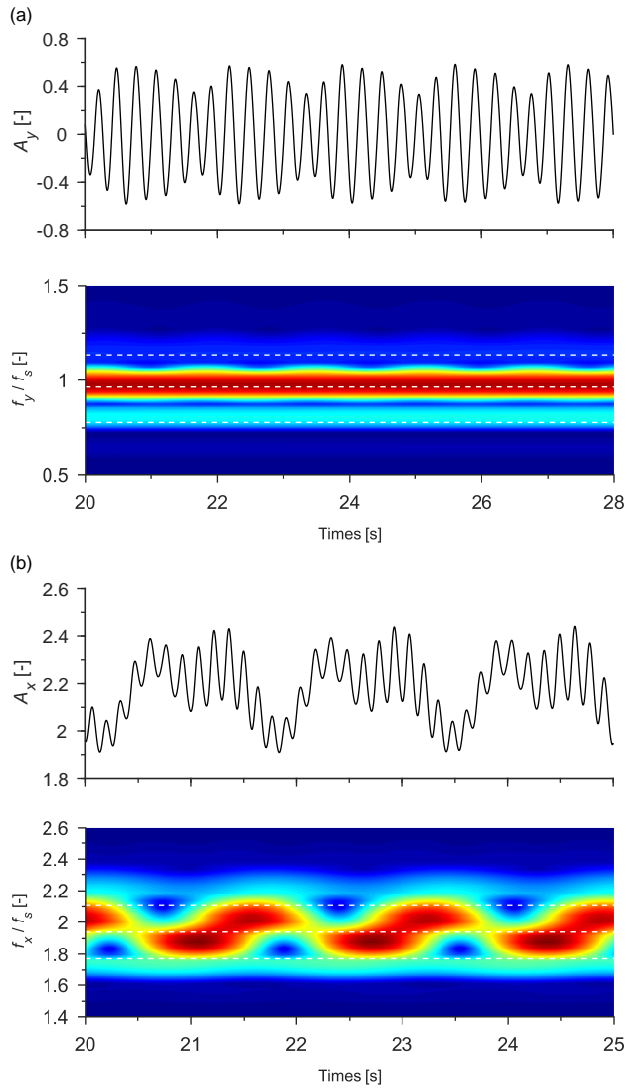
5

Figure 5.7: Selected time series of (a) cross-flow and (b) in-line displacements, and corresponding frequency content as a function of time. The dashed lines represent the dominant frequencies indicated by arrows in Fig. 5.6.

coefficient', defined as the average value of the drag coefficient over one carrier frequency, follows the envelope of the beating motions. If the fluid-structure interaction for a flexible cylinder is similar to that of a rigid cylinder, then it is reasonable to expect that the modulation of the cross-flow motion would lead to the slow variation of the in-line force that follows its envelope and consequently results in a low frequency component in the in-line motion.

5.3.3. COMPARISON OF PREDICTIONS AND EXPERIMENTAL MEASUREMENTS

Non-dimensional parameters have been used to present the simulation results. To illustrate the variation of riser response with respect to the flow velocity, two different types of reduced velocity have been applied. The first type, V_1, is calculated using the fundamental natural frequency f_1 in still water, while the second type is obtained based on the dominant response frequency for the cross-flow f_y and in-line f_x:

$$V_1 = \frac{V}{f_1 D} \tag{5.42}$$

$$V_{x,y} = \frac{V}{f_{x,y} D}. \tag{5.43}$$

The fundamental frequency f_1 is calculated using the finite element model under the riser's initial vertical configuration in still water, subjected to a mean top tension obtained over the time window that has been chosen for analysis. The dominant response frequency is defined as the frequency of the dominant mode. The same approach as that used by Chaplin et al. (2005) has been adopted here to determine the dominant modes. The modal shapes of the riser used in the modal analysis are calculated under an initial vertical position in still water, with the averaged top tension obtained over the time widow that has been chosen for analysis. The use of the term 'modes' here is not rigorous, as the riser will vibrate around its in-line offset due to the drag force, and the top tension is also not constant during the vibration. More importantly, the added mass is not the same in the current as that in the still water. Therefore, the 'modes' used here are only a reasonable approximation. As for the indications of response amplitudes, the cross-flow response standard deviation σ_y and σ_x for in-line, has been calculated as follows (Chaplin et al., 2005):

$$\sigma_{x,y} = \sqrt{\frac{1}{S}\sum_{j=1}^{S}\left[\frac{1}{N}\sum_{i=1}^{N}u_{ji}^2\right]} \tag{5.44}$$

where S is the number of time samples, N is the number of locations along the riser where the response of the riser is read, u_{ji} denotes the displacement of riser at location i and time instance j and only the fluctuating component of the in-line displacement is considered.

With Eq.(5.44), the standard deviations of cross-flow and in-line response amplitudes (with the mean in-line deflection subtracted) have been calculated, and they are shown in Fig.5.8 against reduced velocity V_1. The cases of single frequency response are represented by hollow diamonds, while those of multiple frequency response are represented
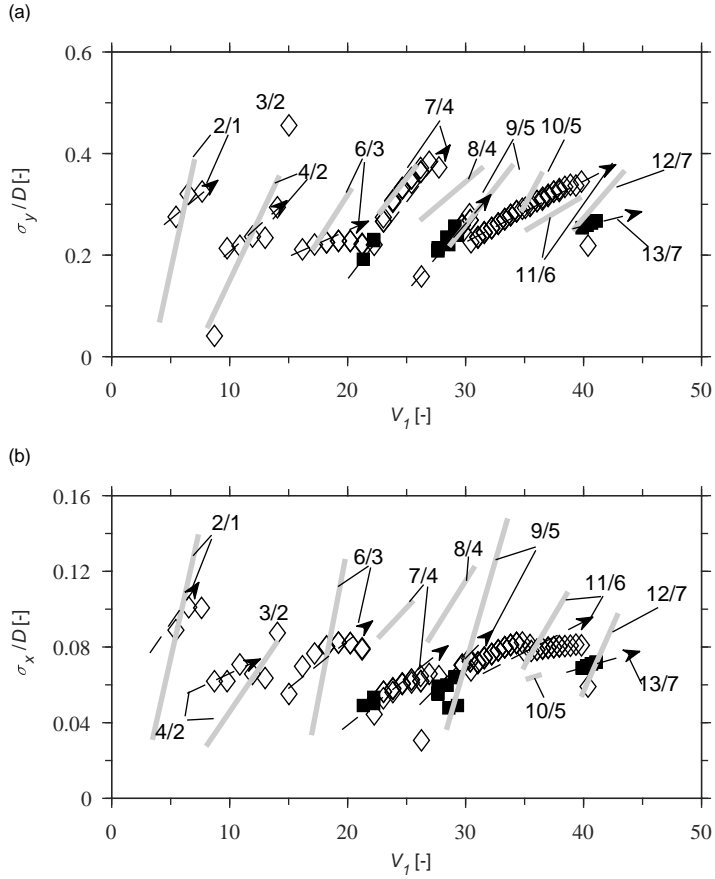
5

Figure 5.8: Standard deviations of (a) cross-flow and (b) in-line displacements. Simulation results are grouped by the arrows with dashed lines labeled with (dominant in-line modes)/(dominant cross-flow modes). Linear approximation of the experimental results by Chaplin et al. (2005) are represented by grey thick lines.

by black squares. For the multiple frequency response, the standard deviations of the in-line displacement are obtained after removing the low frequency components through a high pass filter. The standard deviations of the simulated cross-flow and in-line displacements are plotted in Fig.5.8. Following the same approach taken by Chaplin et al. (2005), the results are grouped according to the combination of dominant in-line and cross-flow modes represented by the arrows with dashed lines, and the thick grey lines represent the linear approximation of the experiment results. As can be seen from Fig.5.8, the standard deviations of the simulated amplitudes appear to be slightly scattered, with most cross-flow values varying from $0.1D$ to $0.4D$, which is in good agreement with the experimental measurements. The standard deviations of the simulated in-line amplitudes, which mostly lie between $0.04D$ and $0.12D$, are generally smaller than those from the experiments. The underestimation of the in-line amplitude is not a surprise; this is because in the prediction of free vibration of the rigid cylinder, the in-line vibration is also underestimated for a small mass ratio system. In general, the response of the riser predicted by the model follows the same pattern as those observed in the experiments. For both cross-flow and in-line displacements, there is a trend of increase with an increased reduced velocity within each group. As the reduced velocity further increases beyond the group, the subsequent group takes over and starts at a much smaller amplitude, generating discontinuities and jumps between groups. Overlaps of groups are also observed, and multiple frequency response usually takes place within these regions. For the cross-flow response, the simulated results are in good agreement with the experimental measurements for reduced velocity $V_1 > 20$. However, at small reduced velocities where the cross-flow mode up to the third is dominant, the simulated cross-flow amplitudes are generally smaller than those in the experimental measurements, and the increasing trends, represented by the slopes of the lines, are less sharp. This may be due to the fact that in the experiments, all the measurements at small reduced velocities, corresponding to mode patterns 2/1, 4/2 and 6/3, are obtained at top tensions that are much higher than the one used in the simulations.

In Fig.5.9, the standard deviations of simulated cross-flow and in-line displacement are now plotted against the reduced velocities based on the dominant frequency $f_{x,y}$. The cross-flow response falls in the region between $V_y = 5$ and $V_y = 7$, while the in-line response collapses around $V_x = 3$. A clear trend of increasing amplitude with reduced velocity is observed in both cross-flow and in-line directions.

The dimensionless frequency, which is obtained by normalising the dominant frequency in the form $f_{x,y}D/U$, is plotted in Fig.5.10 against the reduced velocity V_1. In general, the cross-flow response is around the vortex shedding frequency, which is represented by the straight line in Fig.5.10(a) at 0.17. The in-line dominant frequency, on the other hand, is always double that of the cross-flow frequency, and it concentrates around 0.34. Thick grey lines in the figure represent reasonable linear approximations of the experimental results, indicating the range as well as the variation of the measured dominant frequencies, which are in good agreement with the simulation results. The main difference between the two is observed at high reduced velocities where the experimental results display a trend of becoming more concentrated around the vortex shedding frequency, while those of the simulations still spread over a wide range of reduced velocities. The jumps of the dimensionless frequency is due to the lock-in, which
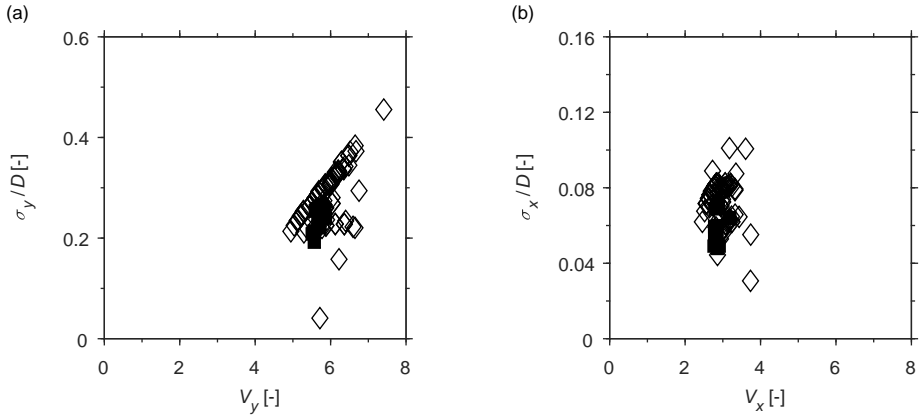
Figure 5.9: Standard deviations of (a) cross-flow and (b) in-line displacements against reduced velocity $V_{x,y}$.
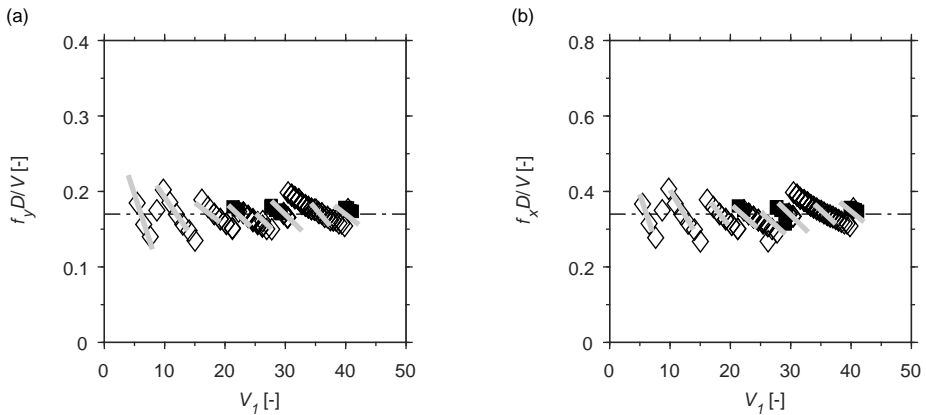

Figure 5.10: Normalised (a) cross-flow and (b) in-line dominant frequencies ($f_{x,y}D/V$) versus V_1. In (a), the straight line represents the frequency corresponding to a Struhal number 0.17; and in (b), the straight line represents the doubled frequency corresponding to a Struhal number 0.17. Linear approximation of the experimental results by Chaplin et al. (2005) are represented by grey thick lines.

is illustrated in a better way in Fig.5.11 where the frequency is normalised by the fundamental frequency. A clear stair-stepping trend in the dimensionless frequency of both cross-flow and in-line responses is noticeable.

In Fig.5.12, the simulated dominant modes as well as those observed in the experiments are plotted. The comparison of the simulation and experiment results reveals good agreements between the two regarding the cross-flow dominant modes. As for the in-line dominant modes, at low reduced velocities, both simulation and experiment results demonstrate that only even-numbered modes appear. For high reduced velocities, both even and odd-numbered modes are observed from the experiments while, interestingly, only odd modes appear in the simulations. The reason for only the odd-numbered modes to be predicted by the model at high reduced velocities is still unclear to the au-
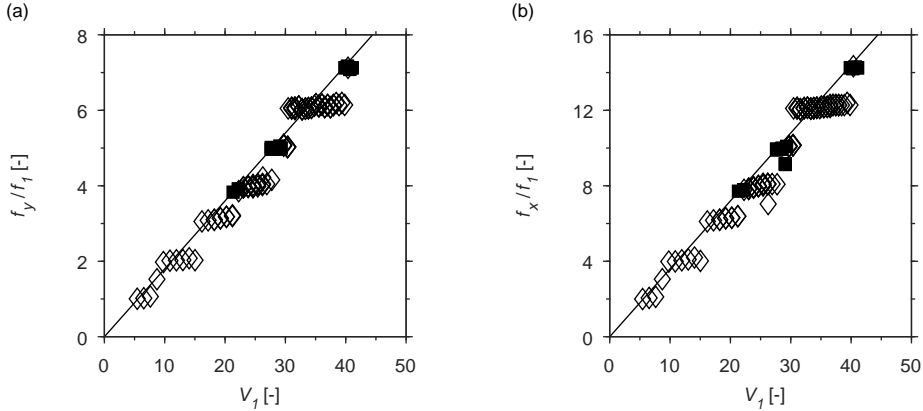
Figure 5.11: Normalised (a) cross-flow and (b) in-line dominant frequencies ($f_{x,y}/f_1$) versus V_1. In (a), the straight line represents the frequency corresponding to a Struhal number 0.17; and in (b), the straight line represents the doubled frequency corresponding to a Struhal number 0.17.
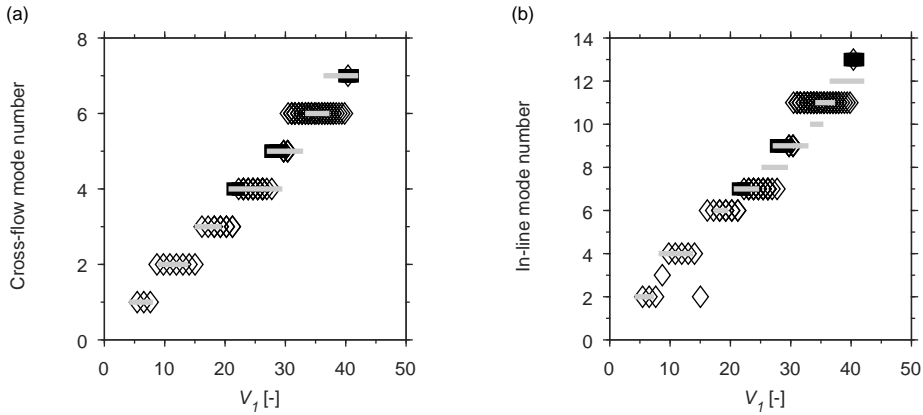
5

Figure 5.12: Dominant mode for (a) cross-flow and (b) in-line displacements. Linear approximation of the experimental results by Chaplin et al. (2005) are represented by grey thick lines.

thor and requires further study.

With regard to the in-line offset of the riser, since the drag force is proportional to the square of the flow speed, it is expected that the maximum in-line deflection should follow a similar trend. In Fig.5.13, the mean of the maximum in-line deflections $\tilde{x}_{max}$ are plotted against the reduced velocity V_1, and a general quadratic relationship between the two can be found. $\tilde{x}_{max}$ is obtained by finding the maximum in-line deflections along the riser at each time instance and then taking the mean value of these maxima. The line shows that the best quadratic fit to the results yields a coefficient of 6.7e^{-3}, which is in excellent agreement with the experimental measurements where a coefficient of 6.1e^{-3} was obtained. This proves that the amplification of the in-line force due to VIV is properly captured by the model. This reveals one of the main advantages of the current model

over the original one, which has been shown by Mina (2013) and Kallias Ntroumpis (2017) to significantly underestimate the mean in-line deflection of the riser.
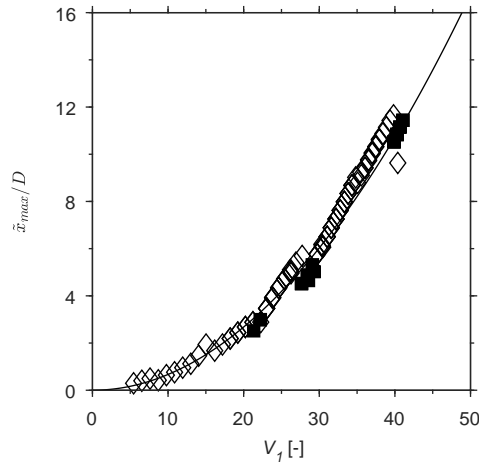

Figure 5.13: Mean of maximum in-line deflection. The curve shows the best quadratic fit to the results with the expression $\tilde{x}_{max}/D = 6.7\mathrm{e}^{-3}V_1^2$

5.4. CONCLUSIONS

In this chapter, a model has been presented for the simulation of the coupled cross-flow and in-line VIV of a flexible cylindrical structure. The structure is described as a geometrically nonlinear extensible Euler-Bernoulli beam, and the interaction between the structural motion and fluid is modelled by the wake oscillator proposed in Chapter 4 that is uniformly distributed along the cylinder. Although the main focus has been on the VIV of a straight flexible cylinder, the same model can, in principle, be used for the prediction of the VIV of curved structures, such as catenary risers. To deal with the cases where the incident flow is not perpendicular to the cylinder axis, a local coordinate frame is introduced, and the independence principle is applied.

The dynamics of the coupled system has been analysed using the finite element method, and the simulation results of a series of experiments where a top-tensioned flexible riser was subjected to a step flow have been presented. A comparison with the experimental results has revealed that the model is able to qualitatively predict most features of the VIV of flexible cylinders, and the predicted vibration amplitudes, frequencies and excited modes are in good agreement with the experimental measurements. Moreover, it has been demonstrated that the current model is able to offer good prediction of the mean in-line deflections, which reflects its superiority over the original model proposed by Ogink and Metrikine (2010), as the latter one significantly underestimates the amplification of the mean in-line force when VIV occurs.

In contrast to the conventional belief that the VIVs of flexible cylinders subjected to a uniform flow should be dominated by a single frequency oscillation, the current model

predicts that over the range of flow velocities through which a transition of the dominant mode of vibration takes place, the riser may exhibit a multi-frequency response. In such cases, the multiple frequency components in the cross-flow response instantaneously coexist, while those of the in-line response are the result of a single frequency that temporally drifts from one predominant frequency to another one. When the multi-frequency response occurs, the in-line response contains significant components at a low frequency, which is caused by the slow variation of the in-line force due to the modulation of the cross-flow displacements.

5

6

QUANTIFICATION OF THE EFFECT OF THE IN-LINE COUPLING IN THE NEW WAKE OSCILLATOR MODEL

6.1. INTRODUCTION

In Chapter 4, a wake oscillator model that is coupled to both the cross-flow and in-line motions has been proposed. Combined with a nonlinear Euler-Bernoulli beam model, the wake oscillator model has been applied to simulate the VIV of flexible cylinders and is validated against experimental measurements in Chapter 5. In this chapter, the influence of the in-line coupling is investigated by comparing the predicted VIV of flexible cylinders using the wake oscillator with and without in-line coupling under uniform and sheared flows.

As presented in Section 4.2, compared to the original model proposed by Ogink and Metrikine (2010), there are two aspects to the main improvements of the new model. The first one is that a term that is proportional to the acceleration of the in-line motion is introduced in the wake oscillator equation to describe the influence of the in-line motion on the dynamics of the wake. The second improvement is related to the in-line force, where a fluctuating component that is coupled to the lift force is added. These two aspects of improvement introduced a strong coupling effect of cross-flow and in-line motions on the interaction between the structure and flow. To investigate the effect of these two improvements, simulations are conducted with different models. Model A denotes the complete model, which includes both improvements. Model B excludes the in-line coupling term in the wake oscillator equation but keeps the fluctuating in-line force. Model C excludes both improvements and is exactly the same as the one proposed by Ogink and Metrikine (2010). Detailed descriptions of all three models can be found in Appendix D. The results obtained from these three models are compared to each other, and the differences are highlighted.

The rest of this chapter is divided into the following sections. The configuration of

Table 6.1: Properties of the riser model

Parameters	Values	Dimension
External diameter	0.03	m
Length	38	m
Aspect ratio	1266	-
Bending Stiffness	572.3	Nm^2
Axial Stiffness	7.82×10^6	N
Mass	1.088	kg/m
Mass ratio	1.54	-

the structure, as well as the definition of the coordinate system, is described in Section 6.2. Then, in Section 6.3, the general structural responses obtained from the three models are presented. A 2D spatial-temporal spectral analysis is carried out, and vibration modes are extracted at dominant frequencies. Section 6.4 investigates the phase difference between the cross-flow and in-line motions. In Section 6.5, the differences between the results from the three models are highlighted from the viewpoint of energy transfer. The fatigue damage estimated by the three models is presented in Section 6.6, and final conclusions are provided in Section 6.7.

6.2. MODEL DESCRIPTION

In this chapter, simulations are performed using parameters used in the experiments undertaken by Shell Oil Company in the MARINTEK Offshore Basin Laboratory (Lie et al., 2012). In the experiments, a riser of 38 meters is dragged horizontally or rotated around one end through still water to simulate a uniform and linearly sheared current. The key properties of the riser are presented in Table 6.1. Consistent with the experiments, two types of simulations are conducted, namely uniform flow simulations and linearly sheared flow simulations. The configuration of the riser, as well as the definition of the coordinate system, is illustrated in Fig.6.1. For each simulation, an initial tension of 6 kN is applied and one end of the riser is attached to a spring, while the other is pinned. The reason for using a spring is to simulate the restoring force provided by the pendulum with heavy clamp weight in the experiments. Without knowing the exact stiffness that the pendulum provides, the stiffness of the spring in the simulation is set to be 5×10^4 N/m.

The same simulation procedure, as well as the same parameters as those used in Section 5.3, is taken. For each simulation, a convergence test is conducted by doubling the number of elements to ensure that the results are reliable. However, due to the strong nonlinear nature of the problem, in some cases, even with the same initial conditions, the response of the riser predicted by the model with a small and a large number of elements was found to correspond to different steady-state branches of the system. In such cases, the convergence tests are performed by taking the steady-state response obtained from the model with fewer elements and using it as the initial condition for the simulation with more elements. In this way, the results are proved to converge, and only the steady-state responses are analysed.
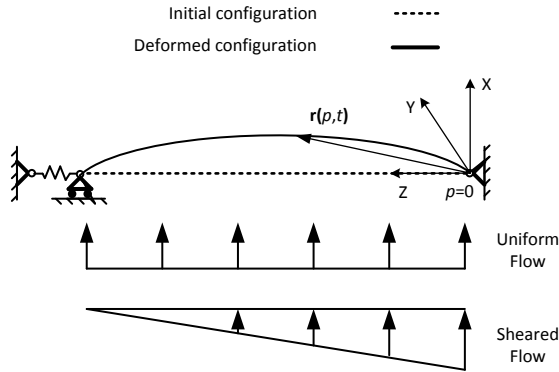
Figure 6.1: Configuration of the riser and the coordinate system .

6.3. RESPONSE OF THE STRUCTURE

In this section, the simulated responses of the riser subjected to uniform and linearly sheared flows are analysed. Simulations have been conducted at several flow velocities. Typical responses at two flow velocities $V = 0.5$ m/s and 1.5 m/s for the uniform flow, as well as at $V = 1.5$ m/s and 2.5 m/s for the linearly sheared flow, are presented. For the linearly sheared flow profile, the notation V represents the maximum flow velocity at $p = 0$.

6.3.1. UNIFORM FLOW

In this subsection, the simulated VIV of the riser subjected to uniform flow is discussed. The structural response patterns are quantified and analysed in the wavenumber-frequency domain after performing a spatial-temporal spectral analysis based on the 2D Fourier transform, and the complex modes at dominant frequencies are extracted.

Flow velocity at $V = 0.5$ m/s

The simulation results of the response of the riser subjected to a uniform flow at $V = 0.5$ m/s are depicted in Fig.6.2 and Fig.6.3, where the 2D PSD of non-dimensional displacements and the corresponding complex modes at dominant frequencies are presented for all three models. For Model A, the 2D PSD of non-dimensional cross-flow and in-line displacements, as illustrated in Figs.6.2(a) and (b), indicate that the structural response is at a single frequency in both directions. The dominant in-line response frequency, indicated by arrows in Fig.6.2(b), is $f_x \approx 1.632 f_s$, which is approximately twice that of the cross-flow response $f_y \approx 0.816 f_s$. In Figs.6.2(a) and (b), it is difficult to determine the wavenumber at which the riser is excited, since the energy seems to spread over a wide range of wavenumbers. As explained in previous sections, this is because the FFT in the spatial domain suffers from a small number of spatial cycles. By observing the complex modes extracted at the dominant frequencies, it is deduced that the wavenumbers corresponding to the 3rd and 6th modes are excited in cross-flow and in-
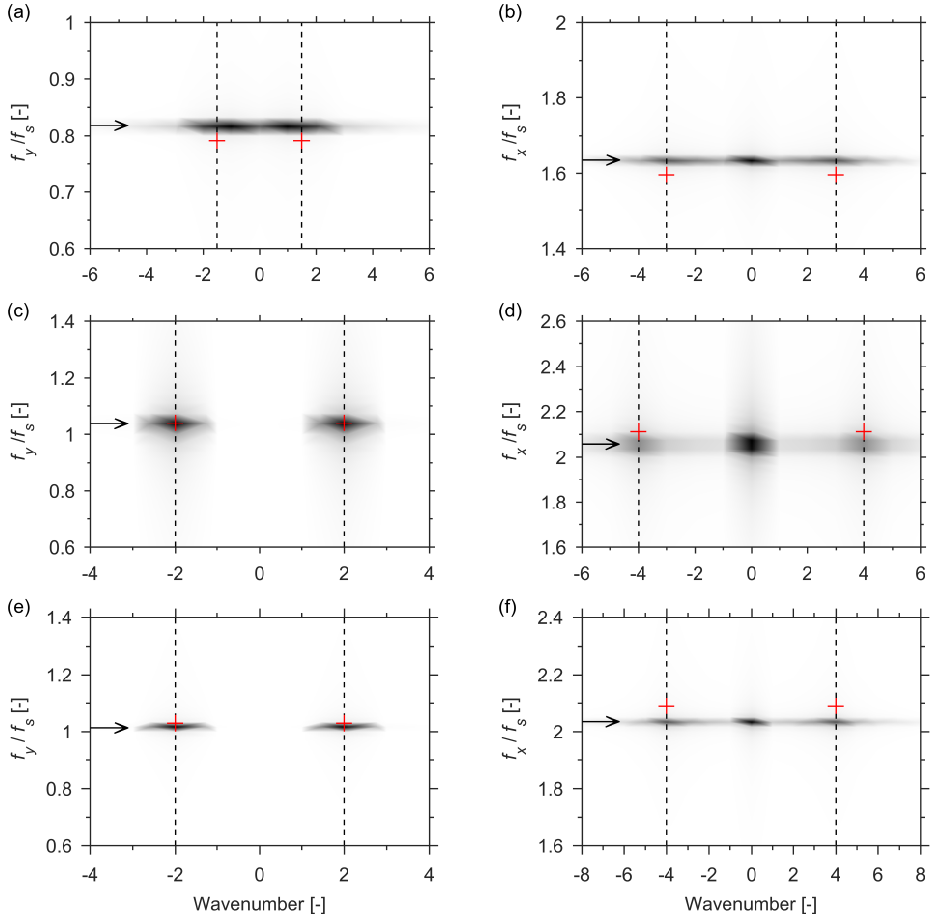
Figure 6.2: Spatio-temporal spectra of (a,c,e) cross-flow and (b,d,f) in-line displacements at uniform flow $V =$ 0.5 m/s using Model A (a,b); Model B (c,d) and Model C (e,f). The arrows represent the dominant frequencies. The wavenumbers and natural frequencies of selected free vibration modes are indicated by black vertical dashed lines and red crosses respectively.

line directions respectively. The natural frequencies of the corresponding free vibration modes are indicated in Figs. 6.2(a) and (b) by red crosses; those natural frequencies are slightly smaller than the actual vibration frequencies in both the cross-flow and in-line directions. In Figs.6.3(a) and (b), the spanwise evolution of the amplitudes and phases of the complex modes extracted at dominant frequencies of structural responses in both cross-flow and in-line directions is presented. The cross-flow vibrations predicted by Model A are clearly in the form of standing waves, as definite nodes and jumps of π in the phase are observed in Fig.6.3(a). The maximum cross-flow vibrations are observed at the antinodes, which are as high as $1.4D$. In the in-line direction, see Fig.6.3(b), the structural response exhibits a mixed standing-travelling character. The evolution of the magnitude and phase of the complex mode suggests that the in-line vibration is excited
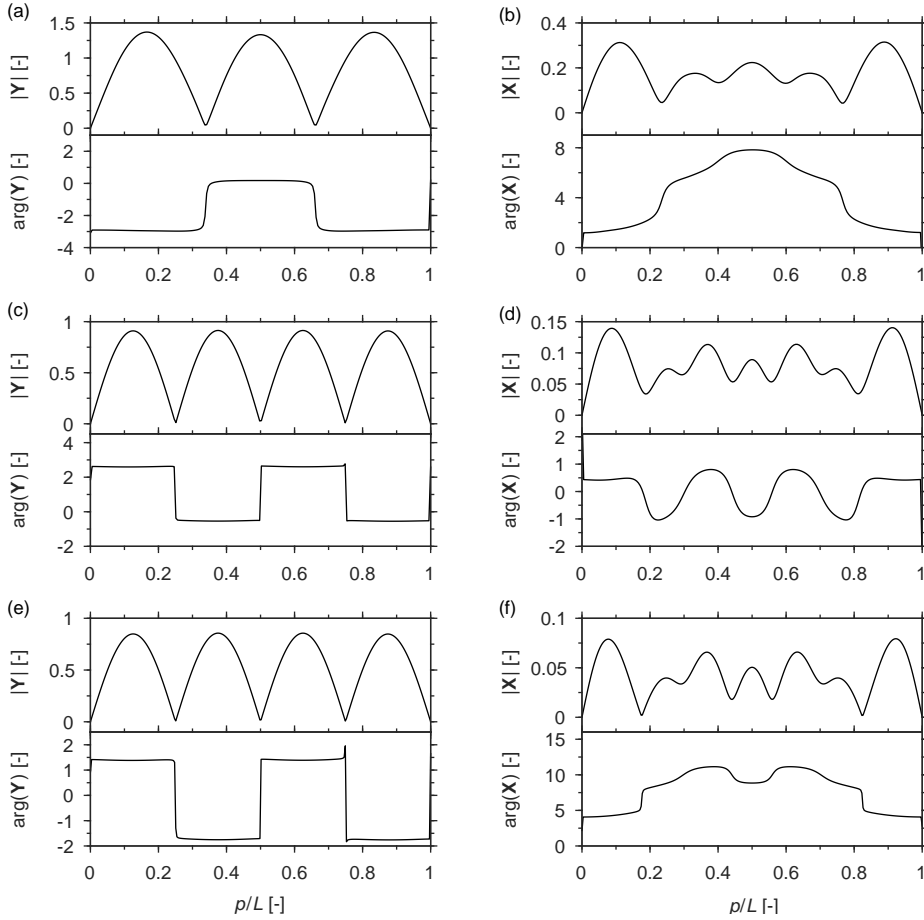
Figure 6.3: Amplitude and phase of (a,c,e) cross-flow and (b,d,f) in-line complex modes at uniform flow $V = 0.5$ m/s. (a,b) correspond to the response obtained using Model A; (c,d) correspond to the response obtained using Model B and (e,f) correspond to the response obtained using Model C. The complex modes are extracted at dominant frequencies identified from Spatio-temporal spectra.

at the middle of the riser and propagates towards both ends, developing strong standing waves near boundaries. The maximum in-line vibration, around $0.3D$, is observed at the anti-nodes of the standing wave near boundaries.

In Fig.6.2(c,d) and Fig.6.3(c,d), the simulated riser responses are illustrated for Model B. As can be seen in Figs.6.2(c) and (d), Model B predicts the riser to vibrate at higher wavenumbers (corresponding to the 4th mode in the cross-flow direction and the 8th mode in the in-line direction) and higher frequencies ($f_y \approx 1.029 f_s$ and $f_x \approx 2.058 f_s$) compared to those of Model A. The simulated cross-flow vibrations are in good agreement with the free vibration structural modes regarding the excited wavenumber and frequency, while slight deviations are observed in the in-line response where the actual vibration frequency is lower than the corresponding natural frequency. The complex

modes at the dominant frequencies, as depicted in Figs.6.3(c) and (d), indicate that the cross-flow vibration is dominated by a standing wave, while a predominant travelling wave is observed in the in-line direction. Although the evolution of the amplitude of the in-line complex mode suggests the same response pattern as that predicted by Model A, the evolution of the phase along the span displays unclear variation patterns. Such variations in the phase along the span were found to be associated with the fact that two different wavenumbers are excited in the in-line direction at the same frequency due to the unconstrained boundary in the Z direction at one end of the riser. Concerning the maximum magnitude of vibration, Model B predicts that the maximum cross-flow and in-line amplitudes of vibration are $0.8D$ and $0.15D$; both are smaller than those of Model A.

The simulation results of Model C, as pictured in Fig.6.2(e,f) and Fig.6.3(e,f), are similar to those of Model B; therefore, they are not discussed in detail here. However, it needs to be noted that while Model C predicts the same level of cross-flow vibration as Model B, it predicts the maximum in-line vibration around $0.075D$, which is much smaller than that simulated by the other two models.

Flow velocity at $V = 1.5$ m/s

For the case of $V = 1.5$ m/s, the 2D PSD of non-dimensional cross-flow and in-line displacements and the corresponding dominant complex modes are presented in Fig.6.4(a,b) and Fig.6.5(a,b), respectively, for Model A. The predominant wavenumbers corresponding to the 8th and 16th modes are excited in the cross-flow and in-line directions at frequencies of $f_y \approx 0.914 f_s$ and $f_x \approx 1.828 f_s$ respectively. In both directions, the actual vibration frequencies are higher than the natural frequencies of the corresponding modes. The different positive and negative wavenumber peaks for the same frequency imply that the structural response is characterised by mixed standing-travelling waves. The mixed standing-travelling character of the structural response is confirmed by the spanwise evolution of the amplitude and phase of the cross-flow and in-line complex modes; see Figs.6.5(a) and (b). The generally decreasing trend of the phase denotes the travelling wave oriented from $p/L = 0$ towards $p/L = 1$. In the case of a pure travelling wave, the variation of the phase is strictly linear. The modulation of the underlying standing character of the structural response leads to a zigzagging evolution pattern of the phase in both the cross-flow and in-line directions. From this point of view, the travelling wave is more predominant in the in-line response, as the evolution of the phase of the in-line complex mode is less modulated. The evolution of the magnitudes along the span reveals that both cross-flow and in-line displacements gradually increase along the direction of the travelling wave and reach their maximum – around $1.7D$ in a cross-flow direction and $0.3D$ in the in-line direction – at the end of the riser where standing waves dominate. This may imply that the energy is continually transferred from the fluid to the riser as the travelling wave propagates. It is also interesting to notice from Fig.6.5(b) that the standing character of the in-line displacement seem to be associated with the cross-flow response. The ripples of the magnitude of the in-line complex mode, as a result of the modulation of the standing wave, display a pattern of a mixture of large cells that are consistent with the cross-flow response and small ripples. This is a result of the nonlinear coupling effect between the cross-flow and in-line motions which can only be captured by a nonlinear structural model.
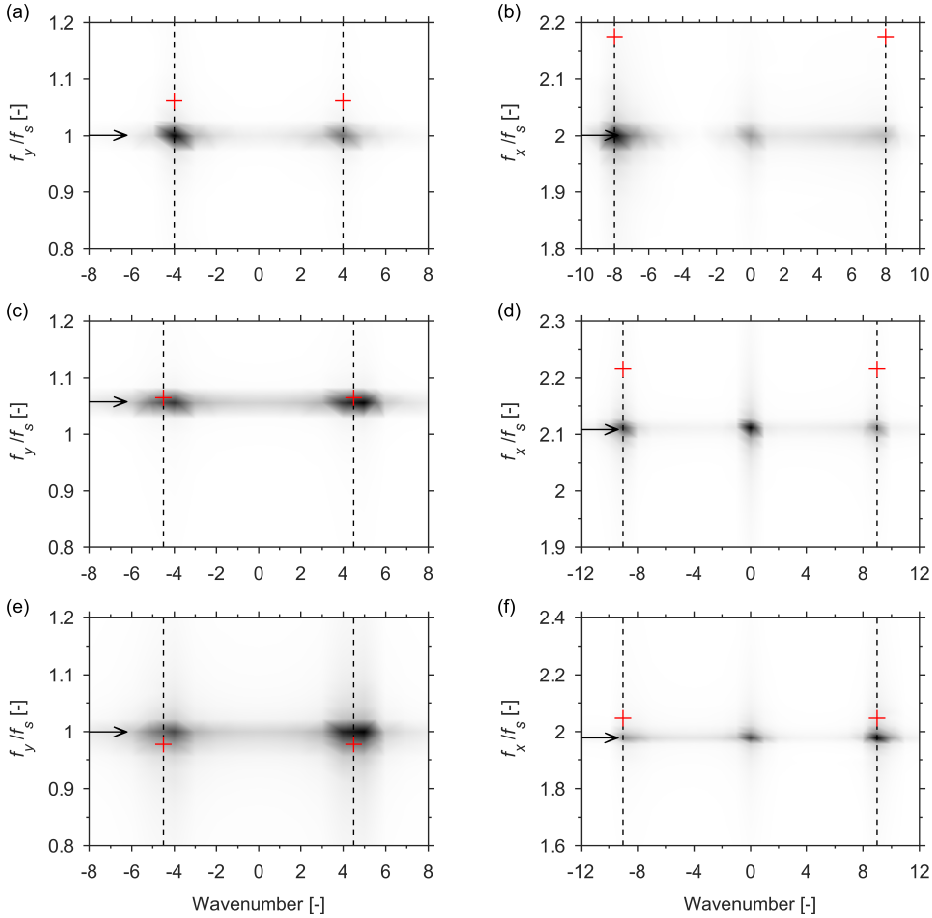
Figure 6.4: Spatio-temporal spectra of (a,c,e) cross-flow and (b,d,f) in-line displacements at uniform flow $V = 1.5$ m/s using Model A (a,b); Model B (c,d) and Model C (e,f). The arrows represent the dominant frequencies. The wavenumbers and natural frequencies of selected free vibration modes are indicated by black vertical dashed lines and red crosses respectively.

Predictions by Models B and C are similar, as can be seen in Fig.6.4(c-f) and Fig.6.5(c-f). Both models predict that wavenumbers corresponding to the 9th and 18th modes will be excited in the cross-flow and in-line directions respectively. However, the cross-flow and in-line dominant frequencies predicted by Model B are $f_y \approx 1.055 f_s$ and $f_x \approx 2.110 f_s$ respectively, which are higher than those predicted by Model C ($f_y \approx 0.992 f_s$ and $f_x \approx 1.984 f_s$). The reason for such a difference is related to the tension increase due to the amplification of in-line forces. Model C, as will be demonstrated in Section 6.5, underestimates the amplification of the in-line force and therefore predicts a smaller tension compared to Model B. As a result, the lock-in at the same mode for the two cases corresponds to different natural frequencies, as indicated by crosses in Figs.6.4(c) and (e). The dominant frequencies are in good agreement with the corresponding natural fre-
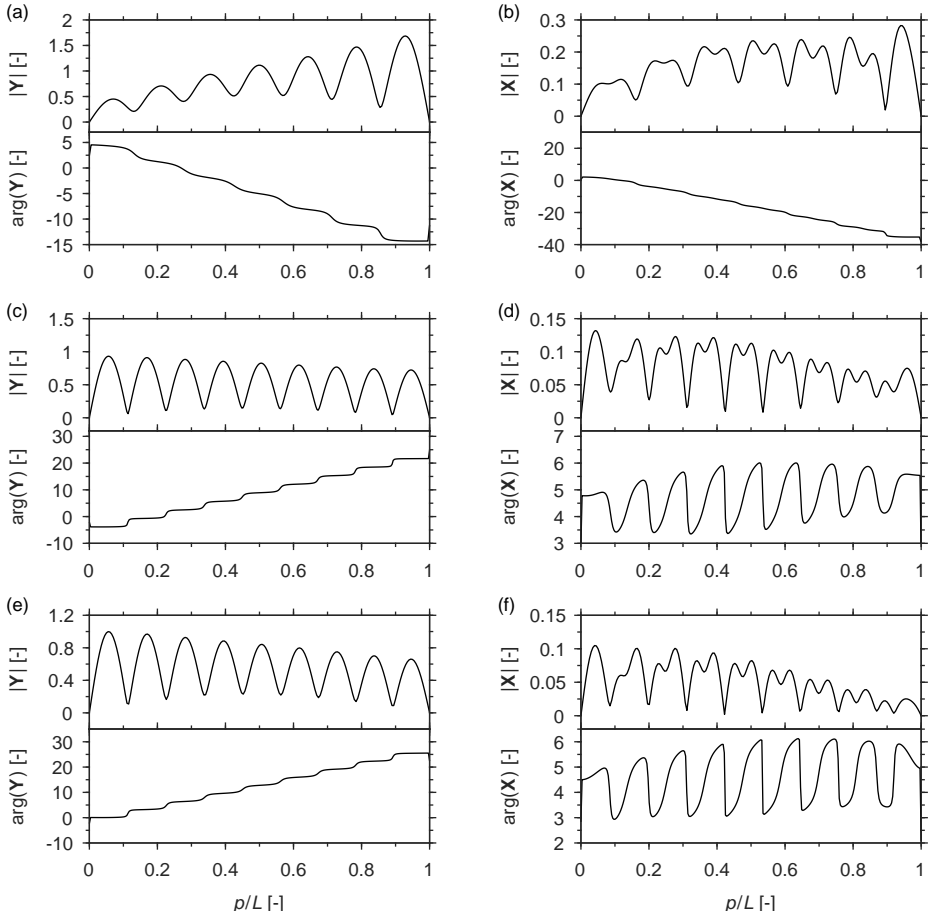
Figure 6.5: Amplitude and phase of (a,c,e) cross-flow and (b,d,f) in-line complex modes at uniform flow $V = 1.5$ m/s. (a,b) correspond to the response obtained using Model A; (c,d) correspond to the response obtained using Model B and (e,f) correspond to the response obtained using Model C. The complex modes are extracted at dominant frequencies identified from Spatio-temporal spectra.

quencies in the cross-flow direction but are higher than natural frequencies in the in-line direction for both models. The cross-flow complex modes at dominant frequencies indicate that for both models, the cross-flow vibration exhibits a standing-travelling character; however, different from Model A, the vibration is dominated by standing waves. The underlying travelling wave pattern for both Models can be observed by the general increasing trend of the phase along the span, indicating that the direction of the travelling wave is opposite to that of Model A. The maximum cross-flow vibration of Model B is around $1.0D$, which is similar to the prediction of Model C, while the predicted maximum in-line vibration of Model B is around $0.13D$, which is slightly larger than the prediction of Model C around $0.1D$.

6.3.2. LINEARLY SHEARED FLOW

In this subsection, the simulation results of the VIV of the riser subjected to linearly sheared flow are presented. The flow profile is such that the velocity at $p/L = 1$ is zero and that at $p/L = 0$ is maximum. The notation V denotes the maximum flow velocity throughout this subsection.

Flow velocity at $V = 1.5$ m/s

In Fig.6.6 the 2D PSD of non-dimensional cross-flow and in-line displacements are presented for all three models. In all plots, the vibration frequencies are normalised by the Strouhal frequency that was calculated at the maximum flow velocity. As can be seen from Fig.6.6, all three models predict a single frequency response in both the cross-flow and in-line directions, and the in-line dominant frequencies are approximately twice
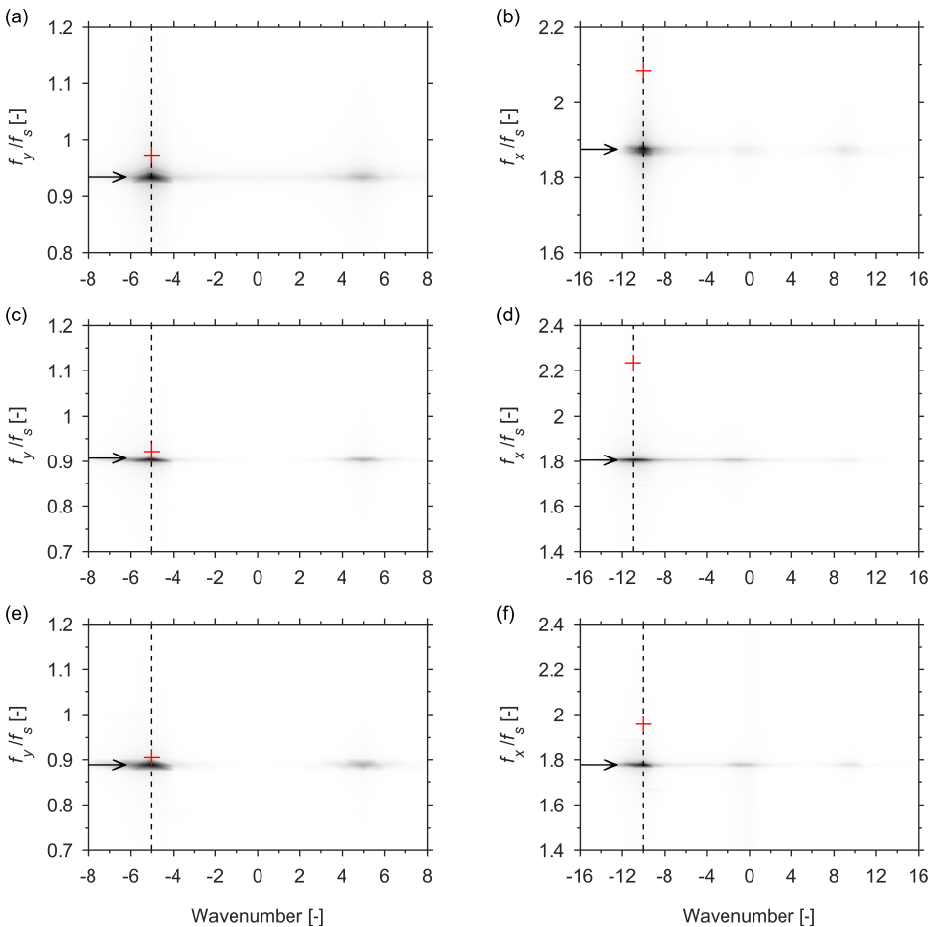

Figure 6.6: Spatio-temporal spectra of (a,c,e) cross-flow and (b,d,f) in-line displacements at sheared flow $V = 1.5$ m/s using Model A (a,b), Model B (c,d) and Model C (e,f). The arrows represent the dominant frequencies. The wavenumbers and natural frequencies of selected free vibration modes are indicated by black vertical dashed lines and red crosses respectively.

those of the cross-flow responses. A comparison of the results reveals that the models without an in-line coupling term in the wake oscillator equation (Models B and C) predict similar responses to the model with in-line coupling (Model A) regarding the excited wavenumber and dominant frequency. In general, Model A predicts that the riser will vibrate at slightly higher frequencies ($f_y \approx 0.933 f_s$ and $f_x \approx 1.867 f_s$) compared to those of Model B ($f_y \approx 0.904 f_s$ and $f_x \approx 1.807 f_s$) and Model C ($f_y \approx 0.891 f_s$ and $f_x \approx 1.782 f_s$). For all three models, the wavenumber corresponding to the 10th mode is excited in the cross-flow direction; moreover, according to Models A and C, the in-line wavenumber corresponding to the 20th mode is excited, whereas Model B predicts that the in-line wavenumber corresponding to the 22th mode is excited. The perceptibly larger negative wavenumber peaks compared to the positive ones imply that the travelling waves are predominant in the structural responses for all three models in both the cross-flow and in-line directions, and these waves propagate from the high-velocity region (near $p/L = 0$) towards the low-velocity region (near $p/L = 1$).

The travelling-wave-dominant structural responses of all three models are confirmed by the complex modes at the dominant frequency, as illustrated in Fig.6.7. In the cross-flow direction, the maximum amplitude of the structural complex mode of Model A is observed around $p/L = 0.45$ and exceeds $0.4D$, while that of Models B and C occurs at $p/L = 0.28$ and is close to $0.3D$. Concerning the in-line vibration, Model A predicts the highest amplitude of vibration around $0.075D$, followed by Model B, with a maximum around $0.045D$, and Model C predicts the smallest maximum amplitude, which is smaller than $0.02D$.

Flow velocity at $V = 2.5$ m/s

The simulation results of the VIV of the riser subjected to a sheared flow velocity with maximum velocity $V = 2.5$ m/s are presented in Fig.6.8, Fig.6.9 and Fig.6.10. In Fig.6.8, the 2D PSD exhibits a multiple frequency response in both the cross-flow and in-line directions for all three models. Although several frequencies are excited in the cross-flow response, only the first two dominant frequencies that contain the most energy are considered; they are indicated by arrows in Figs.6.8(a), (c) and (e). Here, the strongest frequency is denoted as the main dominant frequency and the other one as the secondary dominant frequency. For the in-line response, a substantial amount of energy concentrates at low frequencies; the reason for this has been explained in Section 5.3.2. Apart from this component at low frequencies, the excited frequencies that are close to twice those of the dominant cross-flow frequencies are chosen as the dominant in-line frequencies, indicated by arrows in Figs.6.8(b), (d) and (f). At each dominant frequency, the corresponding excited wavenumber and natural frequency are also presented. For Model A, the main dominant cross-flow frequency is $f_y \approx 0.914 f_s$, with an excited wavenumber corresponding to the 13th mode. Models B and C, on the other hand, predict dominant frequencies $f_y \approx 0.904 f_s$ and $f_y \approx 0.871 f_s$ respectively, with excited wavenumbers that correspond to the 14th mode for both cases. Concerning the secondary dominant cross-flow frequency, all three models predict it to be around $f_y \approx 0.3 f_s$, with an excited wavenumber corresponding to the 4th mode. In the in-line direction, the main dominant frequencies are $f_y \approx 1.838 f_s$, $f_y \approx 1.806 f_s$ and $f_y \approx 1.743 f_s$ for Models A, B and C respectively, and the corresponding excited wavenumbers are at the 26th, 30th and 29th modes. Similar to the cross-flow case, all three models predict
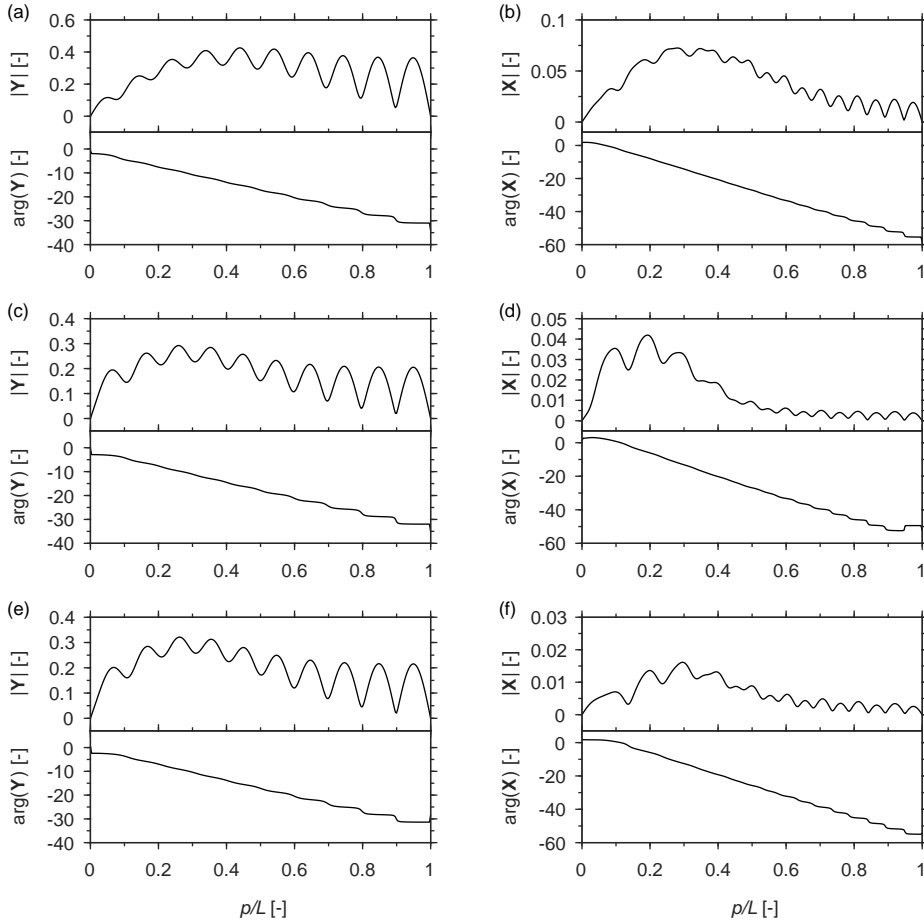
Figure 6.7: Amplitude and phase of (a,c,e) cross-flow and (b,d,f) in-line complex modes at sheared flow $V = 1.5$ m/s. (a,b) correspond to the response obtained using Model A; (c,d) correspond to the response obtained using Model B and (e,f) correspond to the response obtained using Model C. The complex modes are extracted at dominant frequencies identified from Spatio-temporal spectra.

the same secondary dominant in-line frequency around $f_y \approx 0.6 f_s$, with a wavenumber that corresponds to the 8th mode.

The complex modes at the main and secondary dominant frequencies are presented in Fig.6.9 and Fig.6.10 in both the cross-flow and in-line directions. As can be seen from Fig.6.9, at the main dominant frequencies, both cross-flow and in-line vibrations are associated with travelling waves that propagate from the high-velocity region towards the low-velocity region. All three models predict similar maximum cross-flow vibrations – close to $0.4D$ – at the main dominant frequency, while Model A predicts the largest in-line vibration with a maximum value around $0.1D$, followed by Model B around $0.05D$ and Model C around $0.02D$. For the complex modes at the secondary dominant frequency, as illustrated in Fig.6.10, all three models predict similar cross-flow vibrations,
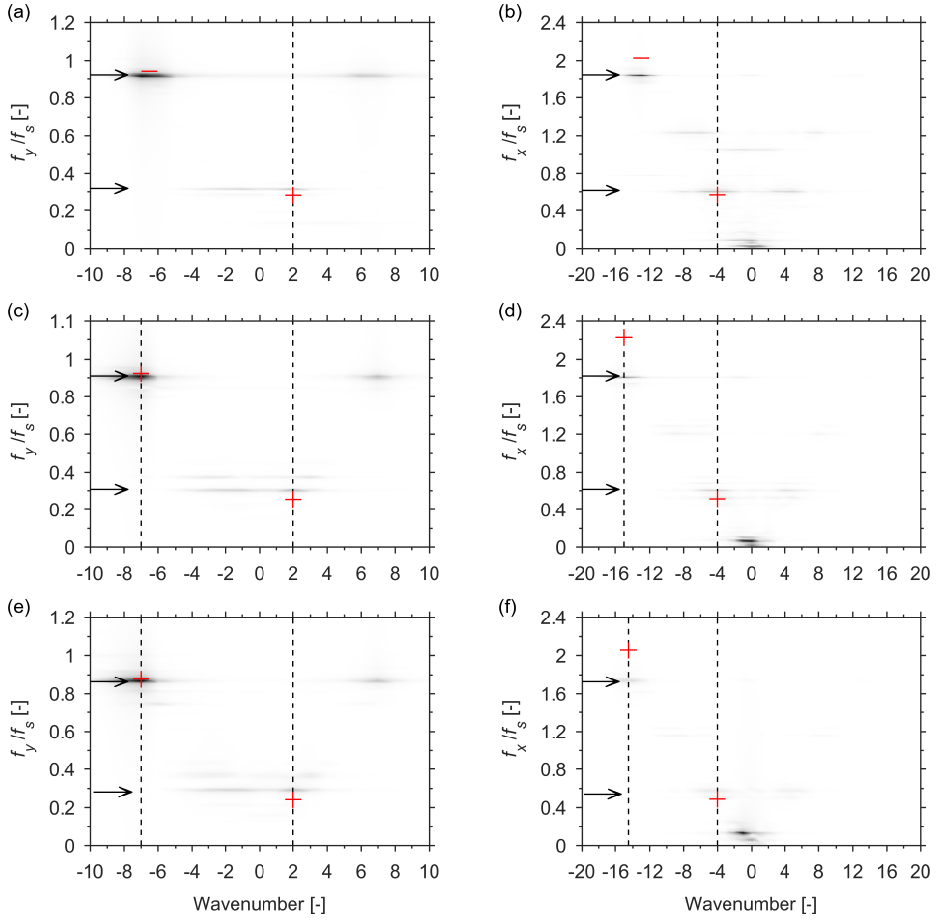
Figure 6.8: Spatio-temporal spectra of (a,c,e) cross-flow and (b,d,f) in-line displacements at sheared flow $V = 2.5$ m/s using Model A (a,b), Model B (c,d) and Model C (e,f). The arrows represent the dominant frequencies. The wavenumbers and natural frequencies of selected free vibration modes are indicated by black vertical dashed lines and red crosses respectively.

which are in the form of decaying travelling waves propagating towards the high-velocity region over a span between $p/L = 0$ and 0.7 and are dominated by standing waves near $p/L = 1$. This implies that the vibrations at the secondary dominant frequency are excited around $p/L = 0.7$ and propagate towards both ends of the riser. Models B and C predict a similar maximum cross-flow vibration around $0.13D$, which is slightly smaller than the prediction of Model A that is close to $0.16D$. Concerning the in-line vibration at the secondary dominant frequency, see Figs.6.10(b), (d) and (f), the pattern of the magnitude of complex modes are similar for all three cases; however, the evolutions of the phase are different. All three models predict that the in-line vibration at the secondary dominant frequency will mainly occur between $p/L = 0.7$ and 1 and will be standing wave dominated. Model A predicts the largest vibration magnitude with a maximum
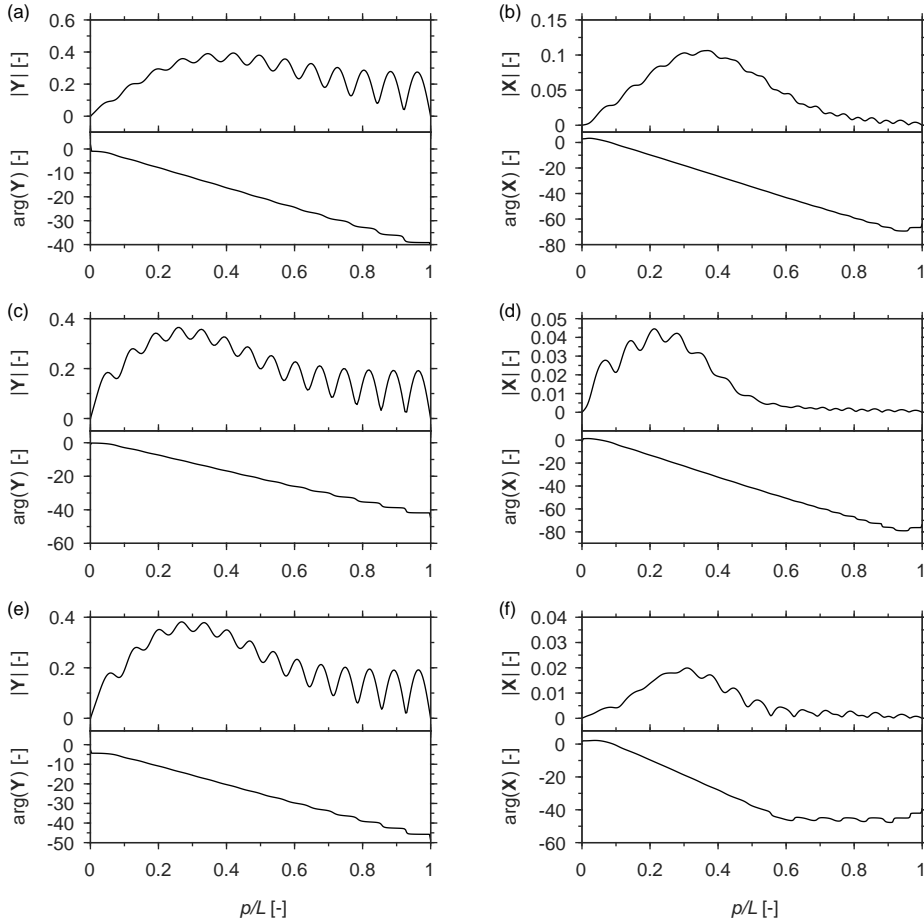
Figure 6.9: Amplitude and phase of (a,c,e) cross-flow and (b,d,f) in-line complex modes at sheared flow $V = 2.5$ m/s for main dominant frequency. (a,b) correspond to the response obtained using Model A; (c,d) correspond to the response obtained using Model B and (e,f) correspond to the response obtained using Model C. The complex modes are extracted at main dominant frequencies identified from Spatio-temporal spectra.

value close to $0.08D$, whereas Models B and C predict smaller values around $0.04D$ and $0.02D$ respectively. For the rest of the span, from $p/L = 0$ to $p/L = 0.7$, the amplitudes of the in-line vibrations are small. Over the span $p/L = 0-0.7$, the almost linearly decreasing phase shown in Fig.6.10(b) indicates that Model A predicts the vibration in the form of a travelling wave that travells towards the low-velocity region. Model B, on the other hand, predicts that a large segment of the riser is associated with a travelling wave that propagates towards the high-velocity region, as indicated in Fig.6.10(d) where the phase increases over $p/L = 0.2-0.6$. In Fig.6.10(f), it can be seen that the phase of the in-line complex mode remains almost constant over $p/L = 0-0.7$, according to Model C.
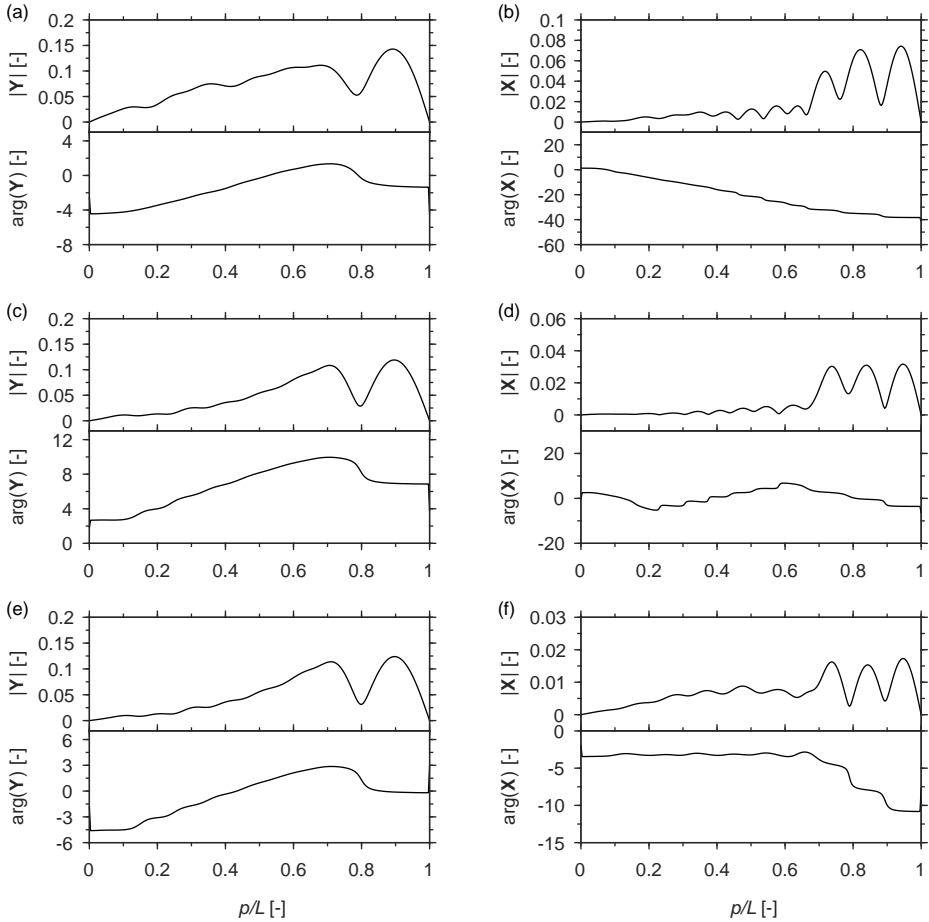
Figure 6.10: Amplitude and phase of (a,c,e) cross-flow and (b,d,f) in-line complex modes at sheared flow $V = 2.5$ m/s for secondary dominant frequency. (a,b) correspond to the response obtained using Model A; (c,d) correspond to the response obtained using Model B and (e,f) correspond to the response obtained using Model C. The complex modes are extracted at secondary dominant frequencies identified from Spatio-temporal spectra.

6.4. PHASE DIFFERENCE BETWEEN CROSS-FLOW AND IN-LINE MOTIONS

The phase difference between the cross-flow and in-line motions has a significant influence on the wake pattern when VIV occurs. It affects the hydrodynamic force acting on the structure and consequently influences the energy transfer between the fluid and structure. As a result, in the case of the VIV of flexible cylinders, the phase difference is naturally related to the distribution of excitation and damping regions. In this section, the definition of the phase difference, as well as the corresponding trajectory of structural motion, is presented in subsection 6.4.1. The phase differences for all simulation

cases are calculated and discussed in subsection 6.4.2.

6.4.1. Definition of phase difference and motion trajectory

Assume that the motion of a cross-section of the riser in the cross-flow and in-line directions can be described by the following equations:

$$y = y_0 \cos\left(\omega t + \phi_y\right) \tag{6.1}$$

$$x = x_0 \cos\left(2\omega t + \phi_x\right). \tag{6.2}$$

Then, the phase difference is defined as $\phi_{xy} = \phi_x - 2\phi_y$. This definition is in accordance with Dahl (2008) but has a shift of 90° compared to the one given by Jauvtis and Williamson (2004) that is taken in Section 4.3.1 for the purpose of comparison. With such a definition, the values of ϕ_{xy} in the range of 0°–180° correspond to a counter-clockwise motion trajectory, and those in the range of 180°–360° correspond to a clockwise orbit. Here, the counter-clockwise motion corresponds to the trajectory where the cylinder moves against undisturbed flow when reaching the cross-flow oscillation maximum, while the clockwise motion is associated with the case where the cylinder moves in the opposite direction.

The in-line and cross-flow phases ϕ_x and ϕ_y can be obtained by the angle of the complex modes determined in the previous section as $\phi_x = \arg(\mathbf{X})$ and $\phi_y = \arg(\mathbf{Y})$.

It must be clarified that the concept of phase difference and the application of $\phi_{xy} = \phi_x - 2\phi_y$ only make sense when the cross-flow and in-line motions are synchronised. Here, synchronisation means that the cross-flow and in-line motions vibrate interdependently at a constant frequency ratio of 2. In the experiments, this is not always the case, as the noise can sometimes be strong (Chaplin et al., 2005). However, this is not a problem here, as the simulation results indicate good synchronisation between the cross-flow and in-line motions along the whole span for all simulated cases. Some examples of such synchronisation and values of ϕ_{xy} that are specified for different motion trajectories are presented in Fig.6.11 for Model A.

6.4.2. Discussion

The phase difference ϕ_{xy} is calculated for all simulation results. The distributions of ϕ_{xy} along the riser are presented in Fig.6.12 and Fig.6.13 for the uniform flow cases and in Fig.6.14 for the sheared flow case. The boundary between the counter-clockwise and clockwise trajectory (180°) is indicated by a vertical thick line.

For the uniform flow case at $V = 0.5$ m/s, as illustrated in Fig.6.12, three models predict different distributions of ϕ_{xy} along the riser. For Model A, the phase difference along the riser covers a wide range of values between 0° and 360°, as can be seen in Fig.6.12(a). Jumps of approximately 310° occur at locations of $p/L = 0.64$ and $p/L = 0.36$, which are close to the locations of nodes between the cells of the cross-flow standing wave. The phase difference predicted by Model B, see Fig.6.12(b), varies around 0° and alternates between the counter-clockwise and clockwise regions. As depicted in Fig.6.3(d), the alternation is found to be closely related to the variation in the phase of the in-line motion, which, as explained in the previous section, is a result of the excitation of two different
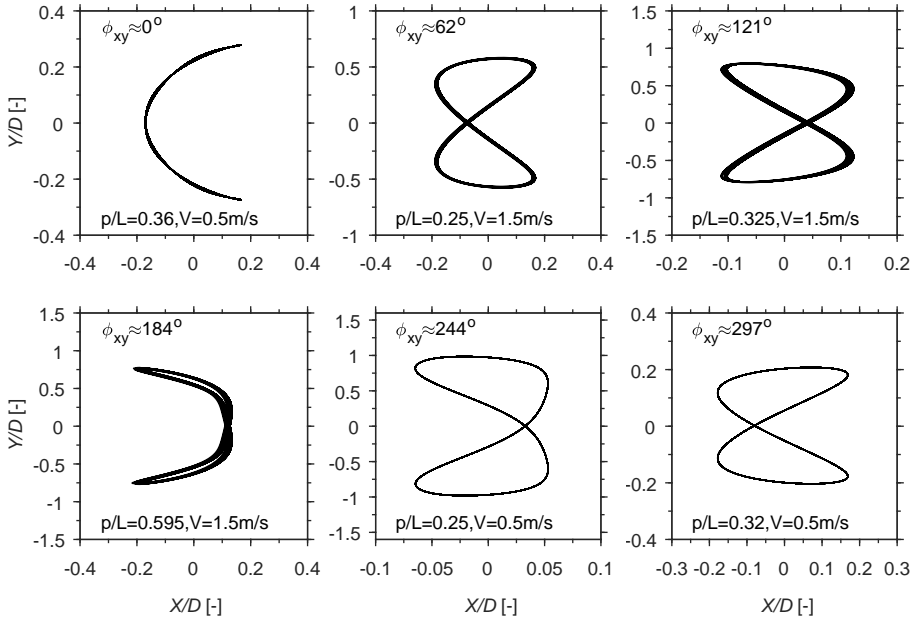
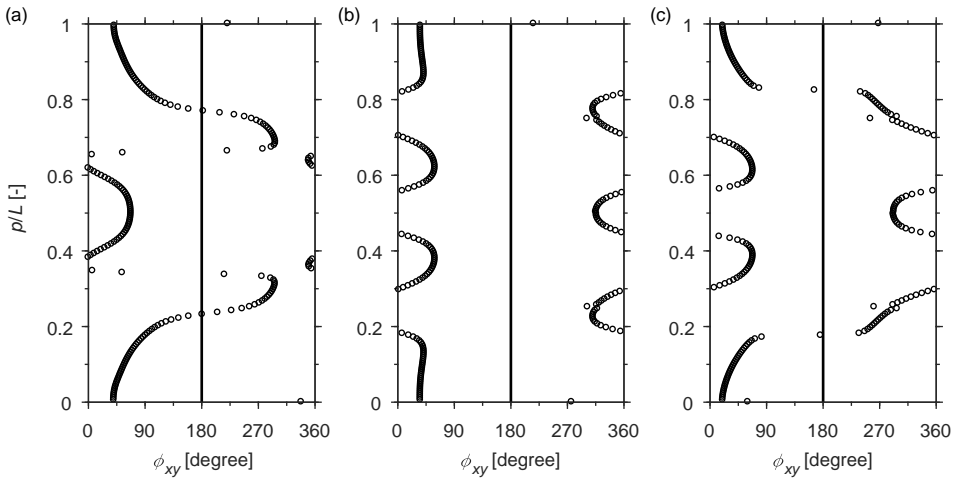Figure 6.11: Selected trajectories of the cylinder and corresponding phase difference from simulations with Model A.

Figure 6.12: Phase difference along the span at uniform flow $V = 0.5$ m/s for (a) Model A, (b) Model B and (c) Model C.

wavenumbers at the same frequency in the in-line direction. For Model C, the phase difference also varies between the counter-clockwise and clockwise regions, as pictured in Fig.6.12(c).

For the uniform flow case at $V = 1.5$ m/s, it is clear that the distribution of ϕ_{xy} for Model A, as portrayed in Fig.6.13(a), exhibits a different pattern compared to that of Models B and C, see Figs.6.13(b) and (c). For Model A, the mixed standing-travelling wave nature of both cross-flow and in-line displacements leads to a zigzagging evolution of ϕ_{xy} along the riser. The zigzagging pattern seems to be associated with the cells of the cross-flow displacement, if one compares Fig.6.13(a) with Fig.6.5(a), within which the phase difference continuously evolves to higher values at nodes and decreases through the cell before jumping again at the next node. The variation of ϕ_{xy} is smooth and confined mainly between 0° and 180°, corresponding to a counter-clockwise trajectory, except in the region near the upper boundary where the jumps of ϕ_{xy} at nodes exceed 180° as a result of dominant standing waves over that region in both the cross-flow and in-line directions. Concerning Models B and C, the evolution of ϕ_{xy} predicted by the two models is similar. As illustrated in Figs.6.13 (b) and (c), although ϕ_{xy} is mostly confined between 0° and 90°, significant segments of the span are associated with the ϕ_{xy} that sweeps through the range 180°−360°.
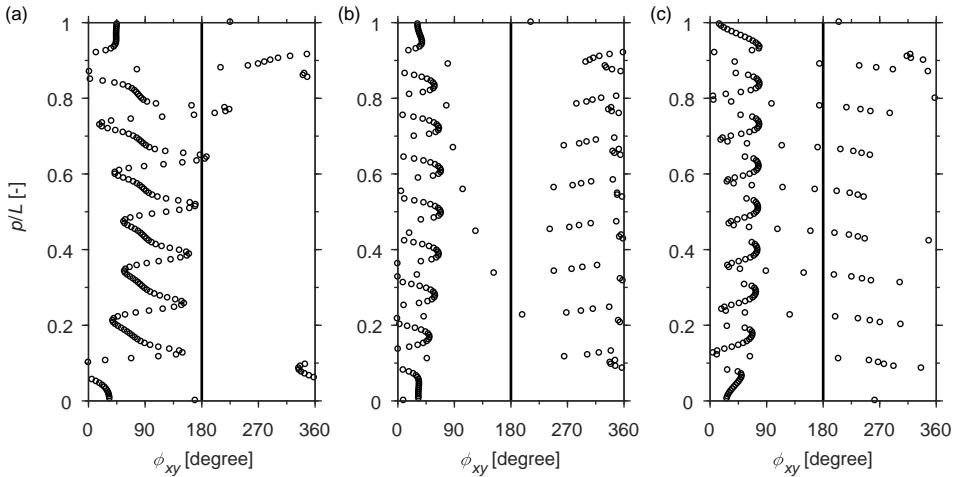

Figure 6.13: Phase difference along the span at uniform flow $V = 1.5$ m/s for (a) Model A, (b) Model B and (c) Model C.

The spanwise variation of the phase difference for the cases of sheared flow are presented in Fig.6.14. At flow velocity $V = 2.5$ m/s, the structural response contains multiple frequency components; therefore, only the results for the case of $V = 1.5$ m/s are presented here. Since the response patterns predicted by the three models are similar in sheared flow cases, it is expected that the distribution of the phase difference should also not be vastly different. The similarities between the predictions by the three models are obvious in Fig.6.14. For all three models, the phase differences are confined within the counter-clockwise region over a large segment of the riser near the high-velocity region as a result of a predominant travelling wave in both the cross-flow and in-line vibrations. The underlying standing character of the vibration leads to a zigzagging evolution of ϕ_{xy} along the span; this is similar to the case of uniform flow velocity $V = 1.5$ m/s in Model
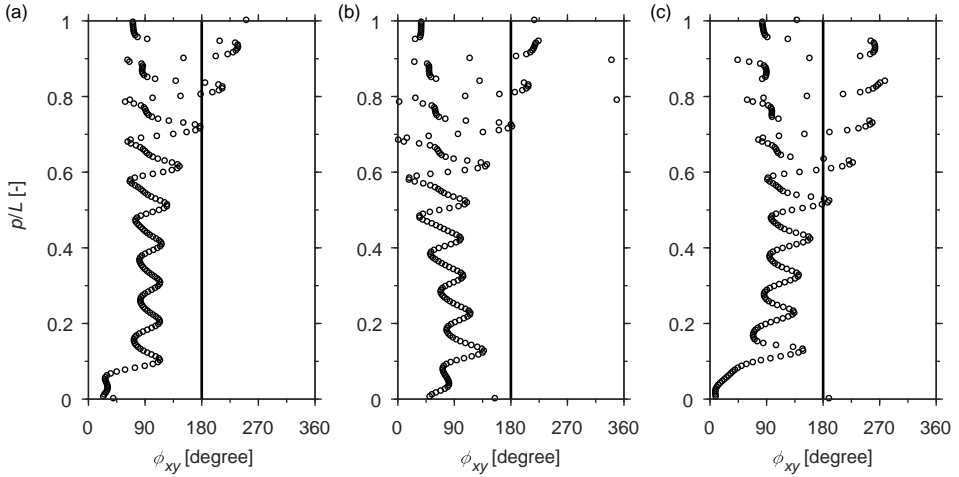
Figure 6.14: Phase difference along the span at sheared flow $V = 1.5$ m/s for (a) Model A, (b) Model B and (c) Model C.

A. In the low-velocity region, close to the end of the riser where the standing wave becomes predominant, the variation of the phase difference becomes large and jumps to the clockwise region at some locations.

In general, if the distribution of the phase difference is compared with the corresponding response pattern, then when the travelling wave is predominant in the response (all the sheared flow cases and uniform flow cases of $V = 1.5$ m/s for Model A), the phase difference has a tendency to be confined within a counter-clockwise range. In contrast, when the standing wave dominates (all the uniform flow cases for Models B and C and the uniform flow case of $V = 0.5$ m/s for Model A), the phase difference alternatively switches between counter-clockwise and clockwise ranges. The observations made on the variation of the phase difference shown in this section will be correlated with the fluid-structure energy transfer in the next section.

6.5. HYDRODYNAMIC FORCES AND FLUID-STRUCTURE ENERGY TRANSFER

In this section, the hydrodynamic forces and the energy transfer between the structure and fluid are studied in relation to the structural responses analysed in Sections 6.3 and 6.4. The fluid forces, as well as the fluid-structure energy transfer, are representative of the nonlinear equilibrium state of the coupled fluid-structure system and decide the global structural behaviour. The prediction of the segments of the structure that the energy flows into (denoted as power-in region) and out from (denoted as power-out region) is of fundamental importance for VIV of flexible structures.

6.5.1. HYDRODYNAMIC FORCES

In this subsection, the hydrodynamic forces, as well as their distribution along the riser, are discussed based on the simulation results. The hydrodynamic forces exerted on the structure are calculated at each nodal location of the riser model from the simulated oscillations of wake variable q using Eqs.(5.14), (5.15) and (5.18). It needs to be pointed out that the hydrodynamic force calculated here excludes the potential added mass. The calculated hydrodynamic force is a vector in the space, and only its components in cross-flow (F_y) and in-line (F_x) directions are considered. The cross-flow and in-line force coefficients, namely C_y and C_x, are obtained by normalising the corresponding forces using the following equation:

$$C_{x,y} = \frac{F_{x,y}}{\frac{1}{2}\rho D V^2}.$$
(6.3)

In Fig.6.15 and Fig.6.16, the RMS values of the mean in-line force coefficients, denoted as $\hat{C}_x$; the fluctuating in-line force coefficients, denoted as $\tilde{C}_x$; and the cross-flow force coefficients C_y are presented for all three models at uniform flow velocities of $V = 0.5$ m/s and $V = 1.5$ m/s. It is clear in Fig.6.15(a) and Fig.6.16(a) that all three models predict the amplification of $\hat{C}_x$ compared to its value, around 1.2, on a fixed cylinder, but at different levels. Model A predicts the most significant amplification of the mean in-line force coefficient and Model C predicts the least. From all three models, the amplification of the mean in-line force coefficient is found to be associated with large cross-flow vibrations of the riser. The maxima of $\hat{C}_x$ are located in the regions of antinodes of cross-flow motion. The same trend was reported in experiments by Huarte (2006). Furthermore, the magnitude of the simulated maximum mean in-line force coefficient by Model A – as high as 6 – is comparable to those observed in the experiments under a similar amplitude of cross-flow displacement. At the location where the cross-flow motion is close to zero, for example the cross-flow nodes at $V = 0.5$ m/s, the mean in-line force coefficient predicted by Model A is around 2, which is still higher compared to the case of a stationary cylinder, while the other two models predict almost no amplification.

The fluctuating component of the in-line force coefficients, as illustrated in Fig.6.15(b) and Fig. 6.16(b), has a similar trend to the mean in-line force. In general, the distribution of $\tilde{C}_x$ follows a shape similar to that of magnitude of cross-flow complex mode, meaning that it is still primarily affected by the cross-flow motion. In addition, the influence of the in-line motion is also significant, as the local maxima of fluctuating in-line forces appear mostly at points associated to the local maxima of the in-line displacements.

The distribution of the cross-flow force, in contrast to the in-line force, exhibits a more irregular pattern, as depicted in Fig.6.15(c) and Fig.6.16(c). The cross-flow forces predicted by Models B and C exhibit a similar pattern of distribution, with the magnitude calculated by Model B slightly higher than that by Model C. The cross-flow force obtained with Model A exhibits a different pattern. Also, Model A predicts, in general, a larger magnitude of cross-flow force. Efforts have been made to relate the variation of the cross-flow force to the structural motions. However, no obvious trend has been observed. This may imply that for all three models, the cross-flow force is sensitive to both the cross-flow and in-line motions.   It is interesting to note that for the uniform flow case at $V = 0.5$ m/s where the cross-flow motion is dominated by standing waves, at
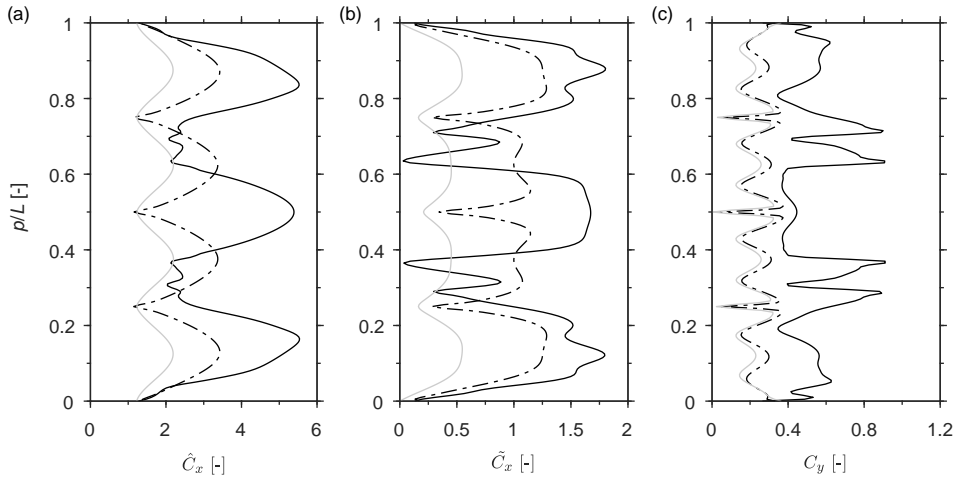
Figure 6.15: RMS values of (a) mean in-line force coefficient $\hat{C}_x$, (b) fluctuating in-line force coefficient $\tilde{C}_x$ and (c) cross-flow force coefficient C_y for uniform flow velocity $V = 0.5$ m/s. Black solid lines represent results from Model A, black dashed lines represent results from Model B and grey solid lines represent results from Model C.

6

Figure 6.16: RMS values of (a) mean in-line force coefficient $\hat{C}_x$, (b) fluctuating in-line force coefficient $\tilde{C}_x$ and (c) cross-flow force coefficient C_y for uniform flow velocity $V = 1.5$ m/s. Black solid lines represent results from Model A, black dashed lines represent results from Model B and grey solid lines represent results from Model C.
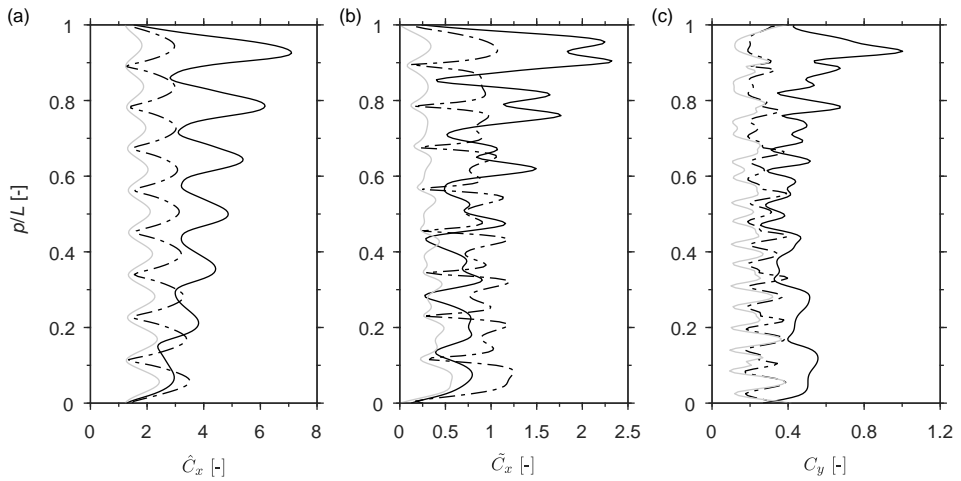
the location where the cross-flow motion is almost zero, the cross-flow force predicted by Models B and C is close to zero, while that predicted by Model A still has a significant value.

The hydrodynamic forces for the sheared flow case with maximum flow velocity $V =$ 1.5 m/s are presented in Fig.6.17. Different from the cases of uniform flow, the force
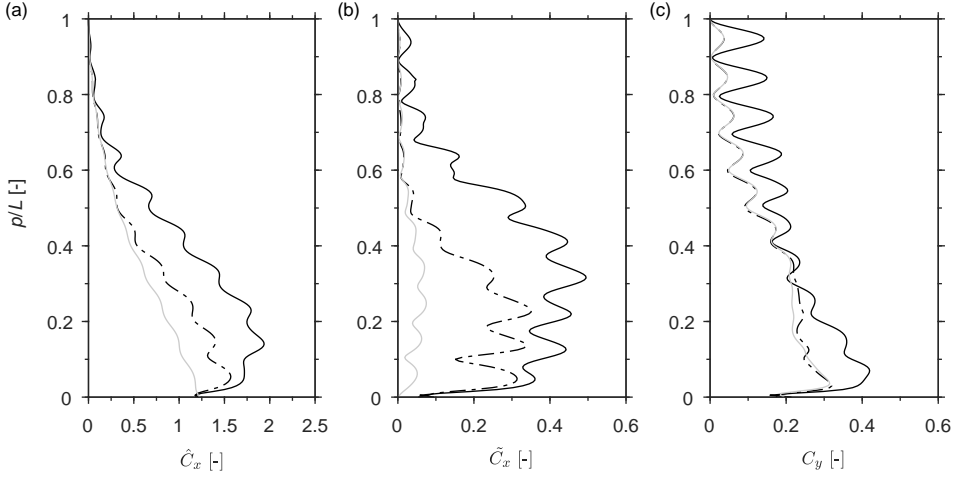
Figure 6.17: RMS values of (a) mean in-line force coefficient $\hat{C}_x$, (b) fluctuating in-line force coefficient $\tilde{C}_x$ and (c) cross-flow force coefficient C_y for sheared flow with maximum velocity $V = 1.5$ m/s. Black solid lines represent results from Model A, black dashed lines represent results from Model B and grey solid lines represent results from Model C.

coefficients are obtained by normalising the force with the maximum flow velocity. As a result, all the force coefficients exhibit a gradual decrease from the high-velocity region to the low-velocity region towards zero. The usage of the maximum flow velocity in the normalisation makes it difficult to make a direct comparison between the force coefficients and the response amplitude of the riser, as has been done for the uniform flow. However, by comparing the positions of the local maxima and minima, it is clear that the large mean and fluctuating in-line coefficients are normally found at locations of large cross-flow oscillation amplitude. With regard to the cross-flow force coefficient, its relation to the cross-flow amplitude is more complex. For example, in Fig.6.17(c), the local maxima of C_y are observed at the local minima of cross-flow vibration for $p/L < 0.5$, while for $p/L > 0.5$ the trend is the opposite.

6.5.2. FLUID-STRUCTURE ENERGY TRANSFER

Follow the concept used by Bourguet et al. (2011), the energy transfer between the fluid and structure in this thesis is quantified by the force coefficient that is in phase with the velocity of the riser; for simplicity, it is denoted as excitation coefficient C_e here. Its components in the cross-flow and in-line directions are defined as

$$C_{e,y} = \frac{\frac{2}{T}\int_T C_y \dot{y}\,dt}{\sqrt{\frac{2}{T}\int_T \dot{y}^2\,dt}} \tag{6.4}$$

and

$$C_{e,x} = \frac{\frac{2}{T}\int_T C_x \dot{x}\,dt}{\sqrt{\frac{2}{T}\int_T \dot{x}^2\,dt}}. \tag{6.5}$$

The total force in phase with the velocity vector is defined as

$$C_e = \frac{\frac{2}{T}\int_T \left(C_y \dot{y} + C_x \dot{x}\right) dt}{\sqrt{\frac{2}{T}\int_T \left(\dot{y}^2 + \dot{x}^2\right) dt}}. \tag{6.6}$$

A positive excitation coefficient means, on average, the energy transfers from fluid to structure and hence excites the structural vibration, while a negative excitation coefficient indicates that the structural motion is damped. The regions corresponding to the positive excitation coefficient are designated as power-in regions, while those with the negative excitation coefficient are refer to as power-out regions.

The spanwise distributions of C_e, $C_{e,y}$ and $C_{e,x}$ at uniform flow velocities of $V = 0.5$ m/s and 1.5 m/s are presented in Fig.6.18 and Fig.6.19. At both flow velocities, Model A predicts the variation of the excitation coefficients along the span in a pattern that is different from those for Models B and C. For flow velocity $V = 0.5$ m/s, as can be seen in Fig.6.18(a), the cross-flow and in-line excitation coefficients share a common power-in region at the middle of the riser between $p/L = 0.4$ and $p/L = 0.6$, according to Model A. Beyond this region, the energy transfer in the two directions seems to be opposite at most locations along the span; i.e. within the region where the riser motion is excited by the fluid forces in the cross-flow direction, it is damped out in the in-line direction and vice versa. The same phenomena are observed and seem to be more perceptible for Models B and C, as illustrated in Figs.6.18(b) and (c), where the signs of $C_{e,x}$ and $C_{e,y}$ are opposite to each other over almost the entire span of the riser. The predictions of the cross-flow excitation coefficient according to Models B and C are almost exact, while the in-line excitation coefficient predicted by Model B is significantly larger than that by Model C. At flow velocity $V = 1.5$ m/s, it has previously been shown that the structural response, predicted by Model A, is characterised by travelling waves that propagate in the direction from $p/L = 0$ towards $p/L = 1$. As a consequence, the general power-in region is expected to be located over the span that is close to $p/L = 0$, while the power-out region is expected to be close to the other end. This is verified in Fig.6.19(a), which illustrates that the excitation coefficient C_e remains positive over approximately the first half span of the riser and becomes alternatively positive and negative over the rest. For Models B and C, in general, the spanwise variation of the excitation coefficient at flow velocity $V = 1.5$ m/s is similar to that at $V = 0.5$ m/s, except that at $V = 1.5$ m/s, the value of the positive C_e is lightly larger over the span close to $p/L = 1$. This is consistent with the insignificant underlying travelling character of the structural response (corresponding to the travelling wave oriented from $p/L = 1$ towards $p/L = 0$).

To study the relationship between the energy transfer and structural motions, the power-in regions, indicated by grey areas, are portrayed together with the magnitude of cross-flow complex mode $|\mathbf{Y}|$ as well as the phase difference ϕ_{xy} in Fig.6.20 and Fig.6.21 for a uniform flow at $V = 0.5$ m/s and $V = 1.5$ m/s. As can be seen in Fig.6.20(a) and Fig.6.21(a), no clear relation is observed between the energy transfer and the cross-flow motion for Model A. Nevertheless, it is interesting to note that according to Model A, the large amplitude of cross-flow vibration does not necessarily correspond to the power-out region. For example, in Fig.6.20(a), although the cross-flow vibration is at its maximum around $p/L = 0.5$, the location is associated with the energy flow into the structure. The
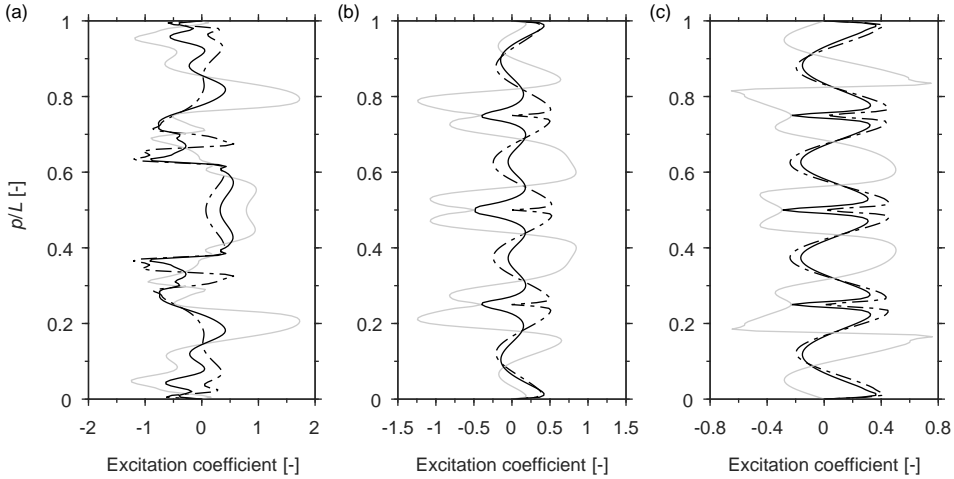
Figure 6.18: Force coefficients in phase with velocity along the riser for uniform flow at $V = 0.5$ m/s: (a) results of Model A, (b) results of Model B and (c) results of Model C. Black solid lines represent total excitation coefficient C_e, and black dashed lines and grey solid lines represent $C_{e,y}$ and $C_{e,x}$ respectively
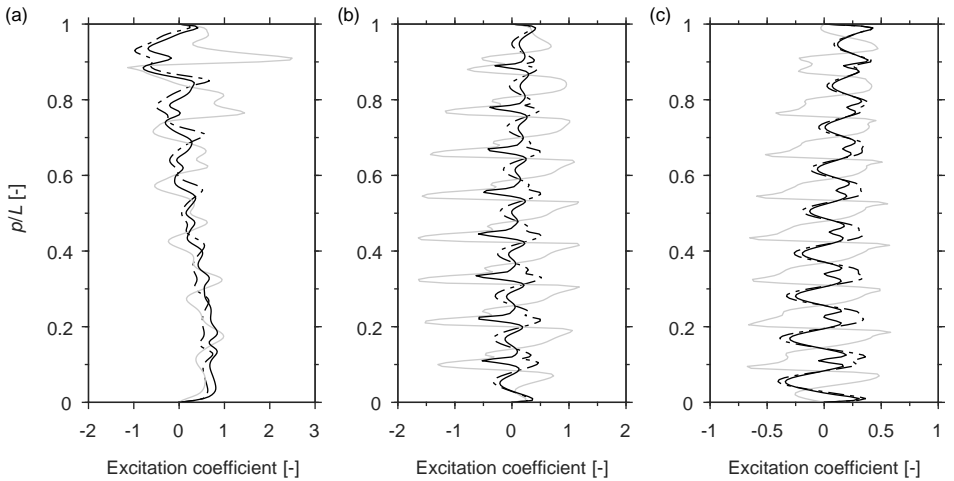

Figure 6.19: Force coefficients in phase with velocity along the riser for uniform flow at $V = 1.5$ m/s: (a) results of Model A, (b) results of Model B and (c) results of Model C. Black solid lines represent total excitation coefficient C_e, and black dashed lines and grey solid lines represent $C_{e,y}$ and $C_{e,x}$ respectively

same phenomenon is observed in experiments by Song et al. (2016). Furthermore, the underlying mechanism is believed to be related to the effect of the coupled cross-flow and in-line motions on the wake dynamics. This reflects the shortcomings of most existing models, including Models B and C presented here, in the prediction of the coupled cross-flow and in-line VIV. When dealing with the two degrees of freedom VIV, the cross-flow vibration is normally treated separately, and based on the force data obtained from

Figure 6.20: Power-in regions identified from C_e in comparison with the amplitudes of the cross-flow complex modes |**Y**| and phase difference ϕ_{xy} at uniform flow velocity $V = 0.5$ m/s: (a) results of Model A, (b) results of Model B and (c) results of Model C. Power-in regions are indicated by grey colored area. Black solid lines represent |**Y**| and circles represent ϕ_{xy}.

6

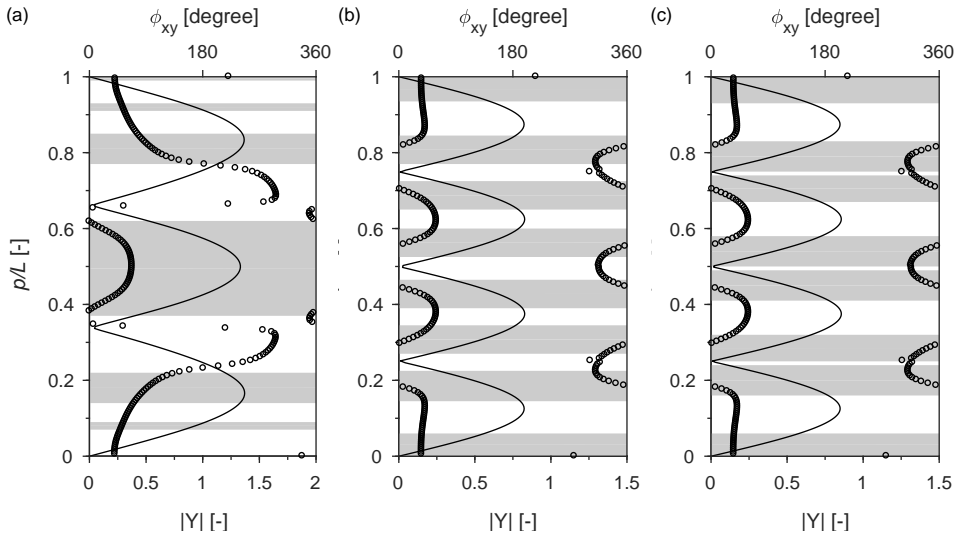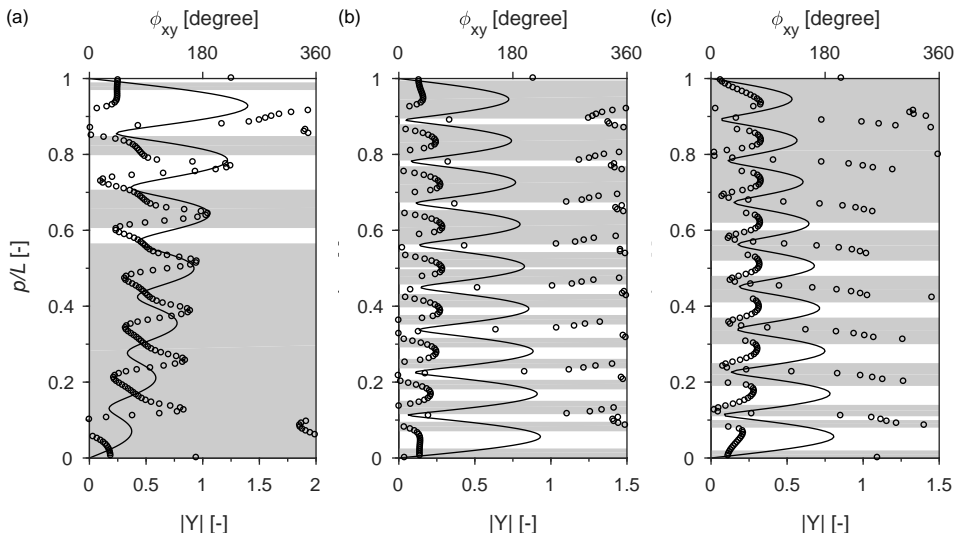
Figure 6.21: Power-in regions identified from C_e in comparison with the amplitudes of the cross-flow complex modes |**Y**| and phase difference ϕ_{xy} at uniform flow velocity $V = 1.5$ m/s: (a) results of Model A, (b) results of Model B and (c) results of Model C. Power-in regions are indicated by grey colored area. Black solid lines represent |**Y**| and circles represent ϕ_{xy}

the forced cross-flow vibration, the models always predict the power-out region at the location of a large cross-flow vibration. This can be verified by the energy transfer predicted by Models B and C, as presented in Fig.6.20(b,c) and Fig.6.21(b,c), which show clearly that the energy is primarily damped out from the structure at locations corresponding to large cross-flow vibrations. Apart from the power-out regions corresponding to large cross-flow vibrations, the energy is also found to be damped out from the structure at locations of small cross-flow vibrations, according to Models B and C. For example, in Figs.6.20(b) and (c), the segments of the riser around the nodes of cross-flow displacement are associated with power-out regions. Looking into the contributions to the energy transfer from the cross-flow and in-line excitation coefficients, as illustrated in Figs.6.18(b) and (c), although the cross-flow excitation coefficients around the location of the nodes are almost zero, it is the negative in-line excitation coefficients that make the total energy transfer at these locations negative.

Concerning the phase difference, no obvious relation is observed between it and the power-in regions for Models B and C, since the energy transfer is primarily determined by the amplitude of cross-flow vibration for these two cases. For Model A, although no solid trend is observed, it seems that the power-in regions are mostly associated with the phase difference that corresponds to the counter-clockwise trajectory (between 0° and 180°).

The excitation coefficients for cases of a sheared flow profile with maximum flow velocity $V = 1.5$ m/s are presented in Fig.6.22. As can be seen in this figure, for all three models, the regions of positive C_e are located in the high-velocity zone, while in the low-velocity region, the C_e remains negative. The cross-flow and in-line excitation coefficients have the same distribution pattern as that of C_e and both make significant contributions to the total energy transfer within the high-velocity region, while in the low-velocity region, the in-line excitation coefficients are small. Fig.6.22 also displays the limit, indicated by a horizontal dashed line, between the power-in and power-out regions. Model A predicts a wider power-in region $p/L = 0-0.38$ compared to that, around $p/L = 0-0.28$, predicted by Models B and C. Different from the uniform flow cases, the energy transfer between the fluid and structure in the sheared flow cases is normally expected to be determined by the reduced velocity. The reduced velocity range of $5-7$ is commonly assumed to be associated with the power-in region. Here, for Model A, the power-in region corresponds to the reduced velocity range of $U_r = 3.83-6.15$, and that for Models B and C corresponds to the range of $U_r = 4.46-6.25$.

The excitation coefficient for the case of sheared flow with maximum flow velocity $V = 2.5$ m/s is shown in Fig.6.23. The distributions of C_e and its cross-flow and in-line components $C_{e,y}$ and $C_{e,x}$ exhibit the same pattern and trend as those at $V = 1.5$ m/s; therefore, they are not discussed in detail here. The reduced velocity is calculated based on the primary dominant cross-flow frequency, and the range that corresponds to the power-in region is found to be $U_r = 3.86-6.14$ for Model A and $U_r = 4.48-6.14$ for Models B and C. These ranges are similar to those at $V = 1.5$ m/s and suggest that for all three models, in the sheared flow cases, the power-in regions are primarily affected by the reduced velocity. Different from the case of $V = 1.5$ m/s, the structural response at $V = 2.5$ m/s contains multiple frequency components, which implies the presence of several power-in regions that correspond to different frequency contents. Therefore, a
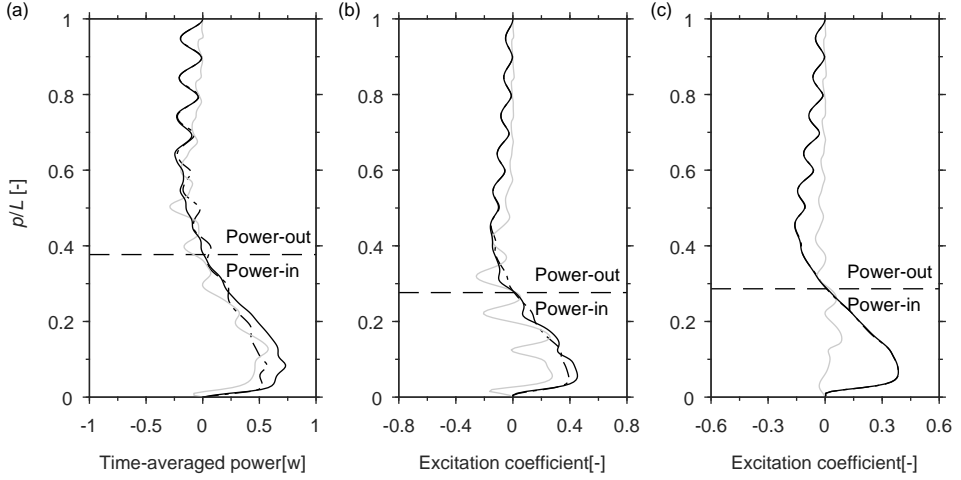
Figure 6.22: Force coefficient in phase with velocity along the riser for sheared flow with maximum velocity $V = 1.5$ m/s: (a) results of Model A, (b) results of Model B and (c) results of Model C. Black solid lines represent total excitation coefficient C_e, and black dashed lines and grey solid lines represent $C_{e,y}$ and $C_{e,x}$ respectively
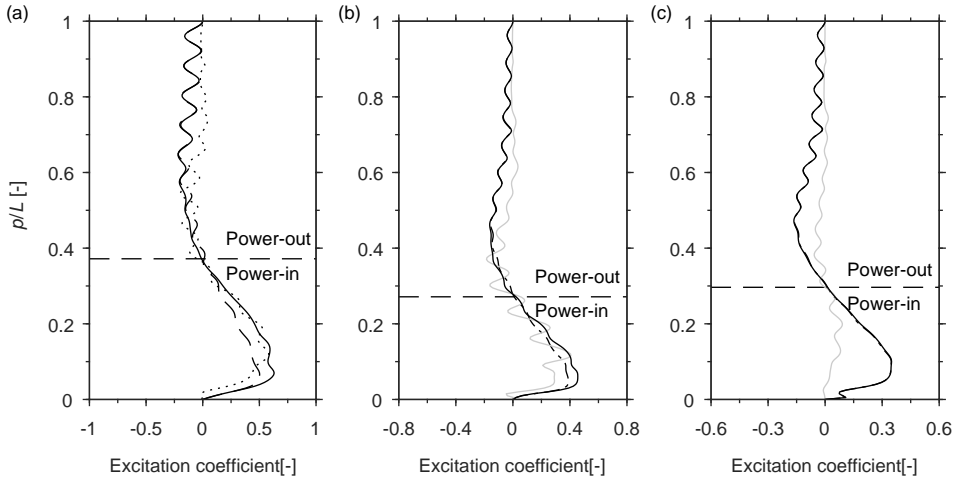
Figure 6.23: Force coefficients in phase with velocity along the riser for sheared flow with maximum velocity $V = 2.5$ m/s: (a) results of Model A; (b) results of Model B and (c) results of Model C. Black solid lines represent total excitation coefficient C_e; black dash lines and grey solid lines represent $C_{e,y}$ and $C_{e,x}$ respectively

frequency decomposition of $C_{e,y}$ and $C_{e,x}$ based on a Fourier transform is performed. The contributions from different frequency components to the cross-flow and in-line excitation coefficients are calculated with the following equations:

$$W_x\left(f\right) = \frac{\mathrm{Re}\left(\mathscr{F}\left[C_x\left(t\right)\right]\overline{\mathscr{F}\left[\dot{x}\left(t\right)\right]}\right)}{\left|\mathscr{F}\left[\dot{x}\left(t\right)\right]\right|} \tag{6.7}$$

and

$$W_y\left(f\right) = \frac{\mathrm{Re}\left(\mathscr{F}\left[C_y\left(t\right)\right]\overline{\mathscr{F}\left[\dot{y}\left(t\right)\right]}\right)}{\left|\mathscr{F}\left[\dot{y}\left(t\right)\right]\right|} \tag{6.8}$$

where $\mathscr{F}\left[\cdot\right]$ denotes Fourier transform and the overline denotes the complex conjugation.

The frequency decomposition of the cross-flow and in-line excitation coefficients are presented in Fig.6.24 and Fig.6.25 for all three models. The previously identified dominant frequencies are indicated by arrows. In the cross-flow direction, as illustrated in Fig.6.24, the frequency decomposition of $C_{e,y}$ does not display obvious differences among the models. For all three models, the most significant positive energy transfer occurs at the main dominant frequency over the same power-in region identified from the total excitation coefficients. Apart from the main power-in region, another region corresponding to a positive $C_{e,y}$ is observed in the low-velocity region around $p/L = 0.7$ close to secondary dominant frequency. It has previously been shown in Fig.6.8 that the cross-flow response exhibits two frequency peaks around the secondary dominant frequency. Therefore, in Fig.6.24, it is not surprising that the positive energy transfer occurs at two distinct frequencies. However, it seems that these two frequencies are well separated for Models B and C, while they are closely spaced for Model A. Concerning the frequency decomposition of the in-line excitation coefficient, similar to the cross-flow case, apart from the strong positive $C_{e,x}$ that occurs at the main dominant frequency, all three models predict another positive energy transfer at the secondary dominant frequency. Different from Models B and C, for which the positive energy transfer at the secondary dominant frequency is mainly located in the low-velocity zone around $p/L = 0.7$, a significant positive $C_{e,x}$ is observed at different locations along the riser for Model A, even in the high-velocity zone, for example at $p/L \approx 0.15$. The difference is believed to be related to the in-line coupling term in the wake oscillator equation. However, further analysis is needed to understand the underlying mechanism. In the in-line direction, apart from the positive energy transfer that occurs at the main and secondary dominant frequencies, a positive $C_{e,x}$ is also observed at a frequency that is approximately twice that of the secondary dominant frequency as a result of the contribution from higher harmonics.

6.6. FATIGUE DAMAGE

In this section, a fatigue analysis is conducted for the simulation results obtained from the three models. The main purpose is to investigate the higher harmonics and their contributions to fatigue damage. Therefore, the characteristics of the structural response at higher harmonics are presented in the first subsection through the spectra of the strain, and the fatigue damage is calculated and discussed in the second subsection.

6.6.1. STRAIN AND HIGHER HARMONICS

To highlight the higher harmonics, the frequency domain analysis is performed in this subsection based on the bending strains at the surface of the riser. The bending strains
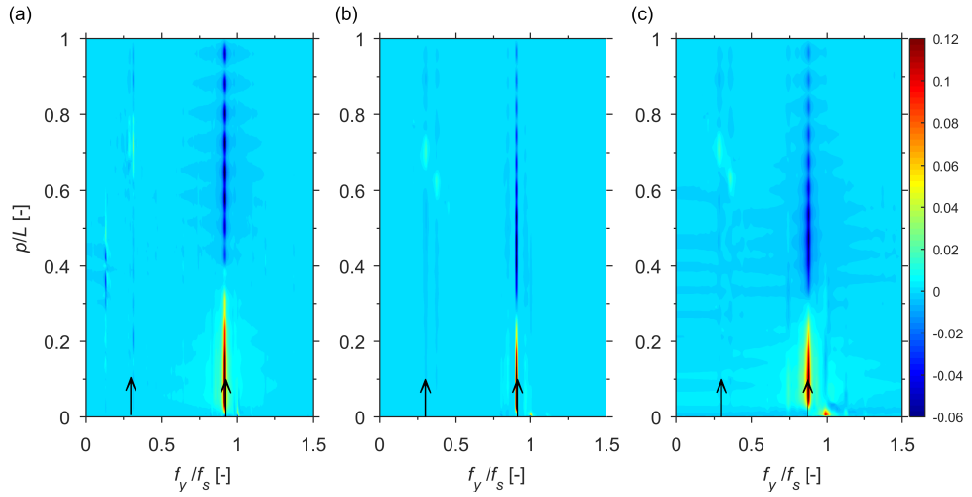
Figure 6.24: Frequency decomposition of the cross-flow excitation coefficient for (a) results of Model A, (b) results of Model B and (c) results of Model C.
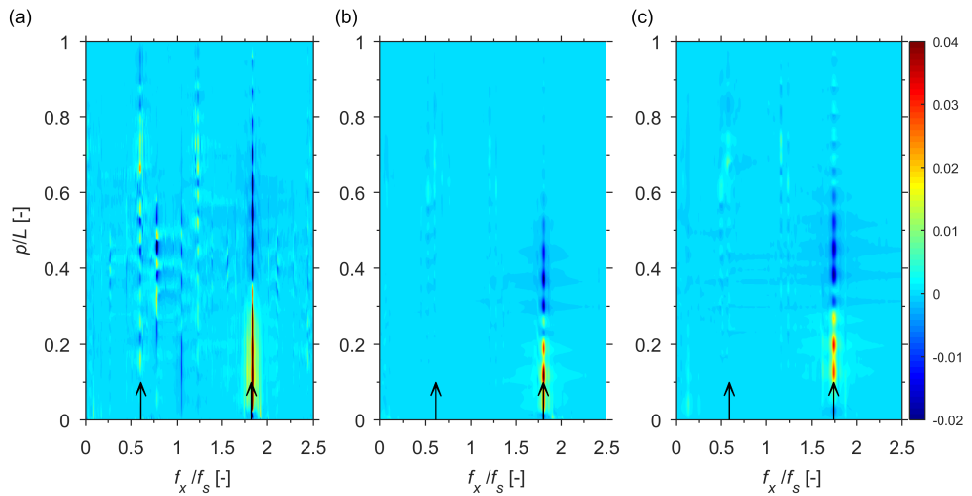
Figure 6.25: Frequency decomposition of the in-line excitation coefficient for (a) results of Model A, (b) results of Model B and (c) results of Model C.

of cross-flow and in-line deflections are calculated by the following equation:

$$\epsilon_{x,y} = K_{x,y} \frac{D}{2} \tag{6.9}$$

where subscripts 'x' and 'y' denote the in-line and cross-flow directions respectively, and $K_{x,y}$ is the curvature calculated as the second derivative of the in-line and cross-flow displacement with respect to the axial coordinate using a central finite difference

approximation.

The PSD of in-line and cross-flow strains are evaluated along the riser, and its span-averaged value is plotted in Fig.6.26–6.29. In these plots, the vibration frequency is normalised by the Strouhal frequency f_s, and the PSD is normalised by its maximum value for the purpose of comparison. The results from Models A, B and C are presented in the same plot and indicated by black solid, black dashed and solid grey lines respectively. The spectrum confirms that the in-line response oscillates at a fundamental frequency twice that of the cross-flow response. In addition, the most important observations from these plots are the appearance of higher harmonics. In the cross-flow direction, the riser response is dominated by a strong primary frequency (denoted by 1×) and has odd higher harmonics (denoted by 3× and 5×), while its even integer multiples (denoted by 2×, 4× and 6×) are found in the in-line direction.
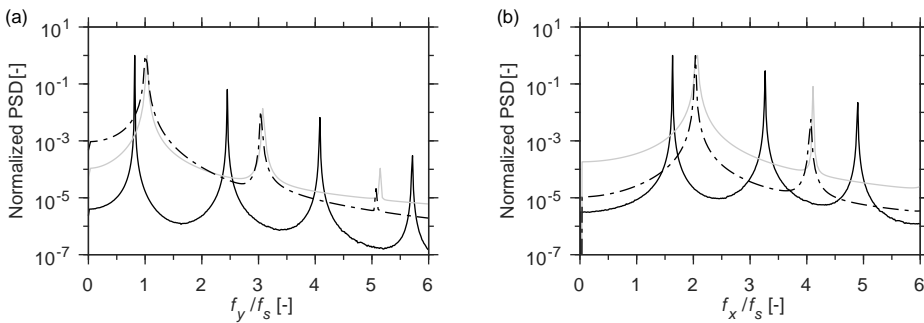
Figure 6.26: Spanwise averaged PSD of bending strain due to (a) cross-flow and (b) in-line deflections for uniform flow $V = 0.5$ m/s. Black solid lines represent results from Model A, black dashed lines represent results from Model B and grey solid lines represent results from Model C.
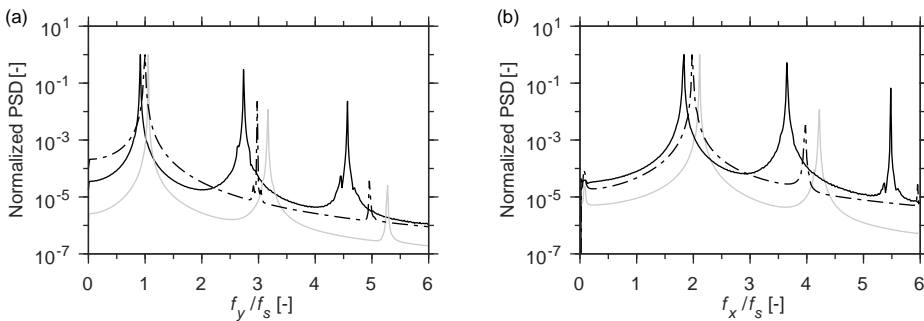
Figure 6.27: Spanwise averaged PSD of bending strain due to (a) cross-flow and (b) in-line deflections for uniform flow $V = 1.5$ m/s. Black solid lines represent results from Model A, black dashed lines represent results from Model B and grey solid lines represent results from Model C.

For the uniform flow cases at $V = 0.5$ m/s and 1.5 m/s, as illustrated in Figs.6.26 and 6.27, it is clear that all three models predict distinct frequency peaks at higher harmonics. In general, the comparison of the results from the three models reveals that Model
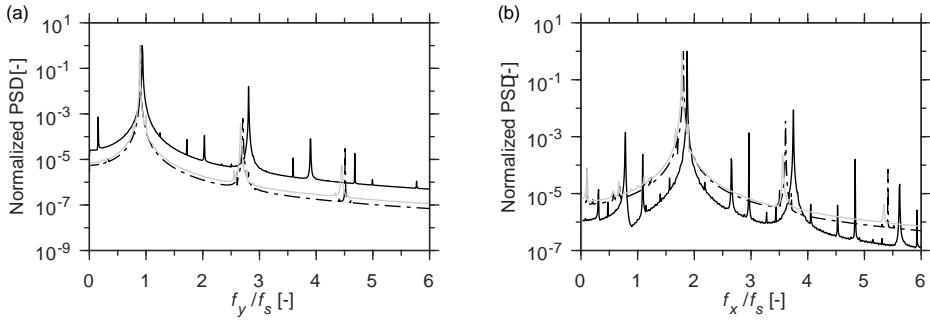
Figure 6.28: Spanwise averaged PSD of bending strain due to (a) cross-flow and (b) in-line deflections for sheared flow with maximum velocity $V = 1.5$ m/s. Black solid lines represent results from Model A, black dashed lines represent results from Model B and grey solid lines represent results from Model C.

Figure 6.29: Spanwise averaged PSD of bending strain due to (a) cross-flow and (b) in-line deflections for sheared flow with maximum velocity $V = 2.5$ m/s. Black solid lines represent results from Model A, black dashed lines represent results from Model B and grey solid lines represent results from Model C.
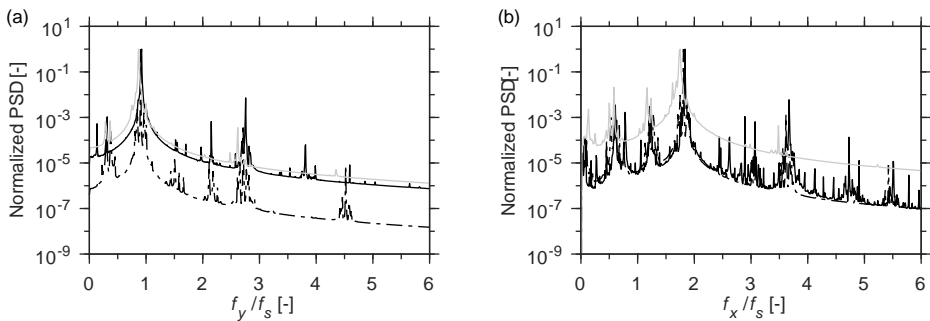
A predicts the most significant components at higher harmonics. The 3× cross-flow response, as reported by Jauvtis and Williamson (2004), is a result of the third harmonic component in the lift force that corresponds to the wake pattern where three vortices are shed. This wake pattern was found to be associated with the large cross-flow vibration when the super-upper branch appears for a small mass ratio system. Since Model A is able to capture this phenomenon of the super-upper branch, it is not surprising that the model predicts the strongest 3× among the three models. Regarding to the 4×, 5× and 6× harmonics, although often observed in experiments of the VIV of flexible cylinders, little research is conducted on them. It is clear that their contributions are considerable, especially the 4× harmonics, whose magnitude predicted by Model A is comparable to the 2× harmonics.

In Fig.6.28 and Fig.6.29, the spanwise averaged PSD of strain for sheared flow cases is presented. It can be seen that at both flow velocities, the frequency spectrum of the strain for Model A is characterised by the richness of the frequency content with small peaks, and this is much more significant compared to that of Models B and C. The relative contributions of higher harmonics are clearly smaller in sheared flow than those in

uniform flow. Nevertheless, Model A still predicts the strongest high-harmonic components.

6.6.2. FATIGUE DAMAGE RATE

In this subsection, the fatigue damage is calculated by applying the Miner summation, and the fatigue damage at a specific location along the riser is given by

$$D_a = \sum_{i=1} \frac{n_i}{N_i} = \frac{1}{a} \sum_{i=1} n_i (\Delta\sigma_i)^m \tag{6.10}$$

where N_i represents the number of cycles to failure at stress amplitude $\Delta\sigma_i$, and n_i denotes the corresponding stress cycles that take place. The number of cycles to failure for a given stress amplitude can be found from an S-N curve, which is associated with the parameters a and m. Here, $\log a = 11.687$ and $m = 3.0$ are taken as suggested by Trim et al. (2005). The rainflow counting method is applied to find n_i for a given time series of strain, and the stress amplitude is obtained by simply multiplying the strain with Young's modulus. It needs to be clarified that the concept of fatigue damage is used loosely here, since in practical applications, the effective stress, such as von Mises stress, should be used in the estimation of fatigue damage. For each simulation result, the fatigue damage is estimated on both the original and a filter version of the signal, where the higher harmonics have been removed and only the primary harmonics (1× component in the cross-flow and 2× component in the in-line direction) are kept.

In Figs.6.30 and 6.31, the distributions of the fatigue damage rate along the riser are presented for the uniform flow cases. It is clear from these figures that while for the cases of Models B and C, the total fatigue damage shows no obvious difference relative to that at the primary frequency, Model A predicts the total fatigue damage to be much higher than its component at the primary frequency. At flow velocity $V = 0.5$ m/s, all three models predict a similar order of maximum damage due to the cross-flow vibrations, as can be seen in Figs.6.30(a), (c) and (e). For Model A, the excited third mode in the cross-flow vibration leads to a smaller fatigue damage at the primary frequency compared to that of Models B and C for which the cross-flow vibration is dominated by the fourth mode. The significant contributions from higher harmonics make the maximum of the total fatigue damage predicted by Model A comparable to that by Models B and C. In the in-line direction, Model A predicts the highest fatigue damage at the primary frequency, and Model C predicts the least damage. Regarding the total fatigue damage, the significant higher harmonics make the magnitude of total fatigue damage predicted by Model A one order higher than that predicted by Models B and C. At flow velocity $V = 1.5$ m/s, the general trend of differences among the predictions of the three models is similar to those at $V = 0.5$ m/s; therefore, this trend is not discussed in detail here. However, it must be noted that at $V = 1.5$ m/s, the differences between the total fatigue damage and its components at the primary frequency seem to be more significant than at $V = 0.5$ m/s. According to Dahl (2008), the higher harmonic components in the fluid forces are associated with certain favourable motion trajectories. Therefore, the higher harmonics are naturally expected to be stronger in a travelling wave response, as it allows for these favourable motion trajectories to persist over substantial lengths of the riser (Vandiver et al., 2009). Recall that at $V = 1.5$ m/s, the structural response in the cross-flow

Figure 6.30: Predicted fatigue damage rate due to (a,c,e) cross-flow and (b,d,f) in-line deflections at uniform flow $V = 0.5$ m/s for (a,b) Model A, (c,d) Model B and (e,f) Model C. Black solid lines represent the total fatigue damage and grey solid lines represent the fatigue damage estimated from the strain signal after the higher harmonics are removed.

direction is dominated by travelling waves, while that at $V = 0.5$ m/s is standing wave dominated. This may imply that the relation between the higher harmonics and motion trajectories are well captured by Model A. However, more studies are needed to confirm this.

The fatigue damage estimated for the sheared flow cases are presented in Fig.6.32 and Fig.6.33. Similar to the uniform flow cases, both Model B and Model C predict that fatigue damage mainly occurs at the primary frequency. For Model A, although the total fatigue damage is observed to be different from its component at the primary frequency, the difference between the two is much less significant than in the uniform flow cases. This implies that the contribution of higher harmonics in the sheared flow cases may not be as high as those in the uniform flow. Nevertheless, in sheared flow cases, Model A still predicts the highest level of fatigue damage among the three in both cross-flow and in-line directions. While the fatigue damage due to the cross-flow vibrations is approximately the same according to Models B and C, the fatigue caused by in-line vibration for Model C is one order of magnitude smaller than in Model B.
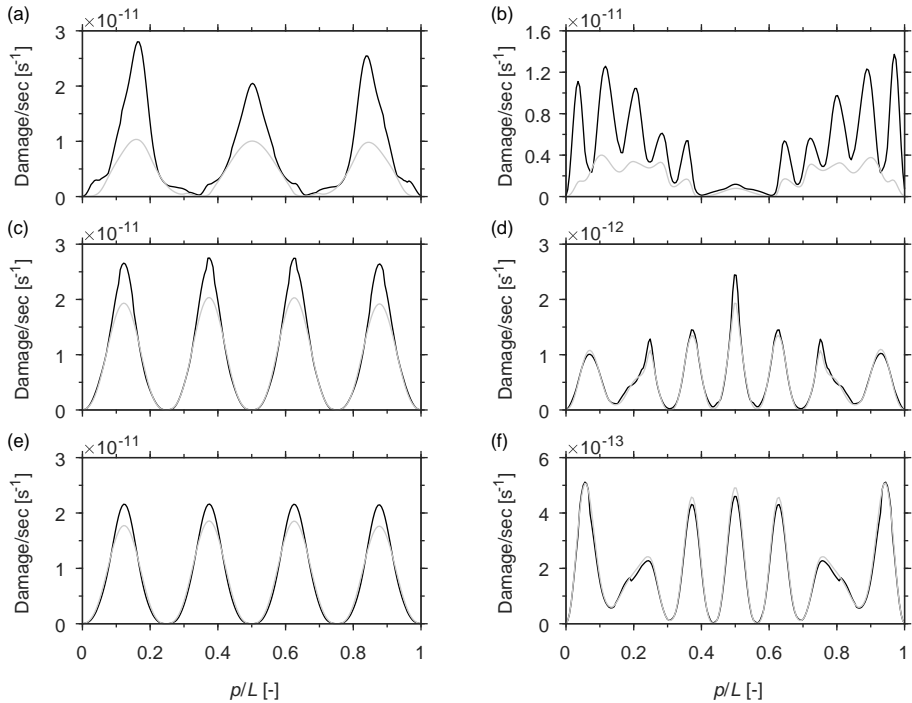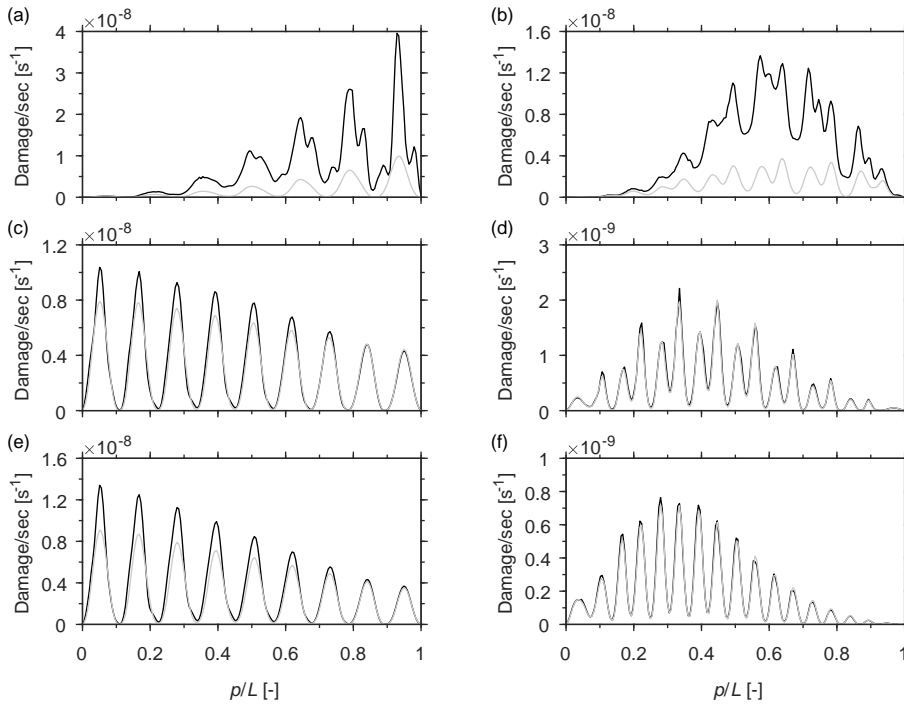
Figure 6.31: Predicted fatigue damage rate due to (a,c,e) cross-flow and (b,d,f) in-line deflections at uniform flow $V = 1.5$ m/s for (a,b) Model A, (c,d) Model B and (e,f) Model C. Black solid lines represent the total fatigue damage and grey solid lines represent the fatigue damage estimated from the strain signal after the higher harmonics are removed.

6
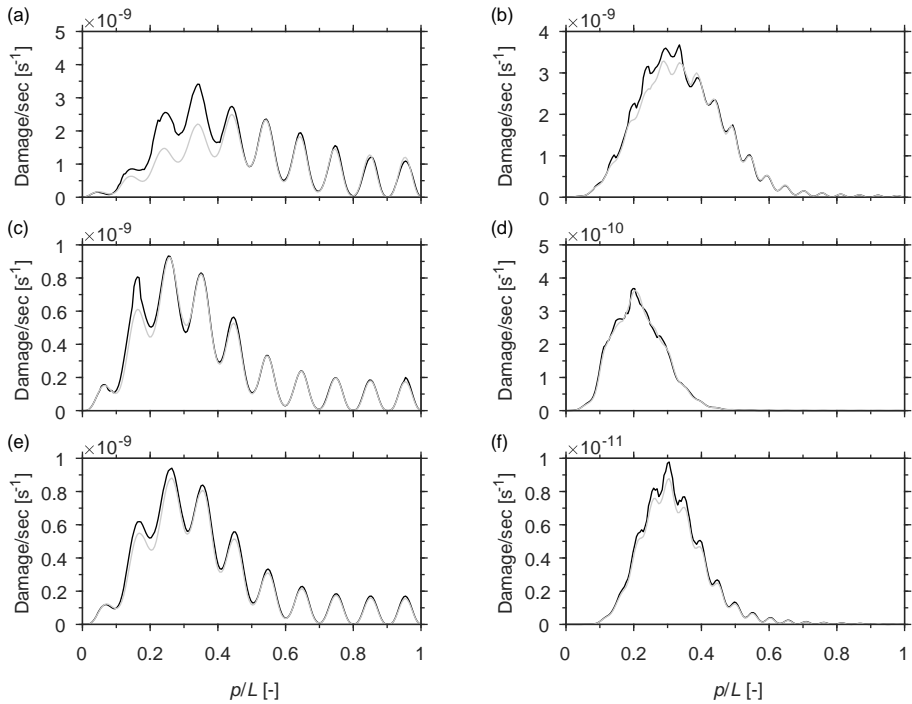
Figure 6.32: Predicted fatigue damage rate due to (a,c,e) cross-flow and (b,d,f) in-line deflections for sheared flow with maximum velocity $V = 1.5$ m/s for (a,b) Model A, (c,d) Model B and (e,f) Model C. Black solid lines represent the total fatigue damage and grey solid lines represent the fatigue damage estimated from the strain signal after the higher harmonics are removed.

Figure 6.33: Predicted fatigue damage rate due to (a,c,e) cross-flow and (b,d,f) in-line deflections for sheared flow with maximum velocity $V = 2.5$ m/s for (a,b) Model A, (c,d) Model B and (e,f) Model C. Black solid lines represent the total fatigue damage and grey solid lines represent the fatigue damage estimated from the strain signal after the higher harmonics are removed.
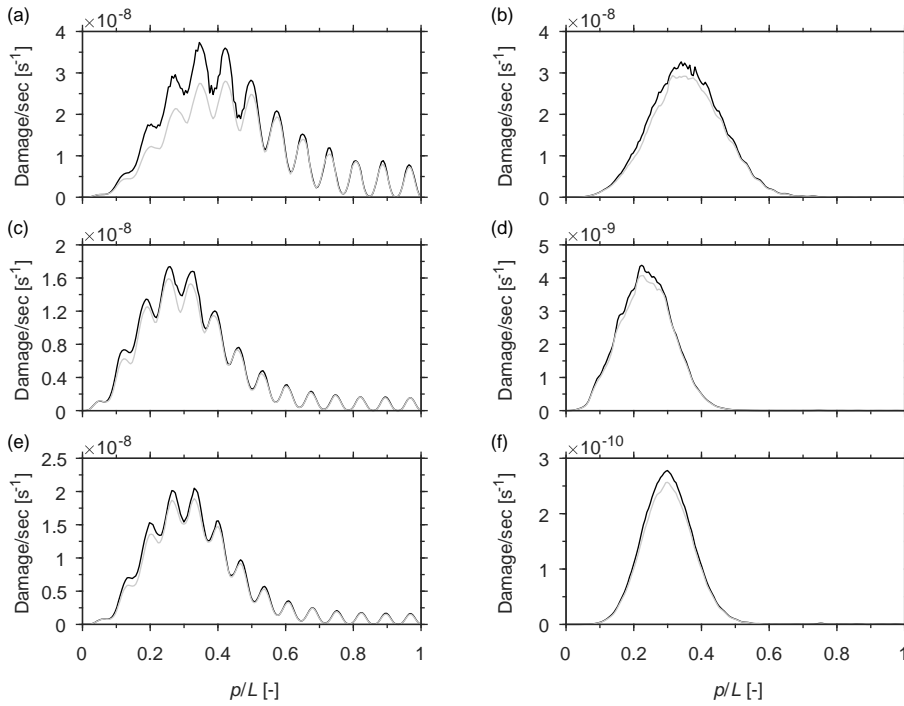
6.7. CONCLUSIONS

In this chapter, three different wake oscillator models are used for simulations of the VIV of flexible cylinders subjected to both uniform and linearly sheared flows. The three models differ from each other with respect to the inclusion of the in-line coupling term in the wake oscillator equation and the in-line fluctuating force that is coupled to the lift force. Model A is the most complete model, and Model B excludes the in-line coupling term, while Model C excludes both and is the same as the original one proposed by Ogink and Metrikine (2010).

In the cases of uniform flow, Models B and C predict similar structural responses, except that the amplitude of in-line vibration predicted by Model C is much smaller than that by Model B. Model A, on the other hand, predicted that the structure would vibrate in a different pattern. Especially at higher flow velocities, according to Models B and C, the structural response in the cross-flow direction is dominated by a standing wave that, according to Model A, has a tendency to vibrate in the form of a travelling wave. Apart from the different response patterns, Model A was found to predict the highest magnitude of both cross-flow and in-line vibrations among the three models.

For sheared flow cases, no obvious difference was observed regarding the response pattern. All three models predicted the structural response to be dominated by the travelling wave that propagates from a high-velocity to a low-velocity region. Similar to the uniform flow cases, Model A predicted the most significant structural response in both cross-flow and in-line directions.

To further investigate the fundamental mechanism that leads to the differences in the predictions by the three models, the hydrodynamic forces and energy transfer between the fluid and structure have been investigated. It has been demonstrated that, compared to Models B and C, Model A predicted the highest level of drag amplification. It also predicted larger fluctuating in-line and cross-flow forces. The energy transfer between the fluid and structure was analysed based on the fluid force that is in phase with the velocity of the structural motion. For sheared flow cases, it was found that for all three models, the energy transfer between the fluid and structure mainly depends on the reduced velocity. Model A predicted that the power-in region would correspond to a wider range of reduced velocities compared to Models B and C. For the uniform flow, it has been revealed that for Models B and C, the direction of the energy flow between the fluid and structure is primarily dependent on the amplitude of the cross-flow vibration. In principal, for Models B and C, a positive energy transfer was identified at locations corresponding to small cross-flow vibrations, while a negative energy transfer occurred when the cross-flow vibration exceeded certain values. In contrast, for Model A, no concrete relations were observed between the energy transfer and the cross-flow motion. The large cross-flow motion does not necessarily correspond to the negative energy transfer, according to Model A; this is consistent with the experimental observations. By further comparing the energy transfer with the phase difference between the cross-flow and in-line motions, a trend was found for Model A: the positive energy transfer was mostly associated with the counter-clockwise motion trajectory. The dependence of the energy transfer on both the amplitude of structural motion and its trajectory reflects the superiority of Model A over the other two models as a result of an improvement to in-line coupling.

Finally, the fatigue damage predicted by the three models has been investigated. It has been demonstrated that in the cases of uniform flow, Model A predicted highly significant contributions to the fatigue from higher harmonics, which resulted in a much higher rate of fatigue damage compared to the rates predicted by Models B and C. In the cases of sheared flow, although Model A's predicted fatigue that is caused by higher harmonics was not as significant as that in the uniform flow cases, Model A still predicted the highest level of fatigue damage among the three. This finding suggests that for a VIV model that does not consider the effect of coupling of cross-flow and in-line motions on the wake dynamics, the fatigue damage can be significantly underestimated, and the results therefore need to be taken carefully.

6

7

CONCLUSION

Vortex-induced vibration (VIV) is a well-known phenomenon for civil and offshore structures. The effects of such vibrations, such as fatigue damage and collision between adjacent structures, make the accurate prediction of vibrations important for the design of a structure. Due to the intrinsic complexity of the problem and the inadequate understanding of the underlying mechanism, the engineering prediction models of VIV currently mainly rely on the force-decomposition method. However, the fundamental assumption of this method, namely applying hydrodynamic forces measured on harmonically oscillating rigid cylinders to the prediction of the VIV of flexible cylinders that normally contain several frequency components, has restricted the applicability of the method to limited cases. Moreover, if one wished to extend the force-decomposition method for the modelling of coupled cross-flow and in-line VIV, then a hydrodynamic force database that includes both the cross-flow and in-line motions is required. Building such a database is a serious challenge, since many governing parameters are involved. The aforementioned limitations make the force-decomposition method less prospective for further development. Therefore, alternative models are needed to meet increasing demands for the more accurate prediction of VIV under more complicated conditions. The wake oscillator model overcomes the main limitations of the force-decomposition method to some extent, and it is one of the promising models that has gained popularity in recent years.

Although the concept of the wake oscillator was first proposed over half a century ago and has been developed much since then, the existing wake oscillator models still have some limitations, which have restricted their applications. One of the main limitations of the current wake oscillator models is that they cannot reproduce the hydrodynamic forces measured in the forced vibration experiments. This, in the author's opinion, is the reason for the wake oscillator model to be less preferable to the industry than the force-decomposition method, as the latter directly applies the measured, in the forced vibration experiments, hydrodynamic force in the prediction of VIV. Another main limitation of the existing wake oscillator models is that they cannot predict the coupled cross-flow and in-line VIV properly. The common approach of introducing a second wake oscillator

equation that is coupled solely to the in-line motion for the description of the fluctuating drag force is physically not rigorous, as the lift and drag forces have the same origin and are interdependent. The inadequacy of the wake oscillator models in existence is emphasised by the fact that none of them is able to capture the distinct characteristic of coupled cross-flow and in-line VIV, namely the appearance of the super-upper branch as the mass ratio of the system decreases, without changing the empirical and tuning parameters.

The main objective of this work is to improve the wake oscillator model for the better prediction of VIV. Attempts have been made in this thesis to improve the wake oscillator model in two aspects: (a) to reproduce the free and forced cross-flow vibration experiments and (b) to develop a single wake oscillator equation that is coupled to both the cross-flow and in-line motions for the prediction of coupled cross-flow and in-line VIV. To this end, the existing wake oscillator model proposed by Ogink and Metrikine (2010) has been reviewed, and the influence of the drag force model has been investigated (Chapter 2). Nonlinear coupling terms have been introduced to better reproduce the forced cross-flow vibration experiments (Chapter 3). A wake oscillator model that is coupled to both cross-flow and in-line motions has been developed and validated against free vibration experiments related to the coupled cross-flow and in-line VIV of an elastically supported rigid cylinder (Chapter 4). The new wake oscillator model has been applied in the simulation of the VIV of flexible cylinders, and the importance of the in-line coupling has been highlighted in comparison to the simulation results with the model without in-line coupling (Chapters 5 and 6). In this last chapter, the most important conclusions of this work are summarised.

A review of the wake oscillator model proposed by Ogink and Metrikine (2010) in Chapter 2 has emphasised the fact that the reproduction of the forced vibration measurements requires the appropriate modelling of both lift (a force that is perpendicular to the relative flow velocity) and drag (a force that is parallel to the relative flow velocity) forces. A deficient drag force model may make it difficult, if not impossible, to formulate the lift force, as the lift needs to compensate for the errors introduced by the drag force. Three main discussable assumptions regarding the drag force model in Ogink and Metrikine (2010) have been identified, namely making a quasi-steady assumption, ignoring the oscillatory components and neglecting the inertia force in the direction of the drag force. With regard to the first two assumptions, the characteristics of the dynamics of the oscillatory lift force—at the frequency of cylinder oscillation—that satisfy the forced vibration experimental measurements are analysed based on three different drag force models. The first model is the one proposed by Ogink and Metrikine (2010); it assumes that the instantaneous drag force coefficient is constant and keeps the mean steady value measured on the fixed cylinder. In the second model, the instantaneous drag force coefficient is still assumed to be constant; however, its value varies as the frequency or amplitude of cylinder motion changes. In the third model, in addition to the constant drag force, an oscillatory part coupled with the lift force is introduced, and the coupling relation keeps the same form as that identified from a fixed cylinder. It has been demonstrated that the oscillatory lift forces determined from the three drag force models are similar, which suggests that the first drag force model is at least not more deficient than the other two. The characteristic of the dynamics of the identified lift force

7

exhibits an obvious resonance pattern at small amplitudes of cylinder oscillation, while it is contradictory to the resonance pattern at large amplitudes. The contradiction may be a result of neglecting the inertia force in the direction of the drag force or simply due to the nonlinearity.

As discussed in Chapter 2, since the drag force models do not have a significant influence on the reproduction of the forced vibration experiments, the first drag force model is applied in Chapter 3, and the possibility of improving the reproduction of the forced vibration experiments by introducing extra nonlinearity in the wake oscillator equation is investigated. The nonlinearity has been introduced through the coupling between the wake oscillator equation and the cylinder motion. As a preliminary test, a set of nonlinear coupling terms in the form of multiplications of displacement, velocity and acceleration of the cylinder have been introduced. The model with constant coupling coefficients has been shown to be able to quantitatively reproduce the added damping measured in the forced vibration experiments over most of the range of frequencies and amplitudes that are of interest; however, that model fails to capture the negative added mass. The importance of the negative added mass has been reflected in the simulation of free vibration experiments where the model was shown to underestimate the lock-in range as well as the frequency of the cylinder oscillation for the system with a small mass ratio. To overcome this discrepancy, the model has been further enhanced by making the nonlinear coupling coefficient frequency-dependent; this is achieved in the time domain by means of convolution integrals. A single set of frequency-dependent complex-valued functions, which are the Laplace transforms of corresponding convolution kernels, that reproduces the forced vibration experiments fairly well at different amplitudes of vibration has been identified over a limited frequency range. Finding such a set of frequency-dependent complex-valued functions has been shown to be impossible for linear coupling (Ogink and Metrikine, 2010). However, the author failed to extend these functional dependencies to the infinite frequency domain that corresponds to a causal decaying signal in the time domain using a complex curve fitting method. The underlying reason is not clear yet and requires further study.

In Chapter 4, a wake oscillator model that is coupled to both cross-flow and in-line motions has been proposed. In addition to conventional coupling to the acceleration of the cross-flow motion, coupling with the in-line motion has been introduced in the form of $\ddot{x}q$. This in-line coupling term is inspired by the experimental observation as well as the heuristic inference from the dynamics of a rigid pendulum. An instability study has revealed that the term $\ddot{x}q$ results in an unbounded unstable region when subjected to a pure in-line forced vibration which is against experimental observation. Therefore, instead of $\ddot{x}q$, a more sophisticated in-line coupling term $\frac{\ddot{x}}{1+\ddot{x}^2}q$, which has the same qualitative dynamic effect, has been adopted. The new in-line coupling term has been shown to be able to constrain the unstable region to the same frequency range of cylinder oscillation as that observed in the experiments. The new wake oscillator model has been used to simulate two free vibration experiments of elastically supported rigid cylinders and shown to be able to capture the lock-in corresponding to the in-line vibration around $V_n = 2.5$ in addition to the conventional lock-in at $V_n = 5$. Most importantly, the new model has been shown to be able to predict the appearance of the super-upper branch as the mass ratio decreases without changing any tuning parameters. The suc-

cessful reproduction of this distinct characteristic of the coupled cross-flow and in-line VIV indicates the superiority of the new model over others. The influence of the mass and damping ratio on the peak amplitude of the coupled cross-flow and in-line VIV of elastically supported rigid cylinders has also been analysed based on the new model, and the results are in good agreement with the experimental data.

Chapter 5 deals with the application of the new wake oscillator model presented in Chapter 4 to the modelling of the coupled cross-flow and in-line VIV of flexible cylinders. The cylinder is modelled as an extensible nonlinear Euler-Bernoulli beam, and the wake oscillators are uniformly attached to it. The finite element method has been applied to solve the dynamics of the coupled system, and the experiments of the VIV of a top-tensioned straight riser subjected to the step flow have been taken for the validation of the model. The model has been shown to be able to capture most features of the VIV of flexible cylinders, and good agreement between the simulation results and the experimental measurements has been observed with regard to both cross-flow and in-line vibration amplitude, frequency and excited mode, as well as the mean in-line deflection due to the amplified in-line force. While it is conventionally expected that the VIV of flexible cylinders subjected to a uniform flow is dominated by a single frequency, a multi-frequency response has been observed in the simulation results over the range of flow velocities through which the transition of the dominant mode of vibration occurs. In such cases, the multiple frequency components in the cross-flow response instantaneously coexist, while those of the in-line response are the result of a single frequency that drifts from one predominant frequency to another. When the multi-frequency response takes place, the in-line response contains significant components at low frequencies, caused by the slow variation of the in-line force due to the modulation of the cross-flow displacements.

To illustrate the importance of in-line coupling and its influence on the prediction of VIV, the simulation results of the coupled cross-flow and in-line VIV of flexible cylinders subjected to both uniform and linearly sheared flows – obtained with three different models – have been studied in Chapter 6. The three models differ from each other with respect to the inclusion of the in-line coupling term in the wake oscillator equation and the in-line fluctuating force that is coupled to the lift force. Model A is the most complete model (Chapter 5), and Model B excludes the in-line coupling term, while Model C excludes both and is the same as the original one proposed by Ogink and Metrikine (2010). It has been shown that in the cases of uniform flow, Models B and C predict similar structural responses, while Model A predicts a different response pattern. Especially at a high flow velocity, according to Models B and C, the structural response in the cross-flow direction is dominated by a standing wave that, according to Model A, is travelling-wave-predominant. For the sheared flow, all three models predict the structural response to be dominated by a travelling wave that is oriented from a high-velocity to a low-velocity region. For both uniform and sheared flow cases, Model A predicts the highest response amplitude in both cross-flow and in-line directions among the three models.

For the uniform flow cases, it has been shown that the energy transfer between the fluid and structure according to Models B and C is primarily determined by the amplitude of cross-flow vibration. In principal, for Models B and C, a positive energy transfer

has been identified at locations corresponding to small cross-flow vibrations, while a negative energy transfer occurs when the amplitude of cross-flow vibration exceeds certain values. Such a dependency is not observed in the results of Model A. Instead, it seems that for Model A, the positive energy transfer is mostly associated with a counter-clockwise motion trajectory. For the sheared flow cases, the energy transfer is found to mainly depend on the reduced velocity, and Model A predicts the power-in region corresponding to a wider range of reduced velocities compared to Models B and C.

The fatigue damage predicted by the three models has also been studied. It has been shown that in the cases of uniform flow, Model A predicts significant contributions to the fatigue damage from higher harmonics, which results in a much higher rate of fatigue damage compared to the rates predicted by Models B and C. The contributions from higher harmonics are less significant for the sheared flow; nevertheless, model A still predicts the highest rate of fatigue damage among the three models.

To conclude, one can say that the new wake oscillator model presented in this thesis outperforms the existing wake oscillator models. The main superior aspects of the proposed model are its ability to predict the super-upper branch and its physical consistency with the fact that the hydrodynamic forcing in both in-line and cross-flow directions is a result of one and the same fluid motion, which is described in the model by a single oscillator equation.

7

REFERENCES

Aguirre Romano, J. E. (1978). *Flow-induced, in-line vibrations of a circular cylinder*. PhD thesis, Imperial College London.

Aronsen, K. H. (2007). *An Experimental Investigation of In-line and Combined In-line and Cross-flow Vortex Induced Vibrations*. PhD thesis, NTNU.

Bai, X. and Qin, W. (2014). Using vortex strength wake oscillator in modelling of vortex induced vibrations in two degrees of freedom. *European Journal of Mechanics - B/Fluids*, 48(Supplement C):165–173.

Birkhoff, G. (1953). Formation of vortex streets. *Journal of Applied Physics*, 24(1):98–103.

Bishop, R. E. D. and Hassan, A. Y. (1964). The lift and drag forces on a circular cylinder oscillating in a flowing fluid. *Proceedings of the Royal Society of London A: Mathematical, Physical and Engineering Sciences*, 277(1368):51–75.

Bittanti, S. and Colaneri, P. (2009). Floquet theory and stability. In *Periodic Systems: Filtering and Control*, pages 81–108. Springer London, London.

Bourguet, R., Karniadakis, G. E., and Triantafyllou, M. S. (2011). Vortex-induced vibrations of a long flexible cylinder in shear flow. *Journal of Fluid Mechanics*, 677:342–382.

Bourguet, R. and Triantafyllou, M. S. (2015). Vortex-induced vibrations of a flexible cylinder at large inclination angle. *Philos Trans A Math Phys Eng Sci*, 373(2033):20140108.

Carberry, J., Govardhan, R., Sheridan, J., Rockwell, D., and Williamson, C. (2004). Wake states and response branches of forced and freely oscillating cylinders. *European Journal of Mechanics - B/Fluids*, 23(1):89–97. Bluff Body Wakes and Vortex-Induced Vibrations.

Chaplin, J., Bearman, P., Huarte, F. H., and Pattenden, R. (2005). Laboratory measurements of vortex-induced vibrations of a vertical tension riser in a stepped current. *Journal of Fluids and Structures*, 21(1):3–24. Fluid-Structure and Flow-Acoustic Interactions involving Bluff Bodies.

Coleman, T. and Li, Y. (1996). An interior trust region approach for nonlinear minimization subject to bounds. *SIAM Journal on Optimization*, 6(2):418–445.

Coleman, T. F. and Li, Y. (1994). On the convergence of interior-reflective newton methods for nonlinear minimization subject to bounds. *Mathematical Programming*, 67(1):189–224.

Dahl, J., Hover, F., and Triantafyllou, M. (2006). Two-degree-of-freedom vortex-induced vibrations using a force assisted apparatus. *Journal of Fluids and Structures*, 22(6):807–818. Bluff Body Wakes and Vortex-Induced Vibrations (BBVIV-4).

Dahl, J. M. (2008). *Vortex-induced vibration of a circular cylinder with combined in-line and cross-flow motion.* PhD thesis, Massachusetts Institute of Technology.

Dahl, J. M., Hover, F. S., Triantafyllou, M. S., Dong, S., and Karniadakis, G. E. (2007). Resonant vibrations of bluff bodies cause multivortex shedding and high frequency forces. *Physical review letters*, 99(14):144503.

de Langre, E. (2006). Frequency lock-in is caused by coupled-mode flutter. *Journal of Fluids and Structures*, 22(6):783–791. Bluff Body Wakes and Vortex-Induced Vibrations (BBVIV-4).

Deschrijver, D., Mrozowski, M., Dhaene, T., and De Zutter, D. (2008). Macromodeling of multiport systems using a fast implementation of the vector fitting method. *IEEE Microwave and Wireless Components Letters*, 18(6):383–385.

Elmore, W. C. and Heald, M. A. (1989). *Physics of Waves.* Dover Publications, New York.

Facchinetti, M., de Langre, E., and Biolley, F. (2004). Coupling of structure and wake oscillators in vortex-induced vibrations. *Journal of Fluids and Structures*, 19:123–140.

Gabbai, R. and Benaroya, H. (2005). An overview of modeling and experiments of vortex-induced vibration of circular cylinders. *Journal of Sound and Vibration*, 282(3):575–616.

Gabbai, R. and Benaroya, H. (2008). A first-principles derivation procedure for wake-body models in vortex-induced vibration: Proof-of-concept. *Journal of Sound and Vibration*, 312(1):19–38.

Ge, F., Long, X., Wang, L., and Hong, Y. (2009). Flow-induced vibrations of long circular cylinders modeled by coupled nonlinear oscillators. *Science in China Series G: Physics, Mechanics and Astronomy*, 52(7):1086–1093.

Gerstmayr, J. and Irschik, H. (2008). On the correct representation of bending and axial deformation in the absolute nodal coordinate formulation with an elastic line approach. *Journal of Sound and Vibration*, 318(3):461–487.

Gerstmayr, J. and Shabana, A. A. (2006). Analysis of thin beams and cables using the absolute nodal co-ordinate formulation. *Nonlinear Dynamics*, 45(1):109–130.

Gopalkrishnan, R. (1993). *Vortex-induced forces on oscillating bluff cylinders.* PhD thesis, Woods Hole Oceanographic Inst., MA.

Govardhan, R. N. and Williamson, C. H. K. (2006). Defining the 'modified Griffin plot' in vortex-induced vibration: revealing the effect of reynolds number using controlled damping. *Journal of Fluid Mechanics*, 561:147–180.

Géradin, M. and Cardona, A. (2001). *Flexible Multibody Dynamics: A Finite Element Approach*. Wiley, New York.

Gustavsen, B. (2006). Improving the pole relocating properties of vector fitting. *IEEE Transactions on Power Delivery*, 21(3):1587–1592.

Gustavsen, B. and Semlyen, A. (1999). Rational approximation of frequency domain responses by vector fitting. *IEEE Transactions on Power Delivery*, 14(3):1052–1061.

Hartlen, R. and Currie, I. (1970). *Lift-Oscillator of Vortex-Induced Vibration*, (EM5):577–591. cited By 1.

Holmes, S., Oakley, J. O. H., and Constantinides, Y. (2006). Simulation of riser viv using fully three dimensional cfd simulations.

Hover, F., Techet, A., and Triantafyllou, M. (1998). Forces on oscillating uniform and tapered cylinders in cross flow. *Journal of Fluid Mechanics*, 363:97–114.

Huang, K., Chen, H.-C., and Chen, C.-R. (2010). Vertical riser viv simulation in uniform current. *Journal of Offshore Mechanics and Arctic Engineering*, 132(3):031101–031101–10.

Huarte, F. (2006). *Multi-mode vortex induced vibration of a flexible circular cylinder*. PhD thesis, Imperial College London.

Iwan, W. and Blevins, R. (1974). A Model for Vortex Induced Oscillation of Structures. *Journal of Applied Mechanics*, 41:581.

Jain, A. and Modarres-Sadeghi, Y. (2013). Vortex-induced vibrations of a flexibly-mounted inclined cylinder. *Journal of Fluids and Structures*, 43:28–40.

Jauvtis, N. and Williamson, C. H. K. (2004). The effect of two degrees of freedom on vortex-induced vibration at low mass and damping. *Journal of Fluid Mechanics*, 509:23–62.

Kallias Ntroumpis, D. F. (2017). VIV analysis of a subsea power cable during installation in high current seas. Master's thesis, Delft University of Technology, the Netherlands.

Khalak, A. and Williamson, C. (1999). Motions, forces and mode transitions in vortex-induced vibrations at low mass-damping. *Journal of Fluids and Structures*, 13(7):813–851.

Kim, W.-J. and Perkins, N. (2002). Two-dimensional vortex-induced vibration of cable suspensions. *Journal of Fluids and Structures*, 16(2):229–245.

Klamo, J. T. (2007). *Effects of damping and Reynolds number on vortex-induced vibrations*. PhD thesis, California Institute of Technology.

Konstantinidis, E. (2014). On the response and wake modes of a cylinder undergoing streamwise vortex-induced vibration. *Journal of Fluids and Structures*, 45:256–262.

7

Kovacic, I., Rand, R., and Mohamed Sah, S. (2018). Mathieu's equation and its general-izations: Overview of stability charts and their features. *Applied Mechanics Reviews*, 70(2):020802.

Landl, R. (1975). A mathematical model for vortex-excited vibrations of bluff bodies. *Journal of Sound and Vibration*, 42(2):219–234.

Lie, H., Braaten, Henningand Jhingran, V. G., Sequeiros, O. E., and Vandiver, K. (2012). Comprehensive riser viv model tests in uniform and sheared flow. Number 44922, pages 923–930.

Lucor, D. and Karniadakis, G. E. (2003). Effects of oblique inflow in vortex-induced vi-brations. *Flow, Turbulence and Combustion*, 71(1):375–389.

Marzouk, O., Nayfeh, A. H., Akhtar, I., and Arafat, H. N. (2007). Modeling steady-state and transient forces on a cylinder. *Journal of Vibration and Control*, 13(7):1065–1091.

Mina, A. (2013). Modeling the vortex-induced vibrations of a multi-span free standing riser. Master's thesis, Delft University of Technology, the Netherlands.

Moe, G. and Wu, Z.-J. (1990). The lift force on a cylinder vibrating in a current. *Journal of Offshore Mechanics and Arctic Engineering*, 112(4):297–303.

Morse, T. and Williamson, C. (2009). Fluid forcing, wake modes, and transitions for a cylinder undergoing controlled oscillations. *Journal of Fluids and Structures*, 25(4):697–712. Bluff Body Wakes and Vortex-Induced Vibrations (BBVIV-5).

Mottaghi, S. and Benaroya, H. (2016). Reduced-order modeling of fluid–structure inter-action and vortex-induced vibration systems using an extension of jourdain's princi-ple. *Journal of Sound and Vibration*, 382:193–212.

Mukundan, H. (2008). *Vortex-induced Vibration of Marine Risers: Motion and Force Re-construction from Field and Experimental Data*. PhD thesis.

Nakamura, A., Okajma, A., and Kosugi, T. (2001). Experiments on flow-induced in-line oscillation of a circular cylinder in a water tunnel. *JSME International Journal Series B Fluids and Thermal Engineering*, 44(4):705–711.

Nayfeh, A., Owis, F., and Hajj, M. (2003). FOCUS: A model for the coupled lift and drag on a circular cylinder. In *ASME International Design Engineering Technical Conferences, Computers and Information in Engineering Conference*, pages 1289–1296.

Nishi, Y., Kokubun, K., Hoshino, K., and Uto, S. (2008). Quasisteady theory for the hydro-dynamic forces on a circular cylinder undergoing vortex-induced vibration. *Journal of Marine Science and Technology*, 14(3):285–295.

Nishihara, T., Kaneko, S., and Watanabe, T. (2005). Characteristics of fluid dynamic forces acting on a circular cylinder oscillated in the streamwise direction and its wake pat-terns. *Journal of Fluids and Structures*, 20(4):505–518. Bluff-Body/Flow Interactions.

Norbegr, C. (2001). Flow around a circular cylinder: Aspects of fluctuating lift. *Journal of Fluids and Structures*, 15(3):459–469.

Ogink, R. and Metrikine, A. (2010). A wake oscillator with frequency dependent coupling for the modeling of vortex-induced vibration. *Journal of Sound and Vibration*, 329:5452–5473.

O'Neill, B. (2006). *Elementary Differential Geometry*. Academic Press, Boston, revised second edition edition.

Postnikov, A., Pavlovskaia, E., and Wiercigroch, M. (2017). 2DOF CFD calibrated wake oscillator model to investigate vortex-induced vibrations. *International Journal of Mechanical Sciences*, 127(Supplement C):176–190. Special Issue from International Conference on Engineering Vibration - ICoEV 2015.

Qin, L. (2004). *Development of Reduced-Order Models for Lift and Drag on Oscillating Cylinders with Higher-Order Spectral Moments*. PhD thesis, Virginia Polytechnic Institute and State University.

Ramberg, S. E. (1983). The effects of yaw and finite length upon the vortex wakes of stationary and vibrating circular cylinders. *Journal of Fluid Mechanics*, 128:81–107.

Sarpkaya, T. (1977). In-line and transverse forces on cylinders in oscillatory flow at high reynolds numbers. *Journal of Ship Research*, 21(4):200–216.

Sarpkaya, T. (1978). Fluid forces on oscillating cylinders. *NASA STI/Recon Technical Report A*, 78:275–290.

Sarpkaya, T. (2004). A critical review of the intrinsic nature of vortex-induced vibrations. *Journal of Fluids and Structures*, 19(4):389–447.

Schulz, K. W. and Meling, T. S. (2004). FOCUS: Multi-strip numerical analysis for flexible riser response. In *23rd International Conference on Offshore Mechanics and Arctic Engineering*, pages 379–384.

Seyed-Aghazadeh, B. and Modarres-Sadeghi, Y. (2016). Reconstructing the vortex-induced-vibration response of flexible cylinders using limited localized measurement points. *Journal of Fluids and Structures*, 65:433–446.

Skop, R. and Balasubramanian, S. (1997). A new twist on an old model for vortex-excited vibrations. *Journal of Fluids and Structures*, 11(4):395–412.

Skop, R. and Griffin, O. (1973). A model for the vortex-excited resonant response of bluff cylinders. *Journal of Sound and Vibration*, 27(2):225–233.

Song, L., Fu, S., Zeng, Y., and Chen, Y. (2016). Hydrodynamic forces and coefficients on flexible risers undergoing vortex-induced vibrations in uniform flow. *Journal of Waterway, Port, Coastal, and Ocean Engineering*, 142(4):04016001.

7

Srinil, N. and Zanganeh, H. (2012). Modelling of coupled cross-flow/in-line vortex-induced vibrations using double duffing and van der pol oscillators. *Ocean Engineering*, 53(Supplement C):83–97.

Sumer, B. M. and Fredsøe, J. (2006). *Hydrodynamics Around Cylindrical Structures.* WORLD SCIENTIFIC, revised edition.

Thorsen, M., Sævik, S., and Larsen, C. (2014). A simplified method for time domain simulation of cross-flow vortex-induced vibrations. *Journal of Fluids and Structures*, 49:135–148.

Thorsen, M., Sævik, S., and Larsen, C. (2015). Fatigue damage from time domain simulation of combined in-line and cross-flow vortex-induced vibrations. *Marine Structures*, 41:200–222.

Thorsen, M., Sævik, S., and Larsen, C. (2016). Time domain simulation of vortex-induced vibrations in stationary and oscillating flows. *Journal of Fluids and Structures*, 61:1–19.

Trim, A., Braaten, H., Lie, H., and Tognarelli, M. (2005). Experimental investigation of vortex-induced vibration of long marine risers. *Journal of Fluids and Structures*, 21(3):335–361. Marine and Aeronautical Fluid-Structure Interactions.

van der Burgh, A. H. P. (1999). Nonlinear dynamics of structures excited by flows. In Habault, D., editor, *Fluid-Structure Interactions in Acoustics*, chapter 6, pages 221–259. Springer-Verlag Wien GmbH.

van Dyke, M. (1982). *An Album of Fluid Motion.* The Parabolic Press, Stanford, California.

Vandiver, J. K., Jaiswal, V., and Jhingran, V. (2009). Insights on vortex-induced, traveling waves on long risers. *Journal of Fluids and Structures*, 25(4):641–653. Bluff Body Wakes and Vortex-Induced Vibrations (BBVIV-5).

Violette, R., de Langre, E., and Szydlowski, J. (2007). Computation of vortex-induced vibrations of long structures using a wake oscillator model: Comparison with dns and experiments. *Computers and Structures*, 85(11):1134–1141. Fourth MIT Conference on Computational Fluid and Solid Mechanics.

Willden, R. H. and Graham, J. R. (2004). Multi-modal vortex-induced vibrations of a vertical riser pipe subject to a uniform current profile. *European Journal of Mechanics - B/Fluids*, 23(1):209–218. Bluff Body Wakes and Vortex-Induced Vibrations.

Williamson, C. and Govardhan, R. (2004). Vortex-induced vibrations. *Annual Review of Fluid Mechanics*, 36(1):413–455.

Williamson, C. and Roshko, A. (1988). Vortex formation in the wake of an oscillating cylinder. *Journal of Fluids and Structures*, 2(4):355–381.

Xu, W.-H., Zeng, X.-H., and Wu, Y.-X. (2008). High aspect ratio (l/d) riser viv prediction using wake oscillator model. *Ocean Engineering*, 35(17):1769–1774.

7

Yamamoto, C., Meneghini, J., Saltara, F., Fregonesi, R., and Ferrari, J. (2004). Numerical simulations of vortex-induced vibration on flexible cylinders. *Journal of Fluids and Structures*, 19(4):467–489.

Zanganeh, H. and Srinil, N. (2016). Three-dimensional viv prediction model for a long flexible cylinder with axial dynamics and mean drag magnifications. *Journal of Fluids and Structures*, 66:127–146.

Zhao, M., Cheng, L., and Zhou, T. (2009). Direct numerical simulation of three-dimensional flow past a yawed circular cylinder of infinite length. *Journal of Fluids and Structures*, 25(5):831–847.

A

CAPTURING THE NEGATIVE ADDED MASS BY INTRODUCING AN EXTRA RESTORING FORCE

The added mass plays an important role in VIV, and the negative added mass observed in the forced vibration experiments is the main reason for the wider lock-in range and higher lock-in frequency for low mass ratio systems compared to high mass ratio systems. It has been shown in Section 3.2 that the added mass is well reproduced at a high frequency of cylinder oscillation, while it does not seem to be possible to capture the negative added mass at low frequencies of cylinder oscillation. It was found that at a low frequency of cylinder oscillation, even though the portion of the added mass contributed by the wake oscillator is negative, the addition of the potential added mass makes the total positive. It seems the assumption of the potential added mass coefficient C_a's constant value of 1 is only applicable at a high frequency of cylinder oscillation, while a smaller or even negative value should be taken when the cylinder oscillates at a low frequency. To achieve this goal, the cross-flow hydrodynamic force F_{AY} in Eq.(2.2) is reformulated as

$$F_{AY} = -m_{a0}\frac{d^2Y}{dt^2} - m_{a1}\omega_s^2 Y \tag{A.1}$$

in which the first term is still the inertia force and added mass $m_{a0} = C_{a0}\pi\rho LD^2/4$, while the second term is a restoring force and $m_{a1} = C_{a1}\pi\rho LD^2/4$. Physically, adding a restoring force in the formulation of a hydrodynamic force seems to be irrational, since for an immersed cylinder, the fluid forces acting on it should not be dependent on the displacement. However, this addition does improve the model's performance.

With the new definition of cross-flow inertia force F_{AY}, as given by Eq.(A.1), the
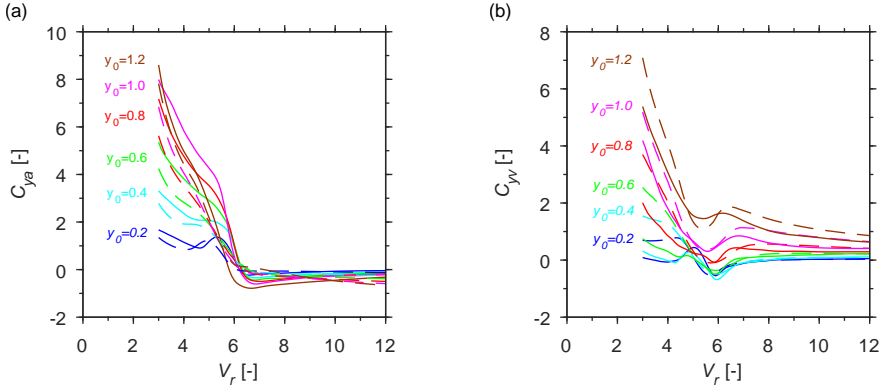
Figure A.1: A comparison of the nonlinear coupling wake oscillator model with the additional restoring force (dashed lines) and the forced vibration measurements (solid lines) for the force coefficient (a) in phase with acceleration C_{ya} and (b) in phase with velocity C_{yv}.

equivalent potential added mass coefficient of the system becomes

$$C_a = \frac{F_{AY}}{\frac{1}{4}\rho\pi LD^2\frac{d^2Y}{dt^2}} = C_{a0} - C_{a1}\omega_s^2\frac{Y}{\frac{d^2Y}{dt^2}}. \tag{A.2}$$

The dimensionless form of above equation is given as

$$C_a = C_{a0} + C_{a1}\frac{y}{\ddot{y}}. \tag{A.3}$$

By substituting $y = y_0\sin(\Omega\tau)$ into Eq. (A.3), one obtains

$$C_a = C_{a0} - \frac{C_{a1}}{\Omega^2}. \tag{A.4}$$

Eq.(A.4) demonstrates that the addition of the restoring force makes the added mass coefficient C_a frequency-dependent, and its value decreases with a decreasing frequency of cylinder oscillation. With $\Omega = 1/\text{St}/V_r$, Eq.(A.4) becomes

$$C_a = C_{a0} - C_{a1}\text{St}^2V_r^2. \tag{A.5}$$

 In still water, when the flow velocity V equals 0, the reduced velocity $V_r = 2\pi V/(\omega D) = 0$, and Eq.(A.5) should conform to the potential theory; therefore, the value for C_{a0} should be 1. Regarding the value of C_{a1}, here $C_{a1} = 0.4$ is used to capture the negative values of C_{ya} at high reduced velocities. The forced vibration simulation results of C_{ya} and C_{yv} with $C_{a0} = 1$ and $C_{a1} = 0.4$ are plotted in Fig.A.1 using the same tuning parameters as those given in Eq.(3.5). It can be seen that with this new term, the model captures the feature of negative values of C_{ya} at $V_c > 6$. According to the measurements, the values of C_{ya} decrease rapidly around $V_c = 6$ with increasing reduced velocity, reaching minimum negative values around $V_c = 7$ and then increasing gradually again, converging to a value slightly smaller than zero. However, the results from the model indicate no minimum
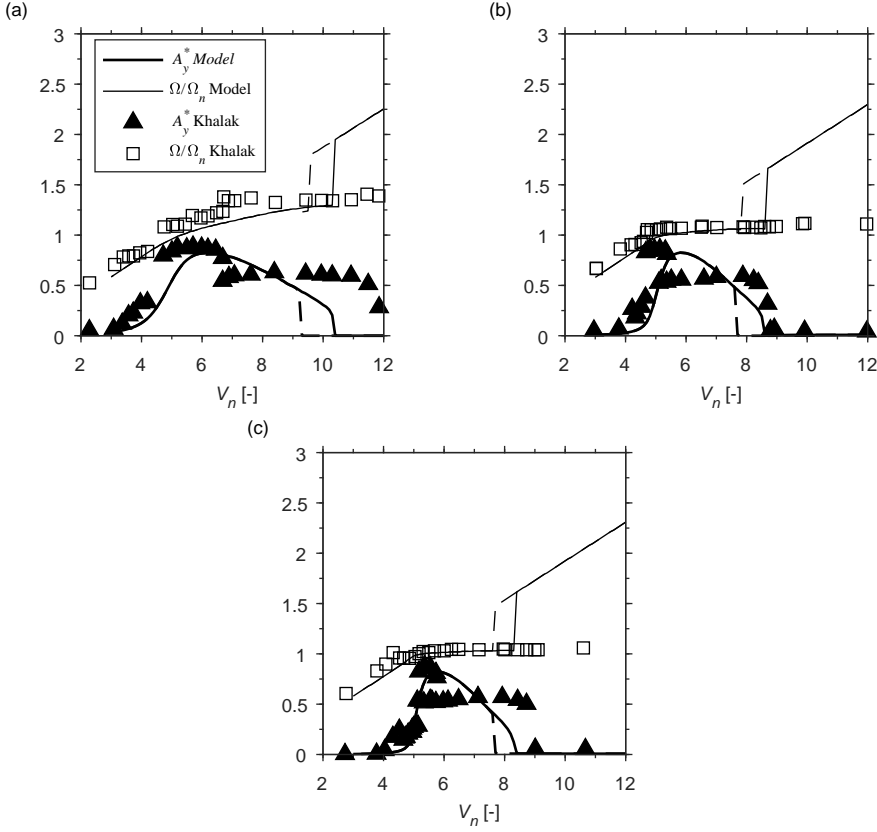
Figure A.2: A comparison of the nonlinear coupling wake oscillator model with the additional restoring force and the free vibration measurements for: (a) $m^* = 2.4, m^*\zeta = 0.014$; (b) $m^* = 10.3, m^*\zeta = 0.017$; (c) $m^* = 20.6$, $m^*\zeta = 0.019$.

value around $V_c = 7$, and the values keep decreasing, reaching values smaller than those observed in the measurements.

With the new added term in the inertia force, the non-dimensional form of the cylinder's equation of motion in Eq. (2.17) now becomes

$$\ddot{y} + 2\zeta\Omega_n\dot{y} + \Omega_n^2 y = \frac{1}{\pi(m^* + C_{a0})} \frac{1}{2\pi^3 \text{St}^2} C_{VY} - C_{a1}\frac{y}{(m^* + C_{a0})}. \tag{A.6}$$

Solving Eq. (A.6), (2.18) and (3.2), the free vibration with $m^* = 2.4$ is simulated, and results are shown in Fig.A.2

Form Fig.A.2 it can be seen that the free vibration of the system with a small mass ratio is properly modeled with respect to the value of frequency and range of lock-in.

B

SIMILARITY BETWEEN THE WAKE OSCILLATOR AND A RIGID PENDULUM

Consider a rigid pendulum with mass m_f that is attached to a foundation with mass m_s that is elastically supported in X and Y directions; see Fig.B.1. The governing equations for the small vibrations of the system can be derived using the Lagrangian formalism, and they are given as

$$\left(m_s + m_f\right)\frac{d^2 X}{d t^2} + k_s X = m_f L\left(\phi\frac{d^2\phi}{d t^2} + \left(\frac{d\phi}{d t}\right)^2\right) \tag{B.1}$$

$$\left(m_s + m_f\right)\frac{d^2 Y}{d t^2} + k_s Y = -m_f L\frac{d^2\phi}{d t^2} \tag{B.2}$$

$$m_f L^2\frac{d^2\phi}{d t^2} + m_f g L\phi - m_f L\frac{d^2 X}{d t^2}\phi = -m_f L\frac{d^2 Y}{d t^2}. \tag{B.3}$$

Using the following relationship:

$$\tau = t\omega_n, \quad \Omega = \frac{\omega_\phi}{\omega_n}, \quad x = \frac{X}{D}, \quad y = \frac{Y}{D} \tag{B.4}$$

where $\omega_n = \sqrt{k_s/\left(m_s + m_f\right)}$ and $\omega_\phi = \sqrt{g/L}$, the dimensionless form of the equations of the motion is obtained as

$$\ddot{x} + x = M\left(\ddot{\phi}\phi + \dot{\phi}^2\right) \tag{B.5}$$

$$\ddot{y} + y = -M\ddot{\phi} \tag{B.6}$$

$$\ddot{\phi} + \Omega^2\phi - \ddot{x}\phi = -\ddot{y} \tag{B.7}$$

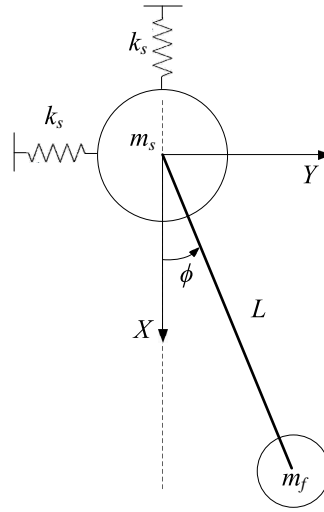where $M = \frac{m_f L}{(m_s + m_f)D}$.

Figure B.1: Pendulum with moving foundation

If only the motion of the foundation in the Y direction is considered, corresponding to the VIV that is constrained to the cross-flow direction, then the equations of motion become

$$\ddot{y} + y = -M\ddot{\phi} \tag{B.8}$$

$$\ddot{\phi} + \Omega^2\phi = -\ddot{y}. \tag{B.9}$$

The above two equations are symmetrically coupled through acceleration; therefore, they are stable. However, if the sign of the pendulum mass is artificially changed from positive to negative, i.e. from m_f to $-m_f$, then Eqs.(**??**) and (B.8) become

$$\ddot{y} + y = M\ddot{\phi} \tag{B.10}$$

$$\ddot{\phi} + \Omega^2\phi = -\ddot{y}. \tag{B.11}$$

If the above equations are compared to the following simplified form of the wake oscillator equation given by de Langre (2006)

$$\ddot{y} + y = \hat{M}\Omega^2 q \tag{B.12}$$

$$\ddot{q} + \Omega^2 q = A\ddot{y} \tag{B.13}$$

then the similarity between the two is obvious. Both systems predict a coupled mode flutter, which, according to de Langre (2006), is the possible fundamental mechanism of VIV.

The similarity between the wake oscillator model and a rigid pendulum with a negative mass for the cross-flow vibration, as described above, provides a possible way in

which to derive the form of coupling between the wake oscillator equation and the in-line motion. By changing m_f to $-m_f$, the equations of the motion of the system in the X direction are given as

$$\ddot{x} + x = -M\left(\ddot{\phi}\phi + \dot{\phi}^2\right) \tag{B.14}$$

$$\ddot{\phi} + \Omega^2\phi - \ddot{x}\phi = 0. \tag{B.15}$$

B

From the above equations, it can be seen that the coupling between the oscillator equation and the in-line motion can be most likely expressed in the form $-\ddot{x}q$, and the force in the in-line direction is in the form $-\left(\ddot{q}q + \dot{q}^2\right)$. For the sake of simplification, as well as for easy implementation, the form of in-line force used in this thesis is q^2, which has the same phase as $-\ddot{q}q$, while the term $\dot{q}^2$ is neglected. Further research is needed to determine whether using $-\left(\ddot{q}q + \dot{q}^2\right)$ instead of q^2 will improve the results. For the cross-flow vibration, the same form as that given by Eqs.(B.12) and (B.13) is still followed. Additional studies are also required to find out whether Eqs.(B.10) and (B.11) are more appropriate for the modelling of cross-flow VIV.

C

FINITE ELEMENT FORMULATION AND TIME INTEGRATION

C.1. DERIVATION OF THE STIFFNESS MATRIX OF THE BEAM ELEMENT

Substituting the variation of ϵ_0 and K, given by Eq. (5.7), and (5.8) into Eq. (5.4) yields

$$\delta W_S = \int_0^L \left(EA \frac{|\mathbf{r}_{,p}| - 1}{|\mathbf{r}_{,p}|} \mathbf{r}_{,p}^T \delta \mathbf{r}_{,p} - 2EI \frac{|\mathbf{r}_{,p} \times \mathbf{r}_{,pp}|^2}{|\mathbf{r}_{,p}|^6} \mathbf{r}_{,p}^T \delta \mathbf{r}_{,p} \right.$$
$$\left. + EI \frac{1}{|\mathbf{r}_{,p}|^4} \left(\mathbf{r}_{,p} \times \mathbf{r}_{,pp} \right)^T \left(\delta \mathbf{r}_{,p} \times \mathbf{r}_{,pp} + \mathbf{r}_{,p} \times \delta \mathbf{r}_{,pp} \right) \right) dp. \tag{C.1}$$

In three dimensions, Binet-Cauchy identity asserts that, for four vectors $\mathbf{a}$, $\mathbf{b}$, $\mathbf{c}$ and $\mathbf{d}$, the following relation holds

$$(\mathbf{a} \times \mathbf{b})^T (\mathbf{c} \times \mathbf{d}) = \left(\mathbf{a}^T \mathbf{c}\right) \left(\mathbf{b}^T \mathbf{d}\right) - \left(\mathbf{a}^T \mathbf{d}\right) \left(\mathbf{b}^T \mathbf{c}\right). \tag{C.2}$$

Applying Binet-Cauchy identity to Eq. (C.1), one obtains

$$\delta W_S = \int_0^L \left(EA \left(1 - \frac{1}{|\mathbf{r}_{,p}|} \right) \mathbf{r}_{,p}^T \delta \mathbf{r}_{,p} + EI \frac{1}{|\mathbf{r}_{,p}|^2} \mathbf{r}_{,pp}^T \delta \mathbf{r}_{,pp} \right.$$
$$- EI \frac{1}{|\mathbf{r}_{,p}|^4} \left(|\mathbf{r}_{,pp}|^2 \mathbf{r}_{,p}^T \delta \mathbf{r}_{,p} + \mathbf{r}_{,p}^T \mathbf{r}_{,pp} \left(\mathbf{r}_{,pp}^T \delta \mathbf{r}_{,p} + \mathbf{r}_{,p}^T \delta \mathbf{r}_{,pp} \right) \right)$$
$$\left. + EI \frac{2}{|\mathbf{r}_{,p}|^6} \left(\mathbf{r}_{,p}^T \mathbf{r}_{,pp} \right)^2 \mathbf{r}_{,p}^T \delta \mathbf{r}_{,p} \right) dp. \tag{C.3}$$

By substituting $\mathbf{r} = \mathbf{Se}$ into above equation, one obtains the expression of δW_S in the form of element coordinates, and it reads

$$
\begin{aligned}
\delta W_S = \mathbf{u}^T \int_0^L &\left(EI\gamma^2 \mathbf{S}_{,pp}^T \mathbf{S}_{,pp} - EI\gamma^4 \left(\mathbf{S}_{,p}^T \mathbf{S}_{,p} \right) \mathbf{u}\mathbf{u}^T \left(\mathbf{S}_{,pp}^T \mathbf{S}_{,pp} \right)^T \right. \\
&-EI\gamma^4 \left(\left(\mathbf{S}_{,pp}^T \mathbf{S}_{,p} \right)^T + \mathbf{S}_{,pp}^T \mathbf{S}_{,p} \right) \mathbf{u}\mathbf{u}^T \left(\mathbf{S}_{,pp}^T \mathbf{S}_{,p} \right) \\
&\left. +2EI\gamma^6 \left(\mathbf{u}^T \mathbf{S}_{,p}^T \mathbf{S}_{,pp} \mathbf{u} \right)^2 \mathbf{S}_{,p}^T \mathbf{S}_{,p} + EA \left(1 - \gamma \right) \mathbf{S}_{,p}^T \mathbf{S}_{,p} \right)^T dp\, \delta\mathbf{u}.
\end{aligned}
\tag{C.4}
$$

where $\gamma = \frac{1}{|\mathbf{r}_{,p}|}$. To make the element computationally more efficient for the cases where the axial deformation of the beam is very small, the γ is approximated as

$$
\gamma^n \approx n + 1 - n|\mathbf{r}_{,p}| = n + 1 - n\sqrt{\left(\mathbf{S}_{,p}\mathbf{u} \right)^T \left(\mathbf{S}_{,p}\mathbf{u} \right)}.
\tag{C.5}
$$

From Eq. (C.4), the stiffness matrix $\mathbf{K}_s^e$ of the beam element is derived as

$$
\begin{aligned}
\mathbf{K}_s^e = \int_0^L &\left(EI\gamma^2 \mathbf{S}_{,pp}^T \mathbf{S}_{,pp} - EI\gamma^4 \left(\mathbf{S}_{,p}^T \mathbf{S}_{,p} \right) \mathbf{u}\mathbf{u}^T \left(\mathbf{S}_{,pp}^T \mathbf{S}_{,pp} \right)^T \right. \\
&-EI\gamma^4 \left(\left(\mathbf{S}_{,pp}^T \mathbf{S}_{,p} \right)^T + \mathbf{S}_{,pp}^T \mathbf{S}_{,p} \right) \mathbf{u}\mathbf{u}^T \left(\mathbf{S}_{,pp}^T \mathbf{S}_{,p} \right) \\
&\left. +2EI\gamma^6 \left(\mathbf{u}^T \mathbf{S}_{,p}^T \mathbf{S}_{,pp} \mathbf{u} \right)^2 \mathbf{S}_{,p}^T \mathbf{S}_{,p} + EA \left(1 - \gamma \right) \mathbf{S}_{,p}^T \mathbf{S}_{,p} \right) dp.
\end{aligned}
\tag{C.6}
$$

To make the expression of the stiffness matrix brief, we denote

$$
Q_1 = \mathbf{S}_{,pp}^T \mathbf{S}_{,pp}, \quad Q_2 = \mathbf{S}_{,pp}^T \mathbf{S}_{,p} \quad and \quad Q_3 = \mathbf{S}_{,p}^T \mathbf{S}_{,p}.
\tag{C.7}
$$

Then, the expression of the stiffness matrix of the beam element becomes

$$
\begin{aligned}
\mathbf{K}_s^e = \int_0^L &\left(EI\gamma^2 Q_1 - EI\gamma^4 Q_3 \mathbf{u}\mathbf{u}^T Q_1 \right. \\
&-EI\gamma^4 \left(Q_2^T + Q_2 \right) \mathbf{u}\mathbf{u}^T Q_2 \\
&\left. +2EI\gamma^6 \left(\mathbf{u}^T Q_2^T \mathbf{u} \right)^2 Q_3 + EA \left(1 - \gamma \right) Q_3 \right) dp.
\end{aligned}
\tag{C.8}
$$

From Eq.(C.8), it can be seen that it would not be possible to factorise the element co-ordinates vector $\mathbf{u}$ out of the integrals because of the presence of γ. Therefore, here, the integrals in Eq.(C.8) are approximated using a Gaussian quadrature with five integration points.

The last term of Eq.(C.8), namely $EA \left(1 - \gamma \right) Q_3$, can be replaced by $\left(EA \left(1 - \gamma \right) + \gamma \left(P_e A_e - P_i A_i \right) \right) Q_3$ if the effective tension is taken into account. Here, P_e and P_i are the external and internal fluid pressures, which, in offshore applications, usually depend on the depth of the water and are therefore functions of the position vector. The above-mentioned term will be treated separately in different cases with a specific definition of the water depth.

C.2. NEWMARK-BETA TIME INTEGRATION SCHEME AND JACO-BIAN MATRIX

To solve the nonlinear equations of motion described by Eqs.(5.38) and (5.39), a step-by-step time history analysis must be employed. The Newmark-β method is one of the most widely used numerical integration approaches and will be used in this thesis.

For a dynamic system with a degree of freedom defined as $\mathbf{e}$, the finite difference approximations for the time interval $\Delta t = t_{i+1} - t_i$ are

$$\mathbf{e}_{i+1} \approx \mathbf{e}_i + \Delta t \dot{\mathbf{e}}_i + \Delta t^2 \left[\left(\frac{1}{2} - \beta \right) \ddot{\mathbf{e}}_i + \beta \ddot{\mathbf{e}}_{i+1} \right] \tag{C.9}$$

and

$$\dot{\mathbf{e}}_{i+1} \approx \dot{\mathbf{e}}_i + \Delta t \left[\left(1 - \gamma \right) \ddot{\mathbf{e}}_i + \gamma \ddot{\mathbf{e}}_{i+1} \right]. \tag{C.10}$$

The above two equations can be rewritten as

$$\ddot{\mathbf{e}}_{i+1} = \frac{1}{\beta \Delta t^2} \left(\mathbf{e}_{i+1} - \mathbf{e}_i \right) - \frac{1}{\beta \Delta t} \dot{\mathbf{e}}_i + \left(1 - \frac{1}{2\beta} \right) \ddot{\mathbf{e}}_i \tag{C.11}$$

and

$$\dot{\mathbf{e}}_{i+1} = \frac{\gamma}{\beta \Delta t} \left(\mathbf{e}_{i+1} - \mathbf{e}_i \right) + \left(1 - \frac{\gamma}{\beta} \right) \dot{\mathbf{e}}_i + \Delta t \left(1 - \frac{\gamma}{2\beta} \right) \ddot{\mathbf{e}}_i. \tag{C.12}$$

By substituting Eqs.(C.11) and (C.12) into the equilibrium of Eqs.(5.38) and (5.39) at time t_{i+1}, one obtains

$$\mathbf{M}^e_{s,i+1} \left[a_1 \left(\mathbf{u}_{i+1} - \mathbf{u}_i \right) + a_2 \dot{\mathbf{u}}_i + a_3 \ddot{\mathbf{u}}_i \right] + \mathbf{C}^e_{s,i+1} \left[b_1 \left(\mathbf{u}_{i+1} - \mathbf{u}_i \right) + b_2 \dot{\mathbf{u}}_i + b_3 \ddot{\mathbf{u}}_i \right] + \mathbf{K}^e_{s,i+1} \mathbf{u}_{i+1} = \mathbf{F}^e_{i+1} \tag{C.13}$$

$$\mathbf{M}^e_{q,i+1} \left[a_1 \left(\mathbf{q}_{i+1} - \mathbf{q}_i \right) + a_2 \dot{\mathbf{q}}_i + a_3 \ddot{\mathbf{q}}_i \right] + \mathbf{C}^e_{q,i+1} \left[b_1 \left(\mathbf{q}_{i+1} - \mathbf{q}_i \right) + b_2 \dot{\mathbf{q}}_i + b_3 \ddot{\mathbf{q}}_i \right] + \mathbf{K}^e_{q,i+1} \mathbf{q}_{i+1} = \mathbf{R}^e_{i+1} \tag{C.14}$$

where

$$\begin{aligned} a_1 &= \frac{1}{\beta \Delta t^2} \\ a_2 &= -\frac{1}{\beta \Delta t} \\ a_3 &= 1 - \frac{1}{2\beta} \\ b_1 &= \frac{\gamma}{\beta \Delta t} \\ b_2 &= 1 - \frac{\gamma}{\beta} \\ b_3 &= \Delta t \left(1 - \frac{\gamma}{2\beta} \right). \end{aligned} \tag{C.15}$$

With the response of the system known at time t_i, the displacement at time t_{i+1} can be obtained by solving algebraic equations Eq.(C.13) and (C.14). However, Eqs.(C.13) and (C.14) are nonlinear, since both the damping and stiffness matrix and the nodal

forces are response-dependent, and they need to be solved through iteration. Here, the Newton-Raphson method is applied, and the tangential stiffness (Jacobian matrix) of the system needs to be determined first.

The jacobian matrix of Eqs. (C.13) and (C.14) can be obtained by differentiating them in terms of the element coordinates $\mathbf{u}_{i+1}$ and $\mathbf{Q}_{i+1}$. For the sake of simplicity, the subscript $i+1$ is not used in the following derivations. Differentiating Eq. (C.13) with respect to $\mathbf{u}$ gives

$$\mathbf{J}_{s,\mathbf{u}}^e = a_1 \mathbf{M}_s^e + b_1 \frac{\partial\left(\mathbf{C}_s^e \mathbf{u}\right)}{\partial \mathbf{u}} + \frac{\partial\left(\mathbf{K}_s^e \mathbf{u}\right)}{\partial \mathbf{u}} - \frac{\partial \mathbf{F}^e}{\partial \mathbf{u}}. \tag{C.16}$$

Differentiating Eq. (C.13) respect to $\mathbf{q}$ yields

$$\mathbf{J}_{s,\mathbf{q}}^e = -\frac{\partial \mathbf{F}^e}{\partial \mathbf{q}}. \tag{C.17}$$

Similarly, differentiating Eq. (C.14) respect to $\mathbf{u}$ and $\mathbf{q}$ yields

$$\mathbf{J}_{q,\mathbf{u}}^e = \frac{\partial\left(\mathbf{K}_q^e \mathbf{q}\right)}{\partial \mathbf{u}} - \frac{\partial \mathbf{R}^e}{\partial \mathbf{u}} \tag{C.18}$$

$$\mathbf{J}_{q,\mathbf{q}}^e = a_1 \mathbf{M}_q^e + b_1 \frac{\partial\left(\mathbf{C}_q^e \dot{\mathbf{q}}\right)}{\partial \mathbf{q}} + \mathbf{K}_q^e. \tag{C.19}$$

Rayleigh damping has been applied to the structure, and from Eq. (5.27) it can be derived that

$$\frac{\partial\left(\mathbf{C}_s^e \mathbf{u}\right)}{\partial \mathbf{u}} = \alpha \mathbf{M}_s^e + \beta \mathbf{J}_s^{e,eq}. \tag{C.20}$$

With the expression of beam stiffness matrix given by Eq. (C.8), it can be derived that

$$\begin{aligned}
\frac{\partial\left(\mathbf{K}_s^e \mathbf{u}\right)}{\partial \mathbf{u}} = \int_0^L & EI\left(\gamma^2 Q_1 - 2\gamma^4 Q_1 \mathbf{u}\mathbf{u}^T Q_3\right. \\
& -\gamma^4\left(\left(\mathbf{u}^T Q_1 \mathbf{u}\right) Q_3 + Q_3 \mathbf{u}\mathbf{u}^T \left(Q_1 + Q_1^T\right)\right) + 4\gamma^6 Q_3 \mathbf{u}\mathbf{u}^T Q_1 \mathbf{u}\mathbf{u}^T Q_3 \\
& -\gamma^4\left(\left(\mathbf{u}^T Q_2 \mathbf{u}\right)\left(Q_2 + Q_2^T\right) + \left(Q_2 + Q_2^T\right)\mathbf{u}\mathbf{u}^T\left(Q_2 + Q_2^T\right)\right) + 4\gamma^6\left(Q_2 + Q_2^T\right)\mathbf{u}\mathbf{u}^T Q_2 \mathbf{u}\mathbf{u}^T Q_3 \\
& +2\gamma^6\left(2 Q_3 \mathbf{u}\mathbf{u}^T Q_2^T \mathbf{u}\mathbf{u}^T\left(Q_2 + Q_2^T\right) + \left(\mathbf{u}^T Q_2^T \mathbf{u}\right)^2 Q_3\right) - 12\gamma^8\left(\mathbf{u}^T Q_2^T \mathbf{u}\right)^2 Q_3 \mathbf{u}\mathbf{u}^T Q_3\right) \\
& + EA\left(\left(1 - \gamma\right) Q_3 + \gamma^3 Q_3 \mathbf{u}\mathbf{u}^T Q_3\right) dp.
\end{aligned} \tag{C.21}$$

As to the external nodal hydrodynamic forces $\mathbf{F}^e$, its derivative respect to $\mathbf{u}$ reads

$$\begin{aligned}
\frac{\partial \mathbf{F}^e}{\partial \mathbf{u}} = & \frac{1}{2}\rho D \frac{C_{L0}}{2} \int_0^L \mathbf{S}^T \left(\mathbf{S}_q \mathbf{q}\right)\left(2\mathbf{D}_{VL}\mathbf{U}_N^T \frac{\partial \mathbf{U}_N}{\partial \mathbf{u}} + |\mathbf{U}_N|^2 \frac{\partial \mathbf{D}_{VL}}{\partial \mathbf{u}}\right) dp \\
& + \frac{1}{2}\rho D C_{D0} \int_0^L \mathbf{S}^T \left(|\mathbf{U}_N|\mathbf{I} + \frac{\mathbf{U}_N \mathbf{U}_N^T}{|\mathbf{U}_N|}\right)\frac{\partial \mathbf{U}_N}{\partial \mathbf{u}} dp \\
& + \frac{1}{2}\rho D \alpha \frac{C_{L0}^2}{4} \int_0^L \left(\mathbf{S}_q \mathbf{q}\right)^2 \mathbf{S}^T \left(\frac{\mathbf{U}_{NX}\mathbf{U}_{NX}^T}{|\mathbf{U}_{NX}|} + |\mathbf{U}_{NX}|\mathbf{I}\right)\frac{\partial \mathbf{U}_{NX}}{\partial \mathbf{u}} dp
\end{aligned} \tag{C.22}$$

where

$$\frac{\partial \mathbf{U}_N}{\partial \mathbf{u}} = b_1 \left[\mathbf{t}^{eq} \left(\mathbf{t}^{eq} \right)^T - \mathbf{I} \right] \mathbf{S} \tag{C.23}$$

$$\frac{\partial \mathbf{D}_{VL}}{\partial \mathbf{u}} = b_1 \left[\frac{\mathbf{I}}{|\mathbf{t}^{eq} \times \mathbf{U}_N|} - \frac{\left(\mathbf{t}^{eq} \times \mathbf{U}_N \right) \left(\mathbf{t}^{eq} \times \mathbf{U}_N \right)^T}{|\mathbf{t}^{eq} \times \mathbf{U}_N|^3} \right] \left[\mathbf{t}^{eq} \right]_{\times} \left[\mathbf{t}^{eq} \left(\mathbf{t}^{eq} \right)^T - \mathbf{I} \right] \mathbf{S} \tag{C.24}$$

$$\frac{\partial \mathbf{U}_{NX}}{\partial \mathbf{u}} = -b_1 \mathbf{n}^{eq} \left(\mathbf{n}^{eq} \right)^T \mathbf{S}. \tag{C.25}$$

In Eq. (C.24), the operator $[]_{\times}$ denotes the skew-symmetric matrix, which is normally used to represent the cross products as matrix multiplications. The derivative of $\mathbf{F}^e$ with respect to $\mathbf{q}$ reads

$$\frac{\partial \mathbf{F}^e}{\partial \mathbf{q}} = \frac{1}{2} \rho D \frac{C_{L0}}{2} \int_0^L \mathbf{S}^T |\mathbf{U}_N|^2 \mathbf{D}_{VL} \mathbf{S}_q dp + \frac{1}{2} \rho D \alpha \frac{C_{L0}^2}{4} \int_0^L 2 \left(\mathbf{S}_q \mathbf{q} \right) |\mathbf{U}_{NX}| \mathbf{S}^T \mathbf{U}_{NX} \mathbf{S}_q dp. \tag{C.26}$$

From Eq. (5.32), it can be derived that

$$\frac{\partial \mathbf{K}_q^e \mathbf{q}}{\partial \mathbf{u}} = a_1 \frac{\kappa}{D} \int_0^L \mathbf{S}_q^T \mathbf{S}_q \mathbf{q} \left(\mathbf{n}^{eq} \right)^T \mathbf{S} dp. \tag{C.27}$$

Similarly, from Eqs.(5.37) and (5.31), the following is obtained.

$$\frac{\partial \mathbf{R}^e}{\partial \mathbf{u}} = \frac{A}{D} \int_0^L \mathbf{S}_q^T \left(\mathbf{b}^{eq} \right) \mathbf{S} dp \tag{C.28}$$

$$\frac{\partial \mathbf{C}_q^e \dot{\mathbf{q}}}{\partial \mathbf{q}} = 4\pi \mathrm{St}/D \int_0^L |\mathbf{V}_N^{eq}| \left(\mathbf{S}_q \mathbf{q} \right) \left(\mathbf{S}_q \dot{\mathbf{q}} \right) \mathbf{S}_q^T \mathbf{S}_q dp + b_1 \mathbf{C}_q^e. \tag{C.29}$$

C.3. VALIDATION OF THE FINITE ELEMENT MODEL

In this section, two numerical examples that are frequently used in the literature on non-linear beams are used to demonstrate the performance of the proposed finite element model. The first example is of the large deformation of a cantilever beam subjected to a tip load. The second example pertains to the dynamics of a 3D flexible pendulum.

C.3.1. STATIC EXAMPLE, CANTILEVER BEAM

The static problem of the large deformation of a cantilever beam subjected to a tip load, as illustrated in Fig.C.1, has already been used in literature for comparison, and the iterative solutions by means of the extensible elastic theory are given in Gerstmayr and Irschik (2008).

The parameters of the beam consist of length $L = 2$ m, the equivalent bending stiffness $EI = 1.725 \times 10^6$ N/m^2 and the equivalent axial stiffness $EA = 2.07 \times 10^9$ N. The tip load has been chosen according to $F_0 = 3EI/L^2$, which leads to a large deformation. Displacements of the tip in X and Y directions, obtained with different numbers of elements, are presented in Table C.1 wherein they are compared with the classical extensible elastic solution given in Gerstmayr and Irschik (2008). The proposed model, with 128 elements, already generates a result that matches the extensible elastic solution up to six digits.
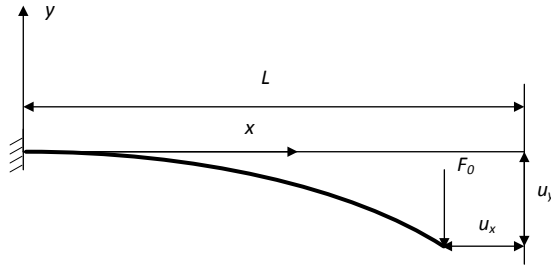
C

Figure C.1: Cantilever beam subjected to tip load.

Table C.1: Axial and transverse displacement of the tip of the cantilever beam using the proposed beam element model and comparison to the analytical solution of the extensible elastica

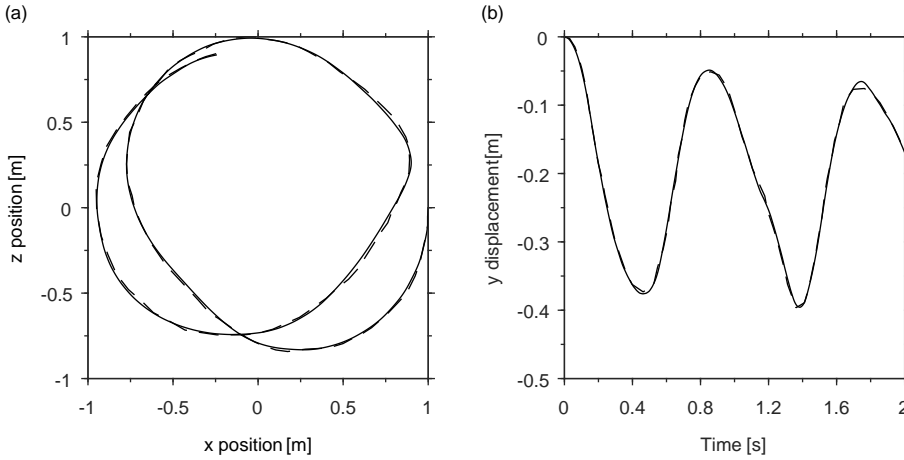| Elements	u_x	u_y
4	0.509715120993764	1.209144995093078
8	0.508604452895885	1.207351964767034
16	0.508541687577717	1.207246521801250
32	0.508537806636057	1.207240038638574
64	0.508537557824162	1.207239635075415
128	0.508537541233588	1.207239609883485
Ext. elastica	0.508537304325877	1.207239854549824

Figure C.2: Dynamic response of a large deformation pendulum. (a) Plot of the Z versus X co-ordinate of the mid-point of the three-dimensional pendulum; (b) Y-displacement of the mid-point of the three-dimensional pendulum as function of time. Simulation results with the proposed model are represented by dashed lines and reference results are represented by solid lines.

C.3.2. DYNAMIC EXAMPLE, LARGE DEFORMATION PENDULUM

The goal of the second example is to evaluate the performance of the proposed model in the case of 3D motion with a large rotation. The initially straight pendulum that is parallel to the X-Z plane has an initial angular velocity of 4 rad/s about the Y axis. Under the effect of gravity, the flexible pendulum will undergo a large rotation as well as deformation. The parameters of the pendulum consist of length $L = 1$ m, the equivalent bending stiffness $EI = 8.3 \times 10^{-5}$ N/m^2, equivalent axial stiffness $EA = 40$ N and the mass $m = 0.008$ kg/m. With only four elements, the implicit Newmark-beta method as described in C.2 is used to calculate the response of the pendulum with time steps of 0.1 ms. Fig.C.2(a) illustrates the position of the tip projected in X-Z plane, and Fig.C.2(b) shows the Y position of the middle point of the pendulum. A comparison are made between the solution of the proposed model and the cable element in Gerstmayr and Shabana (2006). Both figures indicate that the proposed model performs well in the case of 3D motion with a large rotation.

D

THREE DIFFERENT HYDRODYNAMIC FORCE MODELS

In this section, the equations for the three models compared in Chapter 6 are presented.

Model A

$$\ddot{q} + \epsilon(q^2 - 1)\dot{q} + q - \kappa \frac{\ddot{x}}{1 + \ddot{x}^2} q = A\ddot{y} \tag{D.1}$$

$$C_{VX} = \left(C_{DM}\left(1 - 2\pi St\dot{x}\right) + 2\pi St\dot{y}C_{VL}\right)\sqrt{(1 - 2\pi St\dot{x})^2 + \left(2\pi St\dot{y}\right)^2} \\ + \alpha C_{VL}^2 \left(1 - 2\pi St\dot{x}\right)|1 - 2\pi St\dot{x}| \tag{D.2}$$

$$C_{VY} = \left(-2\pi St\dot{y}C_{DM} + C_{VL}\left(1 - 2\pi St\dot{x}\right)\right)\sqrt{(1 - 2\pi St\dot{x})^2 + \left(2\pi St\dot{y}\right)^2} \tag{D.3}$$

where $C_{VL} = \frac{q}{2}C_{L0}$.

Model B

$$\ddot{q} + \epsilon(q^2 - 1)\dot{q} + q = A\ddot{y} \tag{D.4}$$

$$C_{VX} = \left(C_{DM}\left(1 - 2\pi St\dot{x}\right) + 2\pi St\dot{y}C_{VL}\right)\sqrt{(1 - 2\pi St\dot{x})^2 + \left(2\pi St\dot{y}\right)^2} \\ + \alpha C_{VL}^2 \left(1 - 2\pi St\dot{x}\right)|1 - 2\pi St\dot{x}| \tag{D.5}$$

$$C_{VY} = \left(-2\pi St\dot{y}C_{DM} + C_{VL}\left(1 - 2\pi St\dot{x}\right)\right)\sqrt{(1 - 2\pi St\dot{x})^2 + \left(2\pi St\dot{y}\right)^2} \tag{D.6}$$

where $C_{VL} = \frac{q}{2} C_{L0}$.

Model C

$$\ddot{q} + \epsilon(q^2 - 1)\dot{q} + q = A\ddot{y} \tag{D.7}$$

$$C_{VX} = \left(C_{DM}(1 - 2\pi St\dot{x}) + 2\pi St\dot{y}C_{VL}\right)\sqrt{(1 - 2\pi St\dot{x})^2 + \left(2\pi St\dot{y}\right)^2} \tag{D.8}$$

$$C_{VY} = \left(-2\pi St\dot{y}C_{DM} + C_{VL}(1 - 2\pi St\dot{x})\right)\sqrt{(1 - 2\pi St\dot{x})^2 + \left(2\pi St\dot{y}\right)^2} \tag{D.9}$$

where $C_{VL} = \frac{q}{2} C_{L0}$.

The three models differ from each other with respect to the inclusion of the in-line coupling term, namely $\kappa \frac{\ddot{x}}{1+\dot{x}^2} q$, in the wake oscillator equation and the in-line fluctuating force, namely $\alpha C_{VL}^2 (1 - 2\pi St\dot{x})|1 - 2\pi St\dot{x}|$, in the definition of C_{VX}.

Acknowledgements

Finally, this challenging journey of the PhD research has come to an end. Looking back at the 6 years of studying and working at TU Delft, I have a better understanding of the famous words of Han Yu: 'Diligence is the path through the mountain of books if there is a way, and hardship is the boat across the sea of study when there is no end'. There is no shortcut in the exploration of endless new knowledge; patience and persistence are required. During my PhD research, there were times when I felt lost, frustrated and depressed. I would not have made it through without the contributions, support and help from many people.

First, my most profound gratitude goes to my supervisor, Prof. Andrei Metrikine, who decided to accept my application for a PhD position after only a single, short Skype meeting. Andrei, I suppose it is because you saw the potential I have to be a researcher, although I remember telling you during that meeting that I am not particularly good at math. Thank you for leading me through such a challenging research topic and encouraging me to constantly pursue better results. Your confidence and optimistic spirit have helped me get through the dark times. The knowledge and research skills I have learned from you are the most valuable assets that I will benefit from in my future career.

I am grateful to all my colleagues from the research groups of Offshore Engineering and Dynamics of Solids and Structures for their support and making the past years enjoyable. Special thanks go to Joao. Joao, I enjoyed the time when you were tentatively a hydrodynamicist three years ago, and I benefited greatly from the experiment we conducted together. I would also like to thank Pim van der Male for always trying to help and reading my paper despite of his own busy schedule. Karel, Hayo and Richard, many thanks for your support, encouragement and help during the application of the funding. Although we didn't get it, I have learned a lot from the process. Maxim, I would like to thank you for reminding me how difficult and time consuming it can be at the last step of a PhD work. This can be sometimes very stressful, but it indeed pushes and helps me to keep working and finish my PhD as early as possible.

Living abroad is difficult and I would like to express my gratitude to those who make it easier and enjoyable. Special thanks go to Tao and Mingjuan. We are not only colleagues, but also close friends. Many thanks for your support for the past years. I could not experience such a pleasant life without your company. Hengqian, I would like to thank you for helping me arrange the accommodation and for the wonderful time we spend together playing guitar and drum. Many thanks to my old roommates, Zhiwei and Peijun, for your help and company since the first day I arrived. Thanks also go to Tao's wife, Die, for the tasty food (ps: not leftovers) she cooked for us. I would also like to thank all my other friends for their company in the Netherlands: Yaxi Peng, Rui Zhu, Kai Li, Shulan Shu, Zilong Wei, Xiaowei Ouyang, Chenjie Yu, Jianhuan Liu, Yixin Lv, Shanshan Ren, Guanliang Chen, Jintao Yu, Jian Fang, Tiantian Du, Zi Wang, Xuexue Chen, Bowei Huang, Wenjuan Lv, Tianchi Tang, and many others.

Curriculum Vitæ

Yang Qu

20 November 1986	Born in Yantai, Shandong, China.

Education

September 2002– July 2005	Shengli Oil Field No.1 Middle School Dongying, Shandong, China
September 2005– July 2009	Bachelor of Engineering in Mechanical Engineering Shandong University of Technology College of Mechanical Engineering Department of Mechanical Design
September 2009– July 2012	Master of Science in Mechanical Engineering China University of Petroleum(Huadong) College of Mechanical and Electronic Engineering Department of Mechanical and Electronic Engineering
February 2013– April 2019	Ph.D Research Delft University of Technology Faculty of Civil Engineering and Geosciences Department of Hydraulic Engineering Section of Offshore Engineering

LIST OF PUBLICATIONS

JOURNAL PAPERS

1. J.M. de Oliveria Barbosa, **Y. Qu**, A. Metrikine, and E. Lourens (2017). Vortex-induced vibrations of a freely vibrating cylinder near a plane boundary: experimental investigation and theoretical modelling. *Journal of Fluids and Structures*, 69:382-401.

CONFERENCE PAPERS

1. **Y. Qu** and A. Metrikine. Time domain simulation of vortex-induced vibration of a curved beam using a wake oscillator model. In: *Proceedings of the 5th ECCOMAS thematic conference on computational methods in structural dynamics and earthquake engineering*, COMDYN 2015.

2. **Y. Qu** and A. Metrikine. A wake oscillator model with nonlinear coupling for the VIV of rigid cylinder constrained to vibrate in the cross-flow direction. In: *Proceedings of the 35th International Conference on Ocean, Offshore and Arctic Engineering*, OMAE 2016.